

可重构折纸超材料
结构与性能调控研究

Structural Design and Property Tunability
of Reconfigurable Origami Metamaterials

一级学科: 机械工程
研究方向: 折纸超材料
作者姓名: 刘伟奇
指导教师: 陈焱 教授

答辩日期	2024 年 05 月 17 日		
答辩委员会	姓名	职称	工作单位
主席	黄田	教授	天津大学
委员	郭宏伟	教授	哈尔滨工业大学
	蔡建国	教授	东南大学
	何柏岩	教授	天津大学
	马家耀	教授	天津大学

天津大学机械工程学院
二〇二四年六月

独创性声明

本人声明所呈交的学位论文是本人在导师指导下进行的研究工作和取得的研究成果，除了文中特别加以标注和致谢之处外，论文中不包含其他人已经发表或撰写过的研究成果，也不包含为获得天津大学或其他教育机构的学位或证书而使用过的材料。与我一同工作的同志对本研究所做的任何贡献均已在论文中作了明确的说明并表示了谢意。

学位论文作者签名：刘伟奇 签字日期：2024年5月6日

学位论文版权使用授权书

本学位论文作者完全了解天津大学有关保留、使用学位论文的规定。特授权天津大学可以将学位论文的全部或部分内容编入有关数据库进行检索，并采用影印、缩印或扫描等复制手段保存、汇编以供查阅和借阅。同意学校向国家有关部门或机构送交论文的复印件和磁盘。

(保密的学位论文在解密后适用本授权说明)

学位论文作者签名：刘伟奇

导师签名：

陈敏

签字日期：2024年5月6日

签字日期：2024年5月13日

摘要

基于机构运动的折纸结构设计空间广、变形能力强、性能调控范围宽，在大变形机械超材料的设计中发挥着重要的角色。但现有折纸超材料研究在具有多变形模式的单自由度结构设计和性能调控策略方面尚未形成系统方法。本文基于分叉重构机构，提出了一系列单自由度可重构折纸创新设计，包括零厚度折纸、厚板折-剪纸、以及模块化折纸，进行了超材料的性能可调控性分析。

首先，本文开发了结合机构运动协调条件与图形表达的简易算法，可以精准辨识四折痕折纸及其镶嵌的山谷线重构并去除重复构型。利用此算法，研究揭示了三种具有恒定山谷线分布数量的 2D 寡模式折纸图案和一种可以通过调整山谷线分布展现出面内负、零和正泊松比特性的 3D 多模式蜂窝折纸结构。

其次，本文将垂直转移铰链嵌入厚板结构中，设计了一种融合折纸、剪纸和折-剪纸运动模式的单自由度可重构单元及其镶嵌结构。通过对与可重构单元等价的机构的闭环方程显式解的推导，深入分析了设计参数对可重构单元运动学行为的影响。研究表明，通过优化设计参数，单一超材料能够兼具各向异性或各向同性的负泊松比，大折展比、以及多种承载特性。

接着，本文设计了基于单闭环空间七杆机构的模块化折纸单元，并系统分析了几何参数对该单元运动学行为的影响。根据单元的运动分叉特性，提出了两套单自由度的可重构 2D 模块的构造方案。其中，采用背靠背式装配的模块及其镶嵌在变刚度材料或气驱下可实现所有晶体学平面对称群。而通过肩并肩式装配的模块及其构造的一类 3D 棱柱结构，呈现出面内的负、零和正泊松比，甚至任意面内面外泊松比符号的组合。

最后，本文分析了模块化立方体结构中平面连杆组在对称性约束下的分叉行为，揭示了可重构模块在分叉过程中伴随的可调泊松比、手性和刚度等特性。基于几何和运动协调性，提出了混合正、负泊松比模块的组合设计策略，以增强 3D 超材料的可调和可编程性。利用模块的可重构性，实现了超材料正交平面上泊松比在 $(-\infty, +\infty)$ 大范围内的独立编程调控。并以模块化立方体为基础，衍生了一类具有负、零和正泊松比的单自由度可重构棱柱。

本文系统研究了机构分岔理论指导设计具有多形状变化能力的单自由度可重构折纸的方法，为发展具有性能可调和可编程大变形机械超材料及其工程应用提供理论基础与技术支撑。

关键词：分叉可重构机构，折纸超材料，零厚度折纸，厚板折-剪纸，模块化折纸

ABSTRACT

Kinematic-based origami structure, with its flexible design space, powerful deformation capability, and wide range of property tunability, plays a crucial role in designing large deformation mechanical metamaterials. However, existing studies on origami metamaterials have not yet developed systematic approaches in terms of single degree-of-freedom (DOF) structures with multiple deformation modes and property tuning strategies. In this dissertation, a series of innovative designs of single DOF reconfigurable origami, including zero-thickness origami, thick-panel ori-kirigami, and modular origami, are proposed to analyse the property tunability of metamaterials. The highlights of this dissertation are as follows.

Firstly, a straightforward algorithm that combines motion compatibility conditions and graphic representation is developed to accurately assess the mountain-valley (MV) crease reconfiguration and obtain duplicate configurations in origami structures with 4-crease vertices and their tessellations. The analysis has revealed three types of two-dimensional (2D) oligo-modal origami tessellations characterised by a consistent number of MV assignments independent of tessellation size. A three-dimensional (3D) pluri-modal cellular origami structure is proposed that exhibits in-plane negative, zero and positive Poisson's ratios (NPR/ZPR/PPR) through MV crease reconfiguration.

Secondly, by embedding vertically transferable joints (VTJ) into the thick-panel structure, a single DOF reconfigurable ori-kirigami unit and its tessellations integrating origami, kirigami, and ori-kirigami motion branches are designed. Explicit solutions of the closure equations of the assemblies are derived to analyse the effects of the design parameters on the kinematic behaviour of the reconfigurable unit, thus enabling a single mechanical metamaterial to combine the properties of anisotropic or isotropic NPR, large deployable ratio, and multiple load-bearing capacity.

Thirdly, a single closed-loop spatial seven-revolute (7R) linkage in modular origami form is proposed. The effects of geometric parameters on the kinematic bifurcation behaviour of this basic unit are systematically analysed. According to the kinematic bifurcation behaviour of the 7R unit, two types of single DOF reconfigurable 2D modules are constructed. A back-to-back assembly of the modules and their tessellations is employed to realise tunability in all crystallographic planar symmetry groups under variable stiffness materials or pneumatic actuation. It's also found that 2D

modules in shoulder-to-shoulder assembly and their constructed 3D prismatic structures exhibit in-plane NPR, ZPR and PPR, and even arbitrary in-plane and out-of-plane Poisson's ratio signs.

Finally, the bifurcation behaviour of an open-chain planar linkage group (PLG) in a single DOF modular cube under symmetry constraints is analysed, revealing the tuneable Poisson's ratio, chirality, and stiffness that accompany the kinematic bifurcation of this reconfigurable 3D module. To enhance the programmability of metamaterials, a combinatorial design strategy is proposed, i.e., mixing modules with PPR and ZPR, based on geometric and kinematic compatibility. The reconfigurability of the modules is utilized to achieve independent programming of Poisson's ratio in the orthogonal plane of the metamaterial over a wide range from $-\infty$ to $+\infty$. At last, a class of single DOF reconfigurable prismatic structures with NPR, ZPR, and PPR are developed inspired by the modular cube.

In summary, the design method of single DOF reconfigurable origami with multi-shape change capability, directed by kinematic bifurcation theory, is systematically studied in this dissertation, thus providing the theoretical foundation and technical support for developing large deformation mechanical metamaterials with tunability and programmability as well as their engineering applications.

KEY WORDS: Reconfigurable linkage with bifurcation behaviour; Origami metamaterial; Zero-thickness origami; Thick-panel ori-kirigami; Modular origami

Contents

摘要.....	I
ABSTRACT.....	III
Contents.....	V
List of Figures	IX
List of Tables	XIX
Notation.....	XXI
Chapter 1 Introduction	1
1.1 Background and Significance	1
1.2 Review of Previous Works	4
1.2.1 Origami Kinematics	4
1.2.2 Reconfigurable Mechanisms	7
1.2.3 Origami Mechanical Metamaterials	12
1.3 Aim and Scope	24
1.4 Main Contents	24
Chapter 2 Mountain-Valley Crease Reconfiguration of 4-Crease Origami Vertices and Tessellations	27
2.1 Introduction	27
2.2 Evaluation Method for Reconfigurability	27
2.2.1 Kinematics of the Four-crease Vertices and Their Assemblies	27
2.2.2 Graphic Representation of Origami Modules	32
2.2.3 Algorithm Design for Origami Tessellation with Size $m \times n$	35
2.3 Reconfigurability of Origami Tessellations	38
2.3.1 2D Origami Tessellations	38
2.3.2 3D Cellular Origami Structure	43
2.4 Conclusions	48
Chapter 3 Integration of Origami, Kirigami and Ori-Kirigami in Thick Panels by Transferable Joints	49
3.1 Introduction	49
3.2 Single Reconfigurable Unit with Vertically Transferable Joints	50
3.2.1 Vertically Transferable Joints	50
3.2.2 Characterization of a Single Unit	51

3.2.3 Motion Branches of a Single Unit.....	52
3.3 Tessellation of Reconfigurable Units with Tuneable Properties	60
3.3.1 Tessellation Method and Motion Branches	60
3.3.2 Tuneable Properties of the Tessellation.....	66
3.4 Conclusions	72
Chapter 4 Tuneable Metamaterials Based on Spatial 7R Linkage in Modular Origami Form	73
4.1 Introduction	73
4.2 Kinematics of the Spatial 7R Linkage in Modular Origami Form.....	73
4.2.1 Characterization of Modular Origami Unit.....	73
4.2.2 Effect of Geometric Parameters on Motion Behaviours	76
4.3 Reconfiguration of Origami Modules and Their Tessellations	80
4.3.1 Tunability in Two Families of Rosette Groups	80
4.3.2 Tunability in Seven Frieze Groups.....	87
4.3.3 Tunability in Seventeen Wallpaper Groups.....	89
4.3.4 Methods of Active Symmetry Tuning	92
4.4 Modular Origami Tuneable in All Signs of Poisson’s Ratio	96
4.4.1 2D Modules Design and Deformation Mechanism Analysis	96
4.4.2 3D Modules Design and Deformation Mechanism Analysis	101
4.5 Conclusions	107
Chapter 5 3D Programmable Metamaterials Based on Reconfigurable Polyhedron Module	109
5.1 Introduction	109
5.2 Kinematics of the Polyhedron Module	110
5.2.1 Geometry of Wohlhart Cube	110
5.2.2 Reconfigurability of PLG in the Wohlhart Cube.....	110
5.2.3 Bifurcation Behaviours of the Polyhedron Module	114
5.3 Properties of a Single Polyhedron Module	117
5.3.1 The Variations of Geometric Dimensions of the Module	117
5.3.2 Mechanical Properties for a Single Module.....	119
5.4 3D Metamaterials with Programmable Poisson’s Ratio.....	128
5.4.1 The Series Assembly with (m_z+n_z) Modules	129
5.4.2 Metamaterials with the 3D Tessellation of Modules.....	131

5.5 A Family of Single DOF Reconfigurable Polygon Prisms.....	136
5.6 Conclusions	139
Chapter 6 Final Remarks.....	141
6.1 Main Achievements.....	141
6.2 Future Work.....	144
References	147
Appendix	161
中文大摘要.....	173
Publications and Research Projects during PhD's Study	179
Acknowledgements	181

List of Figures

Fig. 1-1	Artworks for origami, kirigami, and modular origami. (a) An origami crane folded from a sheet of paper ^[33] ; (b) a kirigami tower, RES Octagon Star ^[34] , involves cuts in a sheet of paper; (c) a modular origami toy, Snapology ^[35] , created by multiple sheets of paper.2	2
Fig. 1-2	Origami engineering. (a) An origami-based deployable solar array ^[22] ; (b) the metre-scale inflatable shelter ^[23] ; (c) high-load capacity origami transformable wheel ^[24] ; (d) curved display ^[25] ; (e) energy absorption structure with a kirigami-inspired pyramid foldcore ^[26] ; (f) origami soft gripper ^[27] ; (g) kirigami-inspired miniature manipulator for teleoperated microsurgery ^[28] ; (h) active mechanical haptics for immersive virtual reality based on curved origami ^[29] ; (i) modular origami-based mechanical metamaterials with static non-reciprocity ^[36]3	3
Fig. 1-3	Linkage forms of zero-thickness origami vertices and their tessellations. (a) Four-crease vertex with zero thickness and corresponding spherical 4R linkage ^[42] ; (b) origami pattern with multiple four-crease vertices and corresponding mobile network of spherical linkages ^[45]4	4
Fig. 1-4	Linkage forms of thick-panel origami vertices and their tessellations ^[49] . (a) The Miura-ori vertex in thick-panel form and corresponding Bennett 4R linkage; (b) the Miura-ori pattern and corresponding mobile network of spatial linkages.6	6
Fig. 1-5	Reconfigurable 6R linkages with kinematic bifurcation. (a) A special line and plane-symmetric Bricard linkage ^[72] ; (b) plane-symmetric Bricard 6R linkage ^[73] ; (c) line-symmetric Goldberg 6R linkage ^[75] (b) double-centered 6R linkage ^[76]8	8
Fig. 1-6	Mountain-valley crease reconfiguration of the double corrugated vertex in spherical 4R linkage form. Mountain and valley creases are indicated by red solid lines and blue dotted lines.9	9
Fig. 1-7	Single-loop reconfigurable linkages inspired by origami designs. (a) and (b) reconfigurable 6R linkages ^[85,90] ; (c) and (d) reconfigurable 8R linkages ^[92,93]10	10
Fig. 1-8	Reconfigurable polyhedral linkages with single DOF. (a) Constructed by reconfigurable straight elements ^[96] ; (b) constructed by reconfigurable parallelogram linkages ^[98] ; (c) constructed by asymmetric 8R linkage ^[100]11	11
Fig. 1-9	Rigid origami-based mechanical metamaterials with a single deformation path. (a) The Miura-ori pattern with in-plane NPR ^[112] ; (b) graded cellular structures ^[116] ; (c) cellular origami metamaterial formed by zipper-coupled	

	tubes ^[119] ; (d) cellular structure formed by Miura-based closed-loop origami units ^[120] ; (e) Tachi-Miura polyhedron ^[121-123] ; (f) hybrid Miura-based metamaterial ^[118]	14
Fig. 1-10	Reconfigurable origami-based mechanical metamaterials deform along multiple motion paths. (a) The morph pattern with sign switchable Poisson's ratio ^[133] ; (b) reconfiguration of Tachi-Miura polyhedron for heterogeneous metamaterials ^[134] ; (c) variant of the stacked Miura-ori origami for the mechanical logic gate ^[135]	16
Fig. 1-11	Cut-only kirigami-based 2D and 3D mechanical metamaterials. (a) Auxetic behaviour generated by rotating square units ^[136] ; (b) various rotating unit structures ^[137] ; (c) a Kagome lattice and its corresponding two collapsing modes ^[138] ; (d) and (e) are examples of hierarchical kirigami patterns with extremely large strains ^[139,140] ; (f) kirigami-based inverse design enables transformation between two 2D target shapes ^[141] ; (g) kirigami designs for 3D shape programming based on rotating square units ^[143] and (h) rotating triangular units ^[145,146]	18
Fig. 1-12	Ori-kirigami-based mechanical metamaterials. (a) Cuts and creases are introduced in a continuous flat sheet ^[149,158] ; (b) checkerboard kirigami ^[12] ; (c) zigzag kirigami ^[152,159] ; (d) adding creases to existing rigid kirigami patterns ^[154] ; (e) remove some of the panels from a rigid origami pattern ^[153] ; (f) arranging creases and cuts at the surfaces and edges of polyhedrons to obtain rigid kirigami patterns ^[155]	20
Fig. 1-13	Modular origami-inspired mechanical metamaterials with a single deformation path. (a) (a) A Sarrus linkage-based 3D modular structure ^[163] ; (b) 3D metamaterials with programmable almost constant Poisson's ratio ^[164] ; (c) 3D modular metamaterials with customized bi-stability ^[165]	22
Fig. 1-14	Modular origami-inspired mechanical metamaterials with multiple deformation paths. (a) A snapology-inspired transformable metamaterial with multi-DOFs ^[167] ; (b) reconfigurable prismatic architected materials ^[168] ; (c) the inverse design of 3D reconfigurable curvilinear modular origami structures ^[169] ; (d) an eight cube-based kirigami module-based reconfigurable and reprogrammable architected matter ^[170] ; (e) 3D transformable modular kirigami-based programmable metamaterials ^[171] ; (f) 3D metamaterials transformed for different zero modes ^[13]	23
Fig. 1-15	Diagram of the main contents of this dissertation.....	25
Fig. 2-1	Evolution among a generic four-crease vertex and three types of vertices, i.e., double corrugated, Miura-ori, and symmetric Eggbox vertices.....	28
Fig. 2-2	Kinematics of three types of 4-crease vertices. (a-c) From left to right are origami vertices with un-predefined MV assignment, linkage form, and	

	kinematic paths θ_2 vs θ_1 plus MV assignments for the double corrugated, Miura-ori, and symmetric Eggbox vertices, respectively.	31
Fig. 2-3	Motion compatibility of assemblies of spherical 4R linkages. (a) The quadrilateral mesh origami and the corresponding mobile assembly and (b) the motion transmission path.	32
Fig. 2-4	Graphic representations of a single vertex. The blue and red fillings represent MV-I and MV-II assignments, respectively, while circles with black boundaries, circles without boundaries, and triangles with upward or downward orientations represent (a) double corrugated, (b) Miura-ori, and (c) symmetric Eggbox ($\sum\alpha_{i(i+1)} < 2\pi$ and $\sum\alpha_{i(i+1)} > 2\pi$) vertices, respectively.	33
Fig. 2-5	Graphic representations of eighteen typical modules consisting of double corrugated, Miura-ori, symmetric Eggbox vertices and their hybridization.	34
Fig. 2-6	Algorithm design for origami tessellation with size $m \times n$. (a) A tessellation without presupposed MV assignments consists of basic modules, and the connection module can be described as a checkerboard with size $m \times n$ and a null matrix. (b) The matrix can be further assigned values according to graphic representations of modules.....	36
Fig. 2-7	The search results for the number of valid MV assignments of a double corrugated pattern. (a) Valid or unique MV assignments of a $n \times n$ double corrugated pattern tessellations. (b) Duplicates by assessing the symmetry of the matrix. (c) The eighteen unique MV assignments and corresponding graphical representations of 4×4 double corrugated pattern tessellations.	39
Fig. 2-8	Three types of oligo-modal origami with a constant number of MV assignments independent of tessellation sizes. (a) Dual square twist pattern, (b) Huffman pattern, and (c) Helical patterns.	42
Fig. 2-9	Reconfigurability of 3D cellular origami structure. (a) Views of cellular origami structure and chessboard of $3 \times 3 \times 3$ tessellation in the front view. (b-d) Graphic representations of the basic module, connection modules i and ii. (e) The result of the search for the number of valid and unique configurations with different tessellation sizes.	44
Fig. 2-10	The $3 \times 3 \times 3$ tessellation. (a) The bifurcation configuration of the tessellation and its three typical configurations as well as graphic representations. (b) Folding process of the prototype.....	46
Fig. 2-11	Quantitative analysis of Poisson's ratio. (a) The experimental setups. The black speckles of the panels are used to evaluate the dimensions. (b)	

	Comparison of experimental and theoretical results. Data are expressed as the mean and standard deviation of three tests.....	48
Fig. 3-1	Vertically transferrable joint technique. (a) Mountain crease replaced by VTJ and (b) valley crease replaced by VTJ. Arrows and grey circles accompany these representations, where arrowheads indicate the direction of joint transfer, and circles signify the joint axes located in the direction of thickness.....	50
Fig. 3-2	Diamond pattern-based integration design. (a) Modified unit with vertical transferable joints evolved from six-crease vertex; (b) thick-panel form of the modified unit.	52
Fig. 3-3	Thick-panel origami branch of a modified unit in diamond vertex mode. (a) Crease pattern of the unit; (b) thick-panel form of the unit.	53
Fig. 3-4	Relationship between dihedral angles φ_2 and φ_1 and corresponding configurations in thick-panel origami branch. (a) The kinematic paths of a single unit. The path for the case of $\alpha = 30^\circ$ line a is in black, and the one for the case of $\alpha = 45^\circ$ is in red. (b) Motion sequence of the unit with $\alpha = 30^\circ$; (c) motion sequence of the unit with $\alpha = 45^\circ$	53
Fig. 3-5	Thick-panel kirigami branch of the modified unit. (a) Crease pattern of the unit; (b) thick-panel form of the unit.....	54
Fig. 3-6	Relationship between dihedral angles φ_2 and φ_1 , and corresponding configurations in thick-panel origami branch.	55
Fig. 3-7	Thick-panel ori-kirigami branch I of the modified unit with two-fold plane-symmetry. (a) Crease pattern of the unit; (b) thick-panel form of the unit. ...	56
Fig. 3-8	Relationship between dihedral angles φ_2 and φ_1 and corresponding configurations in thick-panel ori-kirigami branch I with two-fold plane-symmetry.	56
Fig. 3-9	Thick-panel ori-kirigami branch II of the modified unit with solo symmetry plane. (a) Crease pattern of the unit; (b) thick-panel form of the unit.	57
Fig. 3-10	Relationship between dihedral angles φ_2 and φ_1 and corresponding configurations in thick-panel ori-kirigami branch II.....	58
Fig. 3-11	Thick-panel ori-kirigami branch III of the modified unit with solo symmetry plane. (a) Crease pattern of the unit; (b) thick-panel form of the unit.	59
Fig. 3-12	Relationship between dihedral angles φ_4 and φ_3 and corresponding configurations in thick-panel ori-kirigami branch III. (a) The kinematic paths with $\alpha = 30^\circ$ when $t/l = 1/4$ and $t/l = \sqrt{2}/2$; (b) the kinematic	

	paths with $\alpha = 45^\circ$ when $t/l = 1/4$ and $t/l = \sqrt{2}/2$, respectively; (c-f) motion sequence of the unit with different design parameters.....	59
Fig. 3-13	The prototype of a single unit with $\alpha = 45^\circ$, $l = 40\text{mm}$, $t = 28.28\text{mm}$. Triangular panels are made of cardboard and non-stretchable tapes are made of high density polyethylene fibre.....	61
Fig. 3-14	The formation and connectivity of 2×2 tessellation.....	62
Fig. 3-15	Tessellations of thick-panel origami mode. (a) Crease pattern of 2×2 origami tessellation; (b) and (c) are single DOF motion sequence of 2×2 and 4×4 origami tessellations.....	62
Fig. 3-16	Tessellations of thick-panel kirigami mode. (a) Pattern of 2×2 tessellation and its (b) level-I deformation and (c) level-II deformation; (d) single DOF motion sequence of 4×4 origami tessellations, where i-ii-iii correspond to configurations in level-I deformation, iii-iv-v correspond to configurations of in level-II deformation.	63
Fig. 3-17	Tessellations of thick-panel ori-kirigami I. (a) Crease pattern of 2×2 tessellation; (b) and (c) are single DOF motion sequences of 2×2 and 4×4 tessellations.	64
Fig. 3-18	Tessellations of thick-panel ori-kirigami mode II. (a) Crease pattern of 2×2 tessellation; (b) and (c) are single DOF motion sequence of 2×2 and 4×4 tessellations.	65
Fig. 3-19	Tessellation of thick-panel ori-kirigami mode III. (a) Crease pattern of 2×2 tessellation; (b) single DOF motion sequence of 2×2 tessellations.	65
Fig. 3-20	Singe DOF folding process of the prototype with $\alpha = 45^\circ$, $l = 40\text{mm}$, $t = 28.28\text{mm}$	66
Fig. 3-21	Dimension and Poisson's ratio variations of the 4×4 kirigami tessellation. (a) Variations in dimensions; (b) variations in Poisson's ratio.	67
Fig. 3-22	The simulation results of the in-plane Poisson's ratios ν_{BW} when the tessellation enters the origami branch, ori-kirigami branches I-III. (a)-(d) refer to origami and ori-kirigami branches I-III, respectively.....	68
Fig. 3-23	Deployable ratio of five motion branches. The labels ori-, kiri-, ori-kiri I-III on the x -axis refer to origami, kirigami, and ori-kirigami branches I-III, respectively.....	69
Fig. 3-24	Compression experiments with folding or unfolding configurations along motion branches. (a) Experimental setup; (b)-(f) experimental force-displacement curves for origami, kirigami, ori-kirigami I-III branches, respectively.....	70
Fig. 3-25	Normalised maximum force for origami, kirigami, ori-kirigami I-III branches.....	71

Fig. 4-1	The geometric design of Spatial 7R Linkage in modular origami form. (a) Components of modular origami unit and (b) its equivalent 7R linkage...74
Fig. 4-2	Four possible motion modes M1-M4 of the modular origami unit.....75
Fig. 4-3	Effects of geometric design parameters (b/a and α) on motion branches..77
Fig. 4-4	Effect of geometric parameters on kinematic bifurcation. (a) Kinematic paths of the unit under different design parameters of cases ①-⑥ (assuming $\alpha = 2\beta = 2\gamma = 90^\circ$), where the curve for motion branches M1, M2, M3, and M4 are in blue, black, green and red respectively. And physical interference is indicated by dotted lines. (b-g) The motion sequence of the modular origami unit in cases ①-⑥, where b/a changes from $1/2$ to $3/4$, 1 , $5/4$, $\sqrt{2}$, and $\sqrt{3}$80
Fig. 4-5	Effect of geometric parameters on physical interference. (a) φ_5 vs φ_1 for kinematic paths of modified modular origami unit in case ⑤ with different angles γ ; (b) the motion sequence of the modular origami unit in case ⑤ with $\gamma = 30^\circ$; (c) φ_5 vs φ_1 for kinematic paths of modified modular origami unit in case ⑥ with different angles β ; (d) the motion sequence of the modular origami unit in case ⑥ with $\beta = 35^\circ$. The physical interference is denoted as dotted lines.83
Fig. 4-6	Construction of origami modules by a back-to-back assembly. (a) A folded n -sided ($n=3, 4, 5, 6$) shape and an unfolded $2n$ -sided shape as the target shapes. The dotted grey line shows the shape of the bottom platform. (b) Origami modules are formed by a back-to-back assembly.84
Fig. 4-7	Reconfiguration of the origami module with $n = 4$, $\alpha = 90^\circ$ accompanied by tuneable symmetries. The key reflection axes are represented by centre lines, while the centres of 2-fold and 4-fold rotational symmetry are represented by rhombus and squares, respectively.....85
Fig. 4-8	Reconfiguration of the origami modules with $n=3, 5$, and 6 accompanied by tuneable symmetries.....86
Fig. 4-9	Prototypes with ten 2D crystallographic point groups, i.e., d1, d2, d3, d4, d6, c1, c2, c3, c4, c6, constructed from only two modules with $n=4$ and $n=6$.87
Fig. 4-10	All seven frieze patterns constructed by the modules with $n = 4$, $\alpha = 90^\circ$. (a) Translation unit and its basic generating region (grey area); (b) periodic border designs.88
Fig. 4-11	Seventeen wallpaper patterns constructed by the modules with $n=4$ and 6 . (a) Twelve wallpaper groups with 1-fold, 2-fold, and 4-fold rotational

	symmetry; (b) five wallpaper groups with 3-fold and 6-fold rotational symmetry.	91
Fig. 4-12	Active symmetry tuning by mechanical loading with variable stiffness materials. (a) A PLA sheet with thickness=1mm and a PI film heater with thickness=0.2mm are bound together; (b) origami module with eight variable stiffness beams; (c) deformation mechanisms of a pair of neighbouring beams E and F. (d) The prototype with $n = 4, \alpha = 90^\circ$, and $b/a = 1, l = 3a/4$. (e) Example of tuning the module from d4 symmetry to partially compressed d2 configuration with beams coded “10011001”. (f) Experimental results with d4, c2, d1, c4, d2, d1, and c1 symmetries.	93
Fig. 4-13	Pneumatic actuation. (a) Prototype for pneumatic actuation; (b) mechanism of pneumatic actuation; (c) experimental results with d4, c2, d1, c4, d2, d1, and c1 symmetries where air pockets in the prototype are coded as “0000000”, “00010001”, “00000101”, “01010101”, “10001000”, “01000110”, and “01010010”; (d) twelve configurations featuring distinct symmetry groups of a single 2×2 tessellation.	95
Fig. 4-14	Reconfigurable modules constructed in the form of shoulder-to-shoulder assembly. (a) modified 7R unit; (b) 2D modules with different numbers and design parameters of 7R units.	97
Fig. 4-15	Three possible states for two rectangular panels along either the x or y direction and corresponding variations in the overall dimensions of the 2D module with $n=4$	98
Fig. 4-16	Top views of kinematic paths of the 2D module featuring a regular 4-sided polygon projection when the 7R unit switches between M1 and M2.	99
Fig. 4-17	Prototype of the 2D module with $b/a = \sqrt{2}$, $\alpha = 90^\circ$ and its reconfiguration between four kinematic paths.	100
Fig. 4-18	Plots of ε_w and ε_B vs deformation degree in kinematic paths for the modules.	101
Fig. 4-19	Construction of 3D modules based on four selected polyhedrons, i.e., triangular prism ($N=3$), rectangular prism ($N=4$), pentagonal prism ($N=5$) and hexagonal prism ($N=6$).	102
Fig. 4-20	Kinematic compatibility conditions for 3D modules.	103
Fig. 4-21	Deformation modes for 3D modules with triangular prism ($N=3$), rectangular prism ($N=4$), pentagonal prism ($N=5$) and hexagonal prism ($N=6$).	104
Fig. 4-22	Configurations for the 3D module with $N=4$. (a) The configuration of the 3D module ($N=4$) is a combination of three states of the relative positions	

	of the two L-shaped links in three directions. (b) Six typical configurations.	106
Fig. 4-23	Deformation modes for 3D modules with rectangular prism ($N=4$) contour.	107
Fig. 5-1	The Wohlhart cube formed by connecting PLGs with cube connectors. (a) The geometry of rigid link, square centre body, and cube connector; (b) views of the clockwise rotation PLG and the anti-clockwise rotation PLG; (c) overview of the Wohlhart cube.	110
Fig. 5-2	The coordinate systems of PLG.	111
Fig. 5-3	The kinematic paths and corresponding configurations. (a) Kinematic paths θ_2 vs θ_1 , (b) kinematic paths θ_i vs θ_1 , and (c) bifurcation behaviours, where i, iii, iv, vi, vii, ix are motion sequences, while ii, v, and viii are the bifurcation configurations.	113
Fig. 5-4	The construction method of the Wohlhart cube. (a) Components and polyhedron base; (b) construction of the Wohlhart cube with rotation, translation, and locked PLGs.	115
Fig. 5-5	Kinematic bifurcation of the Wohlhart cube. (a) The kinematic paths of the module. B_0, B_x, B_y and B_z are bifurcation configurations; (b) the reciprocate process of the prototype from EC_1^f to LT_z^f with $a=80\text{mm}$, $b=40\text{mm}$	116
Fig. 5-6	The variations of geometric dimensions of the module in the x , y , and z directions following the EC path, EP path or LT path (a) The kinematic paths; (b) overall view of typical configurations; (c) front and top views of typical configurations.	118
Fig. 5-7	Theoretical Poisson's ratios of the module as functions of folding angles and geometric parameters. (a) EC, (b) EP, and (c) LT paths.	120
Fig. 5-8	Experiments and results of Poisson's ratio test of a single module. (a) The uniaxial tension and compression experimental setup for a single module; (b) comparison of theoretical and experimental Poisson's ratios of a module in EC, EP, and LT paths with $a/b = 2$	121
Fig. 5-9	Types of joints and their rotation angles under different paths when configuration EC_1^f is taken as the natural state. Dots of the same color represent the same working mode of the spring under the current path. n_i and φ_i are the number and angle of i -th type of joints respectively.	123
Fig. 5-10	Tuneable stiffness of the module. (a) The kinematic paths and corresponding normalized energy in (b), force in (c), and stiffness in (d) of the module when configuration EC_1^f is taken as the natural state.	125

Fig. 5-11	Stiffness of the module in the natural state of configurations B_0 in (a) and B_z in (b).....	126
Fig. 5-12	Control the bifurcated paths by the relative displacements of the cube connectors.	126
Fig. 5-13	Control the bifurcated paths by the combination of force or torque applied to the square central bodies at the bifurcated points.	127
Fig. 5-14	Periodic metamaterials with reconfigurability. (a) 3D metamaterial by tessellating multiple modules; (b) 2×2 tessellation, whose connection between modules is represented by orange solid lines; (c) the motion sequences of the physical model of a 2×2 tessellation, where I-II-III is NPR mode, III-IV-V is PPR mode, V-VI is ZPR mode.	128
Fig. 5-15	Schematic diagram of a two-module assembly with one in PPR state and one in NPR state. (a) Connection rules for two modules and their (b) visualizations.....	129
Fig. 5-16	The series assembly with $(m_z + n_z)$ modules. (a) Reconfiguration of module states to regulate n_z / m_z ($m_{z1}n_{z1} = m_{z2}n_{z2} = m_{z3}n_{z3}$); (b) a series assembly of m_z PPR and n_z NPR modules with $a/b=2$ and its contour plot of Poisson's ratio ν_{HB}	130
Fig. 5-17	Experiments and results of Poisson's ratio test of series assemblies ($n_z / m_z = 1, n_z / m_z = 2, n_z / m_z = 1/2$). (a) The uniaxial tension experimental setup for series assembly; (b-d) comparative plots of theoretical and experimental Poisson's ratios of modules stacked in series with $n_z / m_z = 1, n_z / m_z = 2$ and $n_z / m_z = 1/2$	132
Fig. 5-18	Metamaterials with 3D tessellation of mechanism modules. (a) Design scheme I, where each column consists of $(m_z + n_z)$ modules. (b) design scheme II of 3D metamaterials with $(m_x + n_x), (m_y + n_y), (m_z + n_z)$ modules in x, y, z direction (c-d) The contour plots of ν_{HB} and ν_{BW} for 3D metamaterials in scheme II as a function of n_i / m_i ($i=x, y, z$) when $a / b = 2$ and $\beta = \pi / 6$	134
Fig. 5-19	The reconstruction of the metamaterial with $(m_x + n_x = 6), (m_y + n_y = 5), (m_z + n_z = 8)$ modules. (a) Bifurcation configurations in four typical modes and their Poisson's ratios ν_{HB} in (b) and ν_{BW} in (c), where $n_x / m_x = 2, n_y / m_y = 3/2, n_z / m_z = 1$ in mode I, $n_x / m_x = 1/2, n_y / m_y = 3/2, n_z / m_z = 1$ in mode II,	

	$n_x / m_x = 1/2, n_y / m_y = 2/3, n_z / m_z = 1$ in mode III, and	
	$n_x / m_x = 1/2, n_y / m_y = 2/3, n_z / m_z = 1/3$ in mode IV.	136
Fig. 5-20	Construction of single DOF reconfigurable polygon prisms.	137
Fig. 5-21	The motion process of single DOF reconfigurable polygon prisms in expandable prism paths, elongated prism paths and twist prism paths.	138
Fig. A1	Prototypes and graphic representations of eighteen typical modules.	164
Fig. B1	Runtime of the algorithm for (a) the $n \times n$ double corrugated pattern and (b) the $m \times n \times p$ cellular origami structure.	164
Fig. C1	All unlocking possibilities of VTJs in a single reconfigurable ori-kirigami unit. (a) Linkage form of the thick-panel unit after the crease has been replaced by VTJs; (b) sixteen unlocking options, where case 1, case 3, case 6, case 8, case 14, and case 16 have global mobility.	165
Fig. D1	All 25 Configurations of the origami module with $n=4$	165
Fig. E1	The schematic diagram of equivalent mechanism with prismatic joints for the tessellation of the modules with $n=4$	166
Fig. E2	The schematic diagram of equivalent mechanism with prismatic joints for the tessellation of the modules with $n=6$	167
Fig. G1	$3^3 = 27$ cases of 3D modules with a rectangular prism ($N=4$) contour. The marker at the top left of configurations, $C_{(x,y,z)}$, $x, y, z = -1, 0, \text{ and } 1$, indicates that rectangular prisms in the x, y, z direction are positioned in “-1”, “0”, and “1” states and that the sign of the infinitesimal strains ε_B , ε_W , and ε_H strain is either negative, zero or positive.	169
Fig. H1	Bi-stable module using flexible beam. a) Rigid unfolding process of the module; b) load-bearing state; (c) origami module containing flexible beams; (d) experimental setup; (e) experimental results of force-displacement curve; (f) recorded deformation processes.	170

List of Tables

Tab. 2-1	The number of valid MV assignments for well-known origami patterns ..	40
Tab. 4-1	Guide to recognizing frieze groups ^[180]	88
Tab. 4-2	Guide to recognizing wallpaper groups ^[181]	90

Notation

Nomenclature

$a_{i(i+1)}$	Link lengths of linkages between joint i and joint $i+1$
R_i	Offset from x_i to x_{i+1} positively about z_i
x_i, y_i, z_i	x, y, z coordinate axis of system i
c_i	The i th crease of the pattern
p_i	The i th panel of the pattern
$V_{i,j}$	The node in row i and column j
B_i	Kinematic bifurcation configuration
W	Width
B	Breadth
H	Height
$n_{e,0}$	The number of layers in the two end-sheets' convex
$m_{e,0}, m_{e,1}$	Numbers of layers in the middle sheets' convex and concave configurations, respectively.
cn	Motifs with only n -fold rotational symmetry
dn	Motifs with both n -fold rotational and reflectional symmetry
kf	Rotational spring modulus of unit length
U	Energy
K	Stiffness
U_{EC}, U_{EP}, U_{LT}	Normalized energy of EC, EP, LT paths
F_{EC}, F_{EP}, F_{LT}	Normalized force of EC, EP, LT paths
K_{EC}, K_{EP}, K_{LT}	Normalized stiffness of EC, EP, LT paths
T	Temperature
t	Thickness of the panel

a, b, l, t_1, t_2, t_3	Edge lengths
n_i	Number of modules in negative Poisson's ratio states
m_i	Number of modules in positive Poisson's ratio states
P_i	The i th prismatic joint of the equivalent mechanism
$T_{(i+1)i}$	4×4 transformation matrix from the i th coordinate system to the $i+1$ th coordinate system
$Q_{(i+1)i}$	3×3 transformation matrix from the i th coordinate system to the $i+1$ th coordinate system
I_n	$n \times n$ identity matrix
A	Matrix used to describe the mountain-valley assignment of $m \times n$ checkerboard

Greek Alphabets

$\alpha_{i(i+1)}$	Twist angle from axes z_i to z_{i+1} positively about x_{i+1}
θ_i	The rotation angle from axes x_i to x_{i+1} about axis z_i in joint i
φ_i	Dihedral angles
α, β, γ	Sector angles of the panel
ν_{HB}	Poisson's ratios in the yoz plane
ν_{BW}	Poisson's ratios in the xoy plane
$\varphi_{i,0}$	Natural dihedral angles

Abbreviations

DOF	Degree of freedom
R	Revolute
2D	Two-dimensional

3D	Three-dimensional
DFS	Depth First Search
PPR	Positive Poisson's ratio
NPR	Negative Poisson's ratio
ZPR	Zero Poisson's ratio
D-H	Denavit-Hartenberg
MV	Mountain-valley
VTJ	Vertically transferable joint
PET	Polyethylene terephthalate
PLA	Polylactic acid
IRM	Internal rearrangement
PLG	Planar link group
EC	Expandable cube path
EP	Elongated prism path
LT	Locked twist path
DIC	Digital image correlation

Chapter 1 Introduction

1.1 Background and Significance

Metamaterials refer to a class of functional materials with artificially designed periodic or non-periodic microstructures that exhibit extraordinary physical properties beyond those of natural materials^[1]. Recognized as a ground-breaking scientific advancement, metamaterials were acknowledged in Science as one of the ten most significant scientific advancements of the first decade of the 21st century, classified as one of the "Six Areas of Disruptive Basic Research" by the US Department of Defense, and listed in China's 13th Five-Year Plan for the Development of National Strategic Emerging Industries^[2]. Mechanical metamaterials^[3,4], a frontier branch in metamaterial research, refer to structures with negative/zero properties such as negative/zero Poisson's ratio^[5,6], stiffness^[7,8], and thermal expansion^[9,10], and ultra-properties, such as ultra-stiffness^[11], ultra-light^[12], as well as structures with vanishing shear modulus^[13], and so on. Nowadays, mechanical metamaterials have also evolved into information processing and logical computing capabilities^[14-18]. Generally, these unique properties of metamaterials are derived from the geometry and spatial tessellation of cell microstructure rather than material composition. Therefore, it is critical to rationally design microstructure and spatial arrangement of unit cells to achieve unprecedented physical properties. Despite the strides made, traditional mechanical metamaterials confront three significant limitations: a narrow strain range, non-tuneable mechanical behaviours, and fixed properties after fabrication^[19]. The prevailing trend in metamaterial research has transitioned towards multifunctionality and high adaptability, necessitating tuneability, i.e., enabling the adjustment of material properties through either active or passive deformation control, and programmability, where the mechanical property is a function of controllable parameters, e.g., geometric parameters, boundary conditions, and topological configurations^[20].

Origami, an ancient art of folding paper that originated in China and flourished in Japan, transforms 2D sheet materials into complex 3D structures along predefined crease patterns^[21]. Evolved beyond traditional constraints, modern origami techniques have progressed from the pure fold (Fig. 1-1(a)), which involves the use of a single sheet of paper without cutting or bonding, to the realms of kirigami (including cut-only kirigami and ori-kirigami) (Fig. 1-1(b)), which introduces cuts, and modular origami

(Fig. 1-1(c)), where multiple sheets can be cut and bonded. Despite the art's rich aesthetic history, the combination of modern origami structure and modern science and technology extends far beyond the art itself and now has inspired a wide range of applications in aerospace^[22], architecture^[23], transportation^[24], flexible electronics^[25], energy absorption^[26], gripper^[27], medical manipulator^[28], and even virtual reality device^[29], as shown in Fig. 1-2. Due to their flexible design space, reliable large deformations, reconfigurable topology, and scale-free properties, kinematics-dominated rigid origami structures play a significant role in the design of mechanical metamaterials with tuneability^[30] and programmability^[31,32]. However, the current works mainly focus on origami metamaterials that deform along a single motion path. Despite attempts to enhance programmability by exploring reconfigurable metamaterials with multiple kinematic paths through origami, kirigami, and modular origami techniques, these endeavours turn out to be typically either a limited number of configurations with insignificant shape changes or with multi-DOFs, resulting in an unreliable and challenging controllable deformation process. Due to the lack of guidance from the underlying mechanism, the designs of reconfigurable metamaterial with multi-pathway but one DOF are rare. Differing from a multi-DOFs system, kinematic bifurcation refers to a critical point in a mechanical system at which the system transitions from one reliable kinematic path to another requiring minimal external intervention. Therefore, a single DOF system with kinematic bifurcation capabilities is an excellent candidate for designing reconfigurable metamaterials, since it can be deformed into various configurations while also having a predefined and reliable path.



Fig. 1-1 Artworks for origami, kirigami, and modular origami. (a) An origami crane folded from a sheet of paper^[33]; (b) a kirigami tower, RES Octagon Star^[34], involves cuts in a sheet of paper; (c) a modular origami toy, Snapology^[35], created by multiple sheets of paper.

This dissertation is focused on the rational design of mechanical metamaterials with large deformation from the perspective of single DOF reconfigurable linkage in the form of origami, which enables the metamaterials to be equipped with the ability to tune their mechanical behaviours without redesigning or reassembling the architecture. It is of great scientific and engineering significance to expand the variety of origami structures, to guide the development of tuneable metamaterials, and to promote the application of reconfigurable mechanisms in shape-morphing systems, such as flexible metamaterials, morphing architectures, and deployable structures.

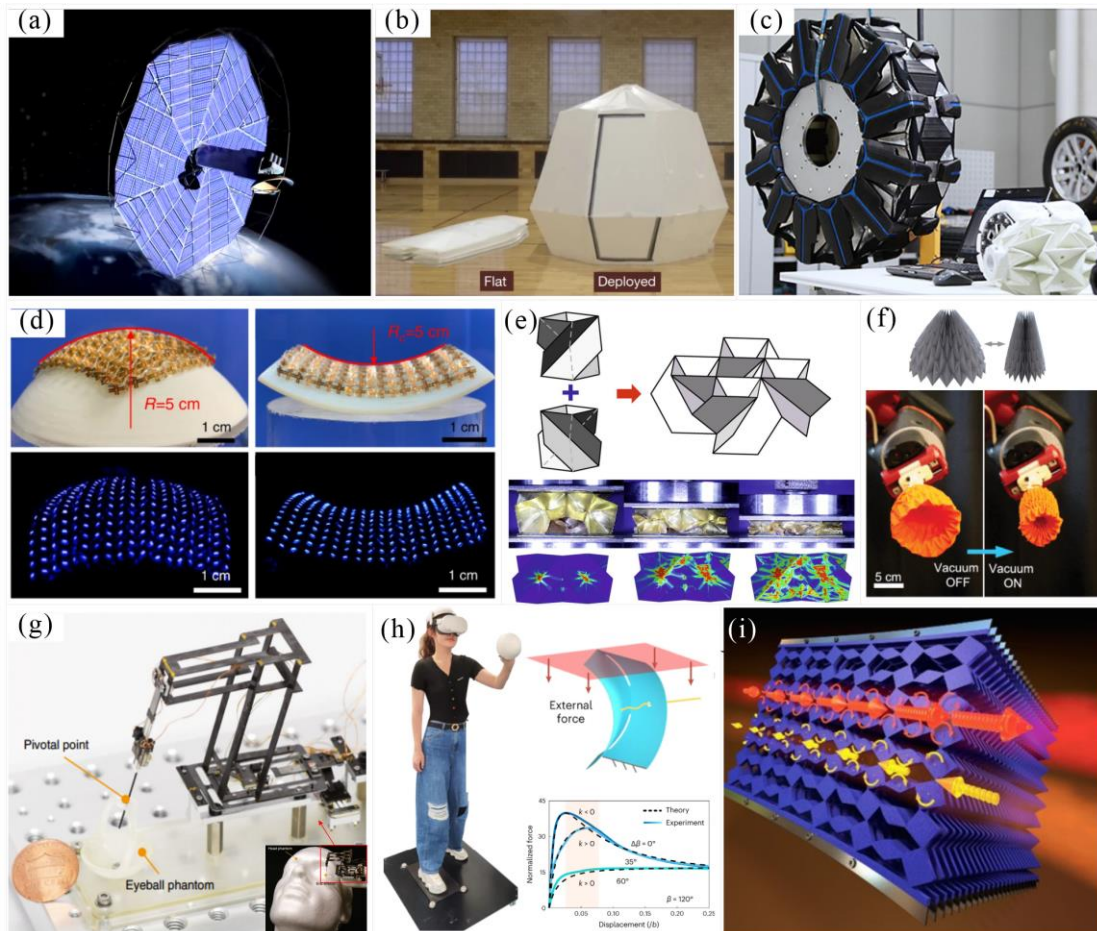


Fig. 1-2 Origami engineering. (a) An origami-based deployable solar array^[22]; (b) the metre-scale inflatable shelter^[23]; (c) high-load capacity origami transformable wheel^[24]; (d) curved display^[25]; (e) energy absorption structure with a kirigami-inspired pyramid foldcore^[26]; (f) origami soft gripper^[27]; (g) kirigami-inspired miniature manipulator for teleoperated microsurgery^[28]; (h) active mechanical haptics for immersive virtual reality based on curved origami^[29]; (i) modular origami-based mechanical metamaterials with static non-reciprocity^[36].

1.2 Review of Previous Works

1.2.1 Origami Kinematics

Kinematics deals with the relationship between input and output motions in terms of position, velocity and acceleration within the mechanical system, which refers to an assembly of bodies connected by joints with a specific topological structure^[37]. The creases and components in rigid origami form can be modelled as revolute joints and links of the linkage form. So, an origami structure consisting of pieces of paper or origami blocks is a mechanism^[38]. Compared to geometric methods^[39] and numerical algorithms^[40,41], kinematic theories show significant advances when applied to quickly assess rigid foldability, accurately describe the folding and unfolding process, and innovatively create origami designs.

Origami studies undoubtedly begin with the predefined crease pattern. For zero-thickness origami, the best-known rigid vertex with four creases meeting at one point is kinematically a spherical 4R linkage with one DOF^[42,43], as shown in Fig. 1-3(a). Similarly, when six creases meet at one vertex, it forms a spherical 6R linkage with three DOFs^[44]. Additionally, a rigid pattern comprising multiple origami vertices can be viewed as a mobile network of spherical linkages^[45], as shown in Fig. 1-3(b). A closed-loop pattern is considered rigidly foldable only if the motion transmitted through the creases returns to its input position, which also serves as the compatibility condition for the corresponding linkage form.

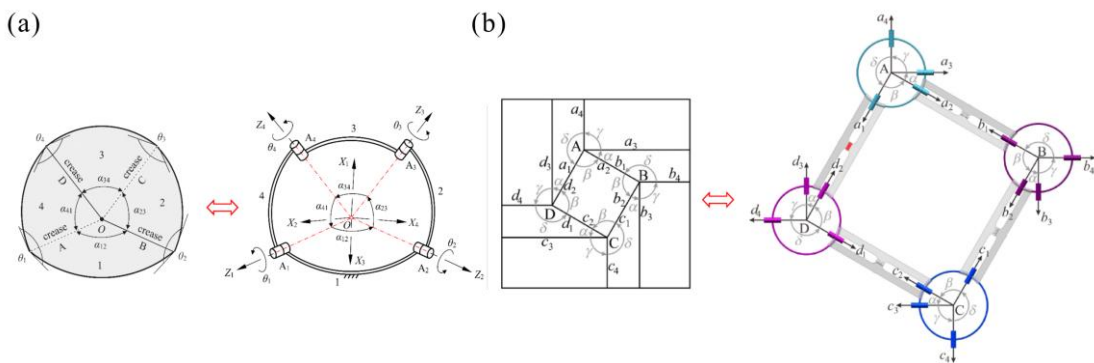


Fig. 1-3 Linkage forms of zero-thickness origami vertices and their tessellations. (a) Four-crease vertex with zero thickness and corresponding spherical 4R linkage^[42]; (b) origami pattern with multiple four-crease vertices and corresponding mobile network of spherical linkages^[45].

In this case, the folding behaviours can be analysed using the matrix method based on the Denavit-Hartenberg (D-H) notation^[46]. For spherical linkages consisting of n links, the lengths $a_{i(i+1)}$ and offsets R_i of each link are zero since the axes cross at a single point. As a result, the closure equation can be expressed as

$$\mathbf{Q}_{21}\mathbf{Q}_{32}\cdots\mathbf{Q}_{1n} = \mathbf{I}_3 \quad (1-1)$$

where \mathbf{I}_3 represents the 3×3 identity matrix, and when $i+1 > n$, it is replaced by 1, and the transformation matrix $\mathbf{Q}_{(i+1)i}$ between the coordinate systems at joints $i+1$ and i is

$$\mathbf{Q}_{(i+1)i} = \begin{bmatrix} \cos \theta_i & -\cos \alpha_{i(i+1)} \sin \theta_i & \sin \alpha_{i(i+1)} \sin \theta_i \\ \sin \theta_i & \cos \alpha_{i(i+1)} \cos \theta_i & -\sin \alpha_{i(i+1)} \cos \theta_i \\ 0 & \sin \alpha_{i(i+1)} & \cos \alpha_{i(i+1)} \end{bmatrix} \quad (1-2)$$

and

$$\mathbf{Q}_{i(i+1)} = \mathbf{Q}_{(i+1)i}^{-1} = \begin{bmatrix} \cos \theta_i & \sin \theta_i & 0 \\ -\cos \alpha_{i(i+1)} \sin \theta_i & \cos \alpha_{i(i+1)} \cos \theta_i & \sin \alpha_{i(i+1)} \\ \sin \alpha_{i(i+1)} \sin \theta_i & -\sin \alpha_{i(i+1)} \cos \theta_i & \cos \alpha_{i(i+1)} \end{bmatrix} \quad (1-3)$$

Here, $\alpha_{i(i+1)}$ is the twist angle from axes z_i to z_{i+1} positively about axes x_{i+1} and θ_i is the angle from x_i to x_{i+1} along the positive direction of z_i . The explicit function between the input angle θ_i and the output angle θ_{i+1} can be derived from Eq. (1-1).

Meanwhile, origami is no longer limited to zero-thickness sheets^[42,45,47–49]. The thickness of various rigid materials cannot be disregarded, and related engineering applications have plagued their folding and unfolding problems. Most structures involving thick panels are derived from conventional origami, initially based on the zero-thickness model. Hinges are translated to the top and bottom surfaces of the thick panels, thereby constructing thick-panel origami by connecting adjacent thick panels^[47]. The thick-panel form's four-crease, five-crease, and six-crease vertices can be modelled as spatial overconstrained 4R, 5R and 6R linkages^[47], respectively. Taking the thick-panel form of the Miure-ori in Fig. 1-4 as an example, it leads to assemblies of Bennett 4R linkages with identical link lengths^[49].

In this case, the folding kinematic behaviours of the entire the thick panel origami structure can be described by the closure equation for a single close-loop spatial linkage consisting of n links, i.e.,

$$\mathbf{T}_{21}\mathbf{T}_{32}\cdots\mathbf{T}_{1n} = \mathbf{I}_4 \quad (1-4)$$

where

$$\mathbf{T}_{(i+1)i} = \begin{bmatrix} \cos \theta_i & -\cos \alpha_{i(i+1)} \sin \theta_i & \sin \alpha_{i(i+1)} \sin \theta_i & a_{i(i+1)} \cos \theta_i \\ \sin \theta_i & \cos \alpha_{i(i+1)} \cos \theta_i & -\sin \alpha_{i(i+1)} \cos \theta_i & a_{i(i+1)} \sin \theta_i \\ 0 & \sin \alpha_{i(i+1)} & \cos \alpha_{i(i+1)} & R_i \\ 0 & 0 & 0 & 1 \end{bmatrix} \quad (1-5)$$

Since the panels must be adjusted to accommodate thickness, most existing solutions to deployable thick panel structures have uneven surfaces in the fully unfolded state. Zhang and Chen proposed a uniform-thickness panel form of a six-crease pattern, i.e., diamond thick-panel^[48] from the mobile assembly of plane-symmetric Bricard 6R linkages. By introducing the cuts, Yang et al. constructed a uniform-thickness panel form of the Miura-ori fold with single DOF, which can be folded from a flat array to compact bundles without any voids^[50], kinematically is an assembly of 8R closed chains. The matrix method proved to be a powerful tool for the design and analysis of these zero-thickness and thick-panel origami structures.

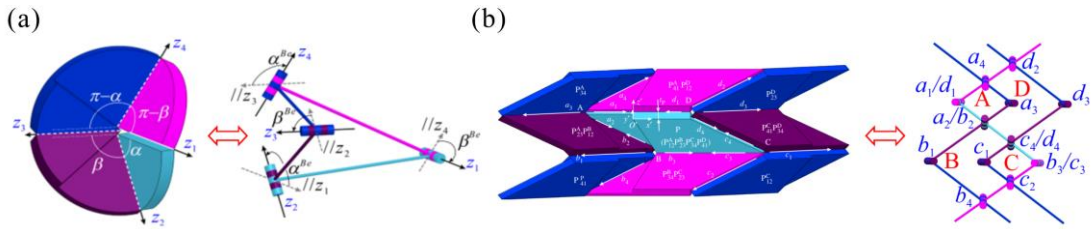


Fig. 1-4 Linkage forms of thick-panel origami vertices and their tessellations^[49]. (a) The Miura-ori vertex in thick-panel form and corresponding Bennett 4R linkage; (b) the Miura-ori pattern and corresponding mobile network of spatial linkages.

For relatively simple origami forms, e.g., kirigami with only cuts and 2D modular origami, which are kinematically planar linkages and their networks^[51], the simplest and most effective method of kinematic analysis besides the D-H method is the vector method^[52]. On the other hand, highly complex mechanisms, for which it is difficult to obtain explicit solutions, can be analysed using additional symmetry constraints^[53] or numerical methods^[54]. In both ori-kirigami and modular origami, which involve folds and cuts, the basic unit of kinematic analysis is no longer a vertex but independent closed loops formed by the creases and rigid components around the cut or hole, which

may be equivalent to planar, spherical and spatial linkages, or even a hybrid of these in kinematics. The analysis and design of this class of origami structures is a kinematic challenge.

1.2.2 Reconfigurable Mechanisms

Over the past two decades, reconfigurable mechanisms have gained significant importance across various fields for their ability to provide multiple functionalities within a single structure, enabling them to perform various tasks. Research on reconfigurable mechanisms can be traced back to the 1990s. Two new types of mechanisms were identified: kinematotropic linkages^[55] and metamorphic mechanisms^[38]. The former exploits the bifurcation phenomenon, extending it to involve mobility change with changes in relative orientations of joint axes^[56], while the latter, inspired by metamorphosis, undergoes form, topology, and configuration alterations, extending the context from biology to changes in the main structural parameters of a mechanism (mobility, connectivity, overconstrainedness, and redundancy)^[57]. In the following development of reconfigurable mechanisms, various ways to achieve reconfiguration were investigated and developed^[58-65].

Of particular interest in this dissertation lies in reconfigurable linkages with kinematic bifurcation. Currently, single-loop overconstrained spatial linkages have emerged as a valuable resource for designing such reconfigurable linkages. Chen and You observed the kinematic bifurcation in a spatial 6R linkage formed by merging two extended Myard 5R linkages^[66]. They also analysed bifurcations of a two-fold symmetric 6R deployable linkage^[67]. Later, Song and Chen constructed reconfigurable spatial 6R linkages with one DOF, employing summation/subtraction of existing overconstrained linkages^[68-70]. This approach has paved the way for synthesising numerous reconfigurable linkages with bifurcation behaviours^[71]. Besides, kinematic analysis is also a powerful tool for unravelling the kinematic bifurcation of specific linkages. For example, Chen and Chai discovered the bifurcation of a special line and plane-symmetric Bricard linkage from the kinematic paths based on closure equations^[72], as shown in Fig. 1-5(a). Feng et al. revealed bifurcation cases of the plane-symmetric Bricard 6R linkage under different geometric conditions by deriving explicit solutions of closure equations using the matrix method^[73], as shown in Fig. 1-5(b). Zhang and Dai^[74] delved into the reconfiguration properties of the plane-symmetric

Bennett plano-spherical 6R hybrid linkage, leveraging screw theory. Li et al. proposed a reconfigurable Goldberg 6R linkage(Fig. 1-5(c)) features one Goldberg 6R motion branch, two line-symmetric Bricard 6R motion branches, and one Bennett motion branch^[75]. Tang and Dai explored a class of multi-bifurcated double-centered linkages combined with higher order kinematic analyses and singular value decomposition^[76], as shown in Fig. 1-5(d). Lu et al. presented the analysis of bifurcations of the doubly collapsible Bricard 6R linkage through the projection of configuration space^[77]. In addition to the fascinating overconstrained 6R, non-overconstrained 7R linkages and 8R linkages with variable and mobility topology are also the focus of reconfigurable research^[78-83].

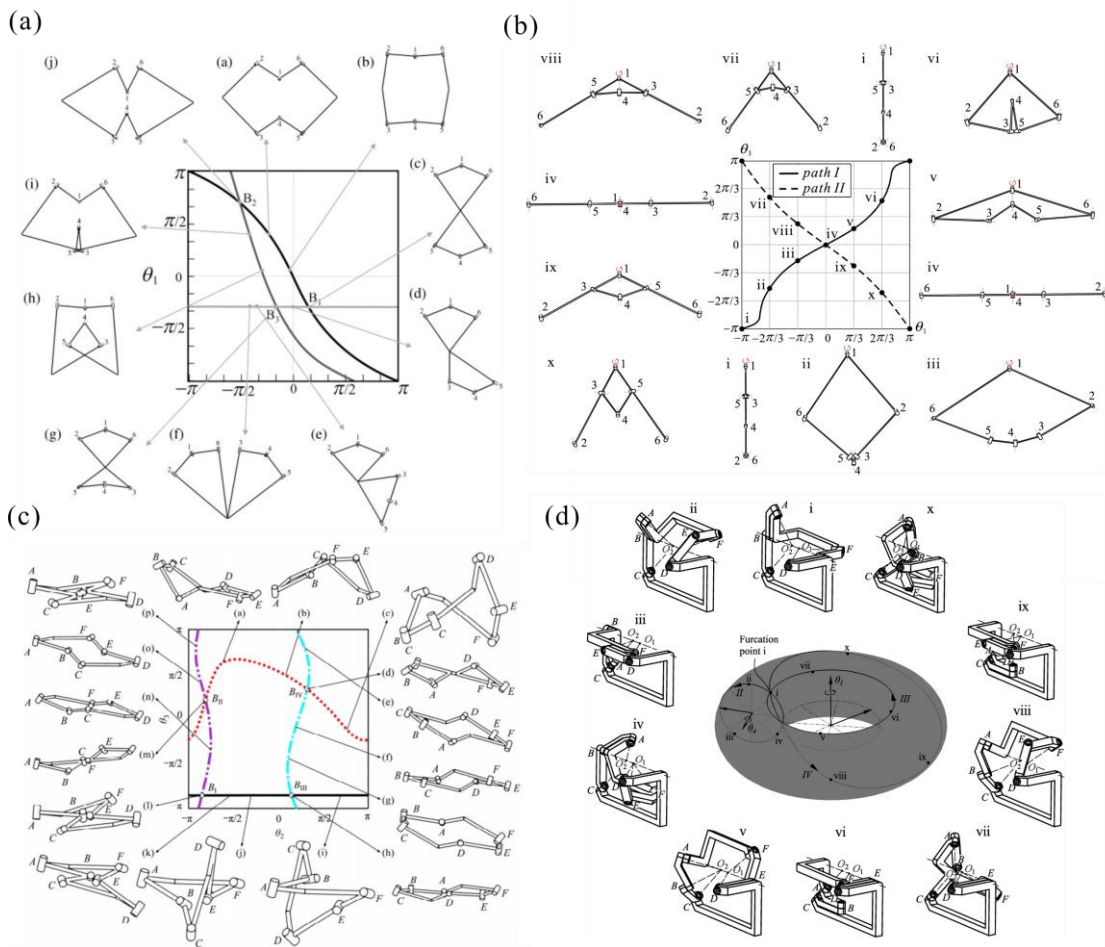


Fig. 1-5 Reconfigurable 6R linkages with kinematic bifurcation. (a) A special line and plane-symmetric Bricard linkage^[72]; (b) plane-symmetric Bricard 6R linkage^[73]; (c) line-symmetric Goldberg 6R linkage^[75] (b) double-centered 6R linkage^[76].

However, traditional reconfigurable linkages often entail complex components and actuation methods, raising concerns about reliability, weight, and energy consumption. In contrast, origami-inspired designs are another primary resource for single-loop reconfigurable linkage, with the advantages of simple components and lightweight. It was revealed that the flat-unfolded state of a single four-crease vertex is a kinematic singularity of spherical 4R linkage that can bifurcate into two or more kinematic paths following different MV assignments^[84], as exemplified in Fig. 1-6.

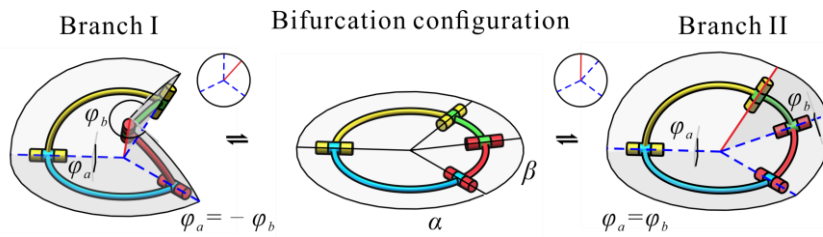


Fig. 1-6 Mountain-valley crease reconfiguration of the double corrugated vertex in spherical 4R linkage form. Mountain and valley creases are indicated by red solid lines and blue dotted lines.

This simple mountain-valley crease reconfiguration, which involves switching creases between mountain and valley and activating/deactivating creases, has in turn sparked the development of various reconfigurable linkages. For example, Zhang and Dai proposed reconfigurable plane-symmetric double spherical 6R linkage^[85] (Fig. 1-7(a)), Sarrus-motion linkage^[86], and 8R linkage^[87] inspired by closed-loop kirigami. Ma and Dai presented the planar-spherical 6R and the Bennett-spherical 6R linkage, both of which have three motion branches inspired by the kirigami fold^[88]. Feng and Chen presented a novel 6R linkage and a variation of doubly collapsible octahedral Bricard 6R linkage by applying the kirigami technique to rigidly foldable origami twist patterns^[89]. Liu and Chen transferred a rigid kirigami pattern into a double spherical linkage (Fig. 1-7(b)) with kinematic bifurcation behaviour^[90]. Through the analysis of kinematic compatibility of a multi-loop origami pattern formed by four four-crease vertices, Liu and Chen proposed three types of reconfigurable 6R linkages with the kirigami technique, including a double spherical linkage, a planar-spherical linkage, and a parallel 6R linkage^[91]. Tang and Dai presented an eight-bar linkage (Fig. 1-7(c)) derived from a rotatable kaleidocycle whose bifurcated motions were revealed by screw theory^[92]. Wang and Dai presented work on a fortune teller origami fold-inspired

reconfigurable 8R linkage (Fig. 1-7(d)) and its evolved Bricard 6R and Bennett 4R linkages^[93]. Interdisciplinary research on linkages and origami not only offers a method to analyse the motion behaviour of origami patterns but also fosters the discovery of novel reconfigurable linkages with kinematic bifurcation.

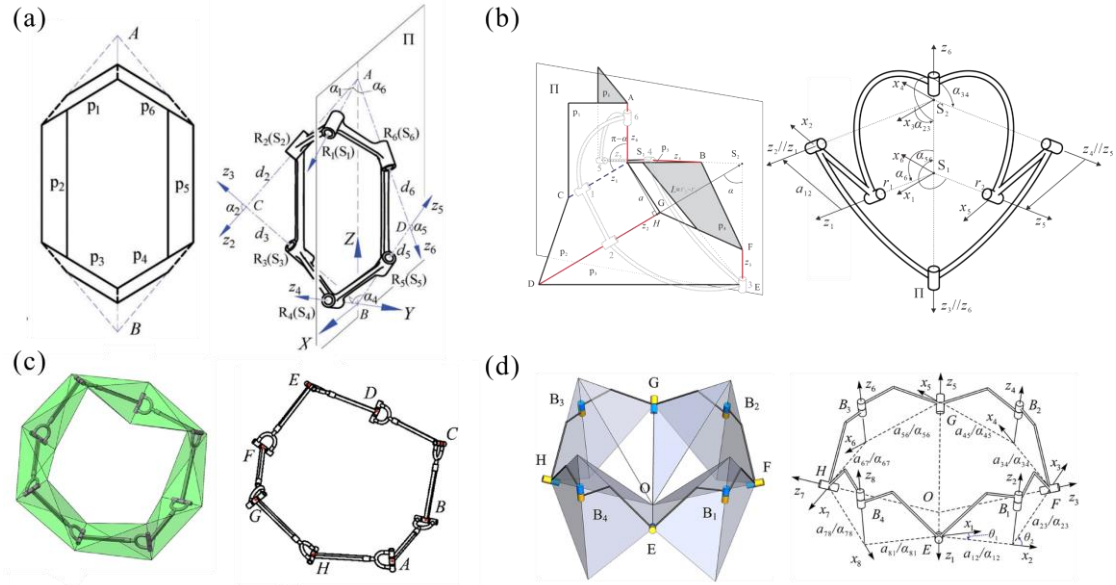


Fig. 1-7 Single-loop reconfigurable linkages inspired by origami designs. (a) and (b) reconfigurable 6R linkages^[85,90]; (c) and (d) reconfigurable 8R linkages^[92,93].

Compared with single-loop reconfigurable linkage, multi-loop reconfigurable linkage is characterised by a large number of loops and a complex structure^[94]. Among multi-loop reconfigurable linkages, one of the notable ones is the single DOF reconfigurable polyhedral linkage, which is a unique multi-loop reconfigurable linkage that adopts polyhedral layouts and allows its global shape to be changed during deployment. Röschel investigated the self-motions of a Fulleroid-like mechanism based on a cube and the conditions for its movability^[95]. Li et al. presented the construction method of single DOF reconfigurable deployable polyhedral mechanisms by inserting straight elements^[96] shown in Fig. 1-8(a) and angulated elements^[97] into the vertices and faces of polyhedrons. They also contributed to the single DOF reconfigurable deployable cube mechanism (Fig. 1-8(b)) by inserting 4-parallelgram mechanisms into six quadrilateral faces^[98]. Hao et al. further analysed the constraints of the adjacent faces of the single DOF cube mechanism, and then obtained the possible motion modes of the cube mechanism^[99]. Liu et al. developed a group of N -sided antiprism

mechanisms based on an asymmetric $8R$ linkage^[100], as shown in Fig. 1-8(c). They have investigated the bifurcation characteristics of mechanisms by analyzing the infinitesimal motions of eight-bar linkages at the singular configurations. Zhang constructed reconfigurable polyhedrons with eight kaleidocycles, which have two motion paths following cuboid symmetry and tetrahedral symmetry^[101]. Although many single DOF deployable polyhedral linkages have been constructed^[102,103], only a few have demonstrated reconfigurable properties. Designing and analysing such reconfigurable polyhedral linkages remains a significant challenge in kinematics.

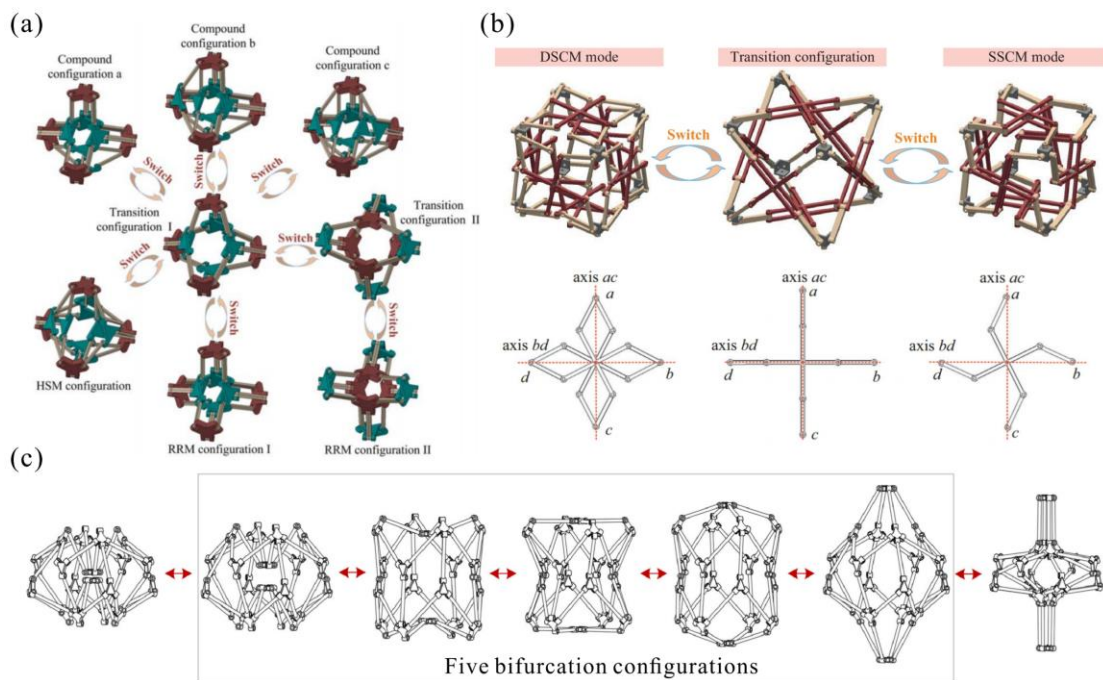


Fig. 1-8 Reconfigurable polyhedral linkages with single DOF. (a) Constructed by reconfigurable straight elements^[96]; (b) constructed by reconfigurable parallelogram linkages^[98]; (c) constructed by asymmetric $8R$ linkage^[100].

In general, multi-DOFs systems and single-DOF systems with kinematic bifurcation are two widely adopted methods to achieve reconfiguration between different shapes or configurations. Multi-DOFs linkages provide versatility through independent motion in various directions, often requiring multiple locking devices or actuators to operate synchronously at each joint. Compared to multi-DOFs linkages, single DOF reconfigurable linkages based on kinematic bifurcation are particularly desirable because they require minimal external intervention to switch or remain in a

given configuration^[72,104]. Note that this choice between different motions is only available in the particular bifurcation points; once the linkage has left this particular configuration, its motion is again determined by a single parameter.

Various tools have been used to study the bifurcation of reconfigurable linkages, including singular value decomposition of the equilibrium matrix^[105–107], screw theory^[86,88,108], matrix method^[73,88,92] and so on. Among them, the matrix method is a commonly used method for kinematic analysis of planar, spherical, and spatial linkages by considering the topological structure and geometric conditions, and its advantage is that it not only determines the mobility but also gives explicit closure equations that can be used to reveal the kinematic bifurcation and configuration evolution of reconfigurable linkages.

1.2.3 Origami Mechanical Metamaterials

One could consider kirigami and modular origami as variations of origami due to their apparent similarities and are frequently related to conventional origami. However, origami, kirigami, and modular origami work on fundamentally different principles, although there is a crossover between the three. Therefore, mechanical metamaterials induced by the folding behaviour based on origami, kirigami, and modular origami are presented.

1.2.3.1 Origami-based Mechanical Metamaterials

The current research interest of conventional rigid origami-based mechanical metamaterials is on those with four-crease vertices (one-DOF type), the Miura pattern^[109] and its variations, and six-crease vertices (multi-DOFs type), e.g., the waterbomb^[110] and Resch^[54] patterns, and other patterns^[84]. Although there are some other rigid origami patterns, such as wrapping origami^[111], more attention is paid to them as non-rigid cases, so they are not discussed further.

The best-known four-crease vertex pattern is the Miura-ori, which consists of repeating parallelograms that form a tessellation on the sheet. As shown in Fig. 1-9(a), the Miura-ori pattern can be folded from a flat sheet into a compact arrangement with one DOF motion while demonstrating fascinating mechanical properties, the most intuitively notable of which is its auxetic behaviour (also known as negative Poisson's ratio). Pioneering work by Schenk and Guest involved the auxetic mechanical

metamaterials based on the Miura-ori pattern, exhibiting transversal contracting deformation under external vertical compression loading^[112]. Meanwhile, Wei et al. showed that the in-plane and out-of-plane Poisson's ratios of Miura-ori folds are equal in magnitude but opposite in sign, independent of material properties^[113].

While the mechanical properties of Miura-ori origami are intriguing, the original single-layer Miura-ori origami is inherently confined to folding into planar structures, posing limitations on its potential applications. To address this limitation, efforts have been made to develop 3D deployable mechanical metamaterials with more complex geometries and performances while retaining their original properties, such as flat foldability and negative in-plane Poisson's ratio, by connecting identical or different Miura-ori origami sheets layer by layer^[112,114,115]. Alternatively, using the concept of gradient, Ma et al. introduced a unidirectional geometric variation into the origami structure^[116]. Subsequently, they developed 2D graded and 3D graded cellular structures based on the Miura-ori pattern (Fig. 1-9(b)), which are capable of generating periodically graded stiffness and superior energy absorption^[117]. Another avenue for obtaining 3D cellular structures involves the summation and subtraction of tubular origami (Fig. 1-9(c-f)). This method involves the construction of a rigid tubular structure by joining pieces of paper containing the vertices of Miura-ori or Miura-variant, followed by the creation of a new stacked origami structure by joining common sides or corners using such a tubular origami structure as a basic unit^[118-123]. As shown in Fig. 1-9(c), Filipov et al. introduced an innovative approach by coupling rigidly foldable origami tubes in a "zipper" fashion^[119]. This novel configuration exhibits significantly higher bending stiffness than the original Miura-ori origami tube. Remarkably, the metamaterials exhibit tuneable stiffness spanning about four orders of magnitude, achieved by altering the loading direction and folding ratio. Using Miura-based closed-loop origami units, Mousanezhad et al. designed a set of foldable tubes, and further constructed a 3D cellular structure (Fig. 1-9(d)) that has one DOF with flat-foldability in out-of-plane and in-plane folding directions^[120]. Tachi et al. drew inspiration from the Miura-ori pattern and designed a Tachi-Miura polyhedron bellow^[121], as illustrated in Fig. 1-9(e). Subsequent studies revealed that mechanical metamaterials based on this Tachi-Miura polyhedron bellow could transition between load-bearing and collapsed states, exhibiting features such as negative Poisson's ratios and bi-stability^[122,123]. Wang et al. proposed a 3D metamaterial with negative Poisson's

ratios simultaneously in the in-plane and out-of-plane directions^[118], by incorporating Miura-ori into the re-entrant honeycomb, as shown in Fig. 1-9(f). This hybrid Miura-based metamaterial enables the programmability of Poisson's ratios from mild to extreme authenticity since it is a function of geometry and configuration of the microstructural.

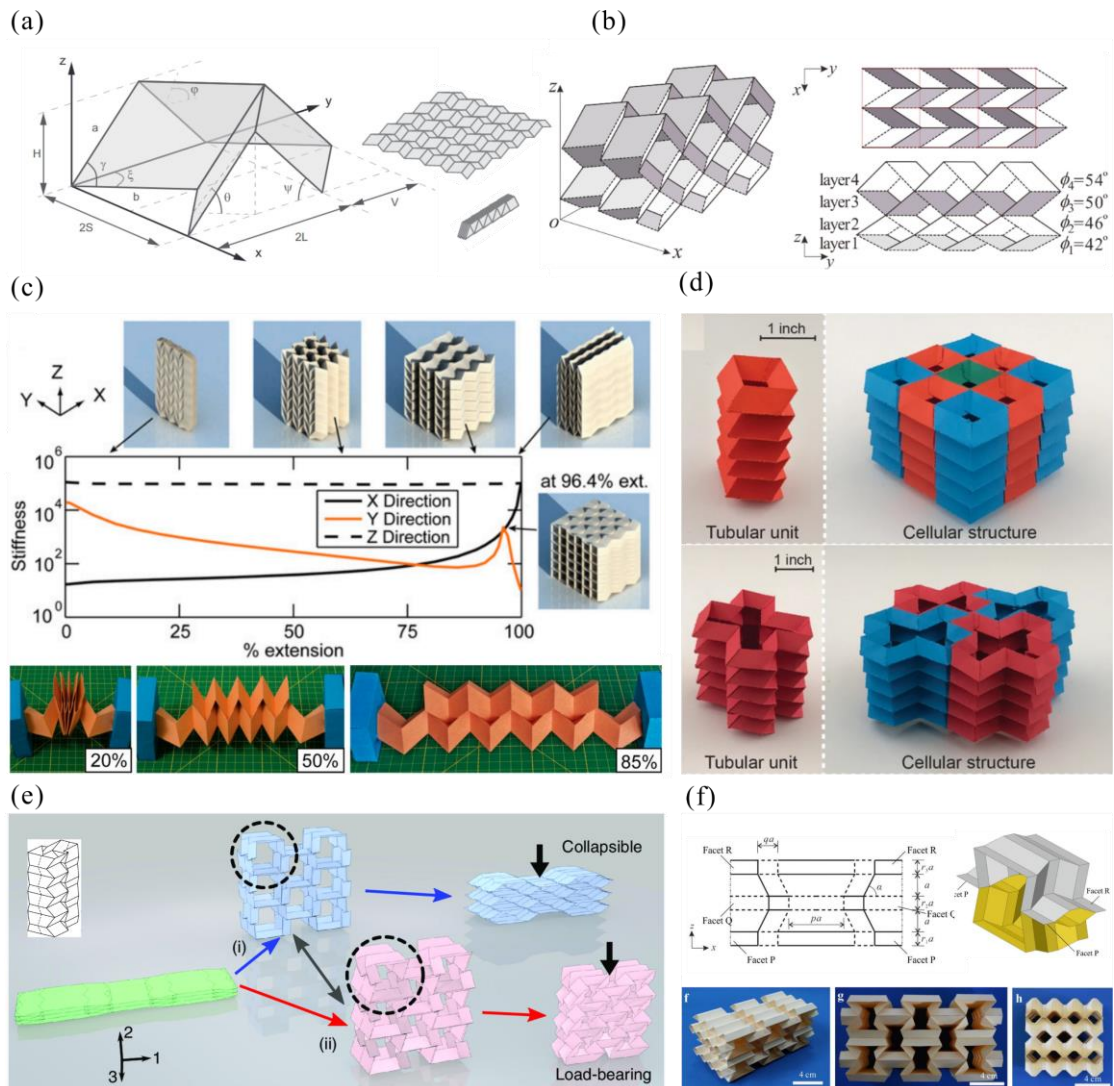


Fig. 1-9 Rigid origami-based mechanical metamaterials with a single deformation path. (a) The Miura-ori pattern with in-plane NPR^[112]; (b) graded cellular structures^[116]; (c) cellular origami metamaterial formed by zipper-coupled tubes^[119]; (d) cellular structure formed by Miura-based closed-loop origami units^[120]; (e) Tachi-Miura polyhedron^[121–123]; (f) hybrid Miura-based metamaterial^[118].

For mechanical metamaterials based on an origami pattern consisting of six-crease vertices, each origami vertex equivalent spherical 6R linkage with three DOFs, thus significantly increasing the overall DOFs when tessellated. Although the folding or unfolding process of such multi-DOFs systems is particularly challenging, it is of considerable value in certain applications, particularly those involving shape morphing, due to its high flexibility. The mechanical metamaterials based on these six-crease patterns generally manifest in two predominant configurations: planar or shell-like and tubular. In the planar category, the research focus for the waterbomb and Resch patterns is on the algorithmic generation of highly adaptable programmable curvatures or surfaces, exploiting the flexibility inherent in multi-DOFs systems^[54,124,125]. Turning attention to tubular structures, the waterbomb pattern has attracted significant attention in metamaterial design due to its programmable stiffness and 3D shape, coupled with compression-torsion deformation due to its rich deformation modes such as contraction, torsion, etc^[53,126,110,127]. In particular, when forming a tubular structure, Resch's origami still has a good ability to withstand axial loads due to its negative Poisson's ratio and self-locking phenomenon^[128].

The geometry of origami provides a facile platform to explore the various desired mechanical properties of a wide class of constraint-based metamaterials. On the one hand, the characteristic of a reliable large deformation path is essential for tuneable properties, making rigid origami widely used in designing the microstructure of metamaterials. On the other hand, the deformation pattern of these rigid origami-based metamaterials is similar to the zero-energy motion of the underlying mechanism. Therefore, external forces can easily excite deformation. However, most of the currently reported rigid origami-based mechanical metamaterials with a single DOF can only deform along a single motion path.

Recently, Chen et al. investigated the effect of MV creases on the rigid foldability of double corrugated patterns^[84] and square twist patterns^[45,129,130], which opened the gate for reconfigurable origami. Nowadays, reconfigurable origami, i.e., exhibits crease topological morphing by switching MV creases, or activating/inactivating creases, has rapidly emerged as the research frontier and hot spot^[131,132]. This remarkable capability enables these structures to be folded into multiple shapes while exhibiting enhanced tuneable mechanical properties, making them highly suitable for multifunctional applications. For example, the morph pattern demonstrated a smooth switchable

Poisson's ratio ranging from negative infinity to positive infinity when it undergoes topological reconfiguration between a Miura-ori mode and an Eggbox mode through the re-assignment of MV creases (Fig. 1-10(a))^[133]. Another example is the Tachi-Miura Polyhedron (Fig. 1-10(b)), whose rich reconfigurations are compatible in a large tessellation, providing a new paradigm for designing heterogeneous metamaterials yielding a wide range of design space^[134]. Furthermore, a variant of the stacked Miura-ori origami structure with multi-stability and shape reconfigurability achieves basic and compound logic gates^[114,135], as shown in Fig. 1-10(c).

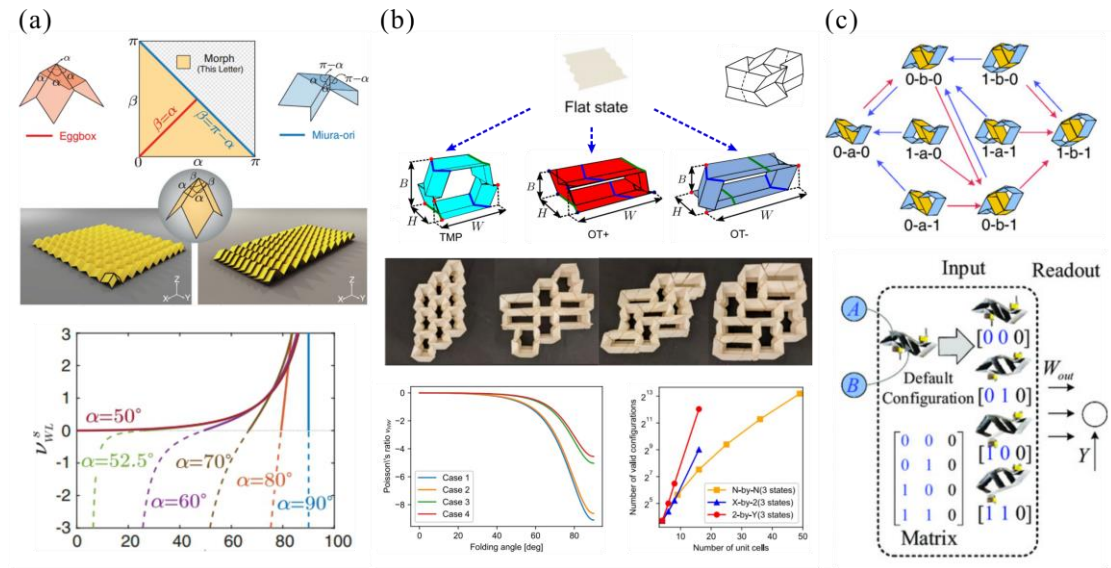


Fig. 1-10 Reconfigurable origami-based mechanical metamaterials deform along multiple motion paths. (a) The morph pattern with sign switchable Poisson's ratio^[133]; (b) reconfiguration of Tachi-Miura polyhedron for heterogeneous metamaterials^[134]; (c) variant of the stacked Miura-ori origami for the mechanical logic gate^[135].

It can be seen that configuration reconfigurations of one DOF rigid origami unlock new possibilities for the tunability of mechanical properties. However, the kinematic nature of all these reconfigurable origamis is that of spherical linkages and their assembly, resulting in a limited design space for conventional origami. Although there are examples that exploit the kinematic bifurcation of single DOF mechanisms, the shape transformations of these reconfigurable origamis are not significant. The major challenge at the structural design level is now to delve further into reconfigurable structures with significant shape changes to achieve breakthroughs in mechanical properties.

1.2.3.2 Kirigami-based Mechanical Metamaterials

Kirigami-based mechanical metamaterials refer to a type of metamaterial that incorporates kirigami principles, that exploit additional DOFs offered by cuts to expand the range of accessible geometries. As a result, after cutting the paper appropriately based on kirigami techniques, the folding process could generally be easier to obtain a wider variety of metamaterials with different types of deformations. Unlike origami, kirigami is not usually categorized by patterns, kirigami patterns are categorized into two groups: (a) cut-only kirigami, and (b) ori-kirigami.

Rigid kirigami techniques involving only cutting are usually used to create rotating units in a continuous flat sheet that generate auxetic behaviour in 2D mechanical metamaterials. By careful cutting, a continuous sheet can be strategically divided into a tessellation of polygon facets connected at hinge points, e.g., a rigid square structure that is a planar 4R linkage with a single DOF in kinematics^[136]. The organized arrangement of these rigid units, coupled with their rotational motion in either clockwise or anti-clockwise directions, contributes to the creation of auxetic behaviour, as shown in Fig. 1-11(a). The rotating square unit structure is the simplest 2D structure with a rotating motif. By scaling and tilting these basic square unit structures, rectangular and parallelogram unit structures are obtained. Moreover, the substitution of the rotating unit with two or more heterogeneous unit types, as depicted in Fig. 1-11(b), introduces notable variations^[137]. One such prominent case is the triangular unit, also known as the Kagome lattices^[138]. Since each independent loop has six joint points (planar 6R mechanism, if the point is considered as a revolute joint), it is a typical multi-DOFs system with a much richer range of transformed modes and their corresponding physical properties. Kagome lattices offer an ideal platform to investigate how to control the large deformation of multi-DOFs systems during expansion and contraction, in response to specific constraints such as symmetry or synchronous actuation. For example, Kagome lattices (see Fig. 1-11(c)) could exhibit negative Poisson's ratio -1, when the triangular units rotate against every joint and deformation is locally isotropic (d3 symmetry), or its Poisson's ratio as a function of the nominal strain, when it is producing a pattern of alternately tilted distorted hexagonal pores (c2 symmetry). In addition, to generating auxetic behaviour, hierarchical kirigami patterns composed of rigid square units allow for extreme expandability (>800%)^[139,140](see Fig. 1-11(d) and (e)) and 2D shape changes^[141,142]

(see Fig. 1-11 (f)). Furthermore, rigid kirigami can also be deformed into a 3D configuration without panel deformation. As shown in Fig. 1-11(g) and (h), when the thickness of the panel is small enough to be ignored, the deformation of joint points turns from a single DOF revolute joint to a 3-DOFs ball joint, and together with an optimization algorithm, the rotating structure starting from a continuous plane can also achieve programmable 3D shapes^[143–146]. Despite their powerful deformation ability, the DOFs increase dramatically as the size increases, making the deformation process challenging to control.

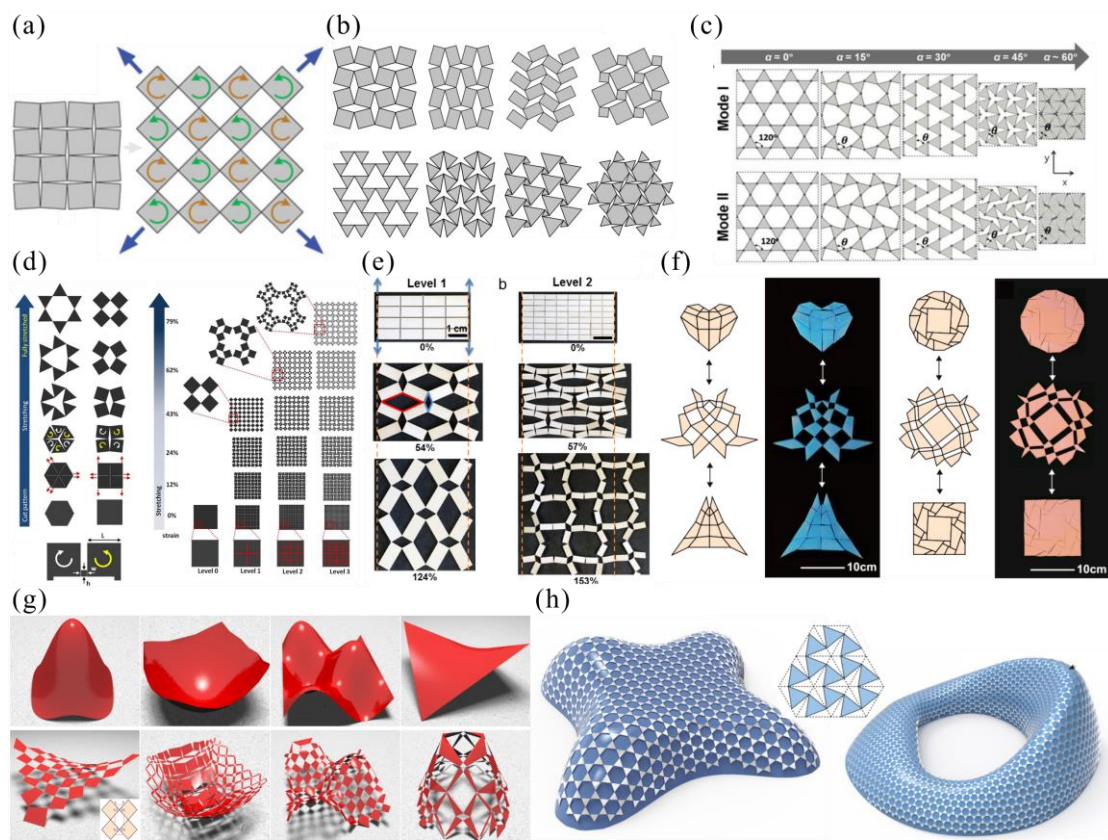


Fig. 1-11 Cut-only kirigami-based 2D and 3D mechanical metamaterials. (a) Auxetic behaviour generated by rotating square units^[136]; (b) various rotating unit structures^[137]; (c) a Kagome lattice and its corresponding two collapsing modes^[138]; (d) and (e) are examples of hierarchical kirigami patterns with extremely large strains^[139,140]; (f) kirigami-based inverse design enables transformation between two 2D target shapes^[141]; (g) kirigami designs for 3D shape programming based on rotating square units^[143] and (h) rotating triangular units^[145,146].

Rigid kirigami design involving cutting and folding (referred to ori-kirigami) is an emerging approach, where a structure is cut off appropriate parts, and then folded to close the missing part to form a 3D structure. First of all, a fundamental strategy involves the strategic introduction of cuts and creases within a continuous flat sheet. The purpose of these cuts is to release the constraints between the panels so that the remaining panels can be rotated around these creases due to their mobility. A noteworthy example is the lattice kirigami proposed by Castle et al., where they introduce defects into the sheets, including cutting and removing (or adding) wedges and then performing dislocations or disclinations to form 3D structures^[147,148]. Sussman et al. further proposed algorithmic lattice kirigami, where a single kirigami pattern can be robustly manipulated into a variety of three-dimensional shapes by adjusting the mountain and valley creases^[149], as shown in Fig. 1-12(a). Another example is a checkerboard pattern featuring pop-up and pop-down blocks. This configuration is achieved by selectively removing panels of the checkerboard pattern alternately in two directions. Xie et al. established parametric relationships between the crease pattern, volumetric, and kinematic parameters of the checkerboard pattern^[150]. Based on the kirigami checkerboard pattern, Zhang and Paik developed a lightweight kirigami metamaterial (see Fig. 1-12(b)) that can withstand high loads (2875 times its own weight)^[12]. Another noteworthy contribution is the zigzag kirigami (see Fig. 1-12(c)) proposed by Eidini, where the unit cell of the patterns comprises two zigzag strips surrounding a hole with a parallelogram shape^[151,152]. It is proved that zigzag kirigami-based mechanical metamaterials not only retain the characteristics of the Miura-ori, including negative Poisson's ratio, flat-foldable, and developable, but also perform lower density and higher programmability than Miura-ori.

Furthermore, adding creases to existing rigid kirigami patterns and cuts to existing rigid origami, is another potential method for designing novel kirigami patterns, albeit at the cost of introducing potentially undesirable multi-DOFs, whilst enriching the deformation modes of the metamaterials^[153,154]. For example, Yin et al. added more creases to rotating square and triangular structures to reconstruct the underlying patterns^[154], as shown in Fig. 1-12(d). The results showed that the supplemented folds did not only enrich the structural reconfiguration beyond sole cuts but also demonstrated that multi-DOFs in the deformation of unit cells enable metamaterials to perform diverse mechanical properties. Jamalimehr et al. designed a class of rigidly

foldable cellular metamaterials, with unit cells obtained by removing the centre panel of a pattern of origami twist family^[153], as shown in Fig. 1-12(e). These metamaterials can be flat folded and locked into several states that are stiff across multiple directions, even including the deployment direction.

Finally, an innovation involves strategically arranging creases and cuts at the surfaces and edges of polyhedrons to obtain rigid kirigami patterns^[155–157]. For example, Zhang et al. innovatively transformed a cuboid into a foldable 3 DOF kirigami design (Fig. 1-12(f)), which evolved into a tri-stable kirigami meta-structure with specific elastic joints, enabling a frequency-reconfigurable antenna with three programmable working frequencies^[155].

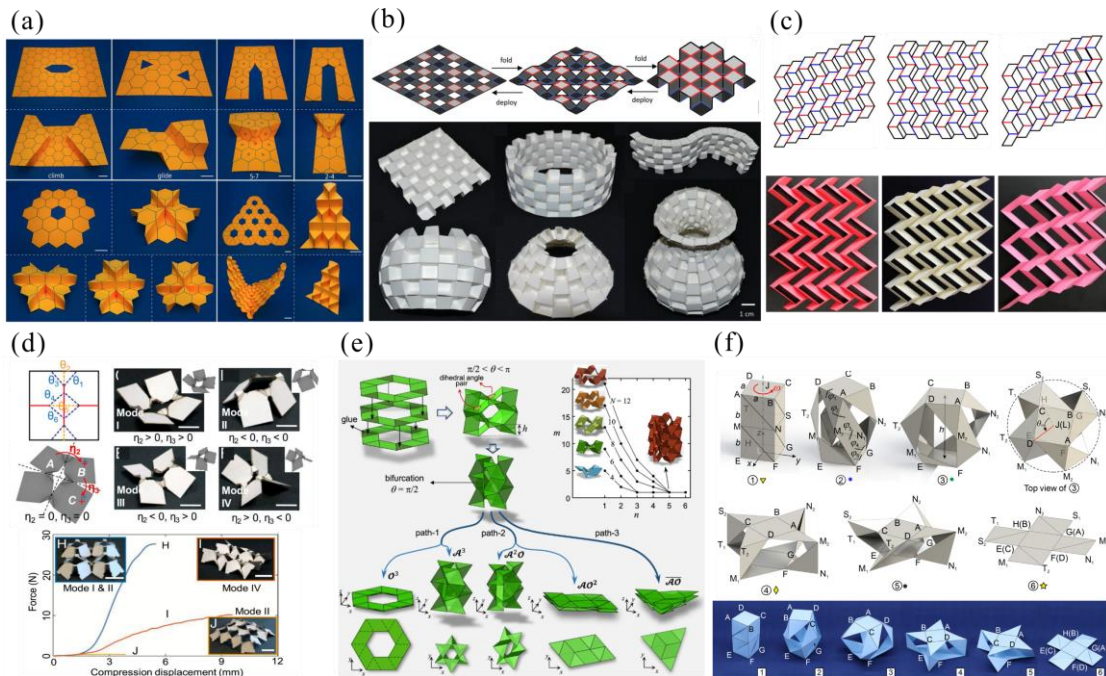


Fig. 1-12 Ori-kirigami-based mechanical metamaterials. (a) Cuts and creases are introduced in a continuous flat sheet^[149,158]; (b) checkerboard kirigami^[12]; (c) zigzag kirigami^[152,159]; (d) adding creases to existing rigid kirigami patterns^[154]; (e) remove some of the panels from a rigid origami pattern^[153]; (f) arranging creases and cuts at the surfaces and edges of polyhedrons to obtain rigid kirigami patterns^[155].

In general, existing rigid kirigami metamaterials achieve tuneable and programmable mechanical properties by releasing continuous constraints in structures and significantly increasing the kinematic degrees of freedom. The vast majority of

existing designs, with only a few exceptions, exemplified by single DOF examples that deform solely between two final configurations, feature multi-DOFs unit cells. The absence of kinematic guidance in these design methods typically necessitates a substantial number of cuts and the removal of sufficient panels to grant mobility, allowing the remaining panels to rotate in-plane and out-of-plane and form intricate yet uniform shapes. As a result, to utilize the diverse kinematic modes inherent in these unit cells to achieve programmable properties, the deformation process must occur under certain symmetry, boundary, and actuation conditions. Currently, a critical challenge is determining the number, size, and direction of cuts and folds, to design unit cells with one or less DOF yet with a variety of deformation modes, facilitating the programming of properties in kirigami metamaterials.

1.2.3.3 Modular Origami-based Mechanical Metamaterials

Modular origami, an extension of conventional origami and kirigami techniques, can be traced back to the paper folding of polyhedron units by origami artists^[160,161]. This technique involves folding multiple pieces of paper and then interlocking or connecting these folded modules to create intricate and diverse 3D structures, as shown in Fig. 1-13. Notably, certain modular origami structures exhibit shape transformation due to inherent mobility, which imparts unconventional physical properties to the entire structure. This characteristic has positioned modular origami as a compelling avenue for designing 3D metamaterials that take advantage of their simplicity and versatility. Yang et al. introduced a spatial overconstrained 6R linkage in modular origami, i.e., the Sarrus 6R linkage^[162], characterized by single DOF linear motion, and constructed a series of 3D modular metamaterials with negative Poisson's ratio^[163] (Fig. 1-13(a)) and even programmable almost constant Poisson's ratio in three orthogonal directions^[164] (Fig. 1-13(b)). Ma et al. developed a 3D modular origami-based meta-structure^[165], as shown in see Fig. 1-13(c), which also kinematically equivalent assembly of Sarrus 6R linkage and planar 4R linkage mechanisms featuring continuous mechanism motion and bi-stability, enabling programmable control of both mechanism motion and structural deformation through careful adjustment of geometric parameters and joint stiffness. The examples of modular origami-inspired mechanical metamaterials in Fig. 1-13 have only one deformation path, which means that the ability to tune their properties is limited.

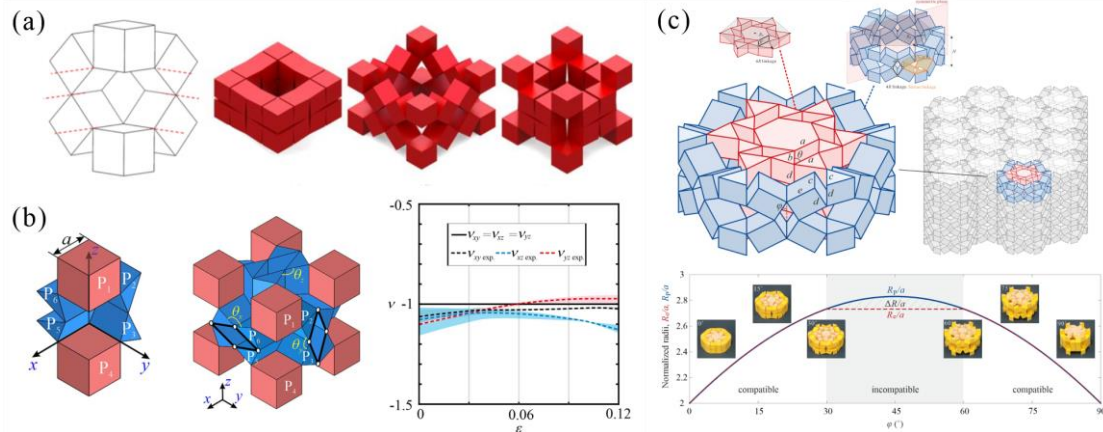


Fig. 1-13 Modular origami-inspired mechanical metamaterials with a single deformation path. (a) (a) A Sarrus linkage-based 3D modular structure^[163]; (b) 3D metamaterials with programmable almost constant Poisson's ratio^[164]; (c) 3D modular metamaterials with customized bi-stability^[165].

As a branch of origami, the appeal of modular origami lies not only in its visual appeal arising from simple folding but also in more powerful, yet pervasive, rich configurations. For example, Yang et al.^[166] assembled single DOF lantern modules (formed by introducing folds and cuts in pieces of paper before gluing them together) into large-scale metamaterials. Since a single module has two mutually compatible deformation modes, each module can have its mechanical properties independently prescribed from their adjacent neighbours, ultimately realizing decoupling local mechanics from the large-scale structure in modular metamaterials. Inspired by the geometries of snapology origami, Overvelde et al. presented a transformable metamaterial (see Fig. 1-14(a)) endowed with multiple degrees of freedom, wherein the shape, volume, and stiffness can be actively controlled through the incorporation of air pockets^[167]. Building on that work, Overvelde et al. also introduce a robust design strategy based on space-filling tessellations of polyhedra to create three-dimensional reconfigurable materials with a wide range of qualitatively different deformations^[168], as shown in Fig. 1-14(b). Inspired by the above pioneering works of Overvelde, Xiao et al. recently proposed an inverse design approach for complex 3D curvilinear modular structures with reconfigurability rather than tessellating a constant building block^[169], as shown in Fig. 1-14(c). Li and Yin innovatively assembled 3D kirigami-inspired modules with multiple transformation paths, each consisting of eight closed-loop connected cubes, as shown in Fig. 1-14(d), kinematically equivalent to a multi-DOFs spatial 8R linkage, which greatly enhances the reconfigurability and shape re-

programmability in architected matter^[170]. Expanding on their work, Li and Yin further developed kirigami inspired module for reconfigurable metamaterials with diverse structures and unique properties, including reconfigurable 2D metamaterials undergoing chirality phase transitions and 3D metamaterials with programmable deformation modes^[171], as shown in Fig. 1-14(e). Very recently, inspired by the 3D modular origami design with decoupled planar 4-bar linkage motions in the three orthogonal planes, Hu et al. propose a type of transformable mechanical metamaterials that can be reversibly transformed among null-, uni-, bi-, tri-, quadra-, penta-, and hexa-modes, leading to tuneable mechanical properties and reprogrammable wave functionalities^[13], as shown in Fig. 1-14(f).

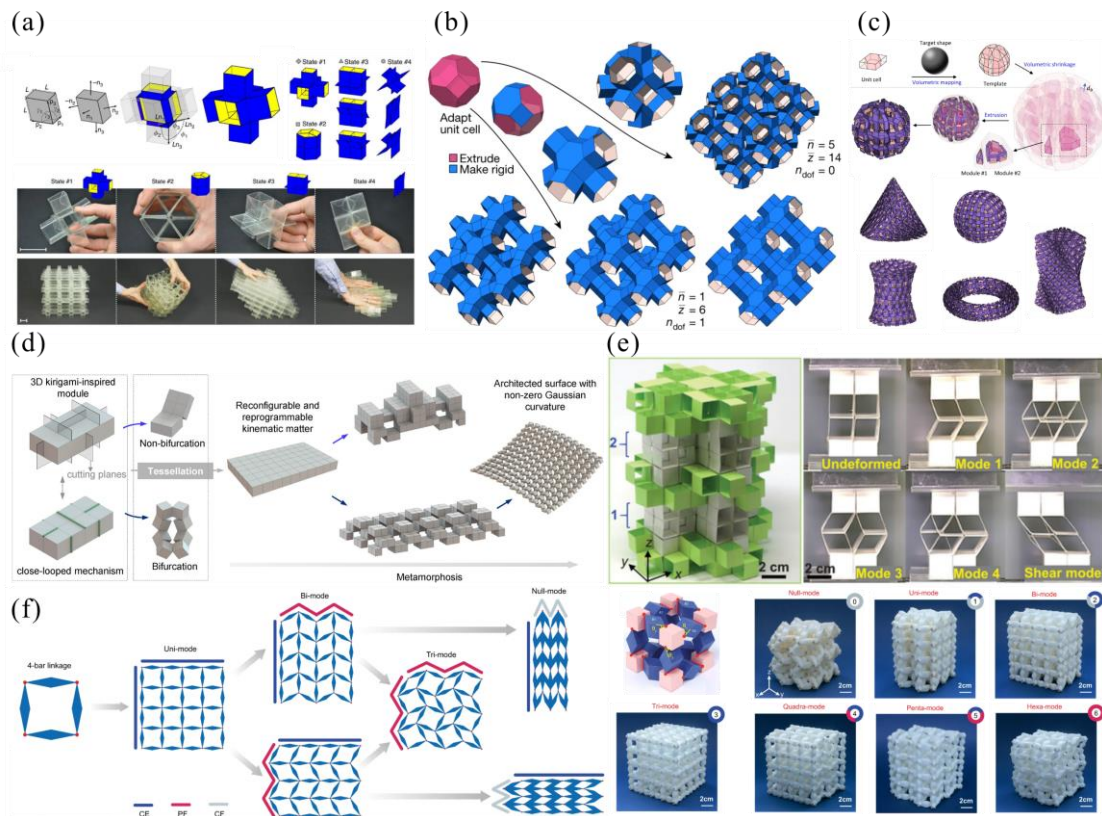


Fig. 1-14 Modular origami-inspired mechanical metamaterials with multiple deformation paths.

(a) A snapology-inspired transformable metamaterial with multi-DOFs^[167]; (b) reconfigurable prismatic architected materials^[168]; (c) the inverse design of 3D reconfigurable curvilinear modular origami structures^[169]; (d) an eight cube-based kirigami module-based reconfigurable and reprogrammable architected matter^[170]; (e) 3D transformable modular kirigami-based programmable metamaterials^[171]; (f) 3D metamaterials transformed for different zero modes^[13].

From a mechanism point of view, modular origami tends to be an alternative form of a hybrid network of planar, spherical, and spatial linkages, and it is its induced multi-DOFs that add rich deformation modes to the origami structure. Modular origami, a sub-category of origami structures, is more flexible in design and richer in configuration than conventional origami and kirigami, but as well as being plagued by the problem of multi-DOFs. Therefore, if one start from the reconfigurability of the underlying linkage of modular origami and its mobile network, it is possible to design single DOF structures with multiple deformation modes, which will entail a great advancement in the tunability and programmability of mechanical metamaterials.

1.3 Aim and Scope

The primary objective of this dissertation is to develop single DOF reconfigurable origami structures endowed with the capability of multiple shape reconfigurations, and further to develop a series of mechanical metamaterials with tuneable properties, to lay a robust theoretical foundation for realising the leap of metamaterials from theoretical research to engineering applications.

In this process, the principles of reconfigurable linkages will be used to guide the design of origami structures with one DOF. Then, the kinematic bifurcation and configuration evolution of origami structures will be analysed according to developed kinematic models. Next, the geometric and kinematic compatibility between different bifurcation configurations will be exploited to determine the connections between the unit cells and to construct homogeneous and heterogeneous 2D or 3D mechanical metamaterials concerning networking methods for reconfigurable and deployable structures. Finally, the analytical relationships between geometry, deformation, topology, and properties are to be established to explore the qualitative and quantitative tuning strategies for the physical properties of origami metamaterials.

1.4 Main Contents

This dissertation consists of six chapters, which are outlined as follows, while a diagram of the main contents is shown in Fig. 1-15.

Chapter 1 introduces the existing kinematic theory and its application in the analysis and design of various origami structures as well as the current state of research

on reconfigurable mechanisms. Besides, mechanical metamaterials induced by the folding behaviour based on origami, kirigami, and modular origami are also reviewed.

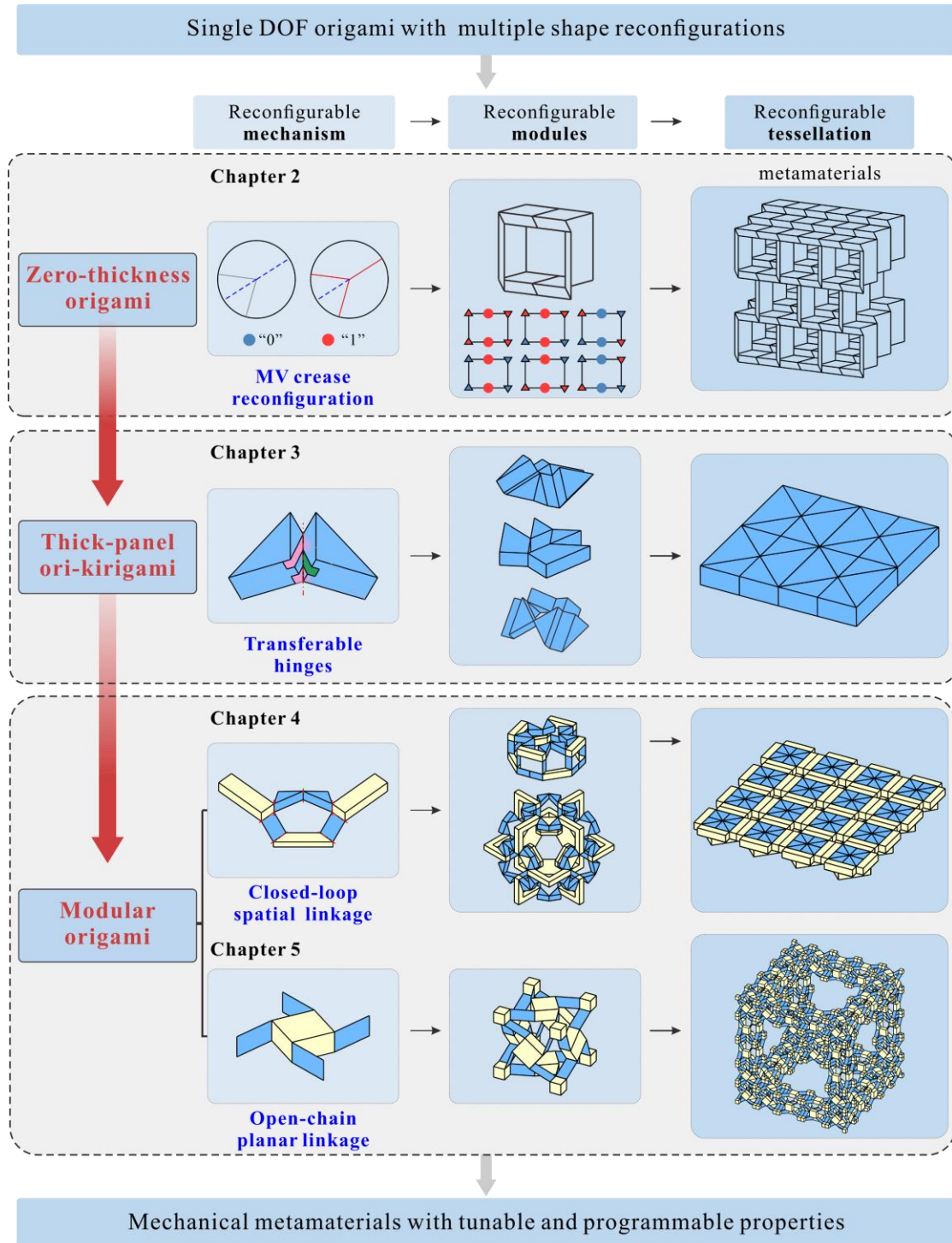


Fig. 1-15 Diagram of the main contents of this dissertation.

Chapter 2 presents a straightforward algorithm that combines graphic representation and motion compatibility conditions to assess the reconfigurability of one-DOF origami structures with 4-crease vertices as well as their 2D and even 3D cellular tessellations.

Chapter 3 focuses on the reconfigurable thick-panel ori-kirigami design using vertically transferable joints and the investigation of the influence of design parameters on the folding behaviour under different motion branches. In addition, the properties of single DOF tessellation are also investigated, including Poisson's ratio, deployable ratio, and load-bearing capacity.

Chapter 4 discusses modular origami design from the perspective of alternative forms of single-loop linkage with kinematic bifurcation. Then, based on the deformation characteristics of different bifurcation configurations, compatible connections between reconfigurable units are proposed for the design of single DOF modules, followed by their constructed mechanical metamaterials with tuneable 2D symmetry groups and customised sign of Poisson's ratios.

Chapter 5 reveals the bifurcation behaviour of a single DOF modular cube by the kinematic model of an open-chain PLG under symmetric constraints. Then, Poisson's ratio, chirality, and stiffness of a single polyhedron module during reconfiguration were also studied. Further, a combinatorial design strategy, i.e., stacking different bifurcation configurations in 3D space, is proposed to enhance the programmability of Poisson's ratio. Finally, the modular cube is generalised to a series of single DOF reconfigurable prism structures, all of which have NPR/ZPR/PPR.

Chapter 6 summarises the main achievements and plans for future work, which conclude this dissertation.

At the crossover of kinematics, structural engineering, mechanics and materials, this endeavour guides the use of kinematic bifurcation from the perspectives of MV crease reconfiguration, transferable hinges, reconfigurable closed-loop spatial linkage and open-chain planar linkage, to design and analyse single DOF zero-thickness origami, thick-panel ori-kirigami, and modular origami structures with multiple shape reconfigurations. In addition, the tunability and programmability of the properties of the developed mechanical metamaterials have been investigated.

Chapter 2 Mountain-Valley Crease Reconfiguration of 4-Crease Origami Vertices and Tessellations

2.1 Introduction

Origami studies undoubtedly begin with the predefined crease pattern, where the most basic rigid-foldable unit for origami designs with one DOF is a four-crease vertex. Most of these studies have concentrated on the fixed crease topology in which an origami pattern folds between two final shapes with a clearly defined MV assignment. Reconfigurable origami-inspired folding has recently gained significant attention due to its potential to achieve multi-shape changes through crease topological morphing, resulting in multi-functionality from a single original structure. Hence, an essential understanding of the topological reconfiguration of four-crease vertices origami and their tessellations is critical to creating advanced functionalities. For any origami pattern with an un-predefined MV assignment, from the kinematic point of view, one of the major challenges is to identify the reconfigurability by inspecting all bifurcation paths precisely. However, there is no generic method that can identify the specific MV assignments with qualitatively different rigid folding behaviour in an origami tessellation consisting of four-crease vertices, which forms the goal of this chapter.

The layout of the chapter is as follows: in section 2.2, a Depth First Search (DFS) algorithm^[172] that combines graphic representation and motion compatibility conditions for evaluating the reconfigurability of origami structures composed of double corrugated, Miura-ori, and symmetric Eggbox vertices is developed. In section 2.3, the efficiency and accuracy of the method are demonstrated by searching for all rigid MV assignments of well-known 2D origami tessellations. Additionally, a 3D cellular origami example is presented in section 2.3, showcasing all possible rigid MV assignments as well as variations in typical folding behaviour. Finally, conclusions are drawn in section 2.4.

2.2 Evaluation Method for Reconfigurability

2.2.1 Kinematics of the Four-crease Vertices and Their Assemblies

Starting with a four-crease vertex where four panels p_i ($i = 1, 2, 3, 4$, counted clockwise) are connected by four creases c_i on the pattern and characterized by four

sector angles $\alpha_{i(i+1)}$, as shown in Fig. 2-1. Referring to the vertex widely used to construct rigid origami patterns, the generic four-crease vertex is categorised into three types: double corrugated, Miura-ori, and Eggbox vertices with symmetric features (Although symmetry is not required for general eggbox vertices, more attention is paid to symmetric one for flat-foldability). Both the double corrugated and Miura-ori vertices satisfy the flat-foldability $\alpha_{12} + \alpha_{34} = \alpha_{23} + \alpha_{41}$ and developability $\alpha_{12} + \alpha_{23} + \alpha_{34} + \alpha_{41} = 2\pi$. The difference is that the former can be folded flat without collinear creases, while the latter possesses a pair of collinear creases. The symmetric Eggbox vertex loses developability while keeping the flat-foldability. The geometric parameters for these three types of vertices are

$$\alpha_{12} = \alpha, \alpha_{23} = \beta, \alpha_{34} = \pi - \alpha, \alpha_{41} = \pi - \beta \quad (2-1)$$

$$\alpha_{12} = \alpha_{23} = \alpha, \alpha_{34} = \alpha_{41} = \pi - \alpha \quad (2-2)$$

and

$$\alpha_{12} = \alpha_{23} = \alpha, \alpha_{34} = \alpha_{41} = \beta, \alpha + \beta \neq \pi \quad (2-3)$$

respectively. Note that α_{12} is set as the smallest sector angle.

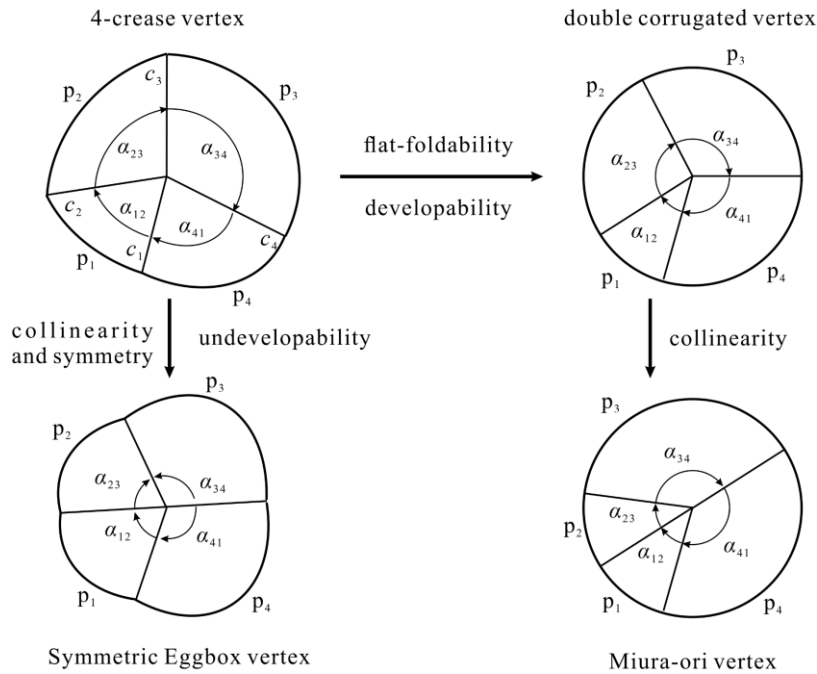


Fig. 2-1 Evolution among a generic four-crease vertex and three types of vertices, i.e., double corrugated, Miura-ori, and symmetric Eggbox vertices.

To describe their rigid motions, panels and creases are represented by links and revolute joints, as shown in Fig. 2-2. Therefore, a single four-crease vertex with creases intersecting at one point is kinematically a spherical 4R linkage and can be analysed with the matrix method in kinematics^[45,132,173]. For the double corrugated vertex shown in Fig. 2-2 (a), the kinematic relationship between the revolute variable θ_i and the geometric parameter $\alpha_{i(i+1)}$ can be derived following D-H notations^[84], i.e.,

$$\frac{\tan \frac{\theta_1}{2}}{\tan \frac{\theta_2}{2}} = -\frac{\sin \frac{\alpha_{23} - \alpha_{12}}{2}}{\sin \frac{\alpha_{23} + \alpha_{12}}{2}}, \quad \theta_1 = -\theta_3, \quad \theta_2 = \theta_4 \quad (2-4)$$

or

$$\frac{\tan \frac{\theta_1}{2}}{\tan \frac{\theta_2}{2}} = -\frac{\cos \frac{\alpha_{23} - \alpha_{12}}{2}}{\cos \frac{\alpha_{23} + \alpha_{12}}{2}}, \quad \theta_1 = \theta_3, \quad \theta_2 = -\theta_4 \quad (2-5)$$

There are two sets of solutions in Eqs. (2-4) and (2-5), and their corresponding kinematic paths θ_2 vs θ_1 as well as MV assignments of the vertex are plotted in Fig. 2-2(a), where the geometric parameters with $\alpha = 30^\circ$, $\beta = 100^\circ$ are taken as an example. There are two different MV assignments MV-I and MV-II, whose kinematic paths are path I and path II, respectively. Here is a trick to distinguish between these two crease topologies for the double corrugated vertex, i.e., if the two adjacent creases of crease c_1 have the same MV assignments, then it belongs to MV-I, otherwise it is MV-II. Both the fully unfolded and folded configurations are bifurcation points, at the unfolded one, MV assignments switch between MV-I and MV-II, while such switching cannot happen as folded one due to the physical interference, i.e., the panels cannot protrude each other. Note that flipping the paper results in the simultaneous interchange of all MV creases, a condition deemed equivalent in crease topology within this study.

Turning attention to the Miura-ori vertex in Fig. 2-2(b), three sets of solutions can be obtained, i.e.,

$$\theta_1 = \theta_3 = 0, \quad \theta_2 = \theta_4 \quad (2-6)$$

$$\frac{\tan \frac{\theta_1}{2}}{\tan \frac{\theta_2}{2}} = \cos \alpha_{12}, \quad \theta_1 = \theta_3, \quad \theta_2 = -\theta_4 \quad (2-7)$$

or

$$\theta_1 = -\theta_3, \theta_2 = \theta_4 = \pi \quad (2-8)$$

The kinematic paths and corresponding MV assignments of the Miura-ori vertex with $\alpha = 30^\circ$ are plotted in Fig. 2-2(b). The unfolded configuration at point (0, 0) is one of the bifurcation points where the Miura-ori vertex can achieve the switch of crease topology between MV-I and MV-II assignments. When the vertex in path I is fully folded where panels p_1 and p_2 are fitted together, it can switch into path III at another bifurcation point $(0, \pm\pi)$. After that, creases c_1 and c_3 are active, and creases c_2 and c_4 become inactive. There are two sets of closure equations for symmetric Eggbox vertex shown in Fig. 2-2(c), i.e.,

$$\begin{aligned} \theta_1 &= \theta_3 \\ \tan \frac{\theta_2}{2} &= \frac{1}{2} ((\cos \alpha_{12} + \sin \alpha_{12} \cot \alpha_{34}) \cot \frac{\theta_1}{2} - (\cos \alpha_{12} - \sin \alpha_{12} \cot \alpha_{34}) \tan \frac{\theta_1}{2}) \\ \tan \frac{\theta_4}{2} &= \frac{1}{2} ((\cos \alpha_{34} + \sin \alpha_{34} \cot \alpha_{12}) \cot \frac{\theta_1}{2} - (\cos \alpha_{34} - \sin \alpha_{34} \cot \alpha_{12}) \tan \frac{\theta_1}{2}) \end{aligned} \quad (2-9)$$

or

$$\theta_1 = -\theta_3, \theta_2 = \theta_4 = \pi \quad (2-10)$$

The kinematic paths and corresponding MV assignments of the symmetric Eggbox vertex are divided into two cases based on the geometric parameters $\sum \alpha_{i(i+1)} < 2\pi$ (Fig. 2-2(c) top) or $\sum \alpha_{i(i+1)} > 2\pi$ (Fig. 2-2(c) bottom). Despite having only two kinematic paths, the symmetric Eggbox vertex exhibits three distinct MV assignments. During motion along path I, a crease topological transition occurs by switching one of its creases between a mountain and a valley. Specifically, in the case of $\sum \alpha_{i(i+1)} < 2\pi$, one of four mountain creases of the symmetric Eggbox vertex, i.e., crease c_2 , switches into a valley crease when panels p_1 and p_2 are coplanar, thus achieving a Miura-like mode of folding motion. In the case of $\sum \alpha_{i(i+1)} > 2\pi$, the symmetric Eggbox vertex has two mountain creases and two valley creases, and the crease c_4 is changed from a mountain crease to a valley crease when panels p_3 and p_4 are coplanar, also achieving a Miura-like folding motion. On path II in both cases of $\sum \alpha_{i(i+1)} < 2\pi$ and $\sum \alpha_{i(i+1)} > 2\pi$, the creases c_2 and c_4 are inactive, leading to MV-III.

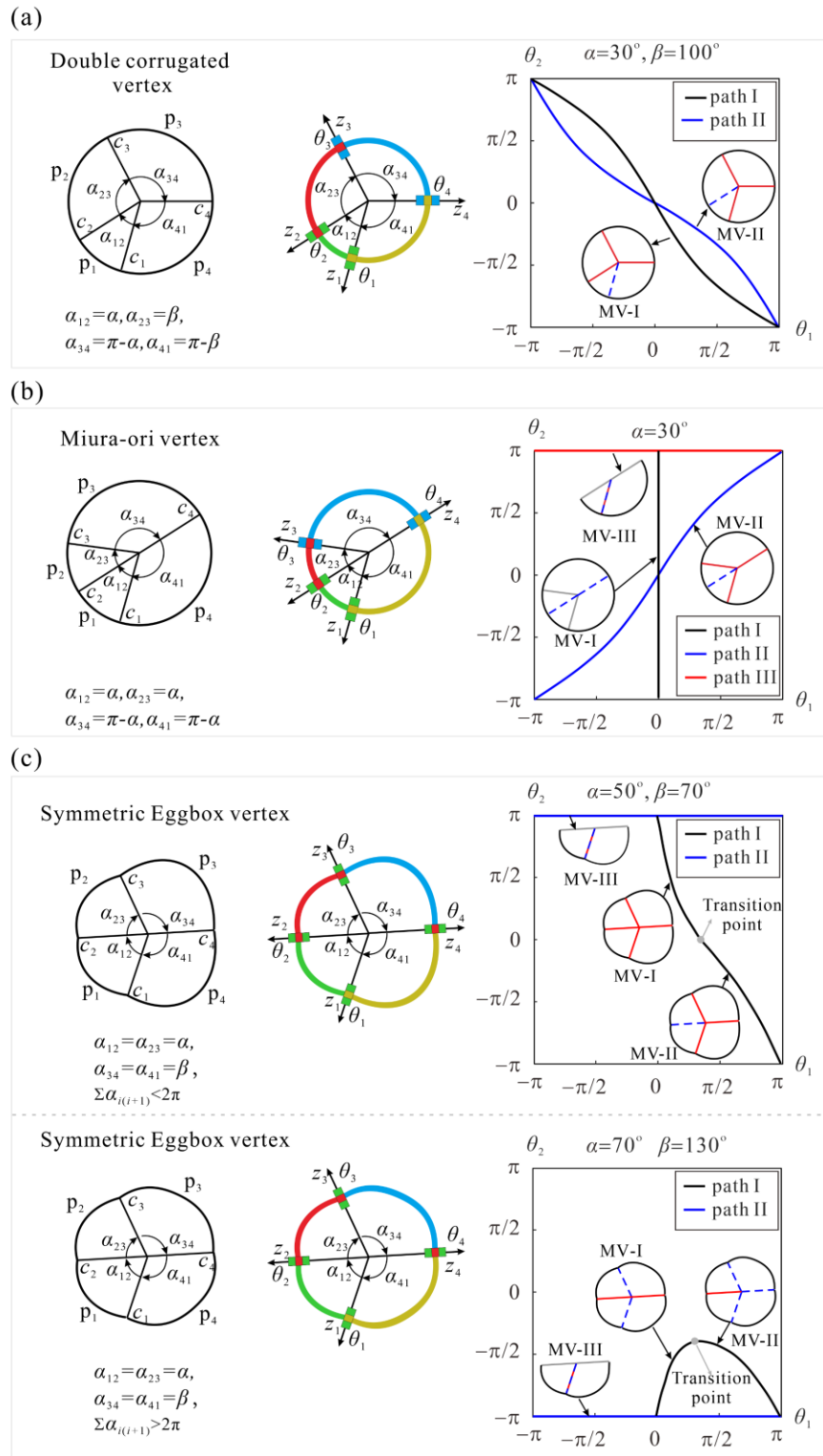


Fig. 2-2 Kinematics of three types of 4-crease vertices. (a-c) From left to right are origami vertices with un-predefined MV assignment, linkage form, and kinematic paths θ_2 vs θ_1 plus MV assignments for the double corrugated, Miura-ori, and symmetric Eggbox vertices, respectively.

To illustrate proposed approach, the quadrilateral mesh shown in Fig. 2-3(a) was taken as an example. As depicted in Fig. 2-3(a), this pattern containing multiple vertices can be conceptualised as an assembly of spherical 4R linkages. The coordinate frames F'_k ($k=A, B, C, D$) following the D-H notations are established at the joints of each spherical 4R linkage, as shown in Fig. 2-3(b). Sector angles $\alpha_{i(i+1)}^k$ at vertex k are marked clockwise and α_{12}^k is the smallest sector angle. The explicit function between the input angle θ_i^k and the output angle θ_{i+1}^k about vertex k is given by Eqs. (2-4)-(2-10), which can also be represented concisely in implicit function form as $f_{i(i+1)}^k(\theta_i^k) = \theta_{i+1}^k$. Hence, as shown in Fig. 2-3(b), the compatibility condition^[84] of the corresponding linkage form is

$$\prod_{k=A}^D f^k = I_4 \quad (2-11)$$

The expression establishes a link between the MV assignments and bifurcation paths by considering geometric parameters and kinematic variables. This relationship enables the transformation of evaluating the number of rigid or valid MV assignments of a pattern containing several vertices into a solvable combinatorial problem.

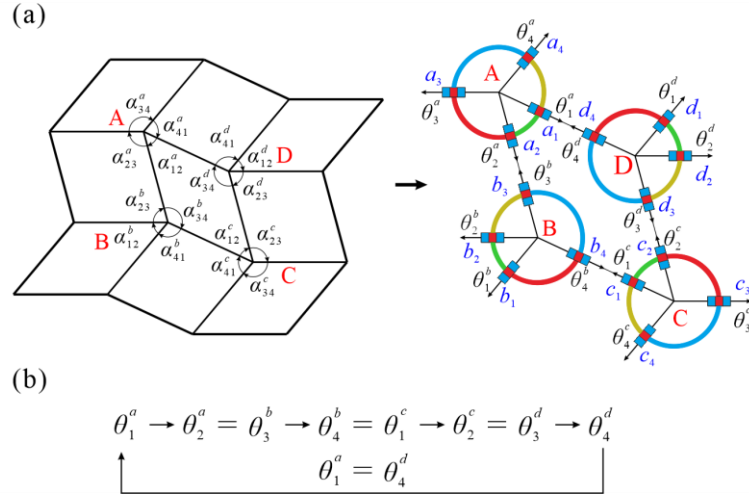


Fig. 2-3 Motion compatibility of assemblies of spherical 4R linkages. (a) The quadrilateral mesh origami and the corresponding mobile assembly and (b) the motion transmission path.

2.2.2 Graphic Representation of Origami Modules

The above kinematic method to understand the reconfigurability of crease patterns is powerful and efficient for a single four-crease vertex, but rather complicated for multi-vertices tessellations due to the inherent complexity arising from the mutual

nesting of motion loops. In contrast, graphic representation, where objects and connections are represented by shapes and lines, works perfectly here. Taking inspiration from the concept of modularity, a single loop unit, encompassing several four-crease vertices, can be initially perceived as a module, and then the physical vertices and modules can be translated into a graphic representation. As illustrated in Fig. 2-4(a), double corrugated vertices with MV-I and MV-II assignments are denoted by central blue and red circles with black boundaries, respectively, whereas Miura-ori vertices with MV-I and MV-II assignments are depicted by central blue and red circles without boundaries (Fig. 2-4(b)). The symmetric Eggbox vertices with MV-I and MV-II assignments (Fig. 2-4(c)) are represented by the central blue and red upward triangles with black boundaries, respectively, in the case of $\sum \alpha_{i(i+1)} < 2\pi$. In contrast, the downward triangle is used in the case of $\sum \alpha_{i(i+1)} > 2\pi$. It is noteworthy that the vertex with MV-III assignments is considered a defective configuration, as the motion curve of this type of vertex indicates that the panel of vertices connected to vertices with MV-III assignments remains fixed. Thus, meaningless defected configurations with MV-III assignments at both Miura-ori and symmetric Eggbox vertices are excluded. Meanwhile, each vertex is assigned a value of “0” or “1” based on conformity to MV-I or MV-II assignments. After that, the compatibility condition in Eq. (2-11) is used to find all valid M-V assignments of the module. It is worth noting that each vertex has two general path options. As a result, there are up to sixteen combinations for quadrilateral-mesh modules. However, there are kinematic relationships between neighbouring vertices, and many of these sixteen combinations are invalid and can be assessed one by one using Eq. (2-11).

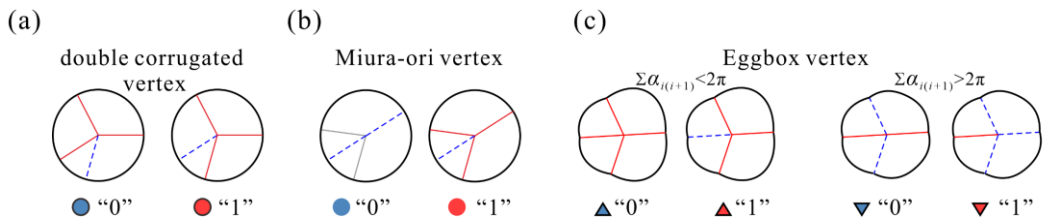


Fig. 2-4 Graphic representations of a single vertex. The blue and red fillings represent MV-I and MV-II assignments, respectively, while circles with black boundaries, circles without boundaries, and triangles with upward or downward orientations represent (a) double corrugated, (b) Miura-ori, and (c) symmetric Eggbox ($\sum \alpha_{i(i+1)} < 2\pi$ and $\sum \alpha_{i(i+1)} > 2\pi$) vertices, respectively.

	Module	Graphic representation	Module	Graphic representation	
1			10		
2			11		
3			12		
4			13		
5			14		
6			15		
7			16		
8			17		
9			18		

Fig. 2-5 Graphic representations of eighteen typical modules consisting of double corrugated, Miura-ori, symmetric Eggbox vertices and their hybridization.

Here, eighteen typical modules distinguished by vertex type and geometric parameters derived from well-known origami patterns are listed in Fig. 2-5, whose prototypes are displayed in Appendix A. Each MV assignment corresponds to the graph for any of the modules one by one. As shown in Fig. 2-5, modules are schematically indicated by graphs, where each line represents a connection and circles or triangles on four corners represent four vertices. It is straightforward that modules 1-10, 11-13, and 14-15 are composed of pure double corrugated, Miura-ori, and symmetric Eggbox vertices, respectively, while hybrid vertices form modules 16-18. Modules 1-5 can be rigidly folded along six different MV assignments according to compatibility conditions. With the enhancement of the constraint generated by the geometry in modules 6-9, the number of valid MV assignments is decreased to four or even two. The common point of modules 1-9 is that two vertices possess MV-I assignments, and the other two satisfy MV-II assignments. Nevertheless, module 10, consisting of a pure double corrugated vertex, requires all four vertices to simultaneously satisfy MV-I or MV-II assignments. Modules 11-13 with Miura-ori vertices have four similar crease topologies, i.e., one column for MV-I and the other column for MV-II, or vice versa, or cases that all for MV-I or MV-II. As for modules 14-15 with symmetric Eggbox vertices, the number of valid MV assignments is four or two, depending on the location of the smallest sector angle. Module 16 is a hybrid of two double corrugated and two symmetric Miura-ori vertices, while modules 17 and 18 are a hybrid of two Miura-ori and two symmetric Eggbox vertices. In the former, the Miura-ori vertex can only be MV-II assignments, while the latter only requires that two vertices in the same column belong to either MV-I or MV-II simultaneously.

2.2.3 Algorithm Design for Origami Tessellation with Size $m \times n$

After addressing the reconfigurability analysis of origami modules based on compatibility conditions, the reconfigurability of origami tessellations using graphic representation and algorithms was further investigated. At first, the origami tessellation is abstracted into a checkerboard with size $m \times n$ (m and n are numbers of vertices in the orthogonal directions), described by a matrix $\mathbf{A} = (a_{ij})_{m \times n}$. Taking the double corrugated pattern (Fig. 2-6(a)) parameterised by α and β as an example, it consists of 3×4 four-crease vertices without predefined MV assignments. So, the 3×4 checkerboard is characterised by a matrix $\mathbf{A} = (a_{ij})_{3 \times 4}$. Next, composed modules are founded according to geometric parameters. As shown in Fig. 2-6(a), it consists of two types of modules

(exactly modules 1 and 2 in Fig. 2-5), one considered as the basic module and the other considered as the connection module to constrain neighbouring basic modules, which can be easily distinguished by the geometry of the central quadrilateral panel. It was found that the two modules in double corrugated pattern share six types of MV assignments with distinct graphic representations, according to Fig. 2-5. Hence, the null matrix $A_{2 \times 2}$ of the module can be assigned values and expressed as $\begin{bmatrix} 0 & 1 \\ 0 & 1 \end{bmatrix}$, $\begin{bmatrix} 0 & 1 \\ 1 & 0 \end{bmatrix}$, $\begin{bmatrix} 0 & 0 \\ 1 & 1 \end{bmatrix}$, $\begin{bmatrix} 1 & 0 \\ 1 & 0 \end{bmatrix}$, $\begin{bmatrix} 1 & 0 \\ 0 & 1 \end{bmatrix}$, and $\begin{bmatrix} 1 & 1 \\ 0 & 0 \end{bmatrix}$. Finally, the notoriously difficult issue of compatibility conditions for origami tessellations under different MV assignments is transformed into the interesting discrete mathematical problem of filling a checkerboard with graphic representations of modules, which can be easily tackled with the aid of programming languages.

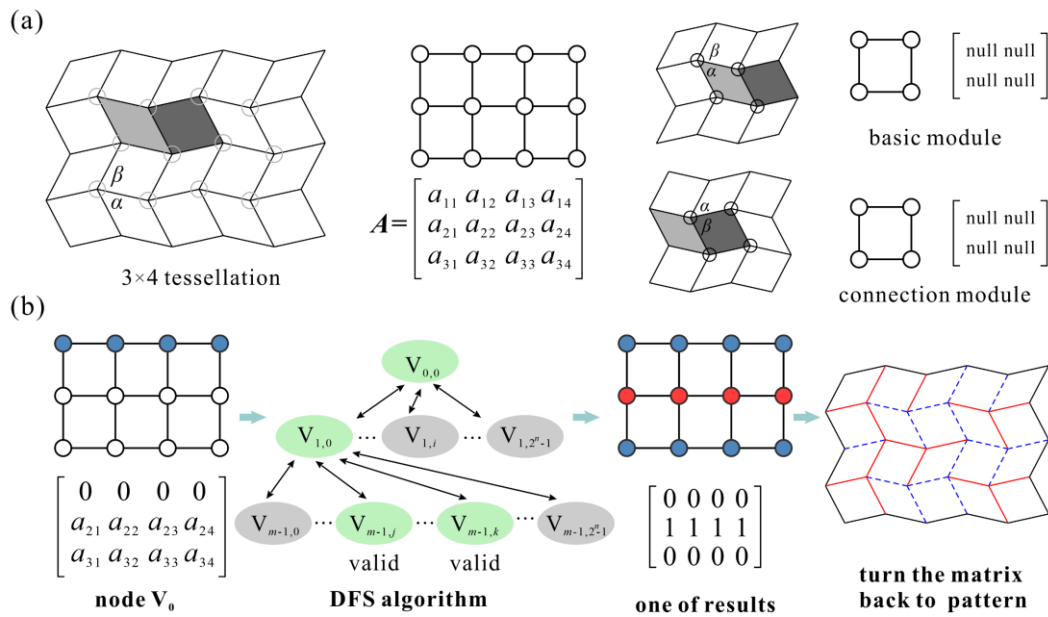


Fig. 2-6 Algorithm design for origami tessellation with size $m \times n$. (a) A tessellation without presupposed MV assignments consists of basic modules, and the connection module can be described as a checkerboard with size $m \times n$ and a null matrix. (b) The matrix can be further assigned values according to graphic representations of modules.

As shown in Fig. 2-6(b), the challenge of identifying origami tessellations with size $m \times n$ is first conceptualized as the pursuit of valid visit sequences in a m -layered graph where each layer contains 2^n nodes (corresponding to 2^n cases of an origami

tessellation row). For any two adjacent layers, connect $V_{i,j}, j \in (0, 2^{n-1})$ and $V_{i+1,k}, k \in (0, 2^{n-1})$ if row j and row k can form a valid origami tessellation (see lines 1-9 of Algorithm 1). Upon constructing the graph, for each node $V_{0,j}, j \in (0, 2^{n-1})$ in the first layer, conduct a depth-first search with $V_{0,j}$ as the current node and an empty visit sequence (see lines 10-12 of Algorithm 1). The algorithm investigates each branch to its fullest, guaranteeing comprehensive path coverage (see lines 14-23 of Algorithm 1). When a branch's end is reached, DFS backtracks to the previous decision point, allowing for the examination of alternative paths (see lines 16-19 of **Algorithm 1**). This process of moving forward and then backtracking enables a thorough exploration of the graph, uncovering every possible path starting from the source node. Therefore, at the end of the process, each valid node visit sequence (i.e., the matrix A) discovered by the algorithm can be turned back to an origami pattern with valid MV assignment.

Algorithm 1: Mountain-valley crease reconfiguration

Input: n, m

Output: valid results

```

1      For  $j$  from 0 to  $2^{n-1}$ :
2          For  $k$  from 0 to  $2^{n-1}$ :
3              If row [ $j$ ] and row [ $k$ ] form a valid origami tessellation:
4                  For  $i$  from 0 to  $m - 2$ :
5                      Connect  $V_{i,j}$  and  $V_{i+1,k}$ 
6                  end for
7              end if
8          end for
9      end for
10     For  $i$  from 0 to  $2^{n-1}$ :
11         DFS( $V_{0,i}$ )
12     end for
13     Return valid results

14     Function DFS(node):
15         Append node to the sequence
16         If the length of the sequence is equal to  $m$  then
17             Append the sequence to valid results
18         return
19     end if
20     For  $i$  in node's adjacent nodes of next layer:
21         DFS( $i$ )
22     end for
23     Delete node from the sequence

```

For a m -layered graph where each layer contains 2^n nodes, the computational complexity of the algorithm to identify all possible paths is usually at least $O(2^{m \times n})$.

However, the rules (e.g., $a_{ij} + a_{i(i+1)} + a_{(i+1)j} + a_{(i+1)(j+1)} = 2$) of basic and connection modules established according to the graphic representation and motion compatibility conditions prune the connections between nodes of any two adjacent layers (from 2^{2^n} to $2^n + 2$), so the size of the search space is effectively reduced. Therefore, the computational complexity of the algorithm is significantly simplified to $O(m \times 2^n + 2^m)$.

2.3 Reconfigurability of Origami Tessellations

2.3.1 2D Origami Tessellations

In this section, the proposed algorithm is examined with 2D tessellations of different 4-crease vertices. First, the variations in the number of valid MV assignments of the double corrugated pattern as the size of the tessellation increases is examined. For a 2×2 double corrugated pattern, there are six valid MV assignments. As raising the size of the tessellation, it is noticed an exponential growth in the number of valid MV assignments for $m \times n$ tessellation. Furthermore, it is also observed that the rate of increase in the number is the same regardless of whether a new column or row is added. Based on the graph evaluations and algorithm feedback, the number of valid MV assignments for $m \times n$ tessellations can be summarised as $2^m + 2^n - 2$. Fig. 2-7(a) visually illustrates search results for the number of valid MV assignments (black bars) for a double corrugated pattern with $n \times n$ tessellation. Note that the algorithm is highly efficient in terms of time consumption, see Appendix B for details. Another advantage of utilising the graphic representation, and DFS algorithm is the ability to remove duplicates by assessing the symmetry of the matrix \mathbf{A} . For example, the two graphic representations of 4×4 double corrugated tessellations depicted in Fig. 2-7(b) are valid MV assignments. However, upon rotating one of them by 180° , it is discovered that it perfectly overlaps the other, indicating that they are essentially the same geometric configuration. Consequently, only one of the two MV assignments is unique. The valid and unique MV assignments for $n \times n$ double corrugated tessellations are displayed in Fig. 2-7(a), bar charts with section lines. Out of the six rigid MV assignments available for 2×2 double corrugated tessellations, only four are valid and unique. Moreover, for 4×4 double corrugated tessellation, only eighteen out of thirty valid MV assignments are unique, whose prototypes and graphic representation are shown in Fig. 2-7(c).

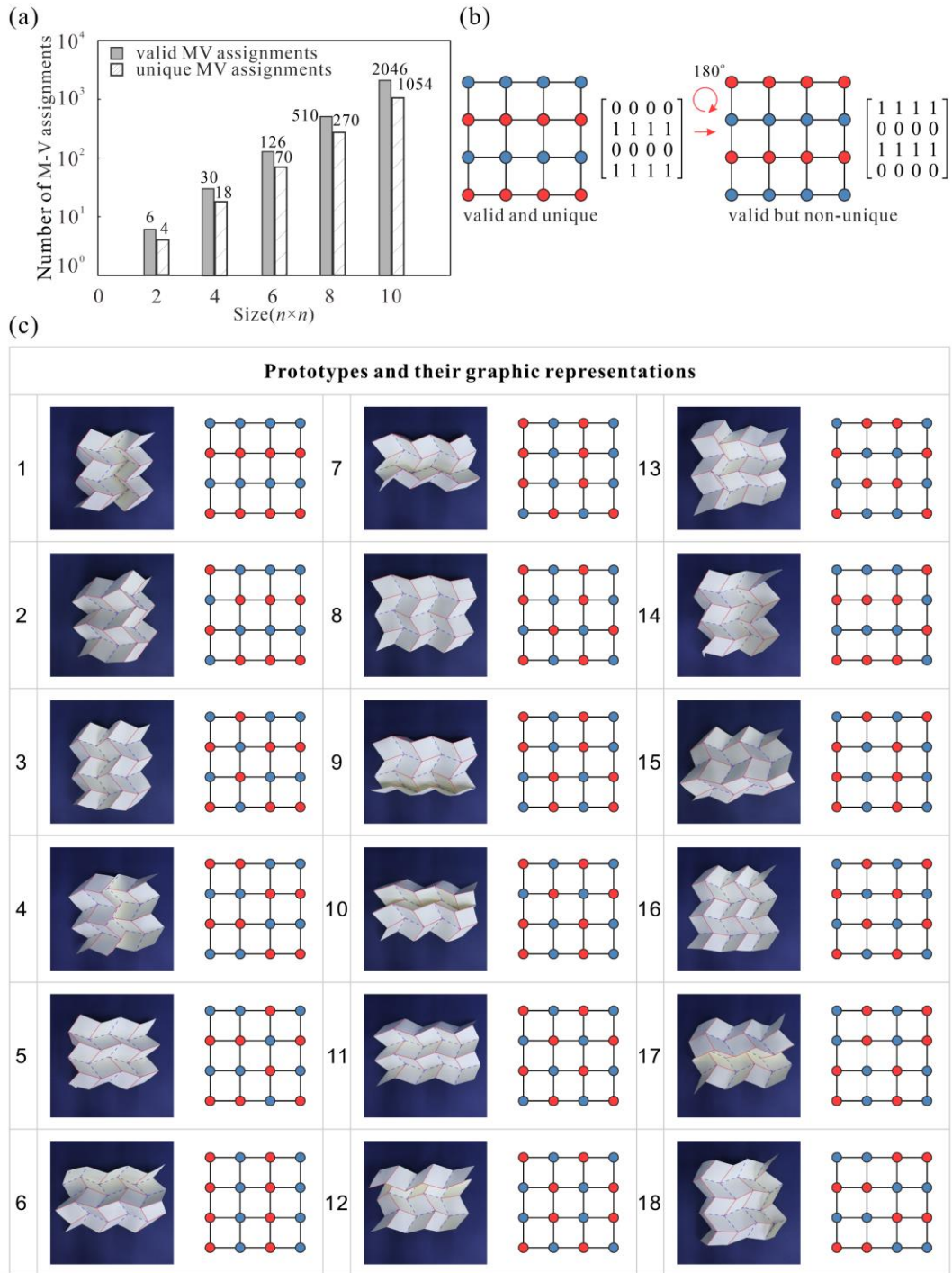
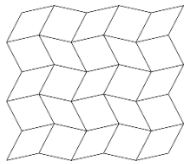
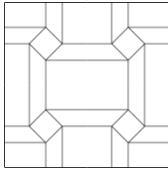
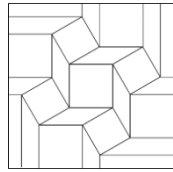


Fig. 2-7 The search results for the number of valid MV assignments of a double corrugated pattern. (a) Valid or unique MV assignments of a $n \times n$ double corrugated pattern tessellations. (b) Duplicates by assessing the symmetry of the matrix. (c) The eighteen unique MV assignments and corresponding graphical representations of 4×4 double corrugated pattern tessellations.

Research on rigid origami has promoted a substantial number of well-known patterns. the reconfigurability of these patterns based on intuitive rules in Fig. 2-5(b) is further investigated. Tab. 2-1 summarises the component modules and the number of valid MV assignments of these well-known patterns^[1, 26, 45-49]. As mentioned, combining modules 1 and 2 produces a double corrugated pattern. There are two tessellation methods of square twist, i.e., fitting modules 3, 4, and 5 creates the first type of square twist tessellation, while fitting modules 1 and 3 creates the second type. Since the modules in double corrugated pattern and square twist tessellations share rules, the number of their valid MV assignments are the same, i.e., $2^m + 2^n - 2$. Meanwhile, the number of valid MV assignments of a generalised Mars pattern is $2^n - 2$. Remarkably, the number of valid MV assignments in a dual square twist is always four with increasing system size, two of which are unique due to the centre symmetry of the pattern, while both the numbers of valid MV assignments in the generalised Huffman pattern and Helical pattern remain two. This means that the dual square twist, generalised Huffman pattern and Helical pattern displayed in Fig. 2-8 belong to oligo-modal origami with a constant number (≥ 2) of zero-energy deformation modes independent of tessellation size^[50]. Besides, the Miura-ori pattern and its derivatives, i.e., the Chicken wire tessellation and the Arc-Miura tessellation, exist 2^n valid MV assignments. It found that the number of valid MV assignments for Eggbox tessellation and quadrilateral creased pattern depends on the even/odd of n yet is independent of m .

Tab. 2-1 The number of valid MV assignments for well-known origami patterns

Tessellations	Component modules	Size	Valid M-V assignments
 Double corrugated tessellation	modules 1 and 2	$m \times n$	$2^m + 2^n - 2$
 Square twist pattern	modules 3, 4, and 5	$m \times n$	$2^m + 2^n - 2$

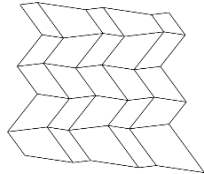


Square twist pattern

modules 1 and 3

$m \times n$

$2^m + 2^n - 2$

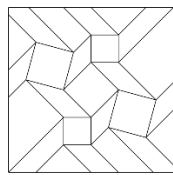


Generalized Mars pattern

module 6

$m \times n$

$2^n - 2$

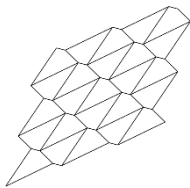


Dual square twist pattern

modules 3, 6 and 7

$m \times n, m, n \geq 4,$
and m, n are
even
numbers

4 (2 of which are
unique)

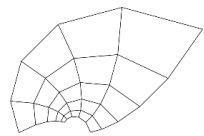


Generalized Huffman grid pattern

module 9

$m \times n$

2

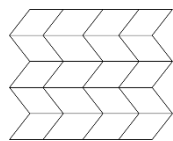


Helical pattern

module 10

$m \times n$

2

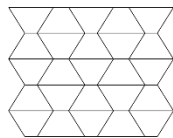


Miura-ori pattern

module 11

$m \times n$

2^n

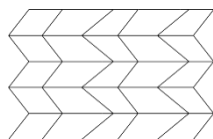


Chicken wire tessellation

module 12

$m \times n$

2^n

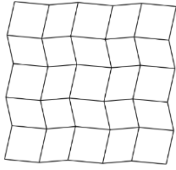
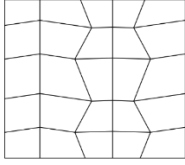


Arc-Miura tessellation

module 13

$m \times n$

2^n

 Eggbox pattern	module 14 and 15	$m \times n$, n is odd	$2^{(n+1)/2}$
		$m \times n$, n is even	$2^{n/2}$
 Quadrilateral creased pattern	module 16	$m \times n$, n is odd	$2^{(n-1)/2}$
		$m \times n$, n is even	$2^{n/2}$

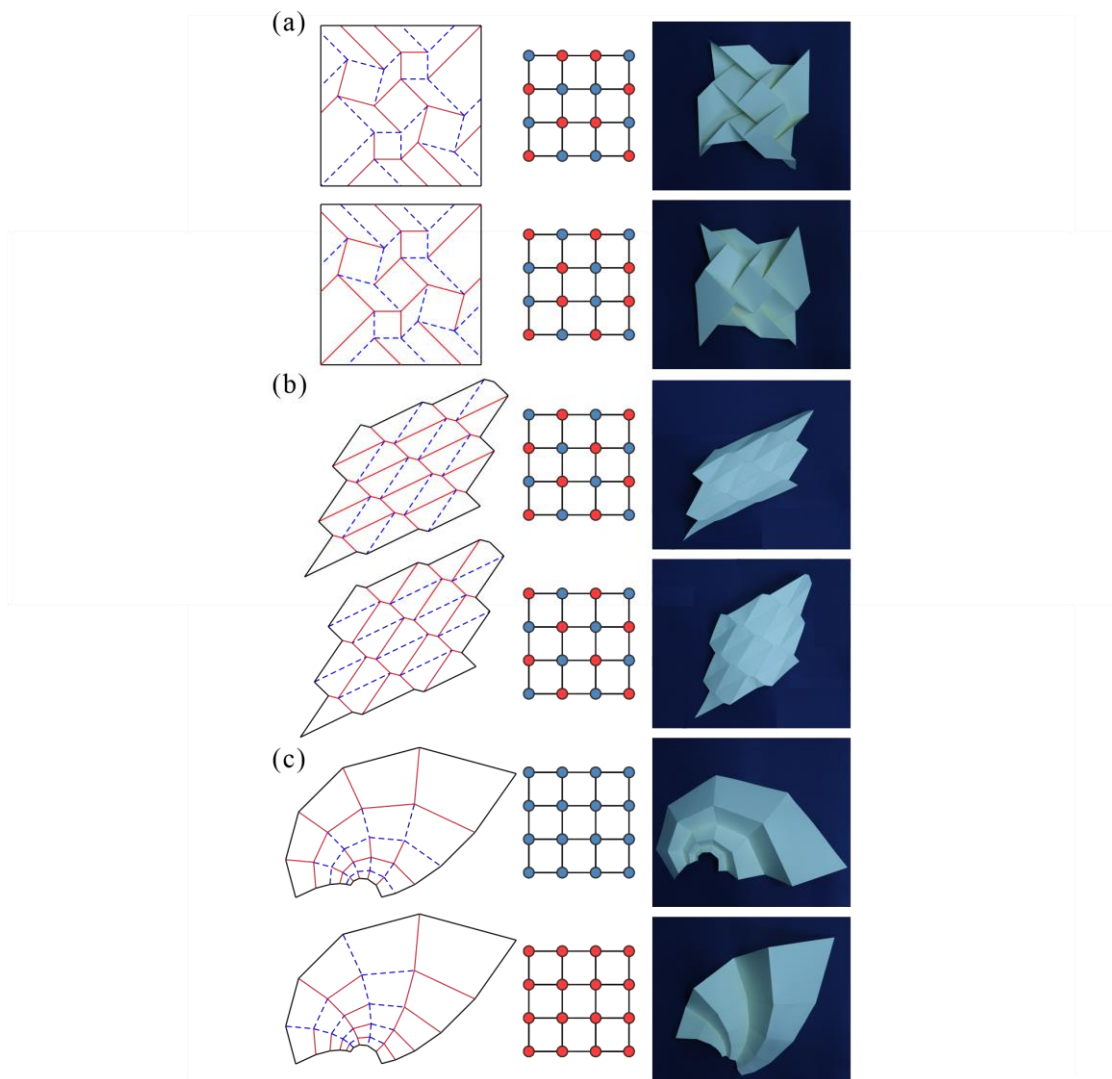


Fig. 2-8 Three types of oligo-modal origami with a constant number of MV assignments independent of tessellation sizes. (a) Dual square twist pattern, (b) Huffman pattern, and (c) Helical patterns.

2.3.2 3D Cellular Origami Structure

In this section, the proposed method is extended to 3D cellular origami structures. The tunability of mechanical properties induced by mountain-valley crease reconfiguration is explored by both theoretical models and experimental results. Fig. 2-9(a) shows different views of a 3D cellular origami structure composed of $m \times n \times p$ Miura-ori tubular origami units^[174,175]. Unlike conventional stacking methods, this cellular structure adopts a shifted stacking strategy between layers of tubular origami units, resulting in a consistent one-unit disparity between the number of tubular units in layers $p-1$ and layer p . Upon examining the top view of the cellular origami, a standard 2D Miura-ori tessellation becomes apparent, implying the independence of the number of valid MV assignments on parameter m . The front view, depicting $3 \times 3 \times 3$ tessellation, can be abstracted as a chessboard, as illustrated in Fig. 2-9(a). To facilitate the algorithm's solution, basic and connected modules in the yoz plane are identified. As shown in Fig. 2-9(b), the basic module is constructed using two identical Miura-ori sheets and two rectangular connecting sheets, resulting in two identical symmetric Eggbox vertices parameterized by $\sum \alpha_{i(i+1)} < 2\pi$ on the left and two identical symmetric Eggbox vertices parameterized by $\sum \alpha_{i(i+1)} > 2\pi$ on the right, forming a Miura-ori tubular origami represented by a rectangular lattice with six nodes. Since this tubular origami corresponds to an assembly of six spherical 4R linkages, six graphic representations (MV assignments) emerge. Additionally, two neighbouring Miura-ori tubular origami in the z -direction, along with the subsequent layer, share four rhombic sheets, abstracted as a trapezoidal lattice with four graphic representations (MV assignments) termed connection module i (Fig. 2-9(c)). Another consideration involves neighbouring Miura-ori tubular origami in the y -direction, sharing rectangular connecting sheets and forming connection module ii. This module is represented as a square lattice with four nodes corresponding to four symmetric Eggbox vertices, encompassing sixteen MV assignments and graphic representations (Fig. 2-9(d)). The proposed algorithms yield insights into the number of valid and unique configurations with different tessellation sizes, revealing an exponential increase in valid and unique configurations as the tessellation size expands (Fig. 2-9(e)). Since there is no symmetry when the number of rows p are even numbers, the number of unique configurations is the same as the number of valid configurations. Whereas when the number of rows p are odd, the number of unique configurations is approximately half the number of valid

configurations due to horizontal symmetry. It is noted that the increase of the size number from two to three contributes directly to the surge of the overall variety of the tessellations (The runtime of the algorithm is provided in Appendix B).

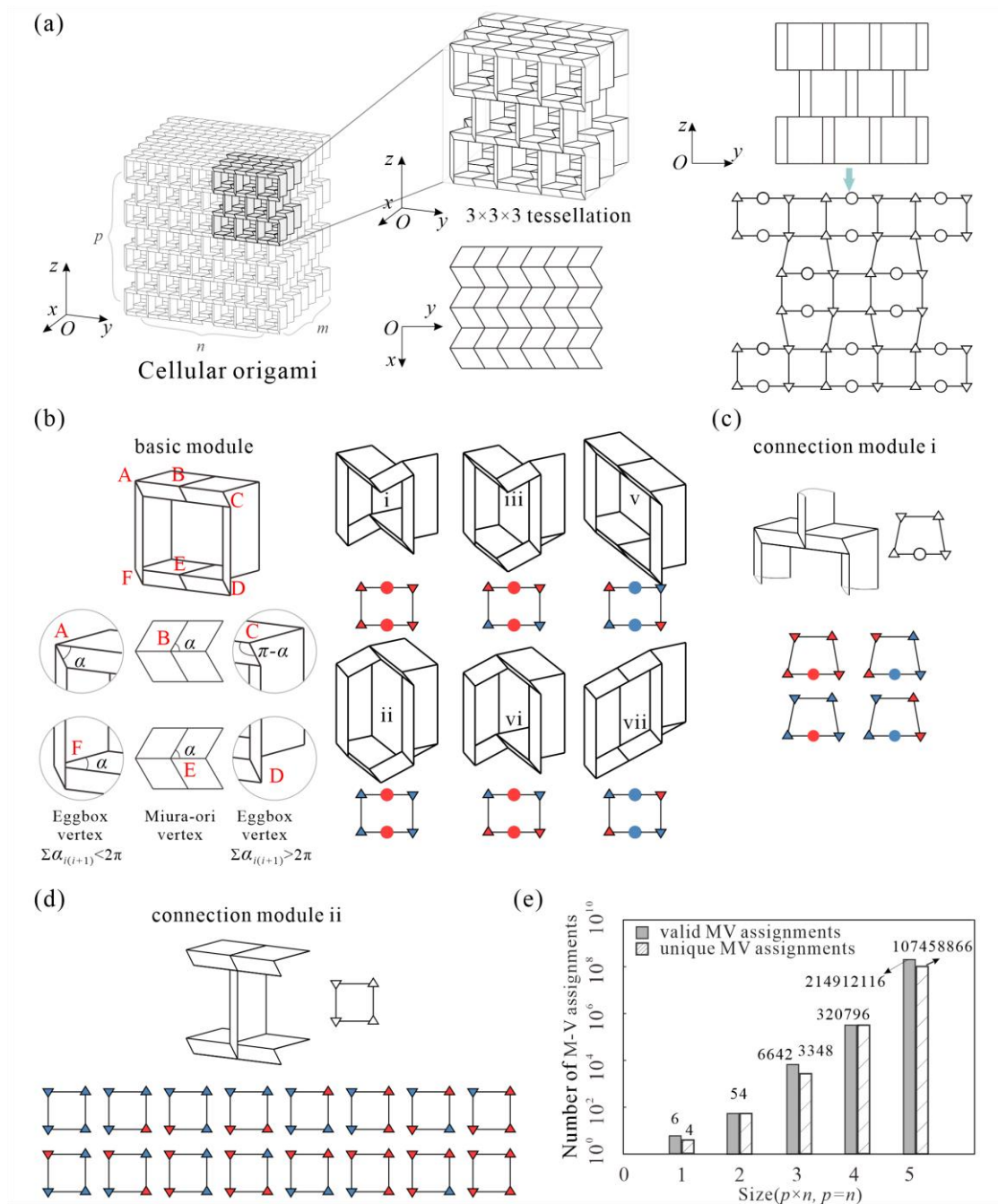


Fig. 2-9 Reconfigurability of 3D cellular origami structure. (a) Views of cellular origami structure and chessboard of $3 \times 3 \times 3$ tessellation in the front view. (b-d) Graphic representations of the basic module, connection modules i and ii. (e) The result of the search for the number of valid and unique configurations with different tessellation sizes.

For a simple $3 \times 3 \times 3$ tessellation, it is surprising that more than 6×10^3 valid configurations exist. These configurations are switched through a common bifurcation point, where the Miura vertices are flat unfolded, as shown in Fig. 2-10(a) left. In the discussion of these specific examples discovered during the exploration process, three typical graphic representations are presented in Fig. 2-10(a) right. Notably, all Miura-ori vertices in these cases adhere to the MV-II assignment. In graphic representation I, the symmetric Eggbox vertices conform to the MV-II assignment, resulting in a concave shape for the tubular origami module. Moving to graphic representation II, a unique configuration emerges wherein the symmetric Eggbox vertices in the top and bottom layers exhibit both MV-I and MV-II assignments, while those in the middle layer adhere solely to the MV-II assignment. Consequently, the entire $3 \times 3 \times 3$ cellular origami structure manifests convexity at the top and bottom ends and concavity at the middle layer. Finally, in graphic representation III, the symmetric Eggbox vertices adhere to the MV-I assignment, yielding all tubular origami modules with a convex contour. Meanwhile, the folding process of the three typical configurations is shown in Fig. 2-10(b). Apparently, the geometric dimensions of the structure, namely the width (W), breadth (B), and height (H) in the x , y , and z directions, undergo significant changes during the folding process. For a $m \times n \times p$ cellular origami structure, its dimensions are

$$\begin{aligned} W &= 2m \sin(\arccos(\cos \alpha / \cos \varphi)) \\ B &= 2nb \cos \varphi + a \cos \alpha / \cos \varphi \\ H &= pc + n_{e,0} b \sin \varphi + n_{m,0} b \sin \varphi - n_{m,1} b \sin \varphi \end{aligned} \quad (2-12)$$

where a , b , and c are length parameters, φ is the angle describing the folding ratio, $n_{e,0}$ is the number of layers in the two end-sheets' convex, while $m_{e,0}$ and $m_{e,1}$ are the number of layers in the middle sheets' convex and concave configurations, respectively.

Particularly intriguing are the changes in dimensions within the yoz plane. The structure is observed to undergo contraction, remains unchanged, or stretches along the z direction in three cases while being contracted in the y direction monotonically, as shown in Fig. 10(b), indicating negative, zero and positive in-plane Poisson's ratio (NPR/ZPR/PPR). To verify these findings, a theoretical model of Poisson's ratio is established by means of the kinematic model. The in-plane Poisson's ratio ν_{BH} of the structure is defined as^[133,176]

$$\nu_{BH} = - \frac{dH}{dB} \times \frac{B}{H} \quad (2-13)$$

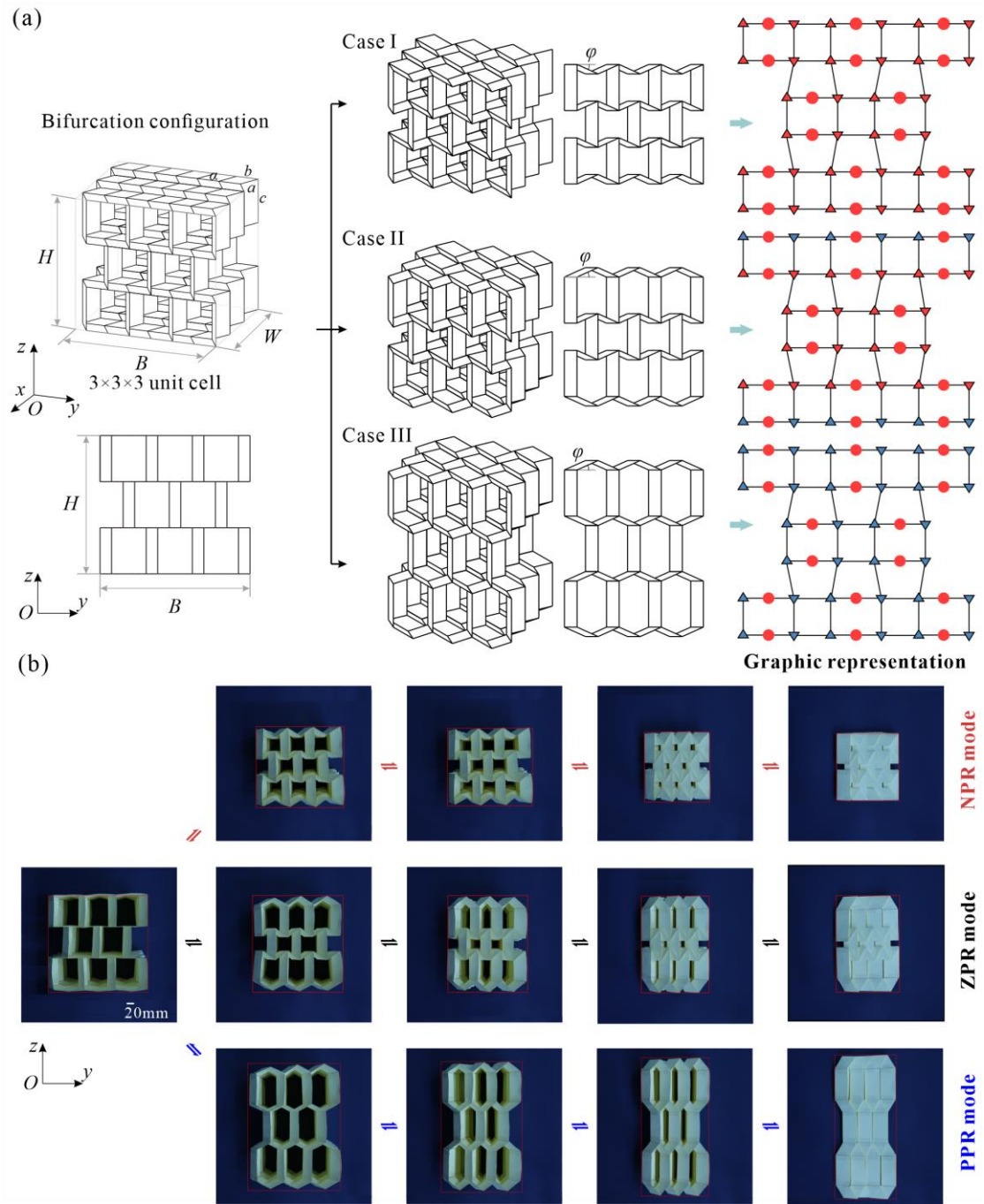


Fig. 2-10 The 3×3×3 tessellation. (a) The bifurcation configuration of the tessellation and its three typical configurations as well as graphic representations. (b) Folding process of the prototype.

Consequently, equation (2-13) can be written as

$$V_{BH} = -\frac{n_{e,0}b \cos \varphi + n_{m,0}b \cos \varphi - n_{m,1}b \cos \varphi}{-2nb \sin \varphi + a \cos \alpha \tan \varphi \sec \varphi} \times \frac{2nb \cos \varphi + a \cos \alpha / \cos \varphi}{pc + n_{e,0}b \sin \varphi + n_{m,0}b \sin \varphi - n_{m,1}b \sin \varphi} \quad (2-14)$$

The quantitative Poisson's ratio experiments on these three typical configurations of the $3 \times 3 \times 3$ tessellation have also been performed. The tested sample was compressed between two smooth flat platens (the one on top is transparent) along the x direction, as shown in Fig. 2-11(a). The compression tests are conducted using a vertical testing machine (Instron 5982) by applying an 80mm displacement and a 0.5 mm s^{-1} loading rate. Due to the prestressing of the hinges made of tape, the compression test of three cases starts from a partially folded configuration rather than a fully unfolded configuration. The motion of the markers used to define the contours in the yoz plane was captured by a CSI Vic-3D9M digital image correlation (DIC) system with a camera resolution of 2704×3384 pixels and a frame period of 500 ms. Thus, the Poisson's ratio associated with the generic frame i of the experimental movie, was computed through

$$\nu_{BH} = -\frac{H_{i+1} - H_i}{B_{i+1} - B_i} \times \frac{B_i}{H_i} \quad (2-15)$$

In Fig. 2-11(b), the experimental results (markers) are compared with the theoretical prediction (continuous lines) provided by Eq. (2-14), where the folding ratio is defined as $(W_{\max} - W)/W_{\max}$. The analysis shows that experiments and theory are in good agreement although the results differ slightly due to fabrication defects. Figure Fig. 2-11(b) shows that the Poisson's ratio ν_{BH} of case I remains negative and changes from -0.48 to -0.13, while the Poisson's ratio ν_{BH} of case II fluctuates around zero, and the Poisson's ratio ν_{BH} of case III remains positive and changes from 0.41 to 0.10. It is also noted that experimental results and the theoretical curve for both positive and negative Poisson's ratio at higher folding ratios with experimental values converging towards zero. This phenomenon is mainly due to the thickness of the material. Specifically, the analysis of the theoretical Poisson's ratio is based on a kinematic model, where the cardboard is ideally zero-thickness materials. In fact, each piece of cardboard in the prototype is only 0.2 mm thick. However, the $3 \times 3 \times 3$ tessellation consists of 12 layers stacked together in the W direction at higher folding ratios, even without considering the thickness of the tape (0.02mm). Consequently, the dimensional change of the prototype in the H direction will be small with compression nears its end. Overall, these results demonstrated that it is achievable to rationally design origami metamaterials with negative, zero and positive in-plane Poisson's ratio (NPR/ZPR/PPR) under large deformation by manipulating the MV assignments, which has not yet been reported previously in conventional origami sheets.

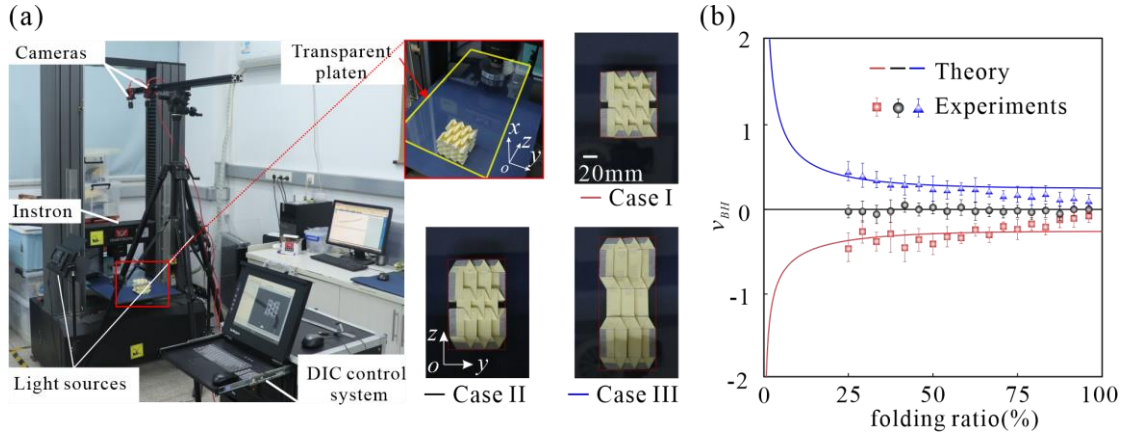


Fig. 2-11 Quantitative analysis of Poisson's ratio. (a) The experimental setups. The black speckles of the panels are used to evaluate the dimensions. (b) Comparison of experimental and theoretical results. Data are expressed as the mean and standard deviation of three tests.

2.4 Conclusions

In this chapter, the challenge of searching for MV assignments that satisfy rigid foldability in large 2D origami tessellations or 3D cellular structures is addressed by transforming it into a chessboard coloring problem and employing programming language for its solution. Specifically, origami tessellation is divided into combinations of modular units. Subsequently, the motion compatibility conditions for assemblies of spherical linkages are used to establish basic rules for the graphic representation of these modules. Eventually, the DFS algorithm is employed to systematically traverse the chessboard, seeking graphical solutions that adhere to the established rules and ultimately transforming them back into origami patterns with specific MV assignments. This method not only provides an analytical value and their precise assignments of MV creases but also eliminates a significant number of duplicate geometric configurations. The efficiency and accuracy of proposed method have been demonstrated through a series of 2D origami tessellations, and further extended to 3D cellular origami structures. In this process, three types of oligo-modal origami tessellations that exhibit a constant number (≥ 2) of rigid MV assignments independent of tessellation size, and a pluri-modal cellular origami whose number exponentially increases with tessellation size, have been identified. Additionally, the analysis of the theoretical and experimental results of mechanical properties reveals that negative, zero, and positive in-plane Poisson's ratio can be achieved under large deformation by manipulating the MV assignments within a single origami structure.

Chapter 3 Integration of Origami, Kirigami and Ori-Kirigami in Thick Panels by Transferable Joints

3.1 Introduction

The challenge of evaluating the reconfigurability of four-crease origami vertices and their tessellations for zero-thickness structures was addressed in chapter 2. However, modern origami extends beyond zero-thickness sheets, with the thickness of rigid materials gaining significance, particularly in engineering applications requiring heightened strength or rigidity. It is found that most studies of origami-based reconfigurable structures focused on zero-thickness origami, except for a few known examples of thick-panel origami. Despite the development of various approaches to accommodate thickness in origami-based designs, the physical interferences arising from thick-panel transformations present challenges in reconfigurable structures. This arises from the necessity to accommodate panel thickness in various folded or unfolded configurations.

On the other hand, joint axes in conventional thick-panel origami are typically located at the top and bottom edges of the panel, while thick-panel kirigami aligns them in the thickness direction. However, ori-kirigami introduces unique design principles, where joint axes can be at the panel's edge or within its thickness simultaneously. Generally, a revolute joint, commonly used to connect two links, provides one DOF relative motion. Once installed, the direction of the joint axis and corresponding linkage parameters are determined. The variations in joint axis orientation prevent connectivity between thick-panel origami, kirigami, and ori-kirigami. This chapter seeks to integrate them using Jacob's Ladder toy-inspired vertically transferable joints (VTJ).

The outline of this chapter is as follows. In section 3.2, the design of the thick-panel ori-kirigami unit is presented, integrating origami, kirigami, and ori-kirigami motion branches by embedding VTJ into flat-foldable six-crease vertices, and the effects of design parameters on the kinematic behaviours are revealed. In section 3.3, the focus is on the tessellation of the reconfigurable units and their accompanied tuneable mechanical properties, including Poisson's ratio, deployable ratio, and load-bearing capacity. The concluding remarks are presented in section 3.4.

3.2 Single Reconfigurable Unit with Vertically Transferable Joints

3.2.1 Vertically Transferable Joints

Extending parallel transferrable joint inspired by the Jacob's Ladder toy^[177], the VTJ technique is introduced, as shown in Fig. 3-1(a) and (b). Each panel is intricately linked to three non-stretchable tapes, A, B, and C. Notably, tapes A and C are attached to the side surface of panel p_1 and extend down in the thickness direction to the bottom surface of panel p_2 . In contrast, tape B is attached to the side surface of panel p_2 and extends down in the thickness direction to the bottom surface of panel p_1 . Such an arrangement of interlaced non-stretchable tapes allows each panel to act as an R joint (one DOF) at either of its two edges. Consequently, when the joint axis relocates from the edge of the bottom surface to that of the side surface at an unfolded configuration (which is also the bifurcated configuration), the mountain crease transitions into an R joint whose axis is in the thickness direction, graphically depicted by the red dashed line plus a grey circle and arrow in Fig. 3-1(a). Meanwhile, by connecting the top and side surfaces of two panels with three interlaced tapes, as shown in Fig. 3-1(b), the axis of the joint can be transferred from the edge of the top panel surface (valley mountain crease) to the thickness direction, graphically indicated by the blue dashed line plus a grey circle and arrow. Despite each VTJ comprising two joints, only one joint operates after passing through the unfolded configuration.

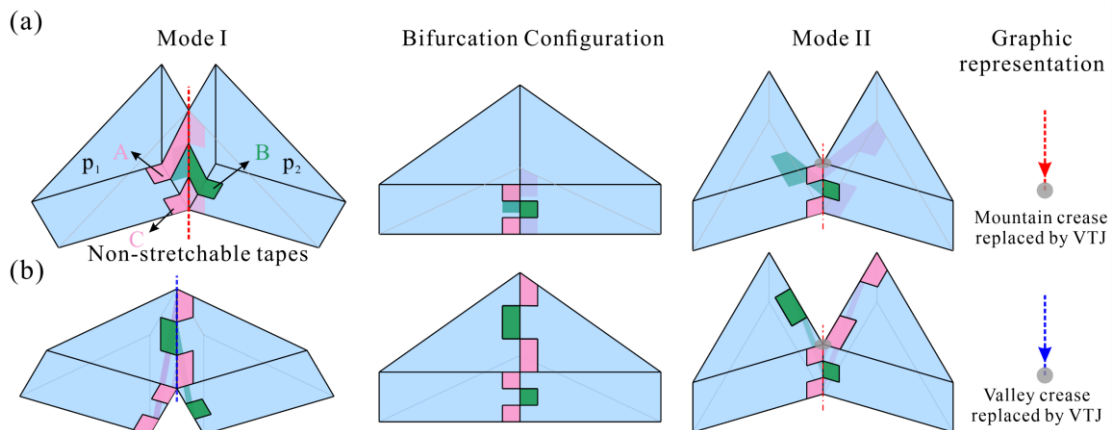


Fig. 3-1 Vertically transferrable joint technique. (a) Mountain crease replaced by VTJ and (b) valley crease replaced by VTJ. Arrows and grey circles accompany these representations, where arrowheads indicate the direction of joint transfer, and circles signify the joint axes located in the direction of thickness.

The proposed VTJ can be selectively activated to be located on the upper and lower surfaces of the panel or in the thickness direction by controlling the adsorption of the strip to the panel. Taking the case in Fig. 3-1(a) as an example, when the tapes B (A and C) are adsorbed on the panel p_2 (p_1), the two panels can only be folded in the way of R joint at mountain creases. And when strip B (A and C) is adsorbed on panel p_1 (p_2), the two panels can only be opened in the way of the joint whose axes located in the direction of thickness.

3.2.2 Characterization of a Single Unit

At the nucleus of integration design is the single diamond vertex, as illustrated in Fig. 3-2(a) left, which is characterized by four diagonal mountain creases (represented by red solid lines) and two co-linear valley creases (represented by blue dashed lines), converging at a point. The square base height is denoted by $2l$, and the design angle is represented by α . Transforming these facets into panels of uniform thickness t yields an assembly where adjacent panels are connected by six revolute joints c_i ($i=1, 2, \dots, 6$). The axis of these joints aligns either along the panels' bottom or top edges for mountain or valley creases, respectively. Fig. 3-2(a) right presents the reconstruction of this origami vertex. Then replacing four joints (c_1, c_2, c_4 and c_6) of the original pattern with VTJs obtains the modified unit as shown in Fig. 3-2(a) right. The replacement of mountain or valley creases by VTJs is visually highlighted by red and blue dotted lines plus arrows and grey circles, respectively. Arrows and grey circles accompany these representations, where arrowheads indicate the direction of joint transfer, and circles signify the joint axes located in the direction of thickness. Consequently, the modified unit undergoes a metamorphosis, now comprising six triangular panels intricately interlinked by ten joints, and its thick-panel form is presented in Fig. 3-2(b).

Obviously, co-linear creases in the modified unit could enable the entire unit to work as open-chain mechanisms with mobility, where an R joint is connected by two links, but more interesting are these single-loop linkage cases. In fact, VJTs serve to lock and unlock joints, allowing for the adjustment of joint axis orientation on the top and bottom surfaces of panels or in the thickness direction without increasing DOF, thereby reconfiguring the type of linkages to form a transformable vertex with multiple motion branches. Thus, there are $2^4 = 16$ potential combinations of activated joints.

Only 10 are unique considering plane symmetry, and only five of these have mobility for single-loop linkage cases (Appendix C).

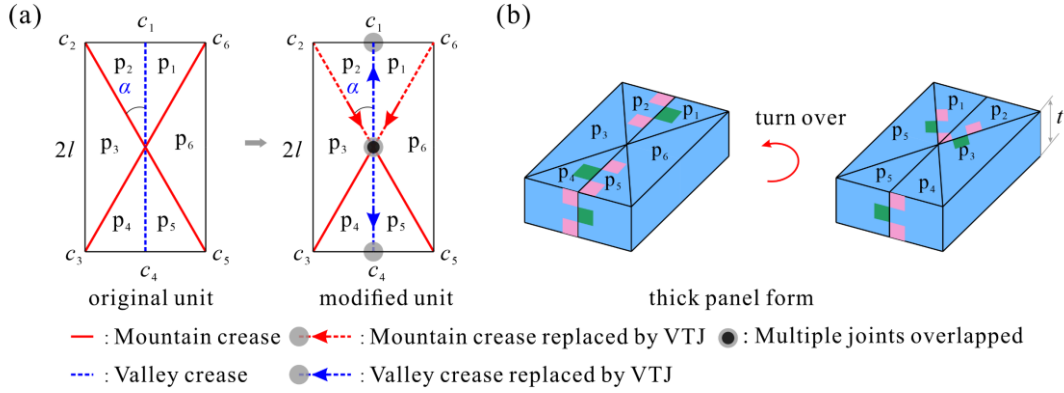


Fig. 3-2 Diamond pattern-based integration design. (a) Modified unit with vertical transferable joints evolved from six-crease vertex; (b) thick-panel form of the modified unit.

3.2.3 Motion Branches of a Single Unit

3.2.3.1 Thick-Panel Origami Motion Branch

Starting from the basic mode, the diamond origami branch (depicted in Fig. 3-3), unlocks all four transferable joints c_1 , c_2 , c_4 and c_6 , positioning their axes on the top or bottom surfaces of the panels. This setup transforms the single unit into a two-fold plane-symmetric Bricard 6R linkage, following the geometric condition

$$\begin{aligned} a_{12} = a_{34} = a_{45} = a_{61} = t, \quad a_{23} = a_{56} = 0 \\ \alpha_{12} = 2\pi - \alpha_{61} = 2\pi - \alpha, \quad \alpha_{23} = 2\pi - \alpha_{56} = \pi - 2\alpha, \quad \alpha_{34} = 2\pi - \alpha_{45} = \alpha \quad (3-1) \\ R_1 = R_2 = R_3 = R_4 = R_5 = R_6 = 0 \end{aligned}$$

where $0 < \alpha \leq \pi/4$, to ensure flat foldability.

Further, the kinematic relationships underlying this linkage are deduced through the following expressions^[47]

$$\varphi_1 = \varphi_4, \quad \varphi_2 = \varphi_3 = \varphi_5 = \varphi_6, \quad \tan \frac{\varphi_1}{2} = \frac{1}{\cos \alpha} \tan \frac{\varphi_2}{2} \quad (3-2)$$

where φ_i denotes dihedral angles.

Equation (3-2) shows that the relationship between dihedral angles is independent of the thickness t and edge length l . Meanwhile, the kinematic curves between φ_2 and φ_1 are plotted in Fig. 3-4(a), where points i-ii-iii-iv-v in black and red correspond to configurations in Fig. 3-4(b) and (c) of the vertex with $\alpha = 30^\circ$ and $\alpha = 45^\circ$, respectively. Regardless of the variation of design angles α , there always exist two fixed

points $(0, 0)$ and (π, π) , implying that the unit is flat-foldable and flat-deployable. While general design angles $(0 < \alpha < \pi/4)$ may yield voids and tabs in the fully folded configuration, as shown in Fig. 3-4(b), the special case of $\alpha = 45^\circ$ enables ideal folding from a flat square panel into a compact stack (Fig. 3-4(c)).

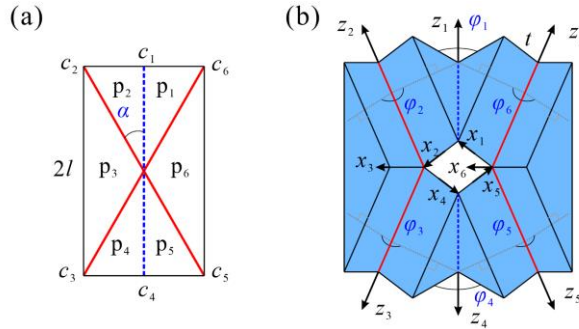


Fig. 3-3 Thick-panel origami branch of a modified unit in diamond vertex mode. (a) Crease pattern of the unit; (b) thick-panel form of the unit.

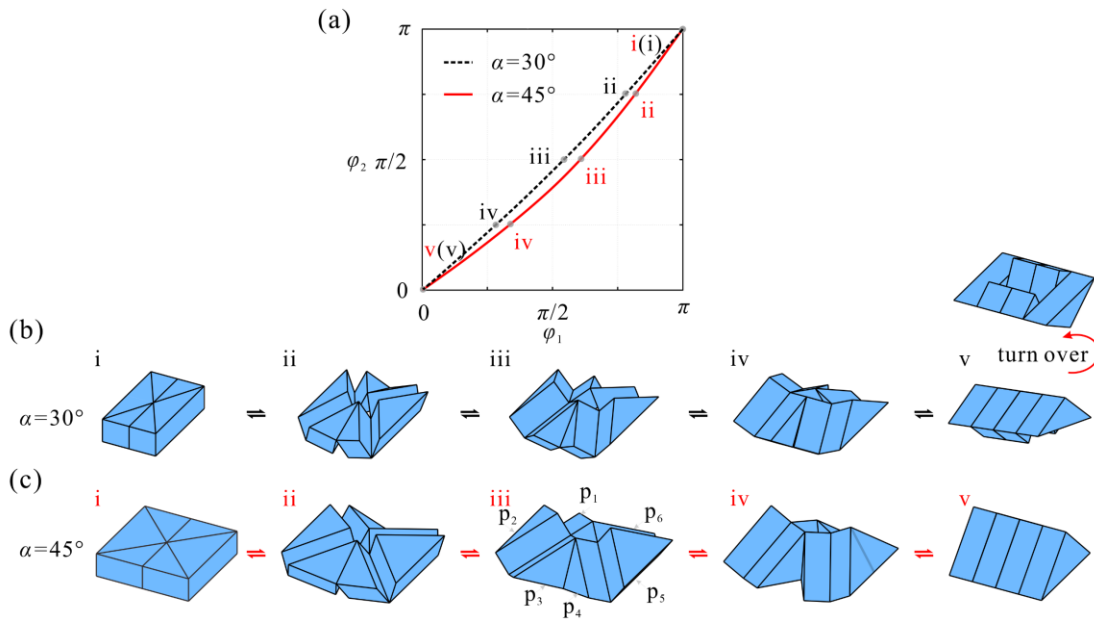


Fig. 3-4 Relationship between dihedral angles φ_2 and φ_1 and corresponding configurations in thick-panel origami branch. (a) The kinematic paths of a single unit. The path for the case of $\alpha = 30^\circ$ line a is in black, and the one for the case of $\alpha = 45^\circ$ is in red. (b) Motion sequence of the unit with $\alpha = 30^\circ$; (c) motion sequence of the unit with $\alpha = 45^\circ$.

3.2.3.2 Thick-Panel Kirigami Motion Branch

A kirigami branch arises when activating four joints (c_1 , c_2 , c_4 and c_6 in Fig. 3-5(a)) located in the thickness direction among transferable joints. This particular geometric configuration results in the automatic dormancy of joints c_3 and c_5 within a single modified unit, as visually indicated by the grey lines in Fig. 3-5(a). Consequently, panels p_3 and p_4 , as well as p_5 and p_6 operate as a unified entity, respectively. Therefore, the thick-panel form depicted in Fig. 3-5(b), featuring a single loop unit composed of four panels, can be deemed kinematically equivalent to a planar 4R linkage.

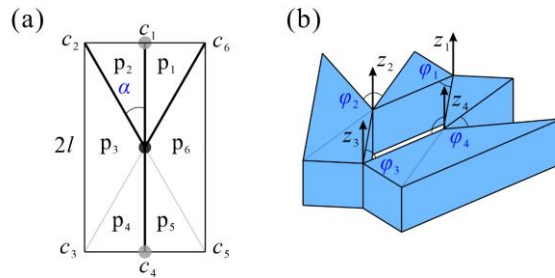


Fig. 3-5 Thick-panel kirigami branch of the modified unit. (a) Crease pattern of the unit; (b) thick-panel form of the unit.

The geometric condition governing this linkage is listed as follows:

$$a_{12} = a_{23} = a_{34} = a_{41} = l \quad (3-3)$$

whose relationship between the dihedral angles is

$$\varphi_1 = \varphi_2 = \varphi_3 = \varphi_4 \quad (3-4)$$

The relationships between φ_2 and φ_1 for varying α , coupled with their configurations, are illustrated in Fig. 3-6(a-c). Intriguingly, these relationships remain independent of the design parameters α . As angle φ_1 increases, it can be seen that the rectangular unit first opens in-plane and then closes to form an isosceles triangle.

3.2.3.3 Thick-Panel Ori-kirigami Motion Branches

Attention is then turned to ori-kirigami scenarios where certain joint axes are located at the top and bottom edges of the panel, while others are aligned with the

thickness direction. As a result, a total of three different ori-kirigami branches were found to exist in a single unit.

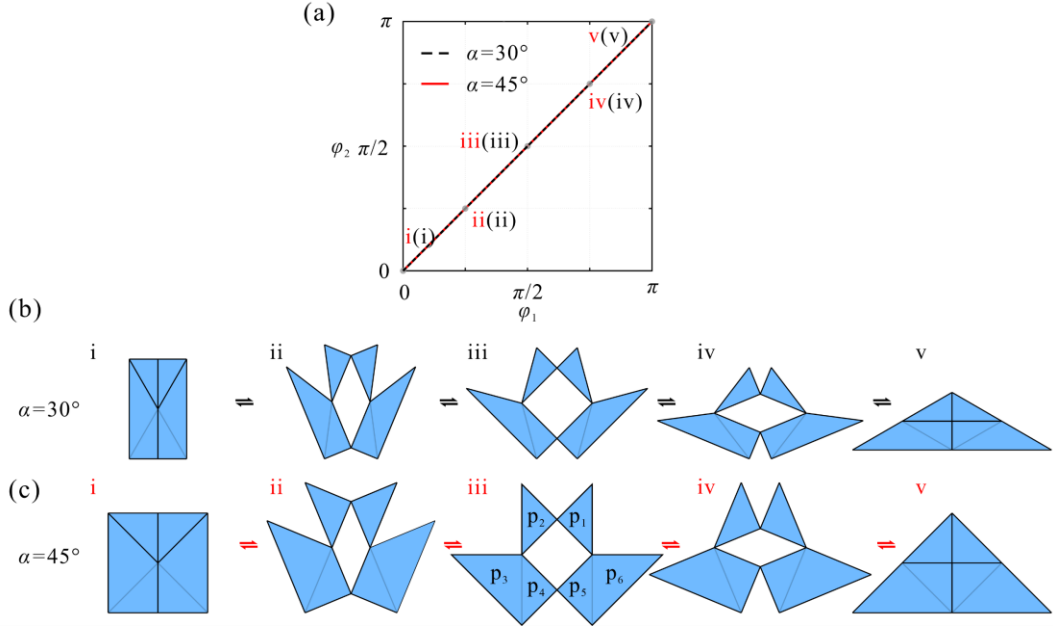


Fig. 3-6 Relationship between dihedral angles φ_2 and φ_1 , and corresponding configurations in thick-panel origami branch.

Firstly, as illustrated in Fig. 3-7(a), the two transferable joints c_2 and c_6 in the modified unit with axes located in the bottom of the panel surfaces and the other two transferable joints c_1 and c_4 with axes located in the thickness direction are activated. Consequently, the corresponding thick-panel ori-kirigami branch I, as shown in Fig. 3-7(b), exhibits a two-fold plane-symmetric property. This particular configuration corresponds to a two-fold plane-symmetric Bricard 6R linkage, characterised by the following geometric condition

$$\begin{aligned}
 a_{12} &= a_{34} = a_{45} = a_{61} = l \sin \alpha, \quad a_{23} = a_{56} = 0 \\
 \alpha_{12} &= 2\pi - \alpha_{61} = \pi / 2, \quad \alpha_{23} = 2\pi - \alpha_{56} = \pi - 2\alpha, \quad \alpha_{34} = 2\pi - \alpha_{45} = 3\pi / 2 \quad (3-5) \\
 R_1 &= R_4 = 0, \quad R_2 = -R_3 = R_5 = -R_6 = -l \cos \alpha
 \end{aligned}$$

and the relationship between angles can be conducted with matrix method, i.e.,

$$\begin{aligned}
 \varphi_1 &= \varphi_4, \quad \varphi_2 = \varphi_3 = \varphi_5 = \varphi_6 \\
 2 \cos \alpha \cos(\alpha + \varphi_1 / 2)^2 - \cos \varphi_2 \sin \alpha \sin(2\alpha + \varphi_1) &= 0 \quad (3-6)
 \end{aligned}$$

The depiction of the kinematic curve describing the relationship between φ_2 and φ_1 , coupled with the folding process for a single loop unit with design angles set at

$\alpha = 30^\circ$ and $\alpha = 45^\circ$ are shown in Fig. 3-8(a-c). For general situations, i.e., $0 < \alpha < \pi/4$, the opening of panels p_1 and p_2 , p_4 and p_5 within two faces facilitate the transformation of the unit from an initial rectangle configuration into a stack. The illustrated example in Fig. 3-8(b) with $\alpha = 30^\circ$ (i-ii-iii-iv-v, black line) encapsulates this folding dynamic, wherein, in the fully folded configuration v, φ_1 is non-zero, indicating the presence of voids and tabs. However, in the special case of $\alpha = 45^\circ$, the limit configuration v reaches point $(0, 0)$. As a result, a single unit can be folded from the flat state of the rectangle to a compact prism state (i-ii-iii-iv-v, red line), with an area reduced to half of its original size and a height doubled, whose motion sequence is illustrated in Fig. 3-8(c).

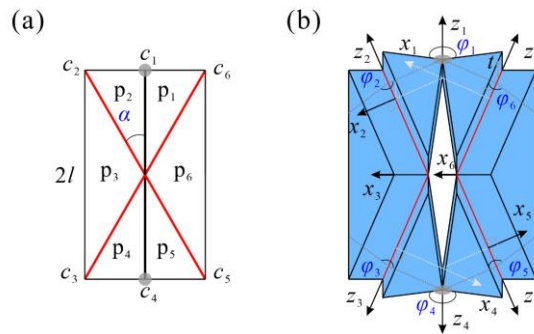


Fig. 3-7 Thick-panel ori-kirigami branch I of the modified unit with two-fold plane-symmetry.

(a) Crease pattern of the unit; (b) thick-panel form of the unit.

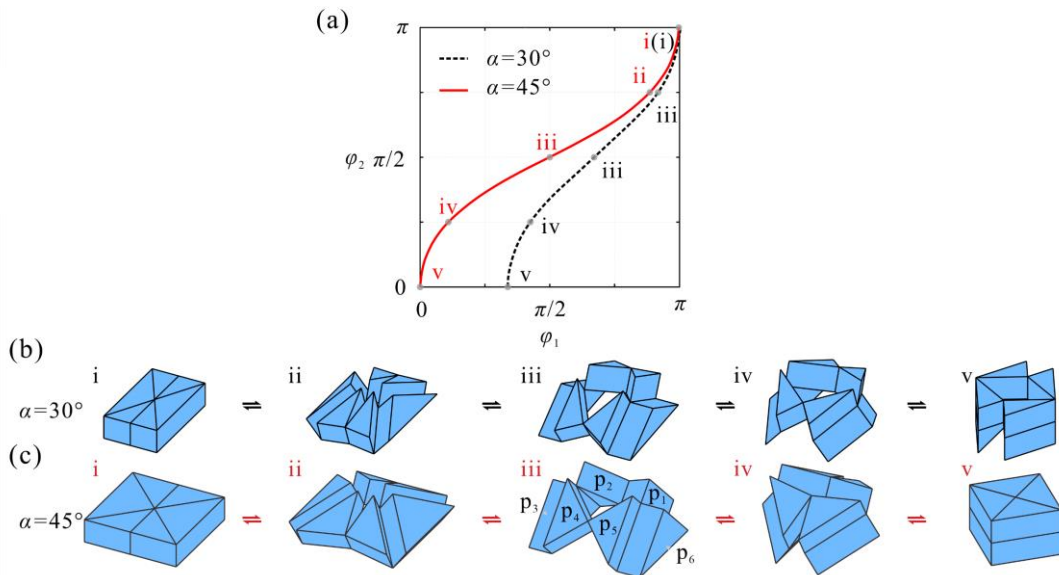


Fig. 3-8 Relationship between dihedral angles φ_2 and φ_1 and corresponding configurations in thick-panel ori-kirigami branch I with two-fold plane-symmetry.

Secondly, in addition to the two-fold plane-symmetric case in Fig. 3-7 and Fig. 3-8, strategically activating the VTJs may also trigger other ori-kirigami branches with solo symmetric plane. As shown in Fig. 3-9(a), the axes of the activated VTJs c_4 is located at the top of the panel surfaces, while the axes of the other three activated VTJs c_1 , c_2 , and c_6 are located in the thickness direction. In this case, the thick-panel ori-kirigami branch II works as Bennett 6R linkage with geometric condition

$$\begin{aligned} a_{12} = a_{61} = l, \quad a_{23} = a_{56} = 0, \quad a_{34} = a_{45} = t \\ \alpha_{12} = \alpha_{61} = 0, \quad \alpha_{23} = 2\pi - \alpha_{56} = \pi/2, \quad \alpha_{34} = 2\pi - \alpha_{45} = \alpha \\ R_1 = R_2 = R_3 = R_4 = R_5 = R_6 = 0 \end{aligned} \quad (3-7)$$

Then, the relationship between dihedral angles can be obtained with the matrix method,

$$\begin{aligned} \varphi_2 = \varphi_6, \quad \varphi_3 = \varphi_5, \quad l \sin(\varphi_1/2) = t \sin(\varphi_4/2) \\ \arcsin(\sin \alpha \sin(\varphi_4/2)) + \varphi_2 = \varphi_1/2 + \alpha \\ \sin \varphi_3 = \cos(\varphi_4/2) / \arcsin(\sin \alpha \sin(\varphi_4/2)) \end{aligned} \quad (3-8)$$

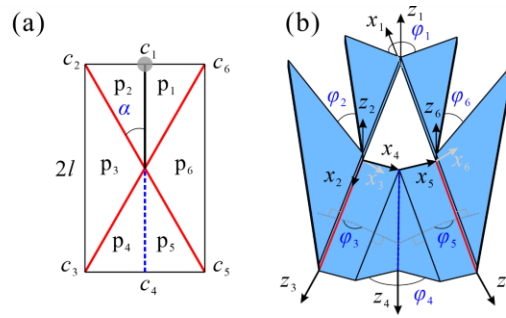


Fig. 3-9 Thick-panel ori-kirigami branch II of the modified unit with solo symmetry plane. (a) Crease pattern of the unit; (b) thick-panel form of the unit.

The kinematic paths φ_4 vs φ_3 and the corresponding motion sequences of the ori-kirigami branch II with $\alpha = 30^\circ$ and 45° are shown in Fig. 3-10(a-c). Both paths have the same starting point $(\pi/2, 0)$ and ending point (π, π) , which indicates that one side of the unit can always be folded compactly while the other side can only be partially opened within the plane, as demonstrated by motion sequence in Fig. 3-10(b) and (c).

Thirdly, the exploration extends to ori-kirigami branch III, as shown in Fig. 3-11(a), where VTJs c_2 and c_6 are located at the bottom of the panel surfaces, while one of VTJs c_1 and c_4 is located at the top of the panel surface and the other in the thickness

direction. As a result, the thick-panel ori-kirigami branch III in Fig. 3-11(b) conforms to a plane-symmetric Bricard 6R linkage with geometric condition

$$\begin{aligned}
 a_{12} = a_{61} = l \sin \alpha, \quad a_{23} = a_{56} = 0, \quad a_{34} = a_{45} = t \\
 \alpha_{12} = 2\pi - \alpha_{61} = \pi/2, \quad \alpha_{23} = 2\pi - \alpha_{56} = \pi - 2\alpha, \quad \alpha_{34} = 2\pi - \alpha_{45} = \alpha \\
 R_1 = R_3 = R_4 = R_5 = 0, \quad R_2 = -R_6 = -l \cos \alpha
 \end{aligned} \quad (3-9)$$

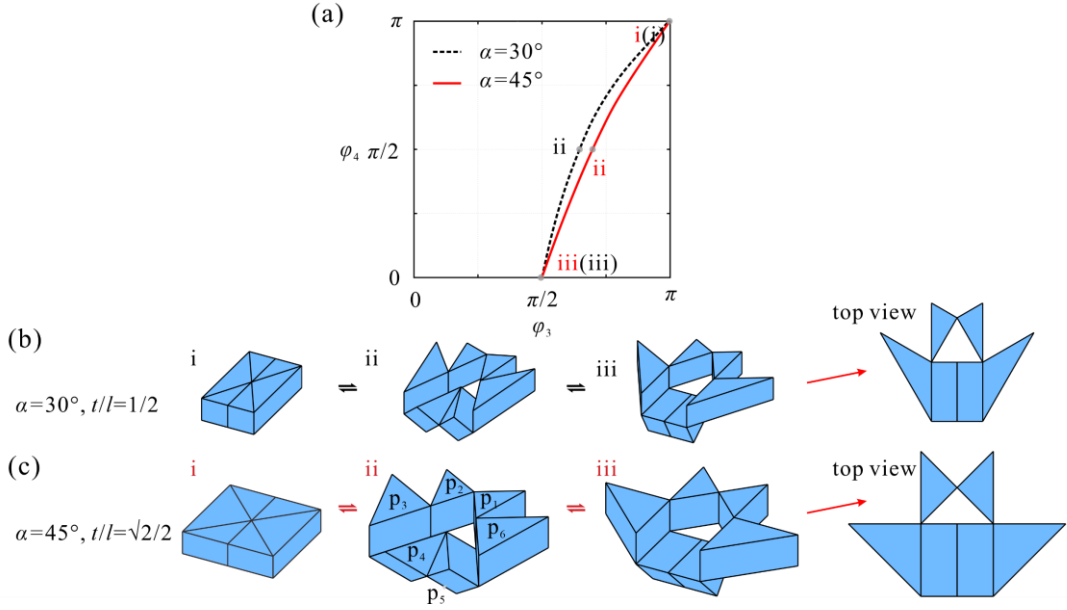


Fig. 3-10 Relationship between dihedral angles φ_2 and φ_1 and corresponding configurations in thick-panel ori-kirigami branch II.

Using explicit closure equations of the general plane-symmetric Bricard 6R linkage derived by Feng^[73], the relationship between dihedral angles can be conducted, i.e.,

$$\begin{aligned}
 \varphi_2 = \varphi_6, \quad \varphi_3 = \varphi_5 \\
 \frac{\sin \alpha (\cos \varphi_2 \sin \varphi_3 + \cos 2\alpha \cos \varphi_2 \cos \varphi_3) + \sin 2\alpha \cos \alpha \cos \varphi_2}{\sin 2\alpha \sin \alpha \cos \varphi_3 - \cos 2\alpha \cos \alpha} = \\
 \frac{t(-\cos \varphi_2 \cos \varphi_3 + \cos 2\alpha \cos \varphi_2 \sin \varphi_3) + l \sin \alpha}{t(\sin 2\alpha \sin \varphi_3) + l \cos \alpha} \quad (3-10) \\
 \tan \frac{\varphi_1 - \pi + 2\alpha}{2} = \frac{\sin \alpha (\cos \varphi_2 \sin \varphi_3 + \cos 2\alpha \cos \varphi_2 \cos \varphi_3) + \sin 2\alpha \cos \alpha \cos \varphi_2}{\sin 2\alpha \sin \alpha \cos \varphi_3 - \cos 2\alpha \cos \alpha} \\
 \tan \frac{\varphi_4}{2} = -\frac{\cos \varphi_2 (\cos \varphi_3 + \sin \varphi_3 \cos 2\alpha)}{\cos \alpha (\cos \varphi_2 \sin \varphi_3 - \cos 2\alpha \cos \varphi_2 \cos \varphi_3) + \sin \alpha \sin 2\alpha \cos \varphi_2}
 \end{aligned}$$

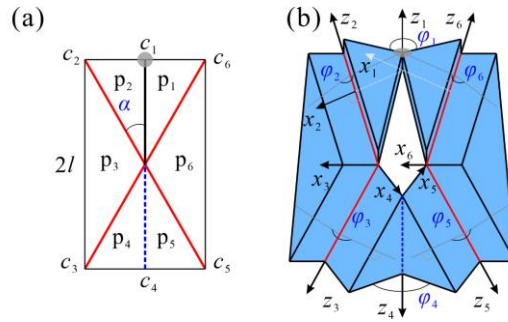


Fig. 3-11 Thick-panel ori-kirigami branch III of the modified unit with solo symmetry plane. (a) Crease pattern of the unit; (b) thick-panel form of the unit.

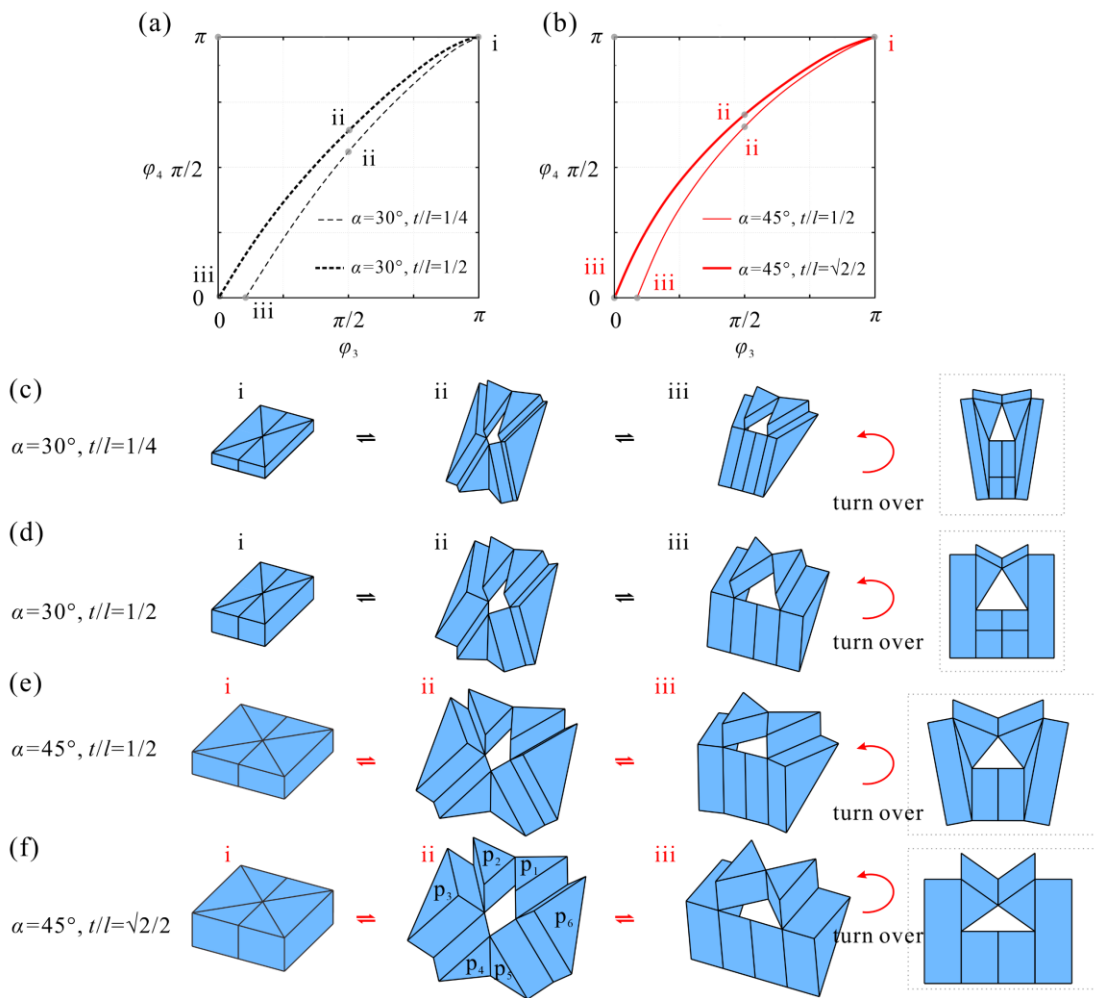


Fig. 3-12 Relationship between dihedral angles φ_4 and φ_3 and corresponding configurations in thick-panel ori-kirigami branch III. (a) The kinematic paths with $\alpha = 30^\circ$ when $t/l = 1/4$ and $t/l = \sqrt{2}/2$; (b) the kinematic paths with $\alpha = 45^\circ$ when $t/l = 1/4$ and $t/l = \sqrt{2}/2$, respectively; (c-f) motion sequence of the unit with different design parameters.

Equation (3-10) shows that the relationship between dihedral angles is dependent on the angle α , the thickness t , and the edge length l , simultaneously. To investigate the effect of design parameters on the motion of structure, $\alpha = 30^\circ, t/l = 1/4$ (black line) and $\alpha = 45^\circ, t/l = 1/4$ (red line) are chosen at first. As shown in Fig. 3-12(a), when the dihedral angle $\varphi_4 = 0$, φ_3 goes to 18.19° and 15.50° under the above two design parameters. The fact that $\varphi_3 \neq 0$ means that the unit does not have a flat and compact folded configuration, which can be visually demonstrated by the V-shaped limit configuration iii of the motion sequence in Fig. 3-12(c) and (e). However, when $t/l = \sin\alpha$, taking $\alpha = 30^\circ, t/l = 1/4$ (black line) and $\alpha = 45^\circ, t/l = 1/4$ (red line) in Fig. 3-12(b) as examples, φ_3 becomes 0, which means the structures are folded towards flattened configurations even with void (limit configuration iii in Fig. 3-12(d) and (f)).

In summary, investigation so far has demonstrated the remarkable reconfigurability of a single unit with VTJs. Specifically, by strategically activating the axis orientation of the transferable joints, a single unit can exhibit five single DOF motion branches, namely origami, kirigami, and ori-kirigami I-III, as shown in Fig. 3-13. The effect of the design parameters on the folding behaviour of the unit is analysed using the closure equations of the underlying linkage. Remarkably, the unit exhibits excellent properties when the angle $\alpha = 45^\circ$ and $t/l = \sin\alpha$. Therefore, subsequent analysis of tessellation will focus on the case of $\alpha = 45^\circ$ and $t/l = \sqrt{2}/2$.

3.3 Tessellation of Reconfigurable Units with Tuneable Properties

3.3.1 Tessellation Method and Motion Branches

The formation and connectivity of tessellations utilizing modified units are illustrated in Fig. 3-14. Initially, the modified unit with $\alpha = 45^\circ$ undergoes a reflection symmetry operation along the horizontal direction. Then, the unit and its mirrored counterpart are interconnected by two joints connecting panels p_4 and p_4' , as well as p_5 and p_5' , whose axes are located along the thickness. Subsequently, resulting assemblies undergo mirroring along the vertical axis and then joined through two VTJs to form a 2×2 tessellation, as depicted in Fig. 3-14. An analysis of the overall DOF of the tessellation reveals a spatial $8R$ linkage formed at the centre of the four units whose configuration can be defined by two neighbouring cells in the rows. Each unit has one DOF, and the connection between two neighbouring cells in the rows is defined by a

single input, i.e., a joint at the valley crease or a planar 4R linkage. Consequently, the overall DOF of the tessellation is one.

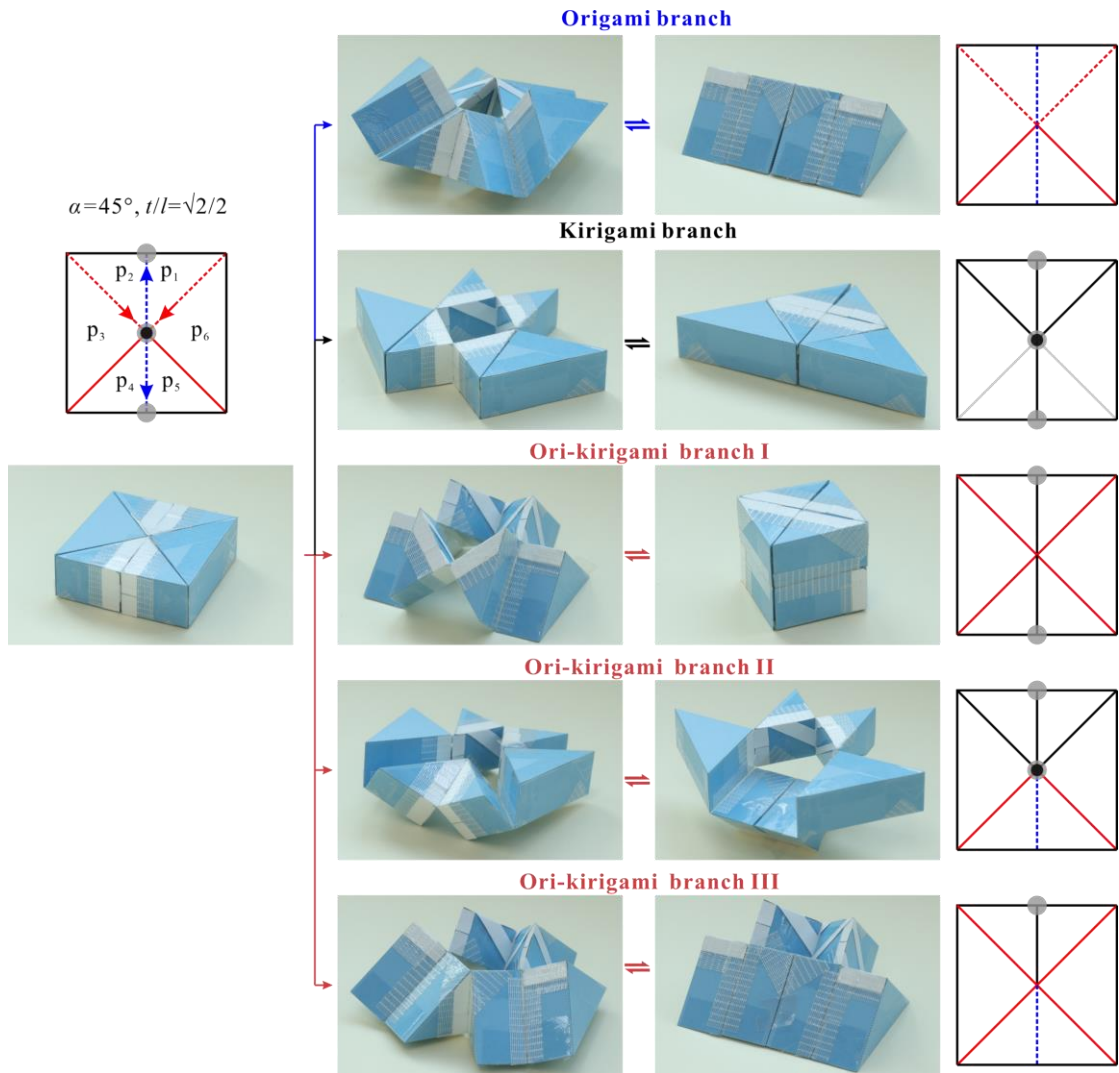


Fig. 3-13 The prototype of a single unit with $\alpha = 45^\circ$, $l = 40\text{mm}$, $t = 28.28\text{mm}$. Triangular panels are made of cardboard and non-stretchable tapes are made of high density polyethylene fibre.

3.3.1.1 Origami Motion Branch of the Tessellation

Upon the selection of a thick-panel origami branch by the modified unit, the 2×2 tessellation undergoes deformation in accordance with the crease pattern depicted in Fig. 3-15(a). Since the units in two adjacent rows are connected to each other by hinges in the thickness direction, p_4 and p_4' , as well as p_5 and p_5' will each work as one large triangular panel when the valley folds connecting them are in action. The folding

process of the 2×2 origami tessellation, as depicted in Fig. 3-15(b), aligns with the standard diamond patterns of the thick panel, a well-known single DOF system, resulting in a reduction of the area to $1/8$ of the original and an increase in thickness by 8 times. As the number of rows of the tessellation increases, unidirectional bending propensity causes the panels to self-intersect, eventually leading to the formation of a tubular structure (iii-iv-v in Fig. 3-15(c)). Meanwhile, the flat thick panels can also be folded into a compact stack within a single DOF mode by keeping some of the co-linear creases dormant (iii-ii-i in Fig. 3-15(c)).

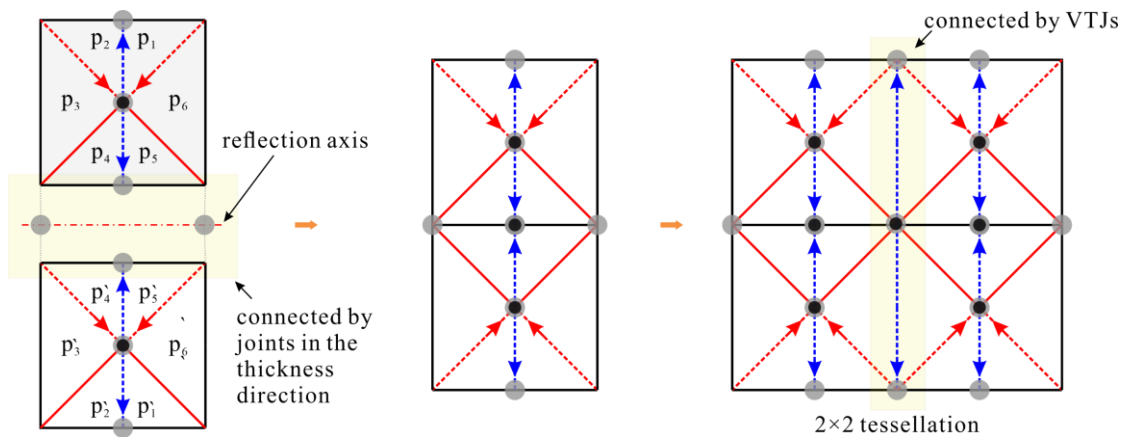


Fig. 3-14 The formation and connectivity of 2×2 tessellation.

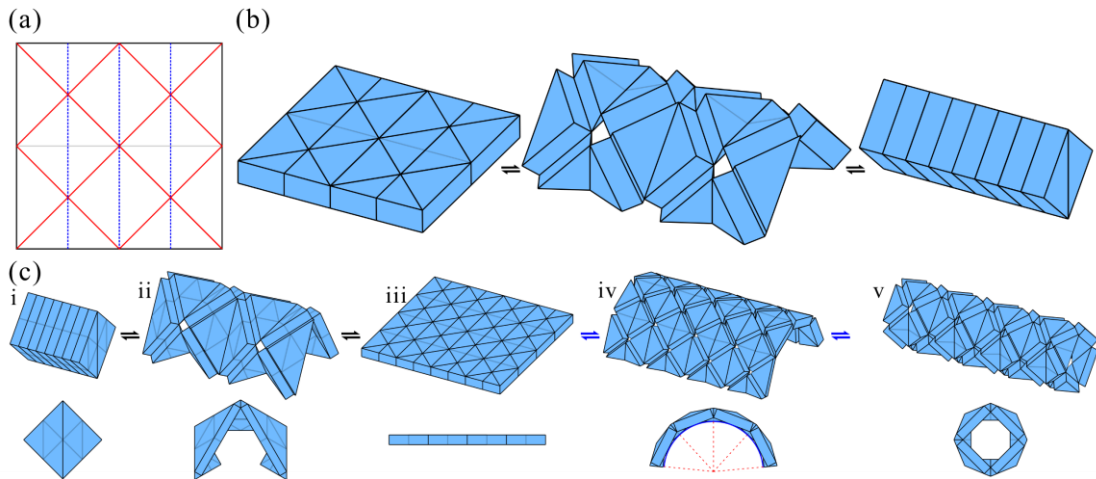


Fig. 3-15 Tessellations of thick-panel origami mode. (a) Crease pattern of 2×2 origami tessellation; (b) and (c) are single DOF motion sequence of 2×2 and 4×4 origami tessellations.

3.3.1.2 Kirigami Motion Branch of the Tessellation

When the modified unit opts for a thick-panel kirigami motion branch, the trend of the 2×2 tessellation deforms following the crease pattern depicted in Fig. 3-16(a). Initially, all units in the tessellation are in planar 4R linkage mode (level-I deformation), as illustrated in Fig. 3-16(b). As the unit reaches its limit configuration, two neighbouring cells in the rows come into contact and merge, thereby triggering the level-II deformation of the 2×2 tessellation, where it functions as a single R joint, as demonstrated in Fig. 3-16(c). As the number of units increases, the tessellation transforms into a standard rotating square structure^[178] during level-II deformation, as demonstrated by the motion sequence of the 2×2 tessellation in Fig. 3-16(d). For either level-I or level-II deformation, there is only in-plane deformation.

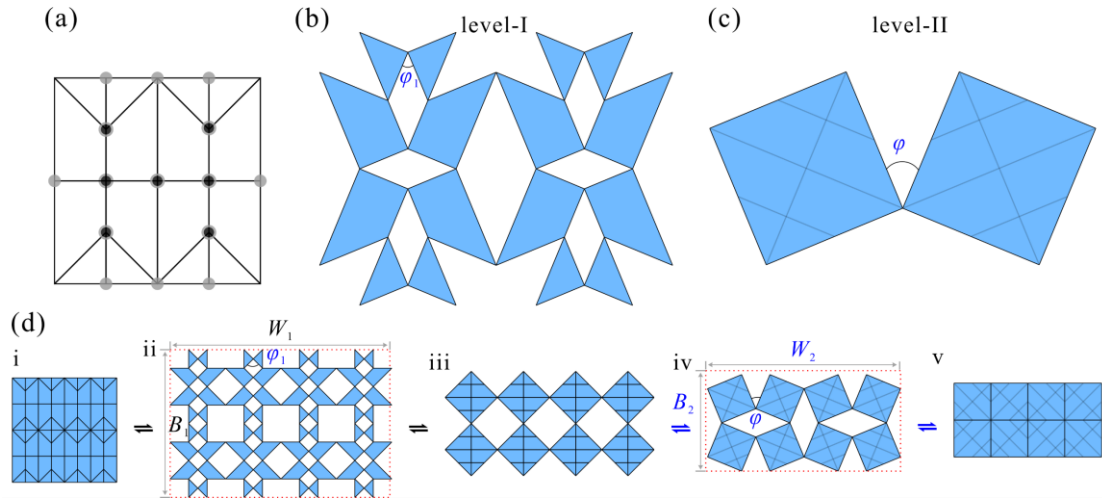


Fig. 3-16 Tessellations of thick-panel kirigami mode. (a) Pattern of 2×2 tessellation and its (b) level-I deformation and (c) level-II deformation; (d) single DOF motion sequence of 4×4 origami tessellations, where i-ii-iii correspond to configurations in level-I deformation, iii-iv-v correspond to configurations of in level-II deformation.

3.3.1.3 Ori-Kirigami Motion Branches of the Tessellation

Lastly, consider the ori-kirigami cases. When the modified unit selects a thick-panel ori-kirigami motion branch I, the 2×2 tessellation trend deforms following the crease pattern shown in Fig. 3-17(a). Studies have shown that a single ori-kirigami I unit can be folded from the flat state of a prism to another prism state (Fig. 3-8), with its area reduced to half of the original size and height doubled. However, in tessellations,

units are only allowed to fold to half of their final state due to panel interference between adjacent units. As a result, the 2×2 tessellation is folded from a planar state into a square arch, as shown in Fig. 3-17(b). As the number of rows increases, the tessellation can eventually fold into a square prism, as shown in Fig. 3-17(c).

When the modified unit selects the thick-panel ori-kirigami branch II, the 2×2 tessellation deforms according to the crease pattern shown in Fig. 3-18(a). Due to the opening or closing of the triangular panels at both ends only within their respective faces, the internal triangles rotate around the valley creases, causing the 2×2 tessellation to fold from a planar state into an inverted V-shape with an angle of 90° . For the 4×4 tessellation, it can be seen as two inverted V-shapes with angles of 90° connected within the plane to form a square arch, as demonstrated in Fig. 3-18(c).

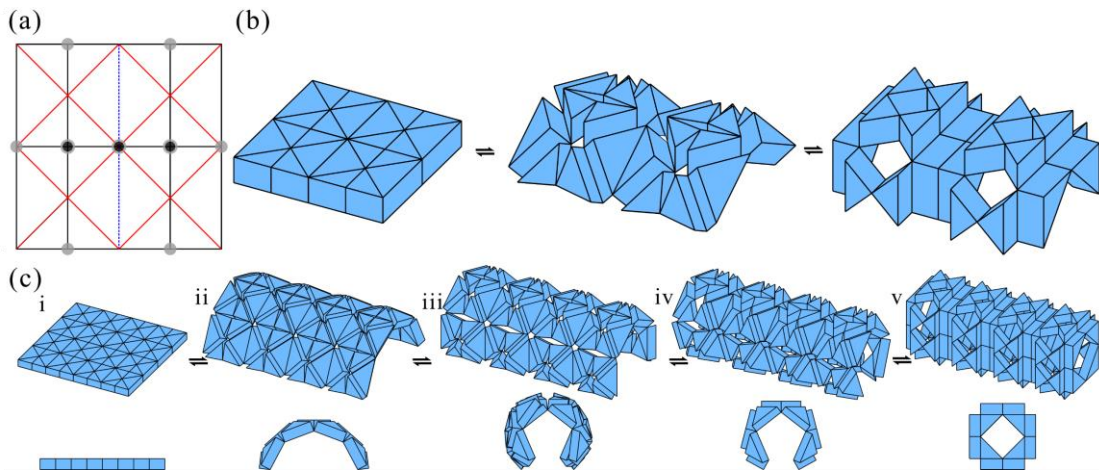


Fig. 3-17 Tessellations of thick-panel ori-kirigami I. (a) Crease pattern of 2×2 tessellation; (b) and (c) are single DOF motion sequences of 2×2 and 4×4 tessellations.

As shown in Fig. 3-19(a) and (b), the 2×2 tessellation is folded from a planar state into a square arch, when the modified unit selects the ori-kirigami branch III. Although both tessellation of ori-kirigami branches III and I are folded into square arches, the fully folded configuration of the tessellation of ori-kirigami branch III exhibits triangular panels on either side of the arch in face-to-face contact, unlike the line-to-line contact in the tessellation of ori-kirigami branch I. Furthermore, when the tessellation of thick-panel ori-kirigami mode III comprises more than three rows, it becomes incompatible. This is due to the tendency for the tessellation to bend in both directions because of the presence of cuts in the unit, as shown in Fig. 3-19.

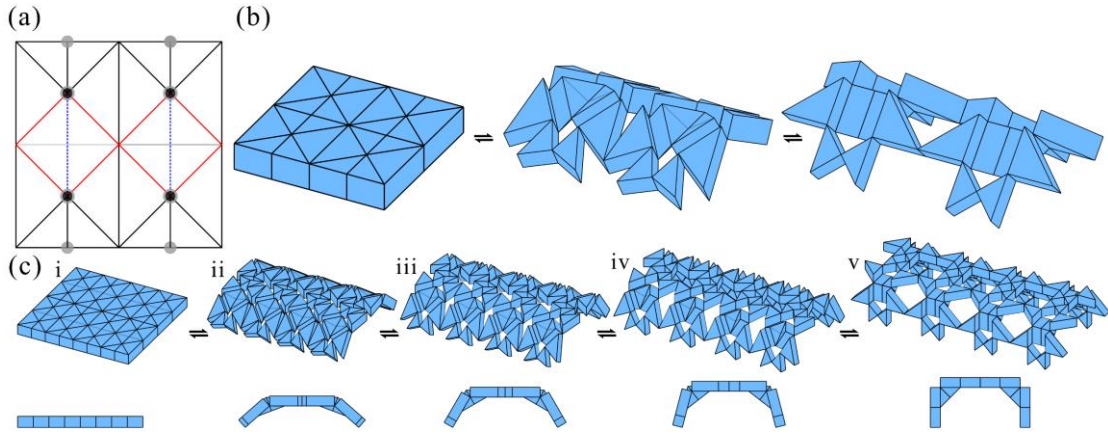


Fig. 3-18 Tessellations of thick-panel ori-kirigami mode II. (a) Crease pattern of 2×2 tessellation; (b) and (c) are single DOF motion sequence of 2×2 and 4×4 tessellations.

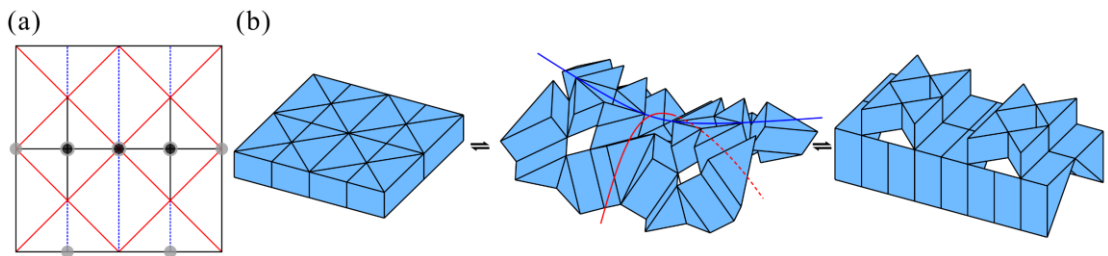


Fig. 3-19 Tessellation of thick-panel ori-kirigami mode III. (a) Crease pattern of 2×2 tessellation; (b) single DOF motion sequence of 2×2 tessellations.

The folding process of the prototype, depicted in Fig. 3-20, demonstrates how transferable joints enhance the reconfigurability of a single thick-panel structure, where triangular panels made of cardboard are connected by high-density polyethylene fibre. Starting from the fully unfolded configuration, by keeping the axes of any of the transferable joints located on the upper and lower surfaces of the panel, the uniform-thickness panels can be folded into a compact volume with no gaps in diamond origami mode. Alternatively, by keeping the axes of all the transfer hinges located in the thickness direction, the uniform-thickness panels can be deformed in the plane in the kirigami branch. If some of the joints are in the top and bottom surfaces of the panel and some are located in the thickness direction, the uniform-thickness panels can be transformed into multiple configurations in three ori-kirigami I-III branches. It is worth noting that with this careful design, the folding process in either thick-panel origami, kirigami, or ori-kirigami modes is a single DOF.

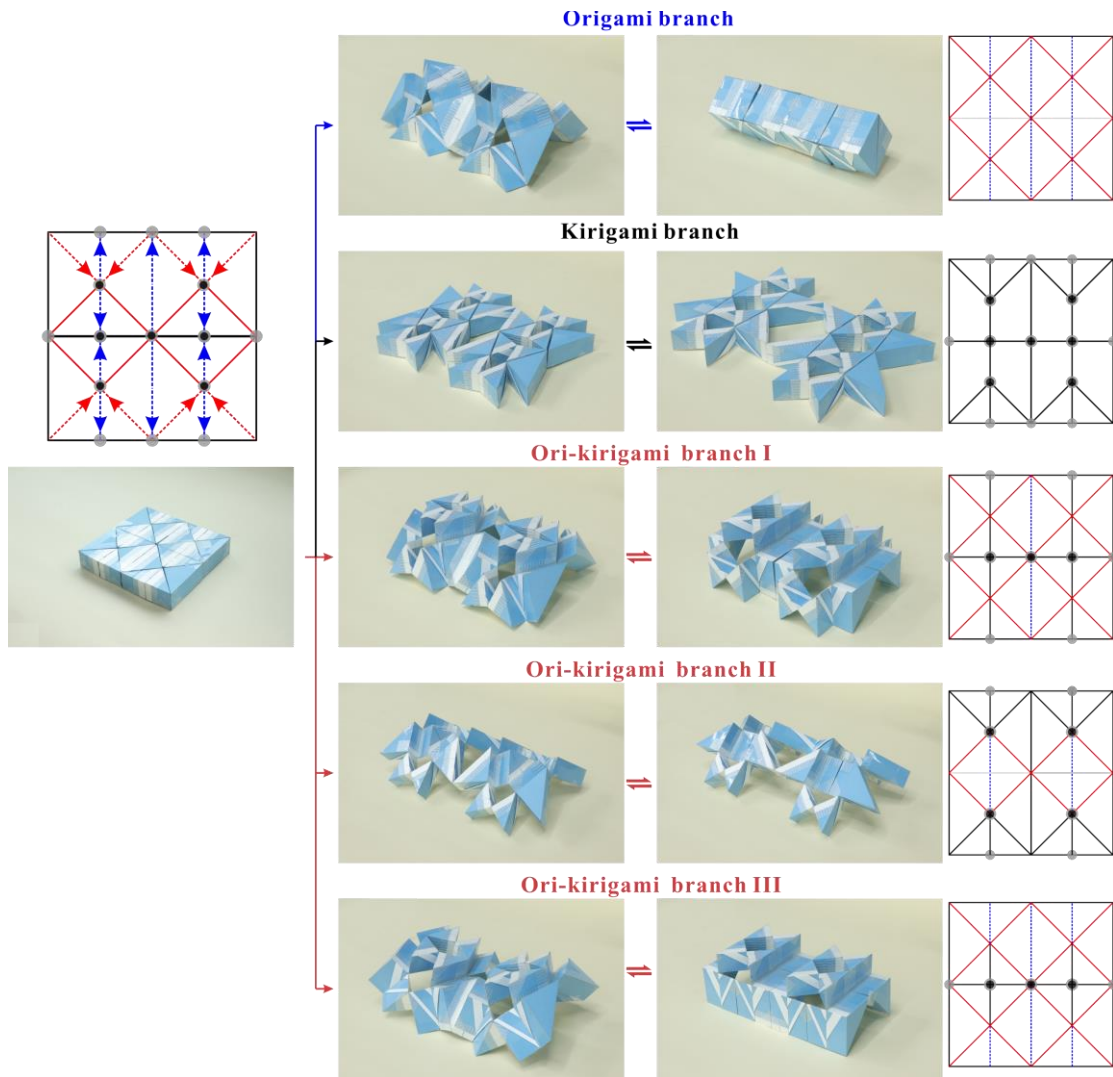


Fig. 3-20 Single DOF folding process of the prototype with $\alpha = 45^\circ$, $l = 40\text{mm}$, $t = 28.28\text{mm}$.

3.3.2 Tuneable Properties of the Tessellation

When the tessellation enters different motion branches, besides changes in shape, there may also be variations in properties. Therefore, this section will discuss the tunability of the Poisson's ratio, deployable ratio, and load-bearing capacity associated with reconfiguration.

3.3.2.1 Poisson's Ratio

Apparently, the dimensions of the tessellations have changed significantly. Of these, the most intriguing is the auxetic behaviour exhibited when the tessellation goes into the kirigami branch with only in-plane deformation. As shown in Fig. 3-16 (d), the dimensions are marked by the red dashed line. At the beginning state of level-I, the

dimensions of the $m \times n$ tessellation, i.e., the width W_1 and breadth B_1 in the x and y directions, are derived as

$$\begin{aligned} W_1 &= n(4l \sin(\varphi_2 / 2) + 2l \tan \alpha \cos(\varphi_1 / 2)) \\ B_1 &= m(2l \cos(\varphi_1 / 2) + 2l \tan \alpha \sin(\varphi_1 / 2)) \end{aligned} \quad (3-11)$$

where m and n are the number of rows and columns of the unit in the tessellation.

Meanwhile, the dimensions W_2 and B_2 of the tessellation in level-II are

$$\begin{aligned} W_2 &= 2n((2\sqrt{2}l \sin(\varphi / 2)) + (2\sqrt{2}l \cos(\varphi / 2))) \\ B_2 &= m((2\sqrt{2}l \sin(\varphi / 2)) + (2\sqrt{2}l \cos(\varphi / 2))) \end{aligned} \quad (3-12)$$

Therefore, in-plane Poisson's ratio ν_{BW} are

$$\nu_{BW} = -\frac{dW_1}{dB_1} \times \frac{B_1}{W_1} = \frac{3\cos 2\alpha - \cos(2\alpha - \varphi_1) - 3\cos \varphi_1 + 1}{3\cos 2\alpha + \cos(2\alpha - \varphi_1) + 3\cos \varphi_1 + 1} \quad (3-13)$$

and

$$\nu_{BW} = -\frac{dW_2}{dB_2} \times \frac{B_2}{W_2} = -1 \quad (3-14)$$

for level-I and level-II deformations, respectively.

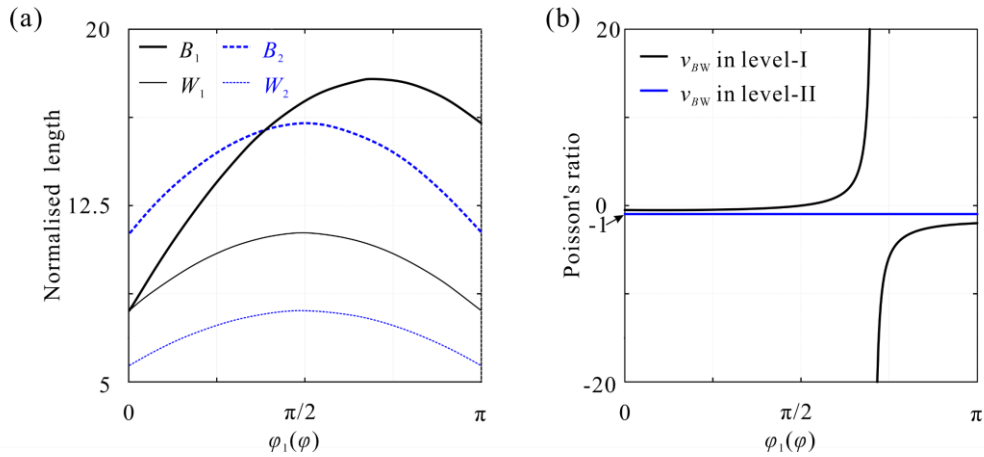


Fig. 3-21 Dimension and Poisson's ratio variations of the 4×4 kirigami tessellation. (a) Variations in dimensions; (b) variations in Poisson's ratio.

The normalised dimension variations and the corresponding Poisson's ratio ν_{BW} for the geometric parameters are $l = 40\text{mm}$, $\alpha = \pi/4$ are plotted in Fig. 3-21(a) and (b). During level-I deformation (i-ii-iii in Fig. 3-21(c)), the tessellation first undergoes a

bidirectional expansion of anisotropy, transforming from a small square to a rectangular contour, exhibiting NPR. Then, the breadth B_1 slowly increases while the width W_1 starts to contract (PPR). Subsequently, as the width B_1 reaches its maximum size, it begins to contract simultaneously with the width W_1 , resulting in NPR behaviour again. After reaching the bifurcation point at $\varphi_1 = \pi$, the dihedral angle φ_1 remains constant, and the tessellation further deforms according to level-II (iii-iv-v in Fig. 3-21(c)). It is found that Poisson's ratio has a constant value of -1, which indicates that the tessellation is isotropic. Overall, the in-plane Poisson's ratio ν_{BW} in kirigami branch can be highly anisotropic or isotropic negative within the same structure as it transitions between level-I or level-II deformations.

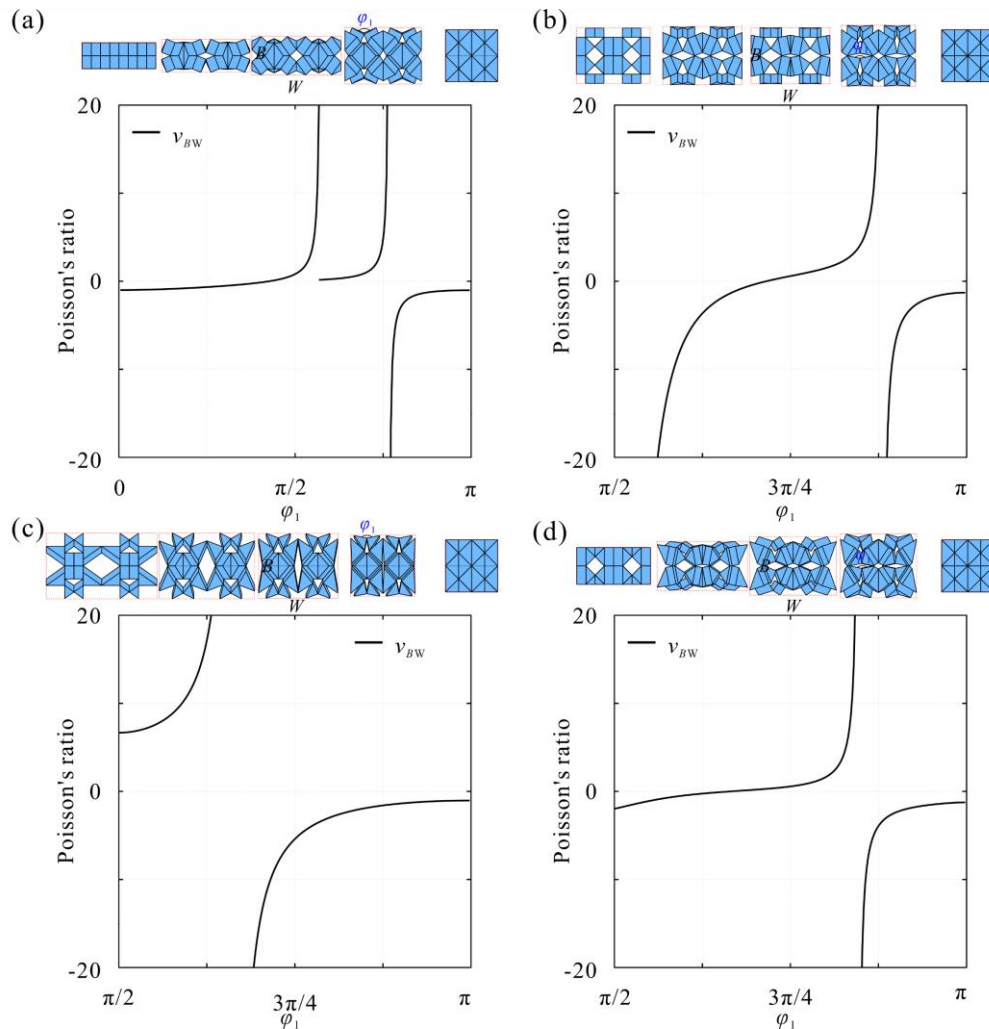


Fig. 3-22 The simulation results of the in-plane Poisson's ratios ν_{BW} when the tessellation enters the origami branch, ori-kirigami branches I-III. (a)-(d) refer to origami and ori-kirigami branches I-III, respectively.

There are both in-plane and out-of-plane deformations as the tessellation enters the other four motion branches, so the dimensions B and W are defined as projections in the xoy plane. The in-plane Poisson's ratios ν_{BW} are provided in Fig. 3-22(a)-(d). In-plane negative Poisson's ratios also exist as the tessellation enters the other four motion branches. The discontinuity in Poisson's ratio curve for the origami branch at $\varphi_3 = 102^\circ$ is due to a change in the projection of the outer contour in the xoy plane. The discontinuity of the Poisson's ratio curves for the other cases is due to the transition of the Poisson's ratio between positive infinity and negative infinity.

3.3.2.2 Deployable Ratio

The deployable ratio of a deployable structure is a measure of how efficiently it can be packed for transportation or storage relative to its deployed size. A higher deployable ratio would mean that the structure can be packed into a smaller volume, which is desirable for transportation and storage efficiency. Here, deployable, is defined as the projection of the maximum folded or unfolded surface area along respective motion branches to flat panel state, where a value greater than 1 means it is deployable, and a value less than 1 means it is folded. As shown in Fig. 3-23, deployable ratio of origami, kirigami, and ori-kirigami branches I-III are 0.125, 3.08, 1.5, 2.65, and 1. The origami branch is the one with the smallest deployable ratio (0.125 times) among the five motion branches, while the kirigami branch is the largest deployable ratio (3.08 times). It means that the deployable of the entire reconfigurable unit is about 1/24, from the smallest to the largest projection surface, as shown in Fig. 3-23.

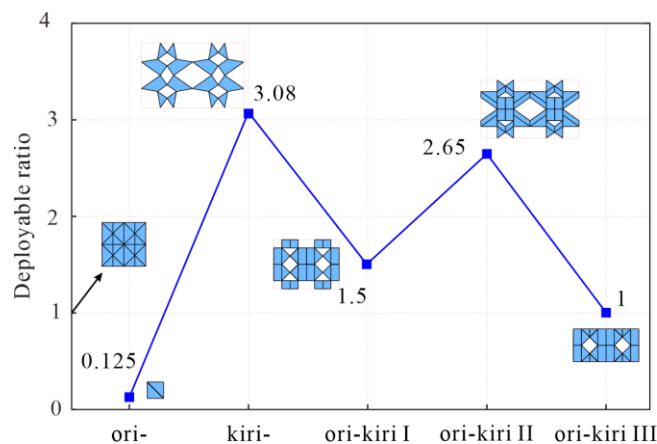


Fig. 3-23 Deployable ratio of five motion branches. The labels ori-, kiri-, ori-kiri I-III on the x -axis refer to origami, kirigami, and ori-kirigami branches I-III, respectively.

3.3.2.3 Load-Bearing Capacity

To explore the load-bearing capacity of the reconfigurable thick panel, 2×2 tessellations are fabricated with cardboard, which were compressed between two smooth flat platens along x, y, z directions, as shown in Fig. 3-24(a). The specimens in fully folded or fully unfolded configurations, along with origami, kirigami, and ori-kirigami I-III branches, were subjected to compression testing using a vertical testing machine (Instron 5982) with a loading rate of 0.5 mm s^{-1} . Experimental force-displacement curves for origami, kirigami, and ori-kirigami I-III branches are presented in Fig. 3-24 (b)-(e), respectively.

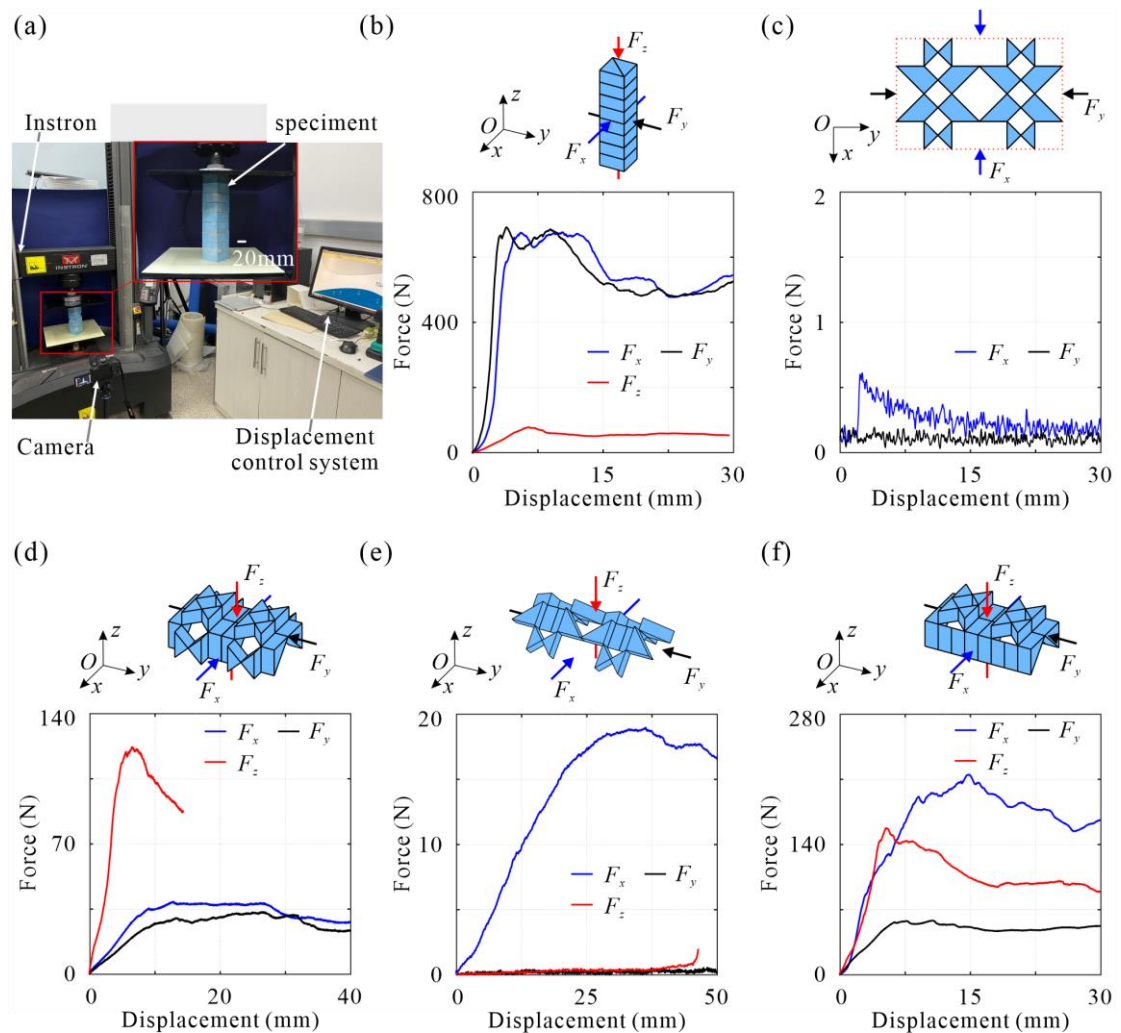


Fig. 3-24 Compression experiments with folding or unfolding configurations along motion branches. (a) Experimental setup; (b)-(f) experimental force-displacement curves for origami, kirigami, ori-kirigami I-III branches, respectively.

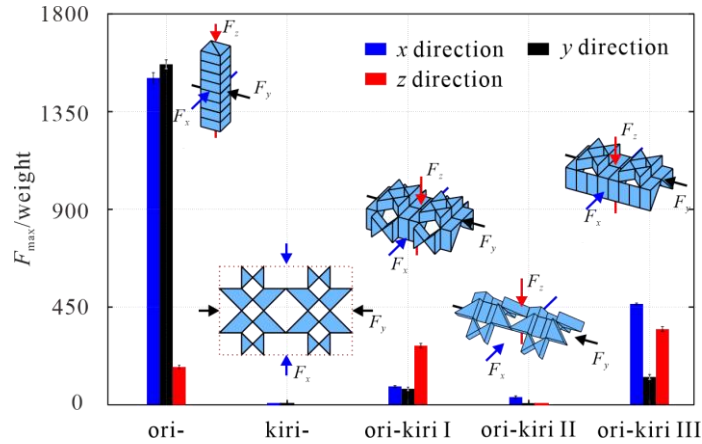


Fig. 3-25 Normalised maximum force for origami, kirigami, ori-kirigami I-III branches.

At the same time, the normalised maximum force (F_{\max} / weight) is shown in Fig. 3-25. Notably, fully folded configurations devoid of any gaps or steps under the origami branch exhibited the highest load-bearing capacity. For instance, paperboard specimens weighing 45g could withstand up to 677.03N under compression along the x direction (1505 times their own weight), 705.45N along the y direction (1567 times their own weight), and 78.89N along the z direction (175 times their own weight). However, when the flat panel was fully unfolded under the kirigami branch, it became collapsible in either the x or y direction (Fig. 3-24 (c)). The tessellation exhibits a self-locking phenomenon arising from interference between panels in the fully unfolded configuration, owing to the combination of creases and cuts, thereby imparting a notable load-bearing capacity. As shown in Fig. 3-24 (d), paperboard specimens in locked configuration under the ori-kirigami branch I can withstand up to 38.88N under compression along the x -direction, 33.31N along the y direction, and 121.89N along the z direction, corresponding to 86, 74, 271 times of its own weight, respectively. Such a self-locking phenomenon also exists when the tessellation is in ori-kirigami branches II and III, as shown in Fig. 3-24 (e) and (f). However, in the fully unfolded configuration under the ori-kirigami branches II, compression along the y or z direction forces the contacting panels to open, resulting in only marginal load-bearing capacity along the x direction (42 times their own weight). In contrast, in the locked state of the ori-kirigami branches III, the triangular panels on either side of the arch are in face contact, significantly reinforcing the load-bearing capacity in all three directions compared to ori-kirigami branches II, as demonstrated by the test results in Fig. 3-24 (f). Specifically, specimens weighing 45g exhibited the ability to withstand up to 215.06N

under compression along the x direction, 58.21N along the y direction, and 157.47N along the z direction, translating to 478, 129, and 350 times their own weight, respectively.

3.4 Conclusions

In this chapter, the VTJs technique is proposed to design reconfigurable thick-panel structures. Starting from an origami vertex with uniform thickness, replacing some of the R joints with VTJs gives the origami structure, which otherwise has a single deformation mode, the ability to be reconfigurable. By strategically activating the VTJs, the reconfigurable unit can undergo various folding behaviours, including origami, kirigami, and three cut-and-fold kirigami motion branches. The kinematic analysis revealed that the choice of design parameters, particularly the angle of the panels and the thickness-to-length ratio, significantly influences the folding behaviour of the structure. Furthermore, the results show that this reconfigurable unit can be tessellated to form large-scale structures with a single DOF while also preserving the motion branches, thus enabling a single mechanical metamaterial to combine the properties of anisotropic (varies from $-\infty$ to $+\infty$) or isotropic (-1) NPR, large deployable ratio (about 1/24), and multiple load-bearing capacity (0.4-1567 times its own weight).

Chapter 4 Tuneable Metamaterials Based on Spatial 7R Linkage in Modular Origami Form

4.1 Introduction

The phenomenon of reconfiguration triggered by kinematic bifurcation in a single closed-loop linkage has attracted the attention of researchers and proved to be a valuable resource for the design of advanced mechanisms. Therefore, the primary aim of this chapter is to first design alternative forms of reconfigurable single-loop spatial mechanisms with a modular origami appearance with more regular shape, richer geometry and enhanced functionality. Subsequently, 2D or 3D modules will be constructed, taking into account the geometric and kinematic compatibility between the different bifurcation configurations, so as to exploit their inherent kinematic bifurcation to achieve advanced mechanical properties for a wide range of metamaterials.

The chapter outline is structured as follows. In section 4.2, a modular origami unit based on a single DOF spatial 7R linkage is introduced initially. The folding process of the unit is described using a kinematic model, facilitating systematic analysis of kinematic properties under varied geometric parameters. In section 4.3, a set of single DOF reconfigurable 2D modules arranged in a back-to-back assembly scheme are presented. The tunability of these modules and their tessellations through reconfiguration within all 2D symmetry groups under the control of a simple compression load, aided by thermal-responsive materials or pressurization schemes, is also explored. In section 4.4, a 2D origami module is created through a shoulder-to-shoulder assembly scheme of units. Subsequently, these 2D origami modules are integrated onto the surfaces of regular prisms, yielding a series of reconfigurable polyhedrons with NPR, ZPR, and PPR, or even customizable Poisson's ratio signs. Finally, this chapter is concluded by the conclusions in section 4.5.

4.2 Kinematics of the Spatial 7R Linkage in Modular Origami Form

4.2.1 Characterization of Modular Origami Unit

The 3D structure of the simple unit operating in plane-symmetry mode is illustrated in Fig. 4-1(a), which is composed of two rectangular panels, two triangular panels, two thin sheets, and a trapezoidal panel. These components are bonded together

along edges to form a closed loop. The unit is parameterized by edge lengths a, b, l, t_1, t_2, t_3 , sector angles α, β, γ , and folding angles $\varphi_1-\varphi_7$. Assuming that all components are rigid, and the structure can fold only along the connected edges that act as R joints whose axes are indicated by red centre lines in Fig. 4-1(a). Such a modular origami unit is kinematically equivalent to a spatial 7R linkage, as shown in Fig. 4-1(b), and thus it is a single DOF system referring to the Kutzbach criterion^[179]. Following the D-H notation^[46], parametric constraints of this linkage form in Fig. 4-1(b) of the modular origami unit are derived as

$$\begin{aligned} a_{12} &= a, a_{23} = 0, a_{34} = a, a_{45} = 0, a_{56} = b, a_{67} = b, a_{71} = 0 \\ \alpha_{12} &= 0, \alpha_{23} = \alpha, \alpha_{34} = 0, \alpha_{56} = 3\pi/2, \alpha_{56} = 0, \alpha_{67} = 0, \alpha_{71} = \pi/2 \\ R_1 &= R_4 = R_5 = R_6 = R_7 = 0, R_2 = -R_3 = a \tan(\alpha/2) \end{aligned} \quad (4-1)$$

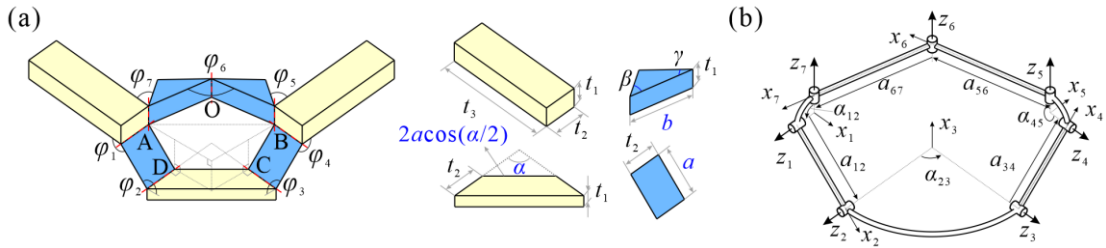


Fig. 4-1 The geometric design of Spatial 7R Linkage in modular origami form. (a) Components of modular origami unit and (b) its equivalent 7R linkage.

The linkage features joints 1 and 2 aligned parallel, joints 3 and 4 aligned parallel, while parallel joints 5, 6, and 7 are all simultaneously perpendicular to joints 1 and 4. Thus, in modular origami form, the trajectories of the rectangular and triangular panels always lie in the same plane that is parallel to the trapezoidal panel, and the two rectangular panels preserve the angle $\pi - \alpha$, during the folding process determined by a single kinematic variable. Reference^[80] states that the singularity of this linkage occurs when two triangular panels are coplanar ($\varphi_6 = \pi$) or when two thin sheets are parallel ($\varphi_1 = \pi/2$). Therefore, for general geometric design parameters, there are a total of four possible motion branches of the modular origami unit (Fig. 4-2), i.e., M1 and M2 involve symmetric and asymmetric configurations with bulged-out triangular panels, while M3 and M4 involve symmetric and asymmetric configurations with nested-in triangular panels.

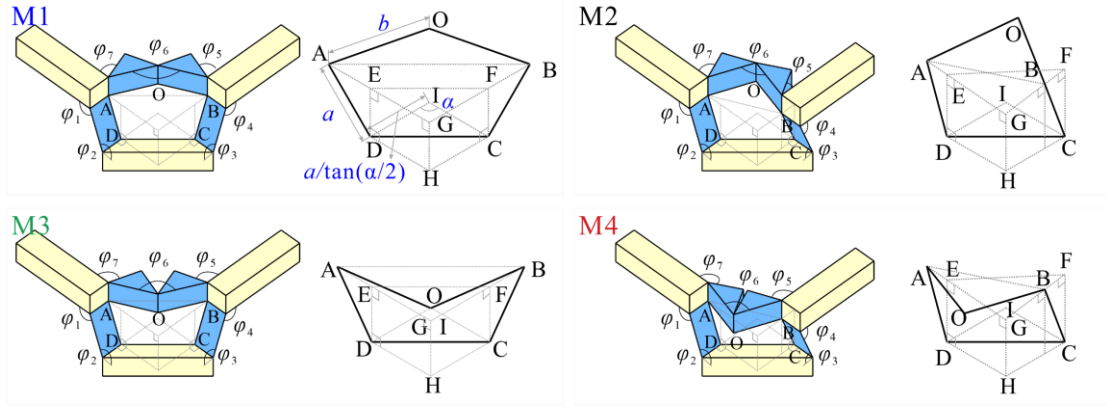


Fig. 4-2 Four possible motion modes M1-M4 of the modular origami unit.

To describe the folding motions of four modes in Fig. 4-2, lines AG and BG are drawn along the edges of the rectangular panel to intersect at point G, and lines DI and CI are drawn along the lateral sides of the trapezoidal panel to intersect at point I, so $\angle AGB = \angle CID = \alpha$. Draw lines DH and CH that are perpendicular to DI and CI leading to $\angle CHD = \pi - \alpha$. Meanwhile, line DE is the common perpendicular of lines AG and DH, and line CF is the common perpendicular of lines BG and CH. In symmetric modes, $|AG|$ and $|BG|$ are equal to $a - a \cos \varphi_1$, while in asymmetric mode, $|AG|$ and $|BG|$ are equal to $a \pm a \cos \varphi_1$, where \pm means one is positive and the other is negative. Notice that line AB is the diagonal of planar quadrilateral OAGB. And, $|AD| = |BC| = a$, $|OA| = |OB| = b$. Therefore, folding angles $\varphi_1 - \varphi_7$ are derived, i.e.,

$$\begin{aligned} \varphi_1 &= \varphi_2 = \varphi_3 = \varphi_4, \quad \varphi_5 = \varphi_7 \\ \varphi_5 &= \varphi_7 = (\pi + \varphi_6 - \alpha) / 2 - \beta \\ b \sin \frac{\varphi_6}{2} &= (a \cos \varphi_1 + a) \cos \frac{\alpha}{2} \end{aligned} \quad (4-2)$$

for motion branch M1,

$$\begin{aligned} \varphi_1 &= \varphi_2 = \pi - \varphi_3 = \pi - \varphi_4 \\ 2b^2 \sin^2 \frac{\varphi_6}{2} &= a^2 (\cos^2 \varphi_1 + 1) - a^2 \cos \alpha (\cos^2 \varphi_1 - 1) \\ \varphi_5 &= \frac{\pi}{2} + \frac{\varphi_6}{2} - \arccos \frac{2a^2 \cos \varphi_1 - b^2 + b^2 \cos \varphi_6}{2ab \sin \frac{\varphi_6}{2} (\cos \varphi_1 - 1)} - \beta \\ \varphi_7 &= \frac{\pi}{2} + \frac{\varphi_6}{2} - \arccos \frac{2a^2 \cos \varphi_1 + b^2 - b^2 \cos \varphi_6}{2ab \sin \frac{\varphi_6}{2} (\cos \varphi_1 + 1)} - \beta \end{aligned} \quad (4-3)$$

for motion branch M2,

$$\begin{aligned}
 \varphi_1 &= \varphi_2 = \pi - \varphi_3 = \pi - \varphi_4 \\
 2b^2 \sin^2 \frac{\varphi_6}{2} &= a^2 (\cos^2 \varphi_1 + 1) - a^2 \cos \alpha (\cos^2 \varphi_1 - 1) \\
 \varphi_5 &= \frac{3\pi}{2} + \frac{\varphi_6}{2} - \arccos \frac{2a^2 \cos \varphi_1 - b^2 + b^2 \cos \varphi_6}{2ab \sin \frac{\varphi_6}{2} (\cos \varphi_1 - 1)} - \beta \\
 \varphi_7 &= \frac{3\pi}{2} + \frac{\varphi_6}{2} - \arccos \frac{2a^2 \cos \varphi_1 + b^2 - b^2 \cos \varphi_6}{2ab \sin \frac{\varphi_6}{2} (\cos \varphi_1 + 1)} - \beta
 \end{aligned} \tag{4-4}$$

for motion branch M3, and

$$\begin{aligned}
 \varphi_1 &= \varphi_2 = \varphi_3 = \varphi_4, \quad \varphi_5 = \varphi_7 \\
 \varphi_5 &= \varphi_7 = (3\pi - \varphi_6 - \alpha) / 2 - \beta \\
 b \sin \frac{\varphi_6}{2} &= (a \cos \varphi_1 + a) \cos \frac{\alpha}{2}
 \end{aligned} \tag{4-5}$$

for motion branch M4.

It shows that once the input angle $\varphi_1 \in [0, \pi]$ is given, the other dihedral angles $\varphi_2 - \varphi_7$ can be determined, also implying that the linkage is one DOF. Meanwhile, the relationships among the dihedral angles $\varphi_1 - \varphi_7$ are not affected by γ, t_1, t_2, t_3 .

4.2.2 Effect of Geometric Parameters on Motion Behaviours

4.2.2.1 Effect of Geometric Parameters on Kinematic Bifurcation

Further investigation revealed that the design parameters b/a and α of the 7R linkage exert a profound influence on the number, range, and evolution of the motion branches, referring to detailed relationships between $\varphi_1 - \varphi_7$. The motion behaviours of this modular origami unit have been studied carefully, which can be divided into six cases, as shown in Fig. 4-3. The bifurcation configurations B_{ij} ($i, j=1, 2, 3, 4$) of motion branches M_i and M_j are located next to the arrows. The ellipse is filled with purple if the module has a complete cycle of motion (φ_1 reachable π) on the M_i motion path, otherwise (φ_1 inaccessible π), it is blank. If there is interference in the motion path, which can be eliminated by adjusting the angle β or γ , the edges of the ellipse are represented as grey, otherwise it is black.

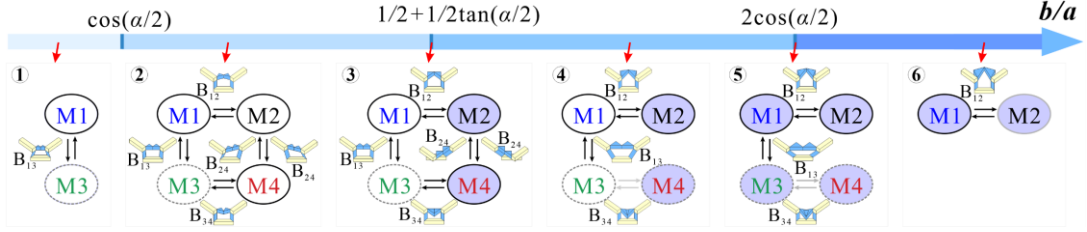
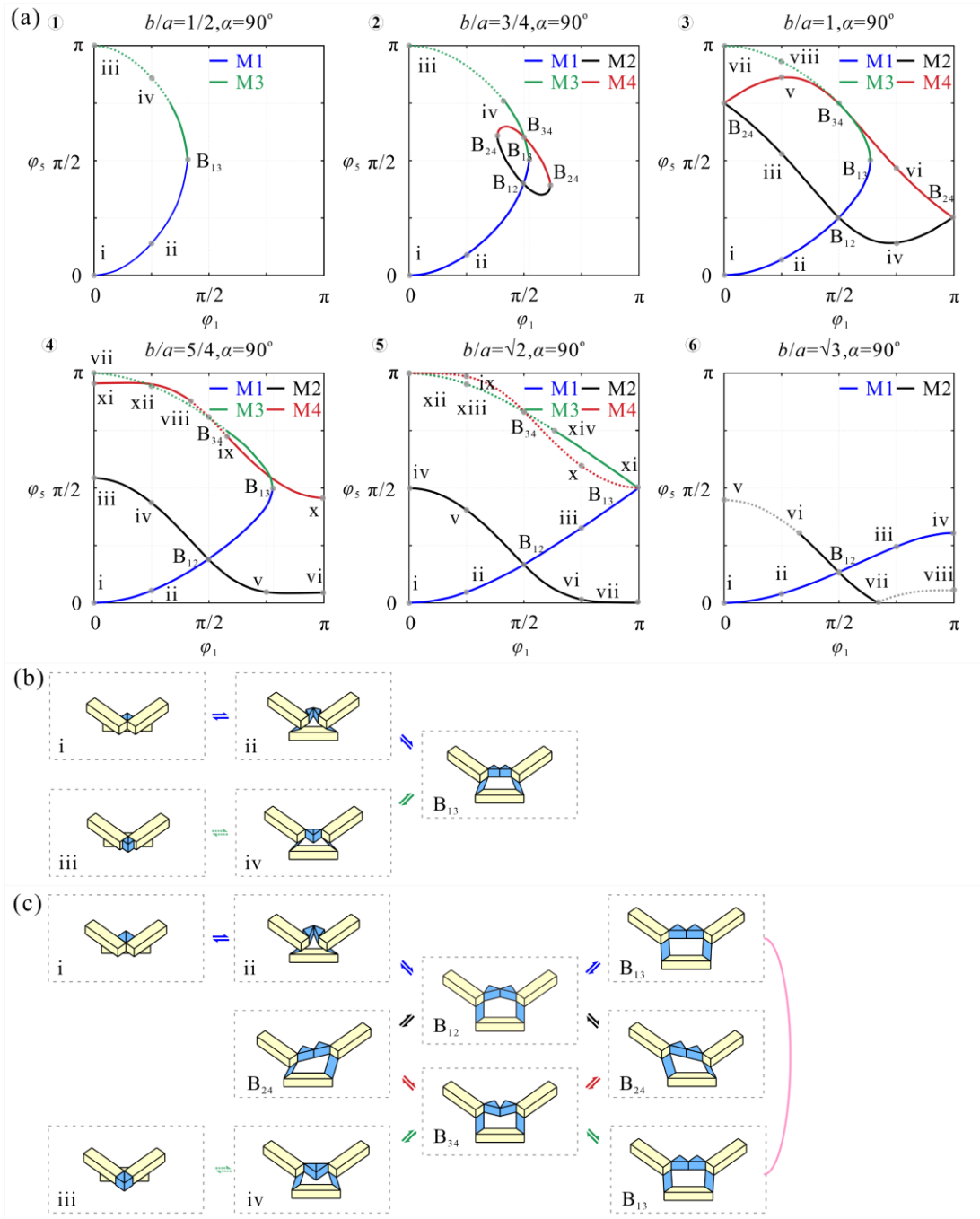


Fig. 4-3 Effects of geometric design parameters (b/a and α) on motion branches.

To better understand the effect of parameter changes on kinematic behaviour, particular parameters were carefully selected by increasing b/a while keeping $\alpha = 2\beta = 2\gamma = 90^\circ$. The resulting kinematic paths and configurations are illustrated in Fig. 4-4(a) and Fig. 4-4(b-g), respectively. In case ①: $|OA| + |OB| \leq |DC|$, where $b/a \leq \cos(\alpha/2)$, leading to $\varphi_1 \leq \pi/2$, there is only one bifurcation between M1 (blue line) and M3 (green line) that occurs at $\varphi_6 = \pi$ for the modular origami unit. Kinematic paths φ_5 vs φ_1 and the motion sequence of the modular origami unit in case ① with $b/a = 1/2$ are shown in Fig. 4-4(a) and (b). Moving to case ②: $|DC| < |OA| + |OB| < |AD| + |CI|$, i.e., $\cos(\alpha/2) < b/a < (1/2 + 1/2 \tan(\alpha))$, there are four motion branches M1-M4 sharing five bifurcation points, as the example in case ② with $b/a = 3/4$ shown in Fig. 4-4(a) and (c). The bifurcations B_{12} and B_{34} occur at $\varphi_1 = \pi/2$, where two thin sheets swinging in the same or opposite direction, while B_{12} and B_{24} occur at $\varphi_6 = \pi$, where bulged-out triangular panels change to nested-in state, or vice versa. In case ③: $|OA| + |OB| = |AD| + |CI|$, i.e., $b/a = (1/2 + 1/2 \tan(\alpha))$, the bifurcation behaviour is similar to that of the case ② except that φ_1 is able to reach its limit angle π in modes M2 and M4. The example of the modular origami unit with $b/a = 1$ in Fig. 4-4(a) and (d) is in this case. In case ④: $(1/2 + 1/2 \tan(\alpha)) < b/a < 2\cos(\alpha/2)$, there are four motion branches, M1-M4, sharing only three bifurcation points B_{12} , B_{13} and B_{24} , as shown in Fig. 4-4(a) and (e). Unlike case ③, M2 and M4 in case ④ are disconnected due to $\varphi_6 < \pi$. When $|OA| + |OB| = |DC| + 2|AD|\cos\alpha$, i.e., case ⑤: $b/a = 2\cos(\alpha/2)$, the bifurcation behaviour of case ⑤ is similar to that of case ④ except that φ_1 in all four modes M1-M4 is able to reach its limit angle π . The example of the modular origami unit with $b/a = \sqrt{2}$ in Fig. 4-4(a) and (f) is in this case. When $|OA| + |OB| > |DC| + 2|AD|\cos\alpha$ (case ⑥: $b/a > 2\cos(\alpha/2)$), there is only one bifurcation between modes M1 and M2 in this case that occurs at $\varphi_1 = \pi/2$ for the unit because angle φ_6 is unable to reach.

The example in case ⑥ with $b/a = \sqrt{3}$ is shown in Fig. 4-4(a) and (g). Referring to the motion curves and the motion sequences, when the unit is reconfigured between the M1 and M2 branches, it undergoes substantial geometric alterations. Conversely, when reconfiguring between M3 and M4, the changes are localized in comparison to those between M1 and M2. In addition, on path M1, the unit symmetrically expands or contracts, while on path M2, it consistently adopts an asymmetric configuration.



continued on next page

continued

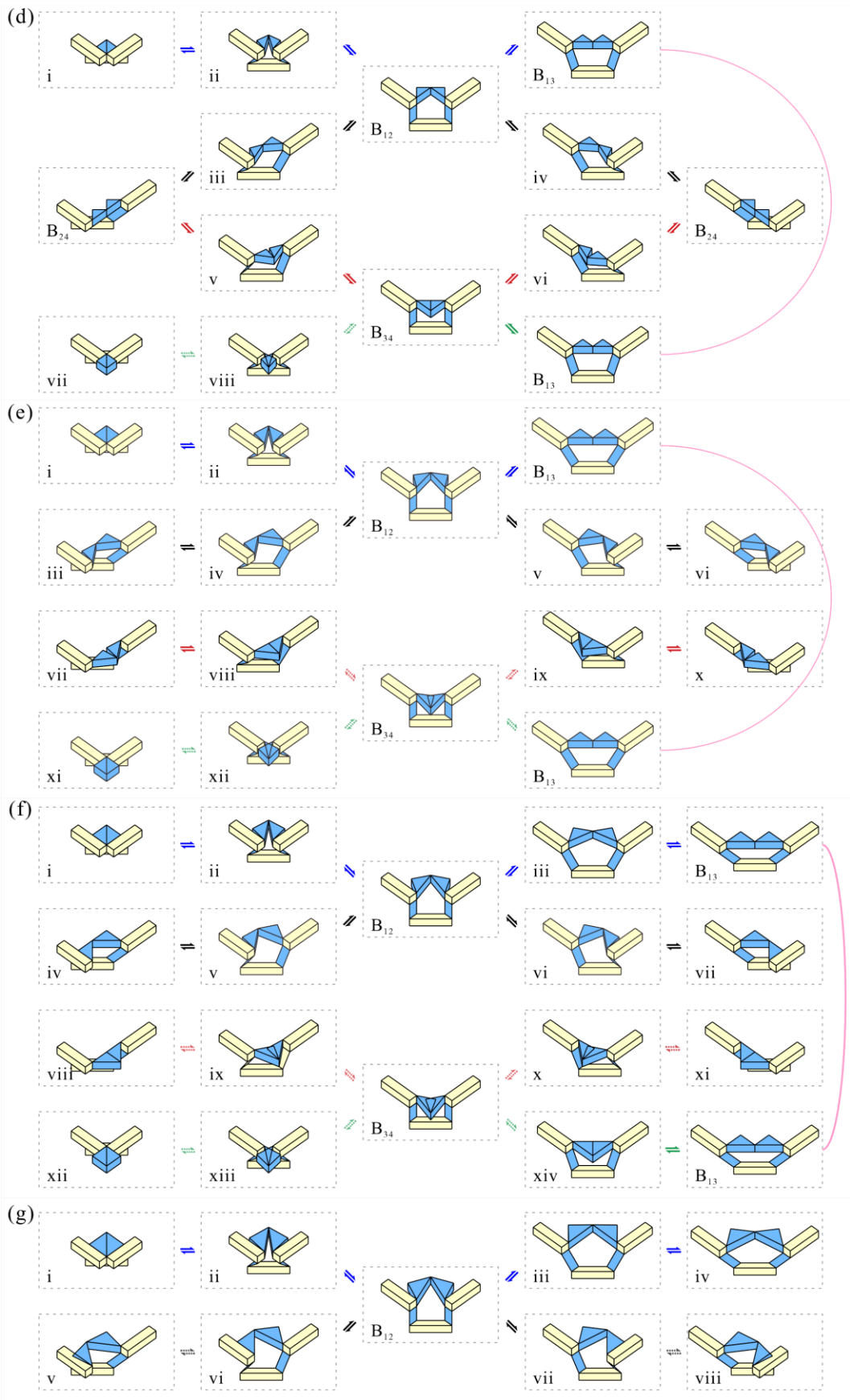


Fig. 4-4 Effect of geometric parameters on kinematic bifurcation. (a) Kinematic paths of the unit under different design parameters of cases ①-⑥ (assuming $\alpha = 2\beta = 2\gamma = 90^\circ$), where the curve for motion branches M1, M2, M3, and M4 are in blue, black, green and red respectively. And physical interference is indicated by dotted lines. (b-g) The motion sequence of the modular origami unit in cases ①-⑥, where b/a changes from $1/2$ to $3/4$, 1 , $5/4$, $\sqrt{2}$, and $\sqrt{3}$.

4.2.2.2 Effect of Geometric Parameters on Physical Interference

Meanwhile, due to physical interference, a section of the motion curves on the paths in Fig. 4-4(a) is dotted, which means it is not achievable. Nonetheless, these physical interferences can be eliminated by adjusting the angle β or γ of the triangular panels (the outline of the ellipse in Fig. 4-3 is represented as dotted), since β and γ are not design parameters of the underlying 7R linkage. For example, it is possible for two nested-in triangular panels to squeeze against each other over a portion of the kinematic path on the M3 and M4 paths in case ①-⑤. Physical interferences in case ①-⑤ can be eliminated by adjusting the angle γ of the triangular panels to expand the motion range and increase the motion mode. Taking case ⑤ as an example, when $\gamma = 45^\circ$ (Fig. 4-5(a) left), the angle φ_1 on path M3 cannot reach $\pi/2$ due to the physical interference, and thus M4 cannot be realized. But when the angle $\gamma \leq 30^\circ$ (Fig. 4-5(a) right), the angle φ_1 on path M3 can reach $\pi/2$, and thus M4 becomes realizable. In Fig. 4-5(b), an example of the motion sequence of the unit in case ⑤ with $\gamma = 30^\circ$ is plotted, and it is noted that the path M4 can be realized. Meanwhile, physical interferences in case ⑥ can be eliminated by adjusting the angle β of the triangular panels, thus extending the motion range. In case ⑥, when $\beta = 45^\circ$ (Fig. 4-5(c) left), the angle φ_1 on path M3 cannot reach π due to physical interference. As β decreases, the motion range of path M2 increases (Fig. 4-5(c) middle and right). Until β equals 35° and φ_1 can reach π . An example of the motion sequence of the unit in case ⑥ with $\beta = 35^\circ$ is plotted in Fig. 4-5(d), where path M2 has a full cycle of motion.

4.3 Reconfiguration of Origami Modules and Their Tessellations

4.3.1 Tunability in Two Families of Rosette Groups

Having identified the modular origami unit with remarkable bifurcation behaviours, it is shown that it can be assembled back-to-back to form origami modules whose shape can be significantly altered. As shown in Fig. 4-6, origami modules with

a folded n -sided ($n=3, 4, 5, 6$) shape and an unfolded $2n$ -sided shape are constructed. To achieve compact folding, the parameter conditions should be satisfied as $\alpha = 2\pi/n$, $\beta = (\pi - \alpha)/2$, $\gamma = \alpha/2$, $b/a = 1/\sin(\alpha/2)$, and $t_3 = 2a$. Without loss of generality, all modular origami units have $t_1 = t_2 = a/2$. First, n modular origami units with $\alpha = 2\pi/n$ are arranged in a circular array around the z -axis, where two adjacent modular origami units share a rectangular area. Next, to ensure that the mechanical assembly with n units still has a single DOF and can form a desired unfolded shape, two additional sheets with a length range $1 \leq l/a \leq 1/\tan(\alpha/2) + t_2/a$ are added between two adjacent units, enabling all trapezoidal panels to move in the same plane. Consequently, a set of modules is constructed, which can also be considered as two platforms connected by eight thin sheets in the middle, as shown in Fig. 4-6.

It is found that the geometric parameters of modular origami units for $n=3, 4, 5$, and 6 all fall into the case of $b/a > \cos(\alpha/2)$. Thus, each basic unit is equipped with the ability to switch between motion branches M1 and M2 through its inherent kinematic bifurcations. At the same time, the two adjacent units plus the two added sheets also form a 7R linkage with $\alpha = 0$. The bifurcation behaviour of this 7R linkage for connection in the M1 branch is similar to that of the basic units, expanding or contracting in a symmetrical way. However, in the M2 branch, it degenerates into a parallelogram linkage. It is noted that the state of this connecting linkage is not independent but is determined by the two thin sheets in the two neighbouring basic units. When the two sheets swing in opposite directions it is M1 and vice versa it is M2. Given the objective of constructing modules with symmetry changes, it becomes imperative to focus on branches M1 and M2, characterized by substantial changes in dimensions. Consequently, setting $l = a$ to avoid branches M3 and M4. Due to the compatibility between the units, origami modules inherit the reconfigurability of the units, which can be reconstructed into different configurations depending on the number and location of the units in the M1 or M2 state. Taking a module for $n=4$ as an example, there exists a total of 25 ($1+2^3+2^4$) kinematic paths when four basic units are in all branches M1 or M2, or two basic units are in branch M1 and the other two are in branch M2. However, due to the similarity in orthogonal directions (see Appendix D for details), only the seven unique cases in Fig. 4-7 will be discussed.

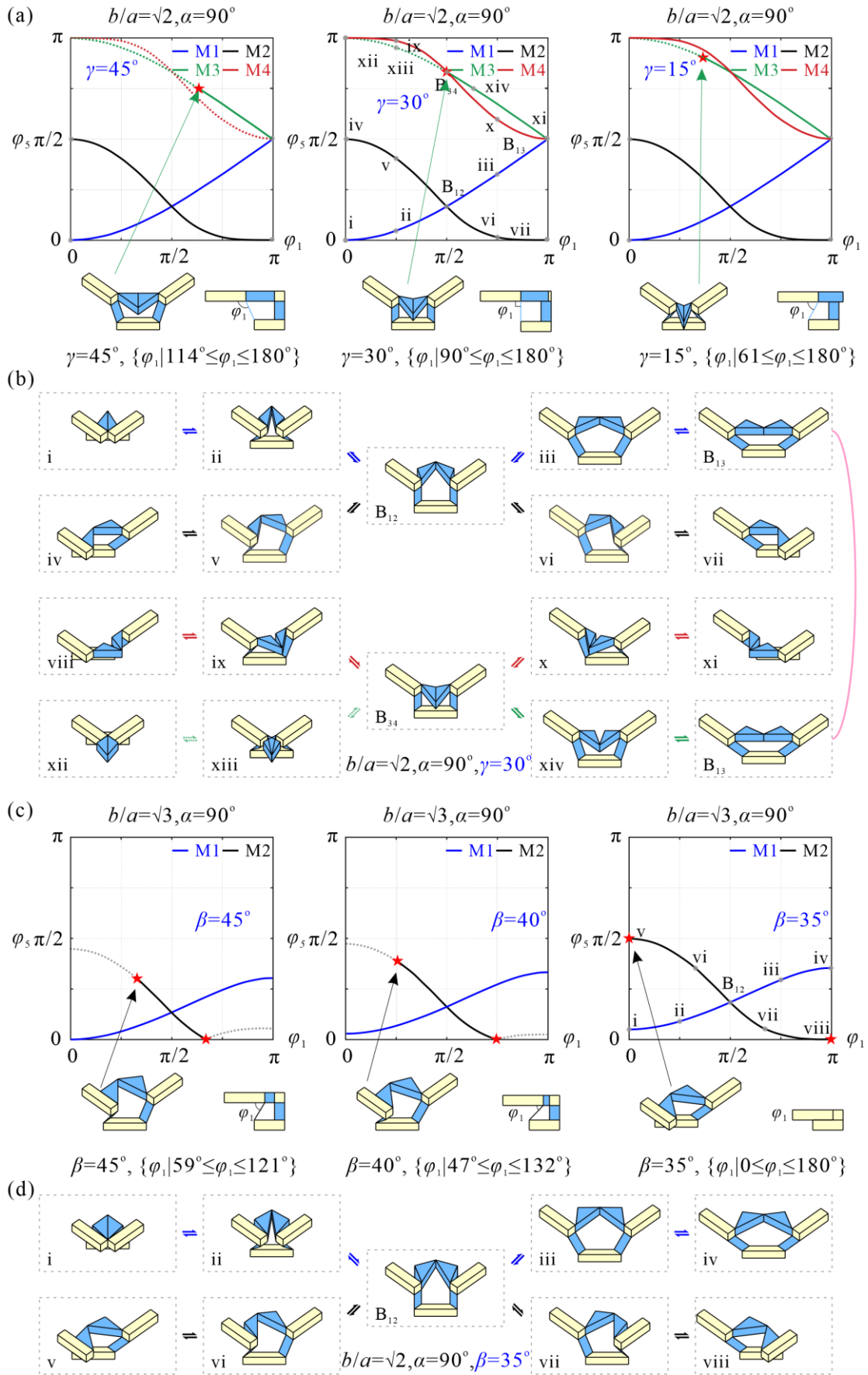


Fig. 4-5 Effect of geometric parameters on physical interference. (a) φ_5 vs φ_1 for kinematic paths of modified modular origami unit in case ⑤ with different angles γ ; (b) the motion sequence of the modular origami unit in case ⑤ with $\gamma = 30^\circ$; (c) φ_5 vs φ_1 for kinematic paths of modified modular origami unit in case ⑥ with different angles β ; (d) the motion sequence of the modular origami unit in case ⑥ with $\beta = 35^\circ$. The physical interference is denoted as dotted lines.

It can be observed that in the early stage of unfolding, the module with the four units in the M1 state travels along path I governed by φ_1 ($\varphi_1 \in [0, \pi/2]$) where the module expands bi-directionally from a smaller square in the xoy plane to a larger one, or vice versa (path I in Fig. 4-7). This expansion continues until the configuration is reached the configuration where all dihedral angles $\varphi_1 = \pi/2$. At this juncture, corresponding to the configuration with maximum height, a kinematic bifurcation occurs, resulting in an instantaneous growth of DOFs and the activation of multiple kinematic paths. Post-bifurcation, the module can seamlessly switch into mono-directional contracted rectangle paths, denoted as paths II and III in the xoy plane. In this configuration, the two basic units are in the M1 state, and the other two are in the M2 state. This setup induces a change in only one dimension in the x or y directions, as the two sheets attached to the ends of the rectangular panel in that direction effectively form a parallelogram. Alternatively, the module switches into invariant square paths IV-VII in the xoy plane (both dimensions invariant in x and y directions) with the four units in the M2 state or two units in the M1 state and the other two in the M2 state where any two sheets attached to the same square panel swing in the same direction.

Besides the geometric dimensions, the symmetry of the module in the xoy plane has undergone significant changes upon reconfiguration, since the module at the bifurcation point can access a new kinematic path that causes a break in symmetry. Here, even though the origami module is in 3D, the focus is mainly on the shape variations of the top platform consisting of rectangular and triangular panels within the xoy plane, because there are only three typical configurations with two symmetries of the bottom platform. To better understand symmetry changes during the reconstruction, notions appear to be handy. Geometrically, for a finite object in 2D, its symmetry according to groups of transformations that leave invariant under reflection and rotation is divided into two types (two families of Rosette Groups)^[180]: those with both rotational and reflectional symmetry, denoted by dn , and those with only rotational symmetry, denoted

by cn , where n represents the number of reflection axes or the order of rotational symmetry. Meanwhile, the reflection axes are represented by red center lines and black dotted lines, while the centers of 2-, 3-, 4- and 6-fold rotational symmetries are represented by rhombus, triangles, squares, and hexagons respectively.

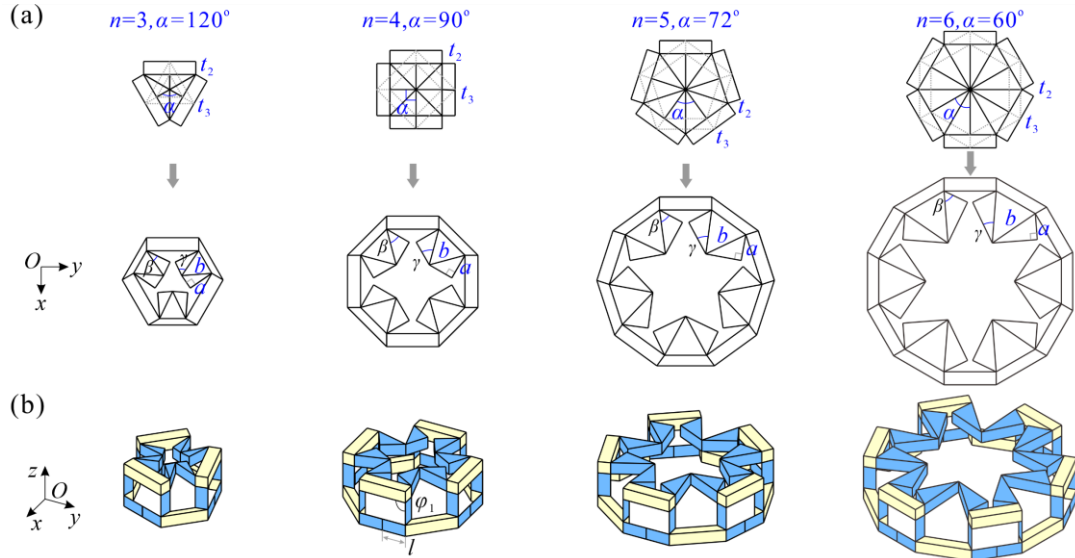


Fig. 4-6 Construction of origami modules by a back-to-back assembly. (a) A folded n -sided ($n=3, 4, 5, 6$) shape and an unfolded $2n$ -sided shape as the target shapes. The dotted grey line shows the shape of the bottom platform. (b) Origami modules are formed by a back-to-back assembly.

As aforementioned, the unit configurations on the path M1 are mirror symmetric, while the unit configurations on the path M2 are asymmetric. Thus, the module in the expanded square path I has d_4 symmetry, i.e., 4-fold rotational symmetry plus reflections in four axes, since all four units are simultaneously in a same mirror symmetric configuration in branch M1 ($\varphi_1 \in [0, \pi/2]$). Its symmetry reduces to c_2 or d_1 upon switching to paths II or III in Fig. 4-7. Specifically, when the module bifurcates into the motion branch II where the symmetric unit in branch M1 (U_1, U_3) and the asymmetric unit in branch M2 (U_2, U_4) alternates, it exhibits global chirality, i.e., c_2 . And when symmetric (U_1, U_2) and asymmetric units (U_3, U_4) occur in pairs, there is only mirror symmetry. It can be seen that this global chirality originates from the symmetry of the location of the units in the M1 or M2 state. Other possibilities are that when the module switches to path IV where four basic units are simultaneously in the same asymmetric configuration in branch M2, the symmetry may change to c_4 . Although all four identical units are themselves asymmetric, they are in an orientation

of 4-fold rotational symmetry and thus giving rise to a global chirality $c4$. The dihedral angle of units $\varphi_1 \in [0, \pi/2)$, presenting $c4$ with left-handed, and when the dihedral angle of units $\varphi_1 \in (\pi/2, \pi]$, presenting $c4$ with right-handed. Furthermore, when the module follows path V, four units are in a symmetric configuration in branch M1 in which two units (U_2, U_4) belong to $\varphi_1 \in [0, \pi/2)$ and the other two (U_1, U_3) belong to $\varphi_1 \in (\pi/2, \pi]$. Such an assignment breaks the rotational symmetry, but due to the mirror symmetry of the unit itself, two reflection lines perpendicular to each other are formed, leading to a $d2$ symmetry. For the module on path VI, configurations of U_1 and U_3 are in branch M2 and configurations of U_2 and U_4 are in branch M1 (one belongs to $\varphi_1 \in [0, \pi/2)$ and the other belongs to $\varphi_1 \in (\pi/2, \pi]$), thus the module has only one reflection axes, i.e., $d1$ symmetry. Lastly, for the module on path VII, two units belonging to different motion intervals on the M1 branch are neighbouring and the module becomes asymmetry, i.e., $c1$ symmetry. In summary, the symmetry of the module for $n = 4, \alpha = 90^\circ$, may be $d4, c4, d2, c2, d1$, and $c1$. The motion bifurcation and symmetry changes for $n=3, 5$, and 6 are also investigated. Similarly, the symmetry changes when the origami module is reconstructed from a bifurcated configuration ($\varphi_1 = \pi/2$) to bifurcated paths. As a result, the module for $n=3$ has $d3, c3$, and $c1$ point groups (Fig. 4-8(a)), the module for $n=5$ has $d5, c5$, and $c1$ point groups (Fig. 4-8(b)), while the module for $n=6$ has $d6, c6, d3, c3, d2, c2, d1$, and $c1$ point groups (Fig. 4-8(c)).

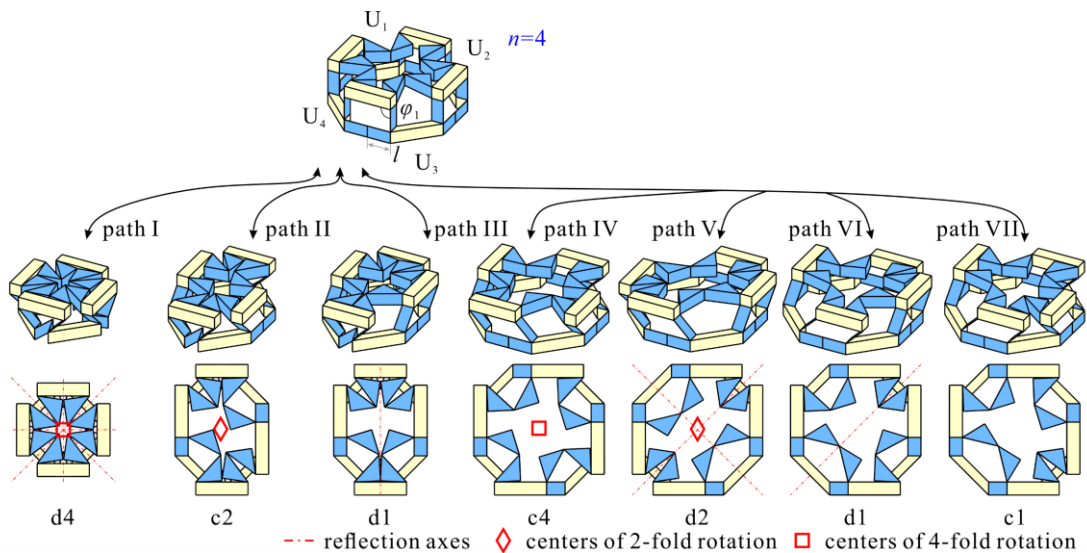


Fig. 4-7 Reconfiguration of the origami module with $n = 4, \alpha = 90^\circ$ accompanied by tuneable symmetries. The key reflection axes are represented by centre lines, while the centres of 2-fold and 4-fold rotational symmetry are represented by rhombus and squares, respectively.

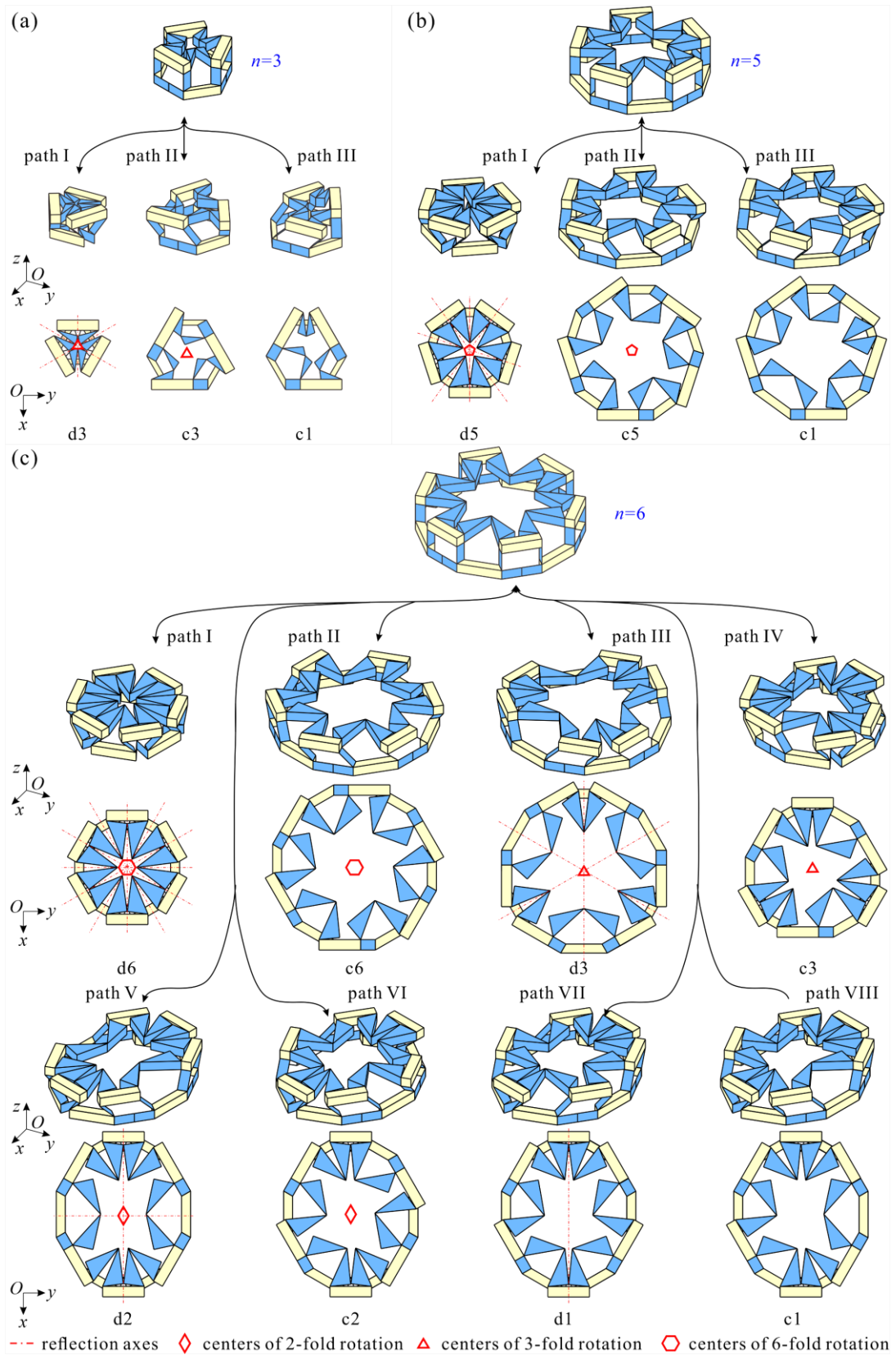


Fig. 4-8 Reconfiguration of the origami modules with $n=3, 5,$ and 6 accompanied by tuneable symmetries.

In general, varying the design parameters α , and then arranging $n = 2\pi/\alpha$ modular origami units into a circular array around the z -axis allows us to obtain 2D geometric objects with arbitrary dn or cn point groups. Meanwhile, the crystallographic restriction theorem restricts the value of n can only be 1, 2, 3, 4, and 6 for both symmetry families. Therefore, only two single DOF modules with $n=4$ and $n=6$ are sufficient to construct ten 2D crystallographic point groups, i.e., $d1$, $d2$, $d3$, $d4$, $d6$, $c1$, $c2$, $c3$, $c4$, $c6$. The findings are validated by fabricating and testing centimeter-scale prototypes of the modules as shown in Fig. 4-9. These examples prove that the dimensions and symmetry of the module can be tuned by manually applying a force, and all ten 2D crystallographic point groups predicted by analysis can be easily realized because of a single DOF with powerful bifurcation capability.

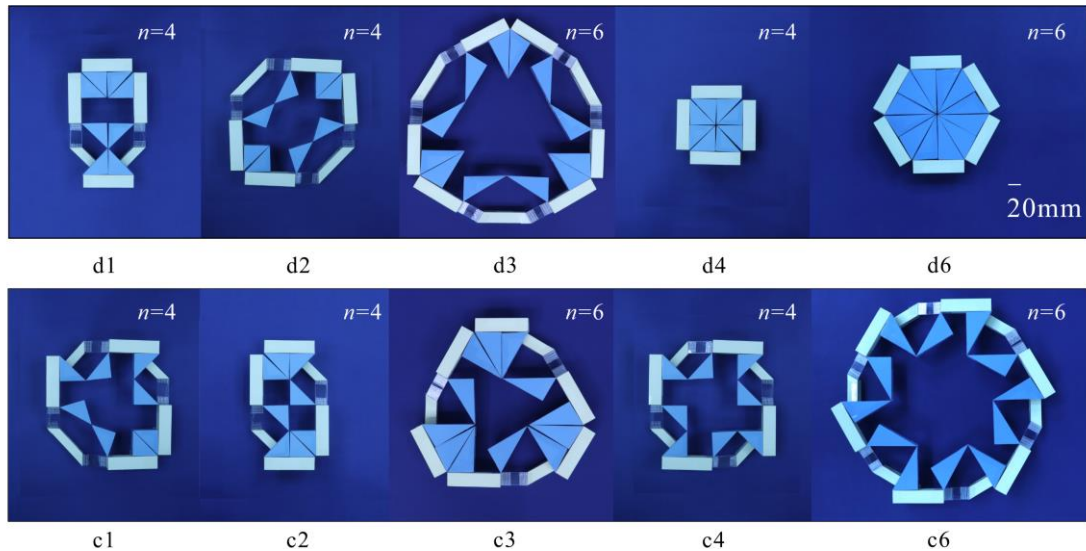


Fig. 4-9 Prototypes with ten 2D crystallographic point groups, i.e., $d1$, $d2$, $d3$, $d4$, $d6$, $c1$, $c2$, $c3$, $c4$, $c6$, constructed from only two modules with $n=4$ and $n=6$.

4.3.2 Tunability in Seven Frieze Groups

From a single module, attention is now shifted to its periodic border, or frieze pattern generated by repeating in one direction since these 2D line groups are related to tessellations^[174]. In mathematics, there are only seven different symmetry groups of frieze patterns, called frieze groups, also known as 2D line groups, i.e., $p111$, $p1a1$, $pm11$, $p1m1$, $p112$, $pma2$, $pmm2$. A guide to recognizing these frieze groups is provided in Tab. 4-1^[180].

Tab. 4-1 Guide to recognizing frieze groups^[180].

Has perpendicular reflections?					
Yes; Has horizontal reflection axis?			No; Has horizontal reflection axis or glide reflection?		
Yes: pmm2	No; Has 2-fold rotation?		Yes; Has horizontal reflection axis?		No; Has 2-fold rotation?
	Yes: pma2	No: pm11	Yes: pm11	No: p1m1	Yes: p112

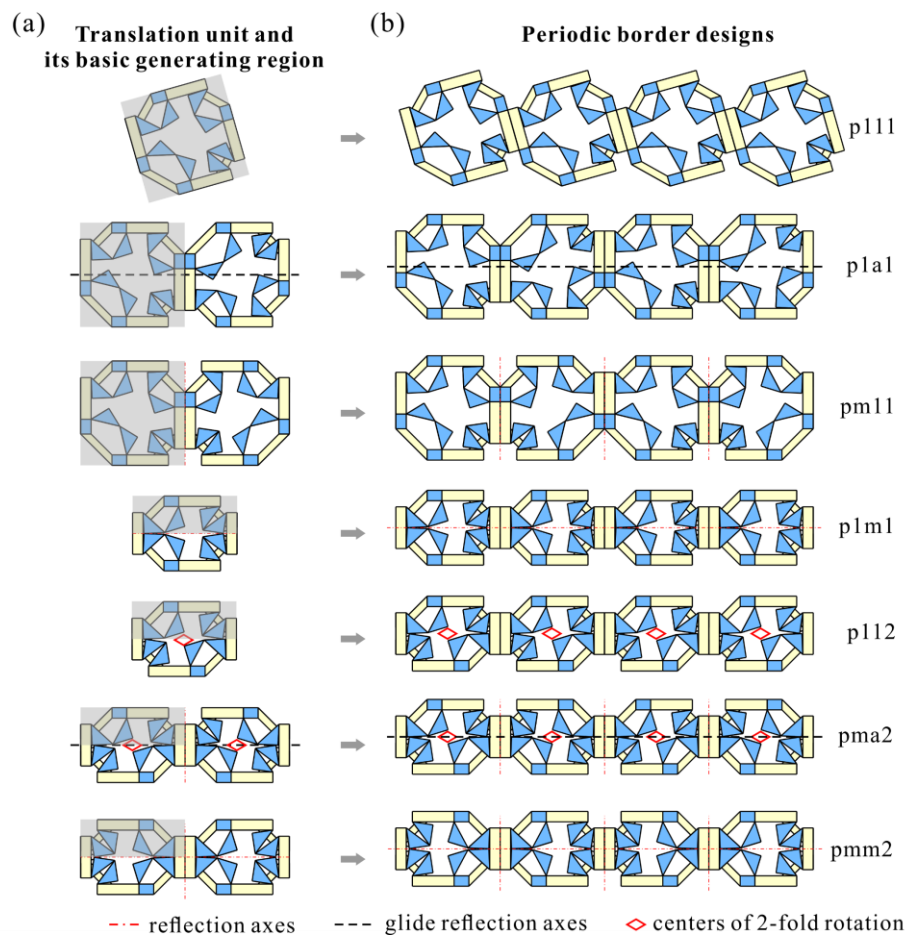


Fig. 4-10 All seven frieze patterns constructed by the modules with $n = 4$, $\alpha = 90^\circ$. (a) Translation unit and its basic generating region (grey area); (b) periodic border designs.

Here, all seven distinct symmetry groups have been achieved with just a linear tessellation of modules with $n=4$, as shown in Fig. 4-10(a) and (b), whose DOFs are equal to the number of modules. Specifically, let's focus on the frieze pattern with line

group $p111$, which is created by repeatedly applying a translation to an asymmetric module with point group $c1$. Then, the symmetry becomes $p1a1$ if the arrangement of modules is reconstructed by applying glide reflection and translation on the asymmetric module with the point group $c1$, or it turns to $pm11$ by continuously reflecting the module with the point group $c1$ about reflection axes. Next, if all modules are reconstructed to the state with point group $d1$ or $c2$ and are in a translational arrangement, the linear tessellation has line groups $p1m1$ or $p112$. To construct the $pma2$ design, neighbouring modules with the point group $c2$ in the $p112$ design need to be reconstructed into mutually chiral configurations (180° rotational symmetry). Finally, the $pmm2$ design is generated by reconstructing neighbouring modules with point group $d1$ in the $p1m1$ design into mirror configurations. It's important to note that all seven frieze patterns are generated by the same number of modules in the same connection (merging rectangular panels), and the difference between these designs lies in the states of bifurcation configurations. Thus, any unique pattern can be reconstructed into other six cases with different line groups.

4.3.3 Tunability in Seventeen Wallpaper Groups

Consider a geometric object that is regularly repeated by translation in two non-parallel directions. It turns out that any infinitely repeating 2D pattern falls into one of seventeen classes based on its symmetries, including translation, rotation, reflection, and glide reflection, known as plane symmetry groups, planar crystallographic groups, or wallpaper groups. A guide for recognizing wallpaper groups is shown in Tab. 4-2^[181].

On one hand, 1- or 2-fold wallpaper groups can be constructed by directly applying symmetry operations to the seven frieze patterns described above, as shown in Fig. 4-11(a). For example, $p1$, pg , or pm are obtained by filling the plane with copies of a frieze pattern $p111$, $p1a1$, or $pm11$ placed directly above/below each other in an ordered fashion. Additionally, a $p2$ wallpaper group can be obtained if the frieze pattern $p112$ is stacked in a shifted manner. Furthermore, wallpaper groups cm , pmm , or cmm are obtained by continuous reflection of frieze patterns $p1a1$, $pmm2$, or $pma2$, respectively. Note that pgg and pmg wallpaper patterns result from the glide reflection of the $p1a1$ and $p1m1$ frieze patterns, respectively. Moreover, motifs with lower symmetry using combinatorial operations or directly with motifs with higher symmetry are expected to realize 4-fold wallpaper patterns. For example, a $p4g$ wallpaper group can be

constructed by rotating the module with a $d1$ point group (path VI in Fig. 4-7) four times and then applying bi-directional translations. Directly repeating modules with point groups $d4$ or $c4$ in both directions construct the $p4m$ or $p4$ wallpaper group.

Tab. 4-2 Guide to recognizing wallpaper groups^[181].

Rotation	Has reflection?			
	Yes		No	
none	Has glide axis off mirrors?		Has glide reflection?	
	Yes: cm	No: pm	Yes: pg	No: $p1$
2-fold	Has perpendicular reflections?		Has glide reflection?	
	Yes; Has rotation centre off mirrors?		No: pmg	Yes: pgg
	Yes: cmm	No: pmm		
3-fold	Has rotation centre off mirrors?		$p3$	
	Yes: $p31m$	No: $p3m1$		
4-fold	Has mirrors at 45° ?		$p4$	
	Yes: $p4m$	No: $p4g$		
6-fold	$p6m$		$p6$	

At this point, twelve out of the seventeen wallpaper groups with 1-fold, 2-fold, and 4-fold rotational symmetry have been successfully constructed using a module with $n=4$. As depicted in Fig. 4-11(a), the modules exhibit consistent connections across different wallpaper groups. Consequently, it becomes feasible to realize these twelve symmetry groups through a single, unified structure. Yet it is impossible to construct the other five wallpaper designs using the module with $n=4$ since this would not induce 3-fold and 6-fold rotational symmetry, and thus turning to modules 6 (Fig. 4-11(b)). Fig. 4-11(b) shows examples of constructing such 5 wallpaper groups with modules for $n=6$. The beehive structure is formed with 6 identical modules in a circle around the center module by merging rectangular panels. Depending on whether the center module has point group $c3$, $d3$, $c6$, or $d6$, the obtained beehive structure belongs to the wallpaper groups $p3$, $p3m1$, $p6$ or, $p6m$. Note that the $p31m$ wallpaper group is constructed a little differently in that the center module has $d6$ symmetry and surrounding it are six modules with $c3$ symmetry, and neighbouring $d3$ modules are mirror images of each

other, with the axis passing through the center of d6 modules. Similarly, the modules are connected in the same way in these five wallpaper groups, so that they can be realized in a single structure. Overall, only two sets of structures with $n=4$ and $n=6$, are sufficient to realize seventeen 2D space groups.

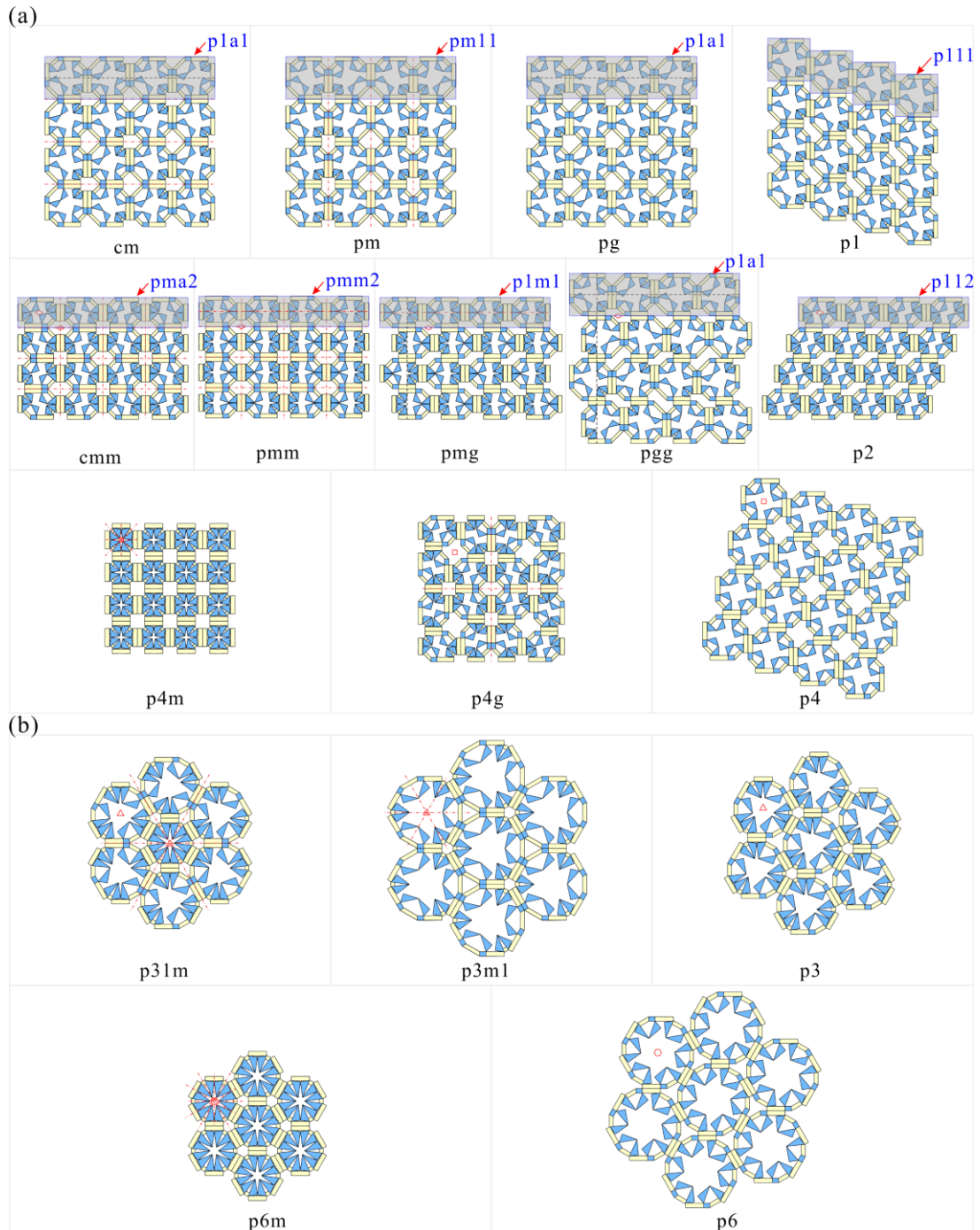


Fig. 4-11 Seventeen wallpaper patterns constructed by the modules with $n=4$ and 6. (a) Twelve wallpaper groups with 1-fold, 2-fold, and 4-fold rotational symmetry; (b) five wallpaper groups with 3-fold and 6-fold rotational symmetry.

It is worth noting that the two tessellations, the former of which has two DOFs and the latter of which has one DOF (See Appendix E for detailed proof).

4.3.4 Methods of Active Symmetry Tuning

4.3.4.1 Mechanical Load Plus Variable Stiffness Materials

In the following investigation, an exploration of a simple mechanical load control mechanism aimed at tuning symmetry is undertaken. A control mechanism involving a simple mechanical load and variable stiffness beams made of thermal-responsive materials is first investigated. As shown in Fig. 4-12(a), the beam is composed of a type of commonly used polymers, polylactic acid (PLA, thickness, 1mm), and a Polyimide (PI) film heater (thickness, 0.1mm). At room temperature ($T = 25^{\circ}\text{C}$), the PLA beam has a Young's modulus of about 2.34 GPa and can work as a rigid beam ("0" state). However, when the temperature increases to 90°C due to PI electrothermal film, Young's modulus of PLA drops sharply below 5MPa and the beam turns to a flexible state ("1" state). Moreover, after cooling to room temperature with the help of the clamp, PLA can be fully recovered to a high Young's modulus state and used again as a flat and rigid beam. Next, eight thin sheets connecting the two platforms in the origami module are replaced with the proposed variable stiffness beams, labelled as A-H, each with an independently controlled PI film heater, as shown in Fig. 4-12(b). Note that to avoid unpredictable kinematic paths of the module at the bifurcation point, the design parameters of the module are carefully modified so that φ_1 cannot reach $\pi/2$, i.e., set $b/a \leq \cos(\alpha/2)$ or $l/a < 1$. Taking the origami module in Fig. 4-12(b) as an example ($n=4, \alpha=90^{\circ}$, $b/a=3\sqrt{2}/4$, and $l/a=3/4$), $\varphi_1 < \pi/2$ throughout the folding process due to $l/a < 1$. Therefore, the unit is not able to switch from M1 to M2. However, one can actively manipulate the stiffness of certain beams to produce a phenomenon similar to the shape on the bifurcation path when the module is compressed from its initial configuration (fully unfolded configuration). Specifically, as shown in Fig. 4-12(c) left and right, if beam F is in a rigid state "0" (flexible state "1") and beam E is in a flexible state "1" (rigid state "0"), beam F(E) rotates rigidly while beam E(F) undergoes a bending deformation under uniaxial compression load. At the same time, the trapezoidal panels of the lower platform do not move while the rectangular panels of the upper platform swing towards the rigid beam (red arrows). In contrast, if beams E and F attached to the two side lines of a rectangular panel are in a

high stiffness state, both beams are generating rotations without deformation, while the two trapezoidal panels are close to each other under mechanical loading, as shown in Fig. 4-12(c) middle.

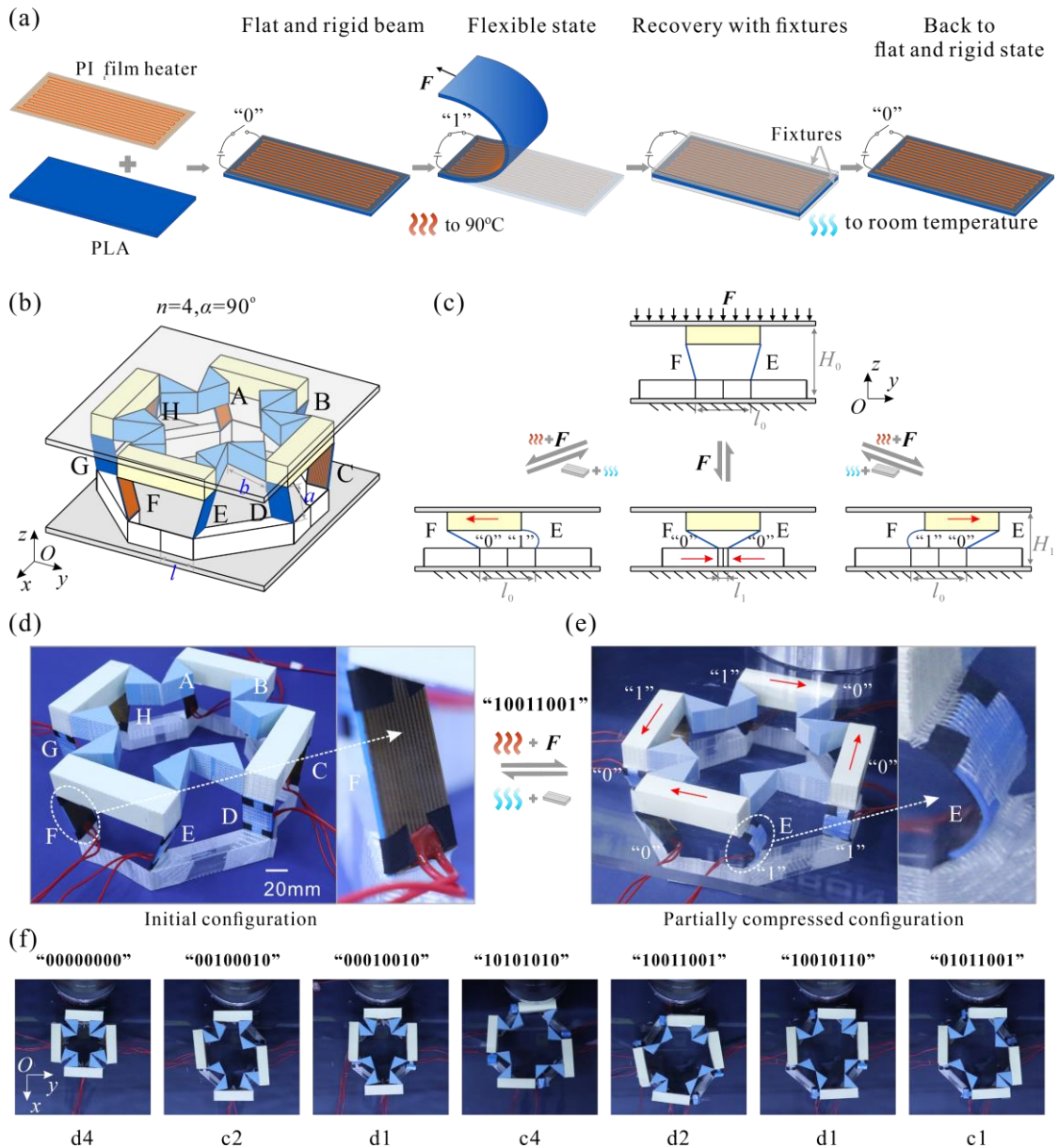


Fig. 4-12 Active symmetry tuning by mechanical loading with variable stiffness materials. (a) A PLA sheet with thickness=1mm and a PI film heater with thickness=0.2mm are bound together; (b) origami module with eight variable stiffness beams; (c) deformation mechanisms of a pair of neighbouring beams E and F. (d) The prototype with $n = 4, \alpha = 90^\circ$, and $b/a = 1, l = 3a/4$. (e) Example of tuning the module from d4 symmetry to partially compressed d2 configuration with beams coded “10011001”. (f) Experimental results with d4, c2, d1, c4, d2, d1, and c1 symmetries.

As a result, one can actively encode the stiffness of the beams in some symmetrical way so that the module takes on a shape with that symmetry when compressed. As shown in Fig. 4-12(d-f), specimens were compressed by a vertical testing machine (Instron 5982) with a transparent fixture (37mm displacement and a 0.5 mm s⁻¹ loading rate). The deformation process was recorded with the camera mounted above. If all eight beams A-H in the module are in a rigid state “00000000”, the module is compressed as a deployable mechanism under uniaxial compressive loading from its initial state to a smaller square, preserving d4 symmetry. If one chooses to energize the films (about 30s) on the four beams A, D, E, and H so that the beams are stiffened in state “10011001”, the d4 symmetry tunes to d2 symmetry under compression (Fig. 4-12(e)). To enable the module to be tuned to other symmetries, clamps are used during the cooling of the beams (about 10 mins), and then they are recovered to their initial configuration before the stiffness of the beam is recorded. In summary, upon compression, these rectangular panels apply a moment to the beams, rotating rigid ones (“0” state) and bending flexible ones (“1” state) and forcing the module to change their shape as well as symmetries. When the stiffnesses of the beams in the prototype are coded as “00000000”, “00100010”, “00010010”, “10101010”, “10011001”, “10010110”, and “01011001”, the module displayed shapes with d4, c2, d1, c4, d2, d1, and c1 point groups respectively under uniaxial compression load with transparent fixture (Fig. 4-12(f)).

4.3.4.2 Pneumatic Actuation

Moving beyond mechanical load and variable stiffness beams, a more responsive solution is explored, utilizing air pockets to tune the symmetry of the module and its tessellation. As shown in Fig. 4-13(a), eight inflatable pockets labeled as A-H are arranged on both sides of the four hinges of a single module ($n = 4, \alpha = 90^\circ, b/a \leq \sqrt{2}$, and $l/a = 1$). Upon pressurization, these pockets apply a moment to the hinges, opening them and forcing the origami modules to change their shape. It was found that there are a total of three relative orientations for two neighboring triangular panels in a 7R unit for all possible configurations for modules with $n=4$, i.e., $\varphi_6 = 0, \varphi_6 = 90^\circ, \varphi_6 = 180^\circ$. As shown in Fig. 4-13(b), inflating air pocket B alone leads to the $\varphi_6 = 90^\circ$ configuration, while inflating air pocket A alone results in the $\varphi_6 = 180^\circ$ configuration.

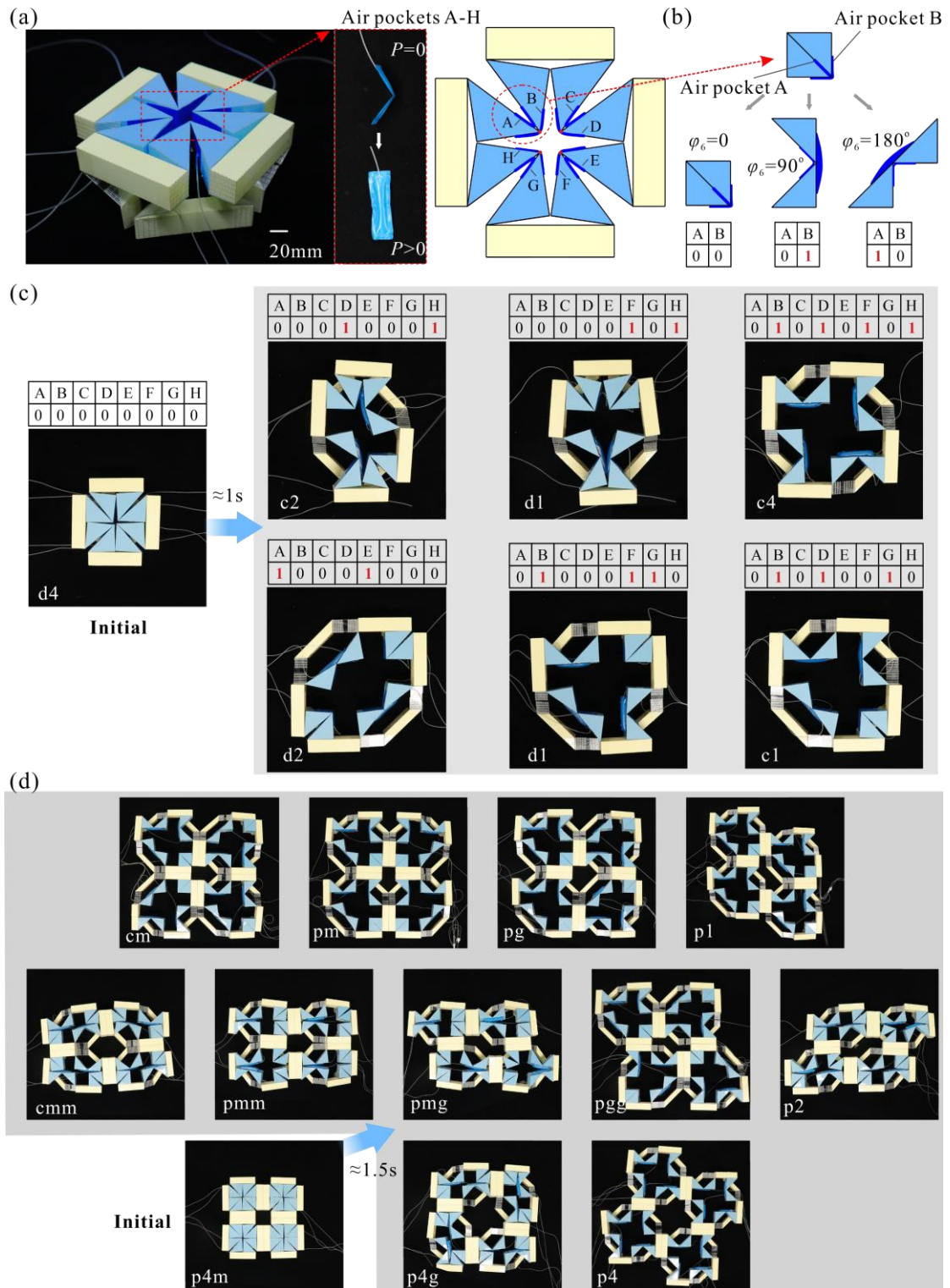


Fig. 4-13 Pneumatic actuation. (a) Prototype for pneumatic actuation; (b) mechanism of pneumatic actuation; (c) experimental results with $d4$, $c2$, $d1$, $c4$, $d2$, $d1$, and $c1$ symmetries where air pockets in the prototype are coded as “0000000”, “00010001”, “00000101”, “01010101”, “10001000”, “01000110”, and “01010010”; (d) twelve configurations featuring distinct symmetry groups of a single 2×2 tessellation.

As a result, by strategically pressurizing specific air pockets, various configurations with desired symmetry groups can be achieved within seconds (Fig. 4-13(c)). For instance, fully unfolded configurations in paths II, III, and V with c_2 , d_1 , or d_2 point groups can be attained from the d_4 state (“0000000”) in approximately 1 second, with only two air pockets (D and H, F and H, or A and E) being pressurized (“00010001”, “00000101”, “10001000”). Moreover, fully unfolded configurations in path IV with c_4 point groups can be reached from the d_4 state by pressurizing four air pockets (B, D, E, and H, i.e., “01010101”). Similarly, fully unfolded configurations in paths VI and VII with d_1 and c_1 point groups can be achieved from the d_4 state by pressurizing three air pockets (B, F, and G, or B, D, and G, i.e., “01000110”, and “01010010”). Having demonstrated that the shape of the origami module can be controlled by pressurizing embedded air pockets, this approach is now extended to the 2×2 tessellation. As depicted in Fig. 4-13(d), 8, 12, or 16 air pockets are strategically positioned on either side of the hinge used to connect the triangular panels, thereby achieving any one of 12 configurations with in 1.5s corresponding to the twelve wallpaper groups in Fig. 4-11(a) through the pressurization of the air pockets. It is noteworthy that constant actuation is not necessary to maintain these configurations with distinct symmetry groups, indicating low energy consumption. Additionally, this method does not require precise control of the angle to achieve the desired configuration and avoids the disadvantage of the low accuracy of the pneumatic actuation.

4.4 Modular Origami Tuneable in All Signs of Poisson’s Ratio

4.4.1 2D Modules Design and Deformation Mechanism Analysis

In section 4.3, the 7R linkage in the form of modular origami was used to construct reconfigurable modules in the form of back-to-back assembly. In this section, the second type of reconfigurable modules is to be constructed in the form of shoulder-to-shoulder assembly of this 7R unit. The structure and geometry of these basic units are illustrated in Fig. 4-14(a). The only modification from the original structure is the replacement of trapezoidal panels with octagonal panels featuring alternating side lengths of $2a\cos(\alpha/2)$ and t_1 . Importantly, this alteration does not impact the relationship between φ_1 - φ_7 since either the trapezoidal panels or the octagonal panels are just alternative forms of the same link. Subsequently, four 2D modules with a single DOF are constructed by arranging n identical basic units around a vertical axis in the

form of shoulder-to-shoulder assembly, as illustrated in Fig. 4-14(b), where the angle α in components satisfies

$$\alpha = (n-2)\pi/n, \quad n = 3, 4, 5, 6. \quad (4-6)$$

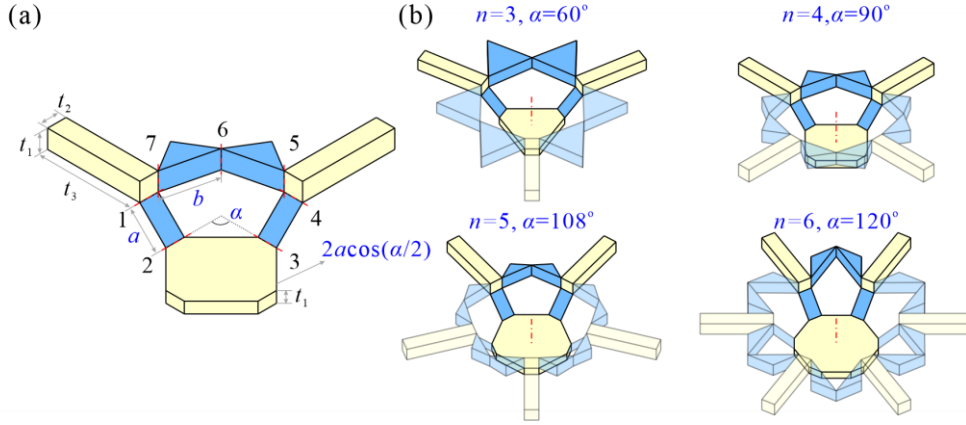


Fig. 4-14 Reconfigurable modules constructed in the form of shoulder-to-shoulder assembly. (a) modified 7R unit; (b) 2D modules with different numbers and design parameters of 7R units.

It has been revealed in section 4.2 that when the unit is reconfigured between the M1 and M2 branches, it undergoes substantial geometric alterations. Without loss of generality, let $b/a = \cos(\alpha/2)$, then the 7R linkage in the form of modular origami in all four 2D modules are equipped to reconfigure between M1 and M2 paths. Consequently, when the modules reach the bifurcation configuration with dihedral angles $\varphi_1 = 90^\circ$, each rectangular panel in these 2D modules can independently choose to swing toward or away from the centre of the polygon prism base. Namely, the 2D module with $\alpha = (n-2)\pi/n$ can be classified into 2^n cases, depending on the number and location of the basic units observed in either case I or case II. For a 2D module featuring a regular 4-sided polygon projection, there are always two rectangular panels with independent swing directions along the x or y direction. Therefore, it is worth highlighting that the 2D modules with $n=4$ exhibit three possible states along either the x or y direction: (i) two rectangular panels positioned close to the polygon prism base, (ii) one rectangular panel positioned close to the polygon prism base while the other is away from it, or (iii) both rectangular panels positioned away from the polygon prism base. Such orthogonal decoupling behaviour leads to three possible variations in either

the overall width (W) or the breadth (B) dimensions of the 2D module with $n=4$, which can be calculated

$$\begin{aligned} W_1(B_1) &= -2a\cos\varphi_1 + 2t_3 + 2a + t_2 \\ W_2(B_2) &= 2t_3 + 2a + t_2 \\ W_3(B_3) &= 2a\cos\varphi_1 + 2t_3 + 2a + t_2 \end{aligned} \quad (4-7)$$

where $\varphi_1 \in [0, \pi/2]$.

To further illustrate this concept, an example of the variation in normalized width (W/t) with respect to the dihedral angle is presented φ_1 , as depicted in Fig. 4-15. When two rectangular panels are positioned near the base of the prism (“-1” state), the rotation of the thin sheet results in an increased normalized width (W/t). Conversely, when one rectangular panel is positioned near the polygon prism base while the other is located farther away (“0” state), the overall size of W/t remains constant. In the case where both rectangular panels are positioned away from the polygon prism base (“1” state), the rotation of the thin sheet leads to a decreased normalized width (W/t). In general, the normalized width (W/t) in the x direction is likely to exhibit an increase, remain constant, or decrease with an increasing dihedral angle. Similarly, these three possibilities also apply to the normalized breadth (B/t) in the y direction.

For the 2D module with $n=4$, 2^4 cases are exactly the combination of these three types of dimensional variations in the W and B directions. As shown in Fig. 4-16, they are further subdivided into four distinct kinematic paths that share a common bifurcation point at $\varphi_1 = 90^\circ$, considering the similarity in orthogonal directions. Obviously, in paths I-IV, the reconstructed module undergoes significant alterations in its external dimensions, which are highlighted by red dotted lines.

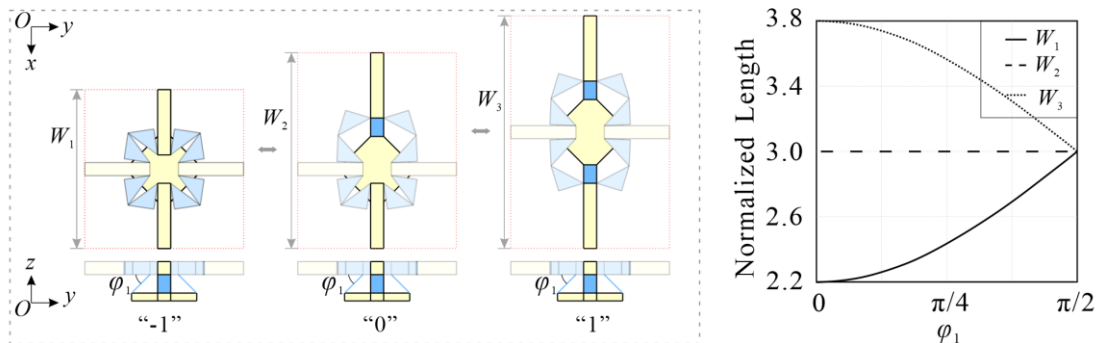


Fig. 4-15 Three possible states for two rectangular panels along either the x or y direction and corresponding variations in the overall dimensions of the 2D module with $n=4$.

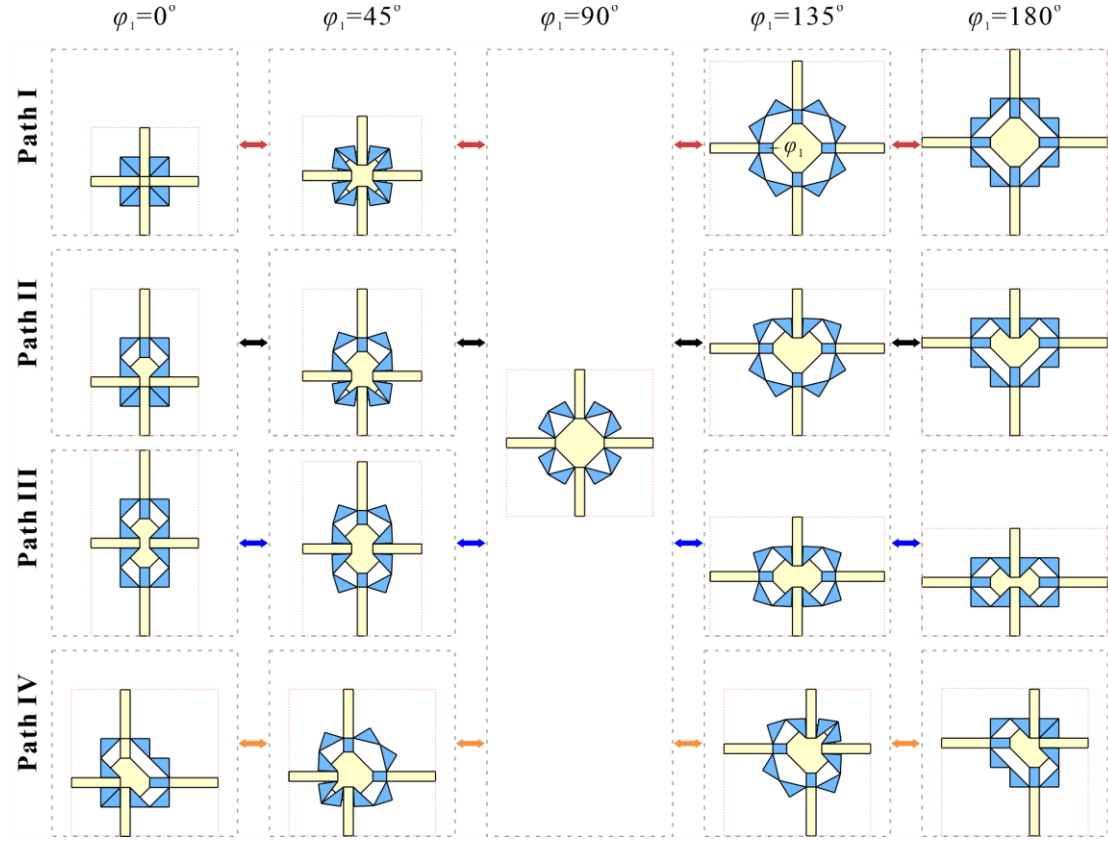


Fig. 4-16 Top views of kinematic paths of the 2D module featuring a regular 4-sided polygon projection when the 7R unit switches between M1 and M2.

The deformation due to the mechanism motion of the modules can be effectively characterized by Poisson's ratio calculated by dividing that lateral strain by the negative of the longitudinal strain

$$\nu_{BW} = -\frac{\varepsilon_W}{\varepsilon_B}, \quad \nu_{HB} = -\frac{\varepsilon_B}{\varepsilon_H} \quad (4-8)$$

where ε_W , ε_B , and ε_H are infinitesimal strains in the x , y , and z directions, respectively, which are given in terms of the module dimensions by

$$\varepsilon_W = \frac{dW}{W}, \quad \varepsilon_B = \frac{dB}{B}, \quad \varepsilon_H = \frac{dH}{H} \quad (4-9)$$

where dW , dB , and dH are an incrementally small changes in the module dimensions W , B , and H due to the applied load. To demonstrate the variation in external dimensions during reconfiguration, a prototype of the 2D module with $b/a = \sqrt{2}$, $\alpha = 90^\circ$ is fabricated, as shown in Fig. 4-17. When the 2D module enters the four paths in Fig. 4-17 from the bifurcation point, it corresponds exactly to the four deformation modes.

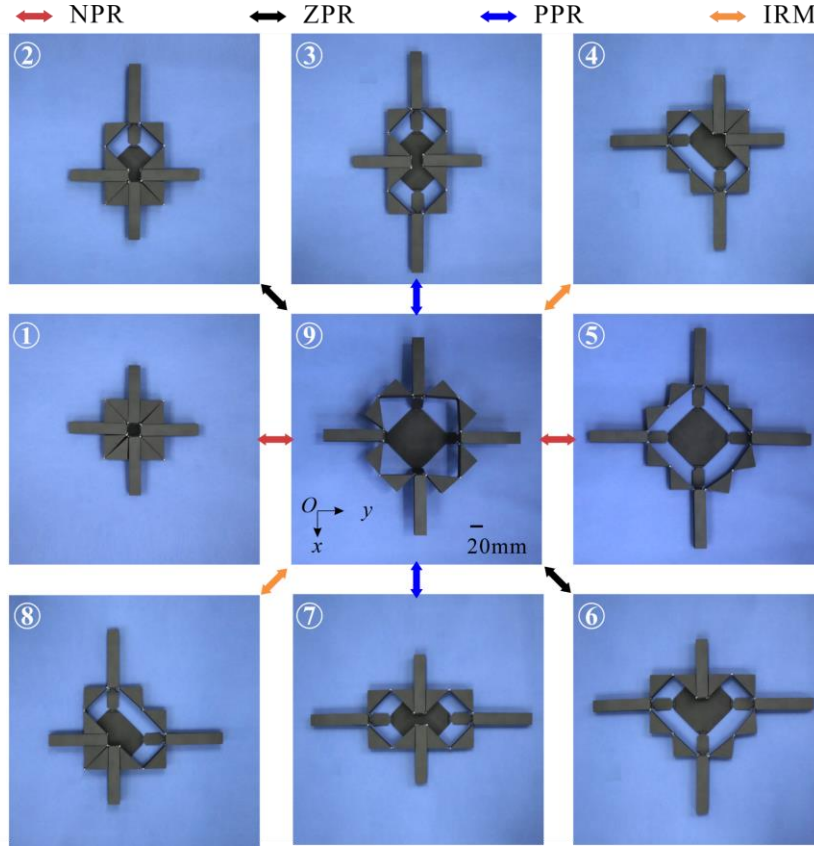


Fig. 4-17 Prototype of the 2D module with $b/a = \sqrt{2}$, $\alpha = 90^\circ$ and its reconfiguration between four kinematic paths

It can be observed that the module in path I is contracted from a larger square at the bifurcation point (configuration ⑨) towards $\varphi_1 = 0^\circ$ to its smallest size (configuration ①) or the module is expanded towards $\varphi_1 = 180^\circ$ to its biggest size (configuration ⑤). Throughout this deformation, infinitesimal strains ε_B and ε_W remain equal negative or positive values ($\varepsilon_W = \varepsilon_B < 0$ or $\varepsilon_W = \varepsilon_B > 0$ as shown in Fig. 4-18(a) and (e)). Consequently, the in-plane Poisson's ratios ν_{BW} were strain-independent and always equal to -1, indicative of an NPR mode. If the module chooses path II at the bifurcation point, there will be a contraction (⑨→②) or expansion (⑨→⑥) of the module in the B direction but no deformation in the W direction. In this case, $\varepsilon_W = 0, \varepsilon_B < 0$, as shown in Fig. 4-18(b) or $\varepsilon_W = 0, \varepsilon_B > 0$, as shown in Fig. 4-18(f), and $\nu_{BW} = 0$, demonstrating a ZPR mode. When the module bifurcates to path III, it will contract transversely while expand vertically (⑨→③, $\varepsilon_W < 0, \varepsilon_B > 0, \nu_{BW} > 0$ as shown in Fig. 4-18(c)), or vice versa (⑨→⑦, $\varepsilon_W > 0, \varepsilon_B < 0, \nu_{BW} > 0$ as shown in Fig. 4-18(g)), akin to conventional PPR mode. Notably, when the module bifurcating to path

IV, this deformation mode does not alter the global dimensions of the module ($\textcircled{9} \rightarrow \textcircled{4}$ or $\textcircled{8}$), as shown in Fig. 4-18(d) and (h)), resulting only in internal rearrangements (IRM).

Similarly, as shown in Appendix E, if the 7R unit is operating in motion mode M3, there are four distinct kinematic paths can be identified based on the number of pairs and positions of nested-in triangular prisms. In contrast, the modules in the reconfiguration process do not change significantly in their external dimensions. Therefore, subsequent discussion will focus mainly on the case of bifurcation between M1 and M2.

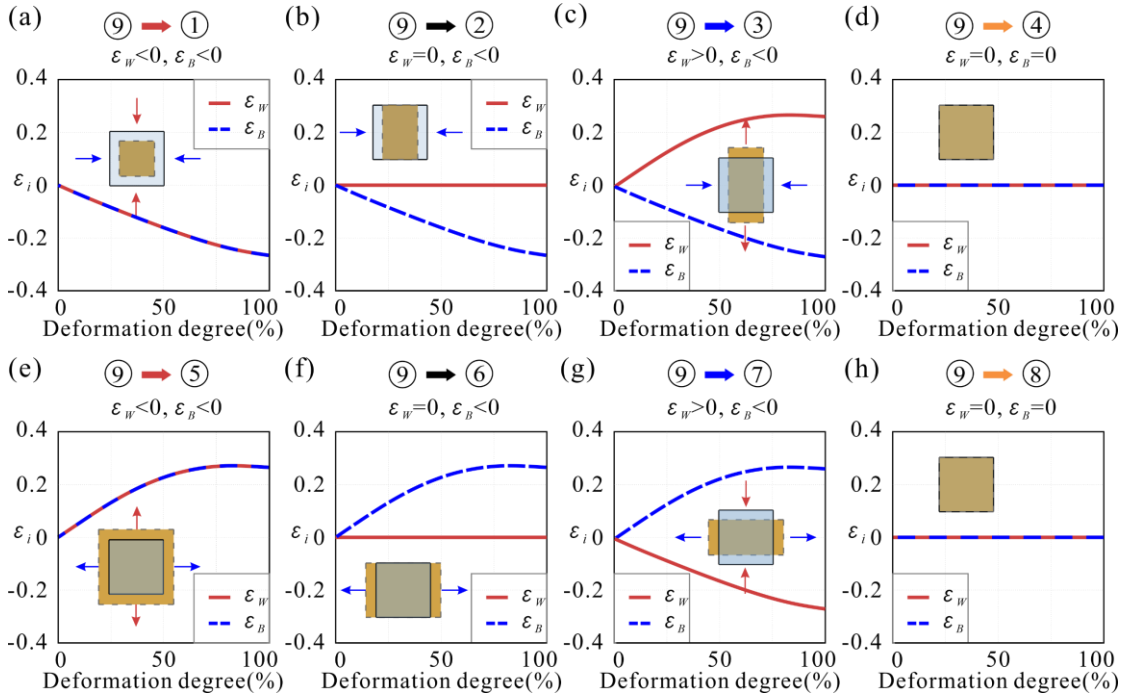


Fig. 4-18 Plots of ε_w and ε_B vs deformation degree in kinematic paths for the modules.

4.4.2 3D Modules Design and Deformation Mechanism Analysis

Moreover, as depicted in Fig. 4-19, a variety of 3D modules are formed by integrating the aforementioned 2D modules in the form of shoulder-to-shoulder assembly onto faces of four carefully selected polyhedrons for the sake of simplicity and ease of scalability, i.e., triangular prism ($N=3$), rectangular prism ($N=4$), pentagonal prism ($N=5$), and hexagonal prism ($N=6$). These selected prisms solid are characterized by N -sided polygons on two end faces and N rectangles on lateral faces. Within this arrangement, the 2D module embedded on end faces exhibits a projection of an n -sided polygon, with the number of its basic units represented by $n_c = N$.

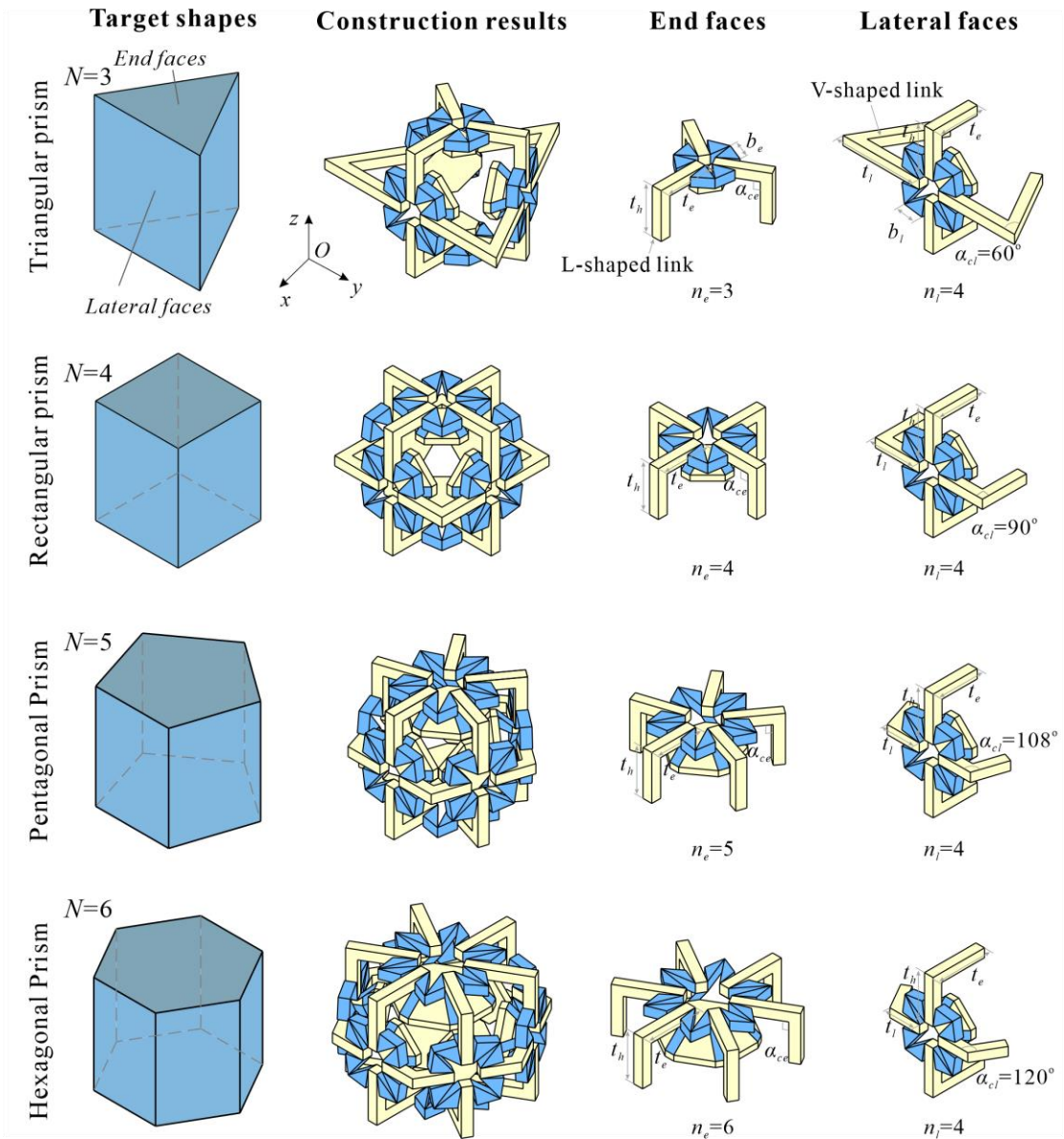


Fig. 4-19 Construction of 3D modules based on four selected polyhedrons, i.e., triangular prism ($N=3$), rectangular prism ($N=4$), pentagonal prism ($N=5$) and hexagonal prism ($N=6$).

Conversely, the 2D modules attached to the lateral faces are always rectangular and consist of $n_l = 4$ basic units. Furthermore, the 2D modules on adjacent lateral faces are interconnected by a shared V-shaped link, characterized by $\alpha_{cl} = (N-2)\pi/N$, which has evolved from the rectangular prisms in the basic unit. On the other hand, neighbouring 2D modules on end faces and lateral faces are connected by means of shared L-shaped links ($\alpha_{ce} = 90^\circ$). Meanwhile, the geometry of the basic units on the end and lateral faces are defined as

$$a_e = a_l \tan(\alpha_{cl} / 2), \quad t_e = t_l \tan(\alpha_{cl} / 2) \quad (4-10)$$

in which the subscripts e or l indicate that the parameter pertains to a module on the end face or lateral face.

When analysing the 3D modules shown in Fig. 4-20, which function as mechanisms with one DOF, there are two essential kinematic compatibility conditions. Firstly, the dimensions of the n 2D modules located on the lateral faces must be identical in the z direction. Secondly, the projections of the 2D modules on end faces and lateral faces should share the same external contour in the xoy plane. The latter condition can be mathematically expressed as

$$|PQ|^2 + |PN|^2 = |MQ|^2 + |MN|^2 \quad (4-11)$$

where these four lines labelled as PQ, PN, MQ, and MN in Fig. 4-20 consist of two segments, each with lengths t and $a \pm a \sin \varphi_l$.

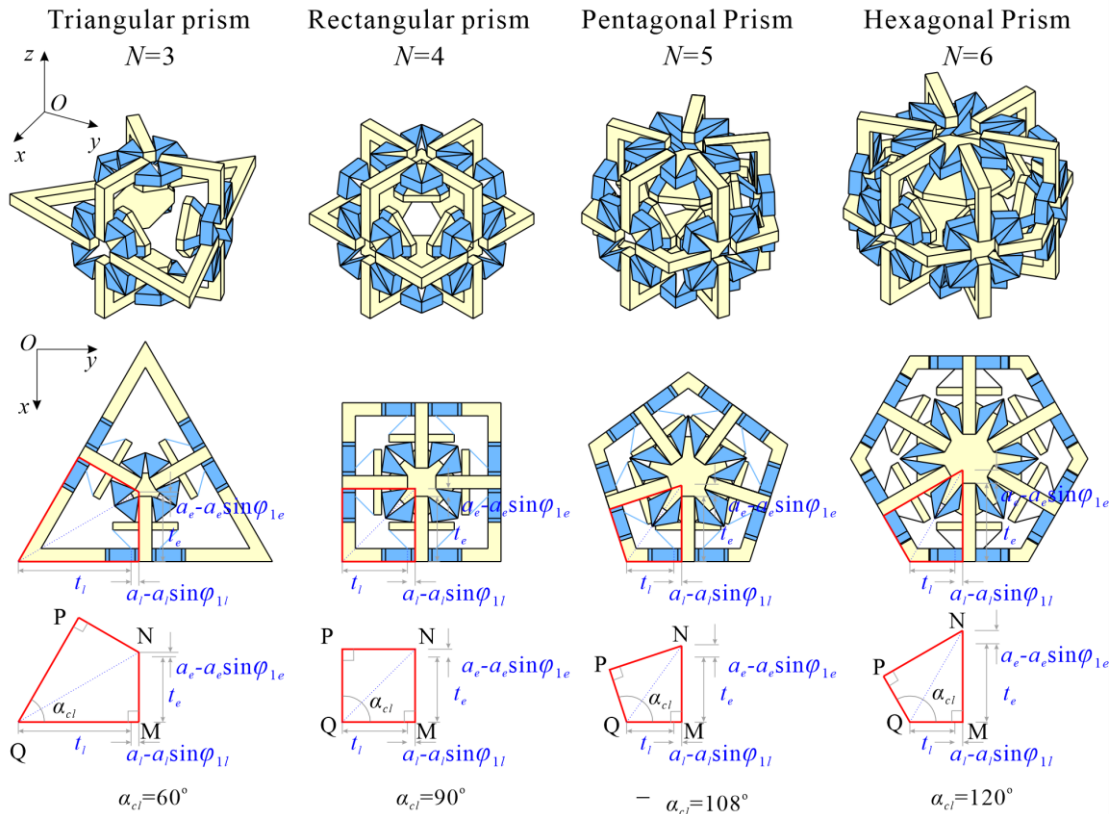


Fig. 4-20 Kinematic compatibility conditions for 3D modules.

Additionally, the sign in $a \pm a \sin \varphi_l$ is negative when the V-shaped or L-shaped links swing towards the centre of the polygon prism base, while the sign is positive otherwise. Therefore, Eq. (4-11) can be rewritten as

$$(t_l + a_l \pm a_l \sin \varphi_{l1})^2 + (t_e + a_e \pm a_e \sin \varphi_{le})^2 = (t_l + a_l \pm a_l \sin \varphi_{l1})^2 + (t_e + a_e \pm a_e \sin \varphi_{le})^2 \quad (4-12)$$

By combining Eq. (4-10) and Eq. (4-12), the second kinematic compatibility condition can be deduced, which necessitates the 2D module on the end faces of 3D modules ($N=3, 5, 6$) to maintain an N -fold symmetry (simultaneous contraction or expansion in the overall dimensions in xoy plane). As aforementioned, the 2D module with $n_l = 4$ exhibits three types of dimensional variations along the z direction, i.e., increase, remain constant, or decrease in the H direction. As a result, there exist NPR, ZPR, and PPR deformation modes in the $yo z$ plane, respectively, for 3D modules with triangular, pentagonal, and hexagonal prism contours, respectively, as shown in Fig. 4-21.

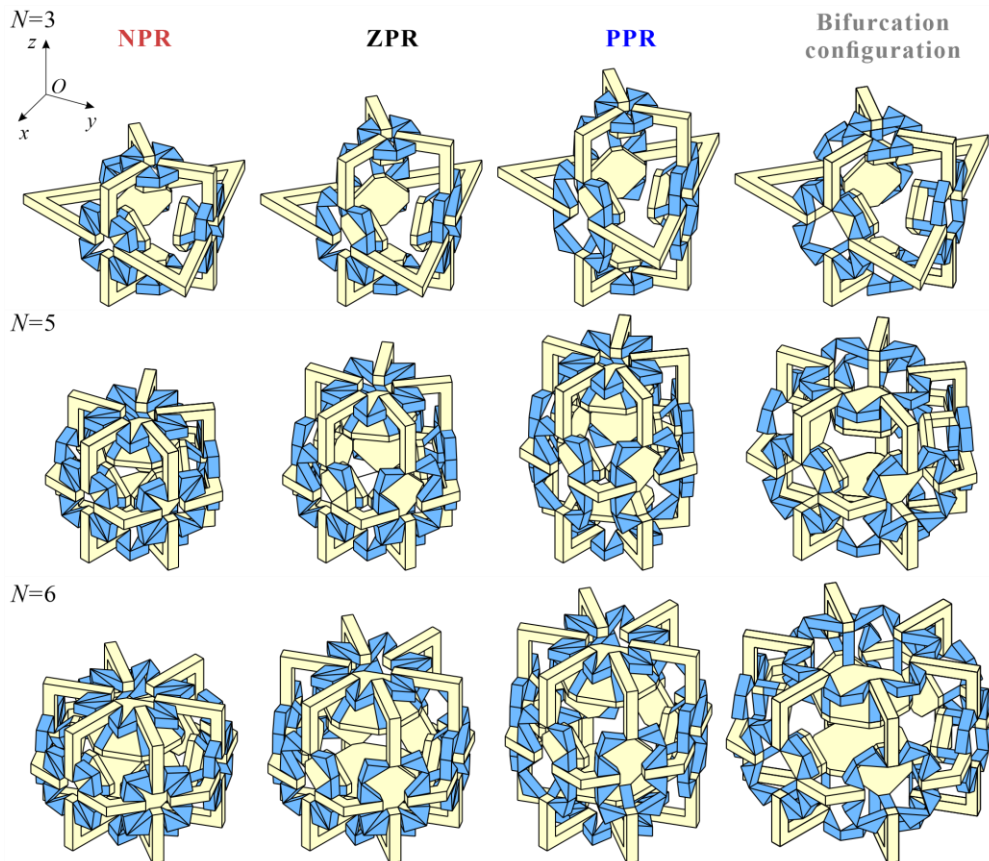


Fig. 4-21 Deformation modes for 3D modules with triangular prism ($N=3$), rectangular prism ($N=4$), pentagonal prism ($N=5$) and hexagonal prism ($N=6$).

For the 3D module with a rectangular prism ($N=4$) contour, there are $a_l = a_e$ and $t_l = t_e$ according to Eq.(4-10). Therefore, Eq. (4-11) can be simplified as

$$|PQ| = |MQ|, \quad |PN| = |MN| \quad (4-13)$$

Equation (4-13) shows that there is also orthogonal decoupling behaviour of the 3D module in the x and y directions. Thus, there exist a total of $3^3 = 27$ cases of 3D modules that are combinations of three states of the relative positions of the two links (denoted as “-1”, “0”, and “1” as shown in Fig. 4-22(a)) in the x , y , z directions, as shown in Appendix F. The marker next to configurations, $C_{(x,y,z)}$, $x, y, z = -1, 0, \text{ and } 1$, indicates that rectangular panels in the x, y, z directions are positioned in “-1”, “0”, and “1” states. Among these 27 cases, a consistent configuration is observed at the bifurcation point when the angle φ_1 of the 2D modules on the three orthogonal planes equals 90° . Due to their similarity in three orthogonal directions, these 27 cases can be further divided into 6 different states, one of whose configurations is displayed in Fig. 4-22(b).

The deformation mechanism of the 3D module with $N=4$ is divided into six modes (Fig. 4-23) when it is reconfigured between different states which are characterized by in-plane Poisson's ratio ν_{BW} and out-of-plane Poisson's ratios ν_{WH} . First, the 3D module in mode I is contracted from a larger cube to the smallest size when the 2D modules on three orthogonal planes shrink simultaneously from the bifurcation point ($\varepsilon_W = \varepsilon_B = \varepsilon_H < 0$). Hence, Poisson's functions are given by $\nu_{BW} = \nu_{WH} = -1$. Then, if the rectangular panel in the yoz plane along the z direction is reconstructed to a state where one is far from the centre of the polygon prism base and the other is close to the centre of the polygon prism base, it is observed the deformation along the z direction is zero ($\varepsilon_W = \varepsilon_B < 0, \varepsilon_H = 0$), so the Poisson's ratio ν_{WH} becomes zero (mode II) while ν_{BW} remains -1. Next, in mode III, rectangular panels in the yoz plane along the z direction all in a state far from the centre of the polygon prism base, both the strain ε_H and Poisson's ratio ν_{WH} of the module turns to be positive ($\varepsilon_W = \varepsilon_B < 0, \varepsilon_H > 0$), and ν_{BW} is -1, the same as mode I and II. After that, one of the rectangular panels in the xoy plane along the y direction is reconstructed to a state away from the centre of the polygon prism base (mode IV); three strains are negative, zero and positive and values respectively ($\varepsilon_W < 0, \varepsilon_B = 0, \varepsilon_H > 0$). Furthermore, if one of the rectangular panels in the xoy plane along the y direction is reconstructed to a state away from the center of

the polygon prism base (mode V), the global dimensions in the xoy plane have not changed despite the internal rearrangement, so $\varepsilon_W = \varepsilon_B < 0$, $\varepsilon_H > 0$ two of strains will switches to zero ($\varepsilon_W = 0$, $\varepsilon_B = 0$). As a result, the module degenerates into a one-dimensional material that is stretched in the z direction ($\varepsilon_H > 0$). Finally, one of the two rectangular panels in mode V on the $yozy$ plane is reconstructed away from the polygon prism base back to a state close to the polygon prism base. The 3D module in mode VI is undergoing internal rearrangement in three orthogonal planes, but its global dimensions, B, W, H , remain constant ($\varepsilon_W = 0$, $\varepsilon_B = 0$, $\varepsilon_H = 0$).

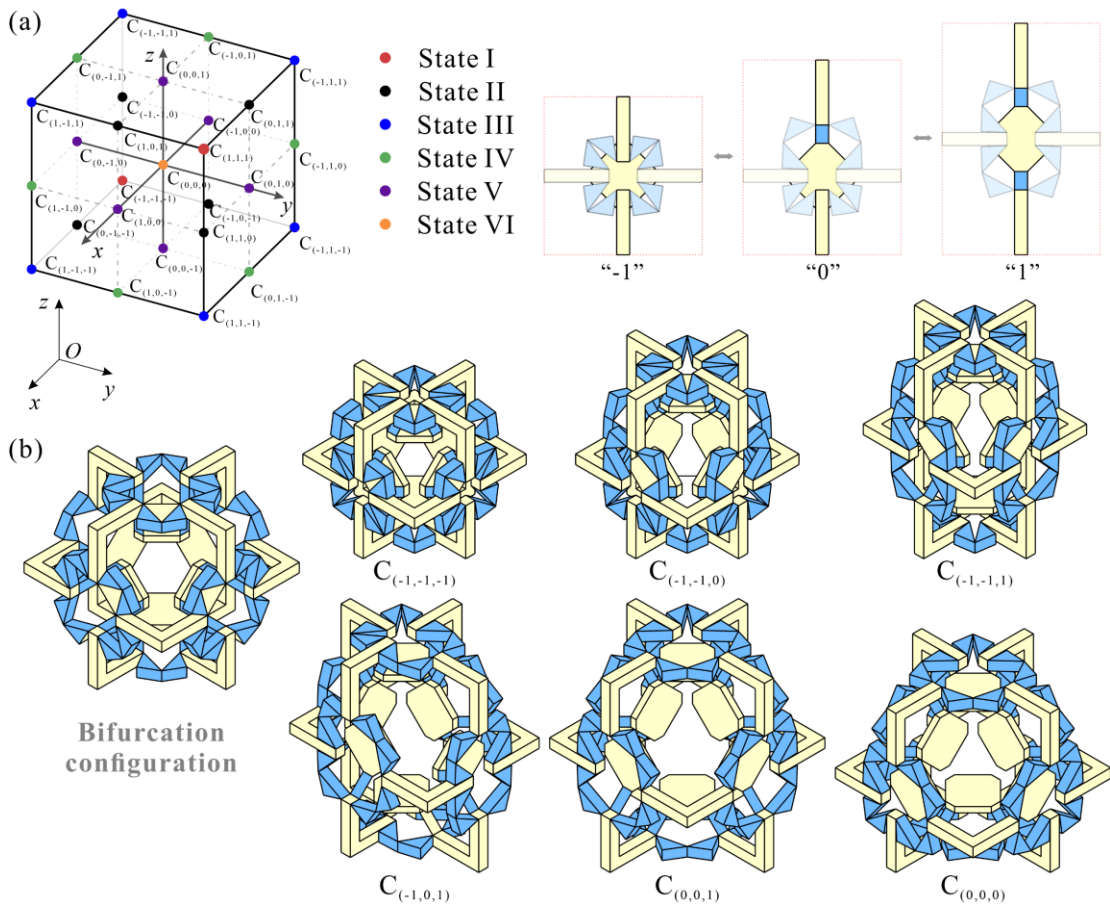
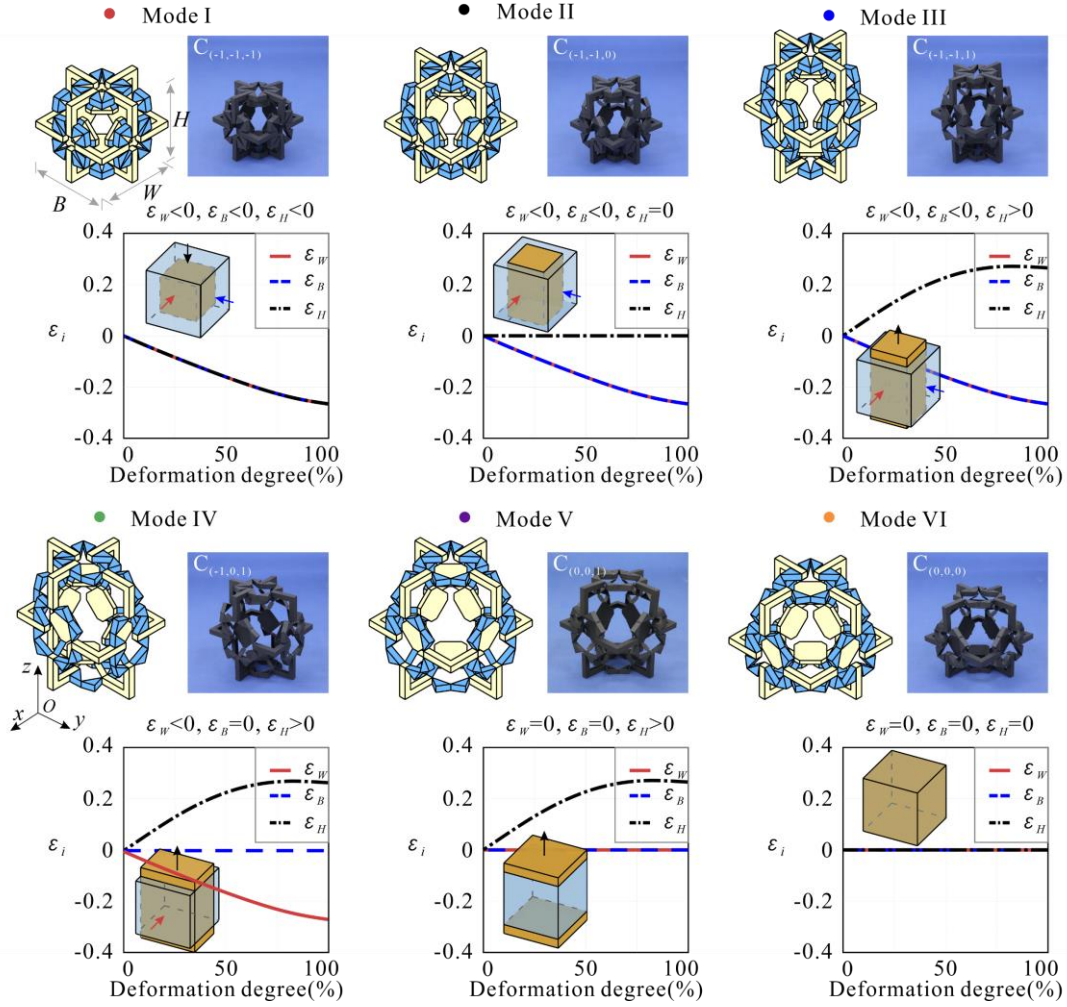


Fig. 4-22 Configurations for the 3D module with $N=4$. (a) The configuration of the 3D module ($N=4$) is a combination of three states of the relative positions of the two L-shaped links in three directions. (b) Six typical configurations.


 Fig. 4-23 Deformation modes for 3D modules with rectangular prism ($N=4$) contour.

4.5 Conclusions

In this chapter, the use of the kinematic bifurcation behaviour inherent to a single DOF spatial 7R linkage was proposed for the design of a reconfigurable modular origami. A comprehensive kinematic analysis was conducted on the modular origami unit first, particularly focusing on the effects of geometric parameters on the number, range, and evolution of the motion branches.

Subsequently, these units can be assembled back-to-back into various single DOF modules with folded n -polygon and unfolded $2n$ polygon shapes. It was demonstrated experimentally that the shape and symmetry of such origami modules can be actively tuned and controlled in a completely predictable manner by strategically activating variable stiffness beams or air pockets. The investigation revealed that it has the potential to realize all three class of discrete symmetry groups, including ten point

groups, seven line groups, and seventeen space groups, within a unified design framework. Notably, due to the rich configurations arising from the bifurcation, two modules, i.e., $n=4$ and $n=6$ modules, are sufficient to realize ten crystallographic point groups. The linear tessellation of $n=4$ modules is sufficient to realize seven line groups by manipulating the reconfiguration of modules within tessellations. Meanwhile, the planar tessellation of modules with $n=4$ and $n=6$ can realize all seventeen space groups.

Lastly, a shoulder-to-shoulder assembly scheme of 7R units is also proposed to construct single DOF reconfigurable 2D modules. In addition, the geometric dimensional variations induced by the reconfiguration between different configurations are investigated based on the kinematic model, and the effect on the sign of Poisson's ratio is theoretically analysed. Furthermore, a variety of single DOF 3D modules are formed by integrating the aforementioned 2D modules on the faces of four carefully selected polyhedrons for simplicity and ease of scalability, i.e. triangular prism ($N=3$), rectangular prism ($N=4$), pentagonal prism ($N=5$) and hexagonal prism ($N=6$). Theoretical analysis suggests that the proposed 3D modules can achieve either purely negative, zero or positive Poisson's ratios due to orthogonal decoupling behaviour arising from kinematic bifurcation. Among them, the 3D module with a rectangular prism ($N=4$) contour is tuneable in all signs of in-plane and out-plane Poisson's ratio.

Due to length constraints, this chapter focuses on the reconstruction-induced changes in properties such as Poisson's ratio and symmetry, and the structure presented in this chapter also has the potential for tuneable dynamic properties. An example of bistability using the origami module is presented in Appendix H.

Chapter 5 3D Programmable Metamaterials Based on Reconfigurable Polyhedron Module

5.1 Introduction

Highly overconstrained polyhedron mechanisms with multiple loops in a polyhedral layout have more regular shapes and simpler networking than single-loop linkage, which are expected to be directly used as modules for constructing modular origami-based 3D metamaterials. However, due to the complex topology, single DOF polyhedron mechanisms with reconfigurability have rarely been reported. In chapter 4, the construction of single DOF reconfigurable polyhedral mechanisms by embedding single DOF reconfigurable 2D modules into the surface of the polyhedrons was presented. The investigation in this chapter delves into the kinematics of the Wohlhart cube^[182], a single DOF geometric construct derived from embedding the planar linkage groups (PLGs) with multiple DOFs onto the surface of the polyhedron.

On the other hand, the shape-reconfigurable system through structural instability or structural deformation has also been identified as an effective method to realize tunability and programmability in mechanical metamaterials. However, in most of the current research, the unit cells in the metamaterial tessellation are of one type with identical deformation properties, which leads to the fact that the resultant metamaterials' characteristics are limited to a small range during the flexible deformation, making it suitable only for a task with specific functional requirements. A new way to design programmable metamaterials is paved through the kinematic bifurcation of reconfigurable polyhedron modules in this chapter.

The layout of this chapter is as follows. In section 5.2, the bifurcation behaviour of a single DOF Wohlhart cube is revealed by the kinematic model of an open-chain PLG under symmetric constraints. The changes in properties, including geometry dimensions, Poisson's ratio, chirality, and stiffness, induced by the reconfiguration of a single module between distinct paths are analysed in section 5.3. Furthermore, to enhance the programmability of metamaterials, a combinatorial design strategy, i.e., stacking different bifurcation configurations in 3D space, is proposed in section 5.4. In section 5.5, reconfigurable polyhedron modules are extended from the Wohlhart cube to a series of single DOF reconfigurable regular prisms. Final conclusions are drawn in section 5.6.

5.2 Kinematics of the Polyhedron Module

5.2.1 Geometry of Wohlhart Cube

The mechanical basis of the module with the Wohlhart cube is depicted in Fig. 5-1. First, the planar link group (PLG) is constructed with four identical rigid links of sides a and b attached to the square centre body (side length $a \times a \times b$) through revolute (R) joints. The folding angle α determines the configuration of PLG by keeping rigid links rotationally symmetric and rotating about the centre O clockwise or anti-clockwise. Second, six identical clockwise rotation PLGs lying on faces of regular hexahedron are interconnected by R joints on the edges of cube connectors (side length b) to form a Wohlhart cube, which is a highly overconstrained system with only one DOF working as an expandable cube. The focus here is on its reconfigurability.

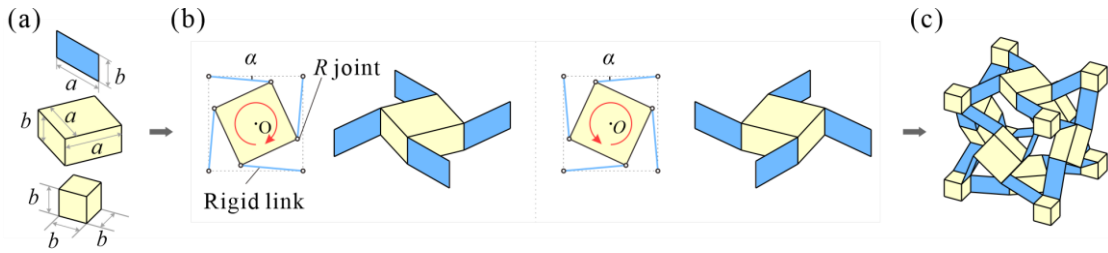


Fig. 5-1 The Wohlhart cube formed by connecting PLGs with cube connectors. (a) The geometry of rigid link, square centre body, and cube connector; (b) views of the clockwise rotation PLG and the anti-clockwise rotation PLG; (c) overview of the Wohlhart cube.

5.2.2 Reconfigurability of PLG in the Wohlhart Cube

A coordinate system for any PLG in the Wohlhart cube is set up, as shown in Fig. 5-2. Because A, B, C, D are coplanar points on the edge of cube connectors, $AB, BC, CD,$ and DA are straight lines. Besides, $\angle ABC, \angle BCD, \angle CDA$ and $\angle DAB$ are right angles. So, points $A, B, C,$ and D form a rectangle. The origin O of the coordinate system is in the centre of the rectangle $ABCD$, the x axis is parallel to AB , and the y axis is parallel to BC . Angles $\angle AEH, \angle BFE, \angle CGF, \angle DHG$ and $\angle AOE$ are indicated as $\theta_1, \theta_2, \theta_3, \theta_4,$ and δ , respectively. The coordinate of the centre of the rectangle $EFGH$ is (u, v) . Then, the coordinates of points $A, B, C,$ and D always satisfy

$$\begin{aligned} x_A &= x_D, x_B = x_C, y_A = y_B, y_C = y_D \\ x_A &= -x_B, x_C = -x_D, y_A = -y_D, y_B = -y_C \end{aligned} \quad (5-1)$$

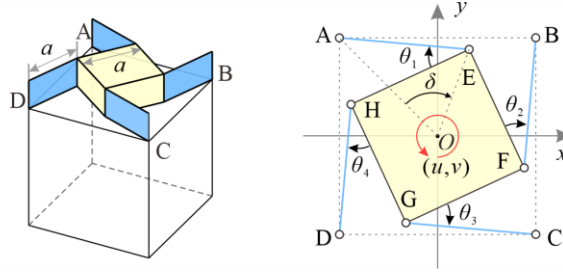


Fig. 5-2 The coordinate systems of PLG.

Equation (5-1) can be written as

$$\begin{aligned}
 \cos(\delta + \theta_4) + \sin(\delta + \theta_1) - \sin \delta &= 0 \\
 \cos(\delta + \theta_2) + \sin(\delta + \theta_3) - \sin \delta &= 0 \\
 \cos(\delta + \theta_1) + \sin(\delta + \theta_2) - \sin \delta &= 0 \\
 \cos(\delta + \theta_3) + \sin(\delta + \theta_4) - \sin \delta &= 0 \\
 2u - a \cos(\delta + \theta_2) - a \sin(\delta + \theta_1) + a \sin \delta &= 0 \\
 2u + a \cos(\delta + \theta_4) + a \sin(\delta + \theta_3) - a \sin \delta &= 0 \\
 2v - a \cos(\delta + \theta_1) - a \sin(\delta + \theta_4) + a \sin \delta &= 0 \\
 2v + a \cos(\delta + \theta_3) + a \sin(\delta + \theta_2) - a \sin \delta &= 0
 \end{aligned} \tag{5-2}$$

If the centre body rotates only, i.e., $u=0, v=0$,

$$\begin{aligned}
 \sin(\delta + \theta_1) - \sin(\delta + \theta_3) = 0, \cos(\delta + \theta_4) - \cos(\delta + \theta_2) = 0 \\
 \cos(\delta + \theta_1) - \cos(\delta + \theta_3) = 0, \sin(\delta + \theta_2) - \sin(\delta + \theta_4) = 0
 \end{aligned} \tag{5-3}$$

which can be simplified as

$$\begin{aligned}
 \sin\left(\frac{\theta_1 - \theta_3}{2}\right) \cos\left(\frac{2\delta + \theta_1 + \theta_3}{2}\right) = 0, \sin\left(\frac{\theta_2 - \theta_4}{2}\right) \sin\left(\frac{2\delta + \theta_2 + \theta_4}{2}\right) = 0 \\
 \sin\left(\frac{\theta_1 - \theta_3}{2}\right) \sin\left(\frac{2\delta + \theta_1 + \theta_3}{2}\right) = 0, \sin\left(\frac{\theta_2 - \theta_4}{2}\right) \cos\left(\frac{2\delta + \theta_2 + \theta_4}{2}\right) = 0
 \end{aligned} \tag{5-4}$$

Equation (5-4) yields

$$\theta_1 = \theta_3, \theta_2 = \theta_4 \tag{5-5}$$

Then, substituting Eq. (5-5) back into Eq. (5-2) result in

$$\sin\left(\frac{\theta_2 - \theta_1}{2}\right) \left(\cos\left(\frac{2\delta + \theta_2 + \theta_1}{2}\right) + \sin\left(\frac{2\delta + \theta_2 + \theta_1}{2}\right) \right) = 0 \tag{5-6}$$

There are two solutions according to Eq. (5-6), i.e.,

$$\theta_1 = \theta_2 \tag{5-7}$$

or

$$\frac{\theta_1 + \theta_2 + 2\delta}{2} = -\frac{\pi}{4} + n\pi, \quad n \in Z \quad (5-8)$$

When $\theta_1 = \theta_2 = \theta_3 = \theta_4$, according to Eq. (5-2), the relationship between θ_1 and δ is

$$\sin \delta = \sqrt{2} \sin\left(\theta_1 + \delta + \frac{\pi}{4}\right) \quad (5-9)$$

If substituting Eq. (5-8) into Eq. (5-6), then

$$\delta = 0, \quad \theta_1 + \theta_2 = -\frac{\pi}{2} + 2n\pi \quad (5-10)$$

If the centre body translates only, i.e., $\delta = 0$, Eq. (5-2) becomes

$$\begin{aligned} \theta_4 = -\theta_1 - \frac{\pi}{2} + 2n\pi \text{ or } \theta_4 = \theta_1 + \frac{\pi}{2} + 2n\pi, \quad \theta_2 = -\theta_3 - \frac{\pi}{2} + 2n\pi \text{ or } \theta_2 = \theta_3 + \frac{\pi}{2} + 2n\pi \\ \theta_1 = -\theta_2 - \frac{\pi}{2} + 2n\pi \text{ or } \theta_1 = \theta_2 + \frac{\pi}{2} + 2n\pi, \quad \theta_3 = -\theta_4 - \frac{\pi}{2} + 2n\pi \text{ or } \theta_3 = \theta_4 + \frac{\pi}{2} + 2n\pi \end{aligned} \quad (5-11)$$

and

$$\begin{aligned} \sin \theta_1 + \cos \theta_2 + \sin \theta_3 + \cos \theta_4 = 0, \quad \cos \theta_1 + \sin \theta_2 + \cos \theta_3 + \sin \theta_4 = 0 \\ \frac{\sin \theta_1 + \cos \theta_2}{\sin \theta_3 + \cos \theta_4} = -1, \quad \frac{\cos \theta_1 + \sin \theta_4}{\sin \theta_2 + \cos \theta_3} = -1 \end{aligned} \quad (5-12)$$

Only two of sixteen combinations in Eq. (5-11) satisfy Eq. (5-12), i.e.,

$$\begin{aligned} \theta_4 = -\theta_1 - \frac{\pi}{2} + 2n\pi, \quad \theta_2 = -\theta_3 - \frac{\pi}{2} + 2n\pi, \\ \theta_1 = \theta_2 + \frac{\pi}{2} + 2n\pi, \quad \theta_3 = \theta_4 + \frac{\pi}{2} + 2n\pi \end{aligned} \quad (5-13)$$

and

$$\begin{aligned} \theta_4 = \theta_1 + \frac{\pi}{2} + 2n\pi, \quad \theta_2 = \theta_3 + \frac{\pi}{2} + 2n\pi, \\ \theta_1 = -\theta_2 - \frac{\pi}{2} + 2n\pi, \quad \theta_3 = -\theta_4 - \frac{\pi}{2} + 2n\pi \end{aligned} \quad (5-14)$$

Combining Eq. (5-13), Eq. (5-2) can be further simplified as

$$u = a \sin \theta_1, \quad v = 0 \quad (5-15)$$

Combining Eq.(5-14), Eq. (5-2) can be further simplified as

$$u = 0, \quad v = a \cos \theta_1 \quad (5-16)$$

In summary, there are four sets of closure equations, i.e.,

case I: $u = 0, v = 0, \theta_1 = \theta_2 = \theta_3 = \theta_4$ and Eq. (5-9);

case II: $\delta = 0, u = 0, v = 0, \theta_1 + \theta_2 = -\frac{\pi}{2} + 2n\pi, \theta_1 = \theta_3, \theta_2 = \theta_4$;

case III: $\delta = 0, u = a \sin \theta_1, v = 0$ and Eq. (5-13);

case IV: $\delta = 0, u = 0, v = a \cos \theta_1$ and Eq.(5-14).

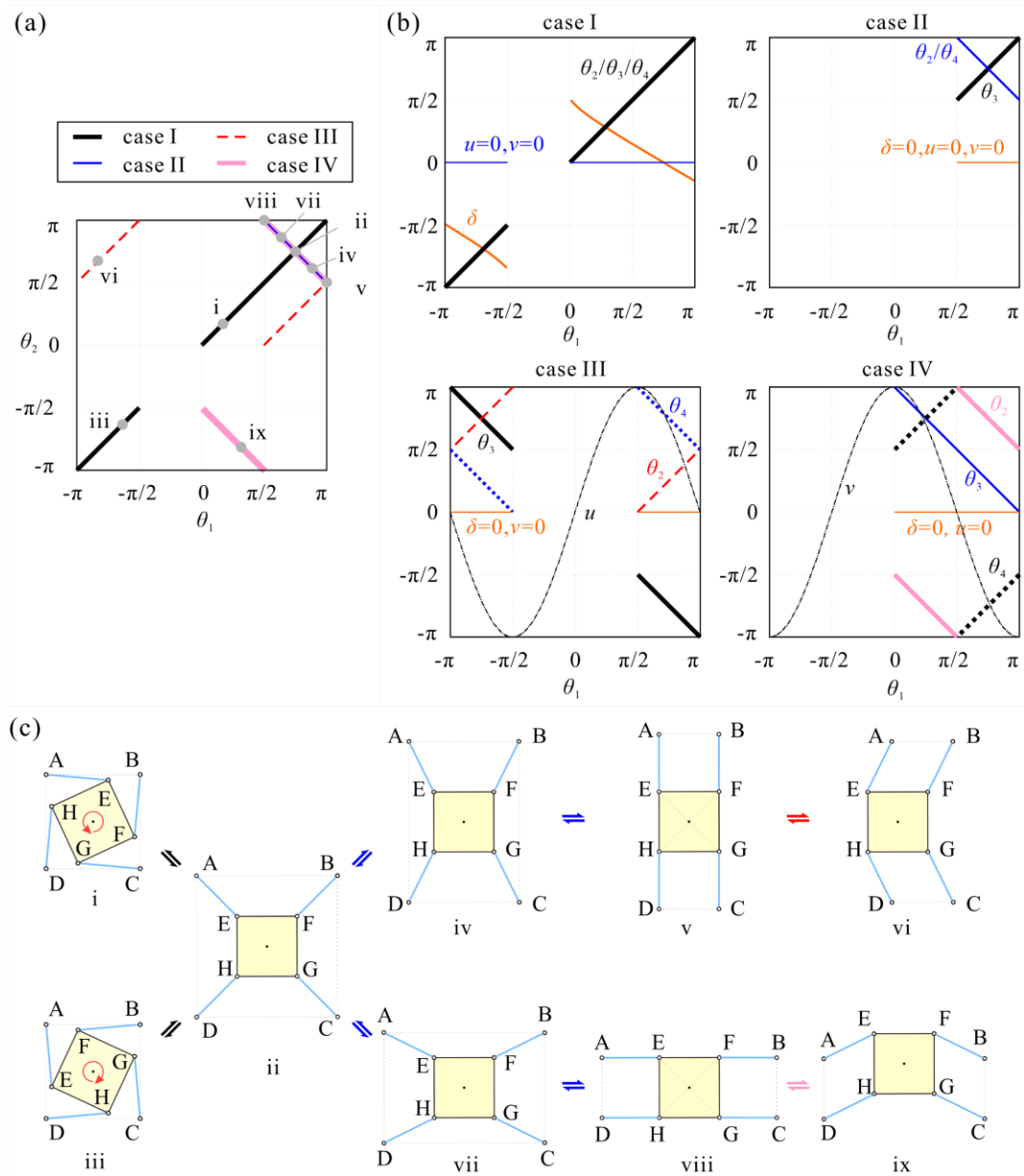


Fig. 5-3 The kinematic paths and corresponding configurations. (a) Kinematic paths θ_2 vs θ_1 , (b) kinematic paths θ_i vs θ_1 , and (c) bifurcation behaviours, where i, iii, iv, vi, vii, ix are motion sequences, while ii, v, and viii are the bifurcation configurations.

Kinematic paths θ_2 vs θ_1 and bifurcation behaviours of PLG in Wohlhart cube are illustrated in Fig. 5-3(a), while the kinematic paths θ_i vs θ_1 of the four cases are plotted in Fig. 5-3(b). Let the link length equal to π to present all variables results in one graph. If taking θ_1 as the input, the other variables in four cases are determined, which means that the PLG in all four cases is a one DOF system under symmetry constraints. The motion range is different in the four cases to avoid physical interference. Note that i, iii, iv, vi, vii, ix are motion sequences, while ii, v, and viii are the bifurcation configurations. It can be seen that i-ii-iii correspond to configurations of the linkage in case I, viii-vii-ii-iv-v correspond to configurations of the linkage in case II, vi-v correspond to configurations of the linkage in case III, and viii-ix correspond to configurations of the linkage in case IV. To distinguish their motion characteristics, configurations i and iii are named clockwise and anti-clockwise rotation PLGs, respectively. Configurations iv and vii are named translation PLG because the virtual platform (AB, BC, CD, DA) is translational relative to the centre body. Configurations vi and ix are named as locked PLGs as the distance of AB, CD in vi and AD, BC in ix remain a . In general, PLG can switch to rotation or translation through bifurcation point ii. It can also switch between translation PLG and locked PLG through bifurcation points v and viii.

5.2.3 Bifurcation Behaviours of the Polyhedron Module

Then the virtual-centre-based method^[102] are introduced, i.e., implanting PLGs into the polyhedron base's faces to construct the Wohlhart cube. As shown in Fig. 5-4(a), components (left) and polyhedron base (right) with its six faces are labelled as f_1 to f_6 and twelve edges are denoted by e_1 to e_{12} . The eight vertices are indicated as A, B, C, D, E, F, G and H. O_1 to O_6 are six face centres. As shown in Fig. 5-4(b), a clockwise rotation PLG is implanted in a manner that the bottom face of PLG is placed on square face f_1 with the centre located on the centre of ABCD. Then the ends of links are laid at four perpendiculars to face f_1 , i.e., e_5 , e_6 , e_7 , and e_8 , respectively. One can implant a rotation or translation PLG similarly into the face f_2 formed by DCGH and connect it with the previous PLG by cube connectors in the second step. The former causes the polyhedron base's contour to be a regular hexahedron, so the PLGs to be implanted on the remaining four square faces should be rotation units (Fig. 5-4(b), top). The latter causes the polyhedron base's contour to be a right square prism, so the rectangular face can only be a translation PLG, and the square faces can only be implanted with rotation PLG (Fig. 5-4(b), middle). In the second step, the implanted object on the face f_2 can

also be a locked PLG, with the result that the length of the CD is a (Fig. 5-4(b), bottom). Then, the polyhedron base's contour to be a locked right square prism with one side length is constant, and its rectangular faces can only be implanted with locked PLGs, while implanted rotation PLGs on the square faces are also locked in a fully folded configuration. Further, using the same procedure and integrating more PLGs into the polyhedron base, three configurations of the Wohlhart cube with different motion characteristics are constructed.

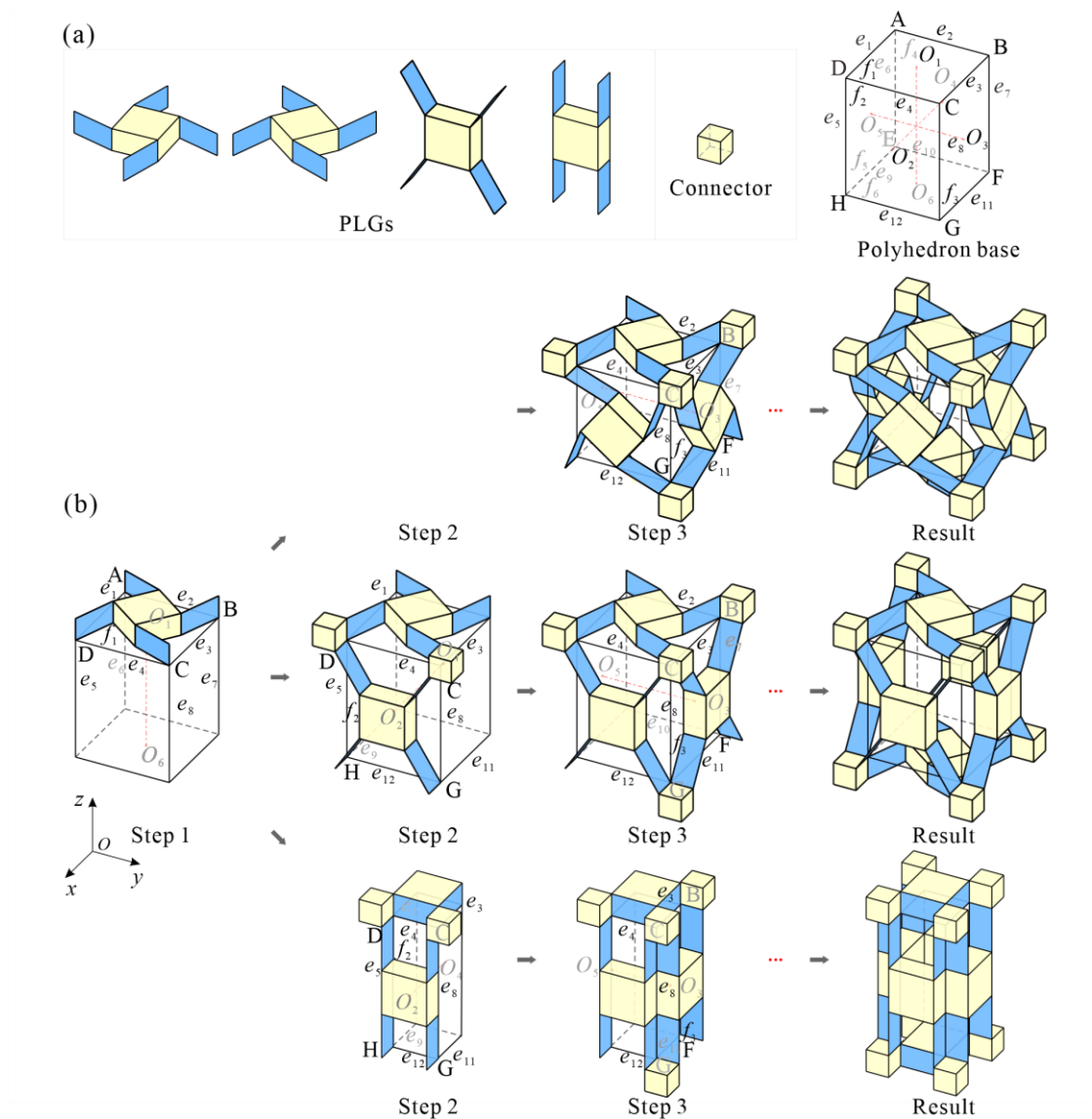


Fig. 5-4 The construction method of the Wohlhart cube. (a) Components and polyhedron base; (b) construction of the Wohlhart cube with rotation, translation, and locked PLGs.

The detailed analysis on the kinematic characteristics of the Wohlhart cube in Fig. 5-5(a) reveals that there are three distinct kinematic paths, i.e., expandable cube (EC) path, elongated prism (EP) path or locked twist (LT) path, and two bifurcation points between EC and EP paths, EP and LT paths. Considering whether the rotation direction of each rotation PLG is clockwise or anti-clockwise about coordinate axes, there are a total of 32 ($=2^6/2$, it is considered as one case when all the PLGs rotate in the opposition direction after passing B_0) cases for EC path, i.e., $EC_i^f-EC_i^p-B_0$, where the subscript i ($=1, \dots, 32$) represents the i -th path, and superscript f and p represent fully folded and partially folded configurations respectively. Meanwhile, the EP path is divided into three cases ($EP_x, EP_y,$ and EP_z) according to the orientation, and so is the LT path ($LT_x, LT_y,$ and LT_z). Configuration B_0 is one of the kinematic bifurcation points where this module can switch between EC and EP paths. Configurations $B_x, B_y,$ and B_z , the folded state of the module in the EP path as well as the unfolded state of the module in the LT path, are another type of bifurcation points, where the module can switch between EP and LT paths.

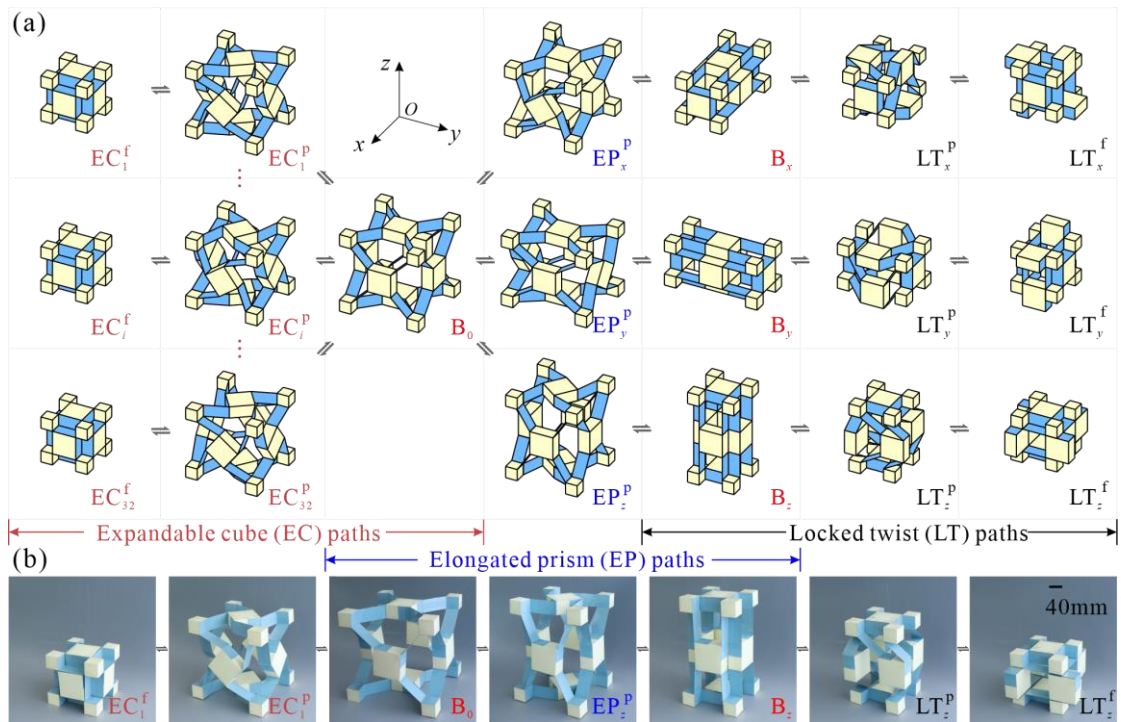


Fig. 5-5 Kinematic bifurcation of the Wohlhart cube. (a) The kinematic paths of the module. B_0, B_x, B_y and B_z are bifurcation configurations; (b) the reciprocate process of the prototype from EC_1^f to LT_z^f with $a=80\text{mm}, b=40\text{mm}$.

A complete motion process of the prototype from EC_1^f to LT_z^f demonstrates the analytical results, as shown in Fig. 5-5(b), where parameters are selected as $a=80\text{mm}$, $b=40\text{mm}$. Due to the similarity in the three orthogonal directions, only the property in z -direction is discuss in the following analysis.

5.3 Properties of a Single Polyhedron Module

5.3.1 The Variations of Geometric Dimensions of the Module

Apparently, the geometric dimensions of the module, i.e., the width, breadth, and height in x , y , and z directions, have undergone significant changes during the motion process. The completed motion curves of this module with three paths are shown in Fig. 5-6. Here the detailed path $EC_1^p-B_0-EP_z^p-B_z-LT_z^p$ is taken as an example to demonstrate the properties of the module. It can be observed that the module in the EC path is expanded from a smaller cube to a larger one as the rotation angles in orthogonal planes increase with $\alpha = \beta = \gamma$. Once the module reaches the bifurcation point B_0 ($\alpha = \beta = \gamma = \pi/4$), there are two possible paths; one is that the module is kept in the EC path as a cube to fold up with $\alpha = \beta = \gamma$ moving toward $\pi/2$, the other one is that the module switches into EP path with PLGs on the four side faces shrink inward in a translational way. When $\beta=0$ on the EP path, $\alpha=0$ or $\pi/2$ depending on the rotation direction of PLGs on the top and bottom faces, the module reaches B_z bifurcation configuration, where the EP path is at the limited end. Hence, the module can return to the EP path or bifurcate to the LT path with two rotation PLGs on top and bottom faces locked at $\alpha=0$ or $\pi/2$, and four PLGs on the side faces twist clockwise or anti-clockwise about z -axis when $\beta = \gamma$.

The geometrical dimensions are calculated according to the contour projection on the orthogonal planes. Hence, the geometrical dimensions of the module in the EC path in the x , y , and z direction are

$$W=B=H=a \sin \alpha + a \cos \alpha + a\sqrt{2 \sin \alpha \cos \alpha} + 2b \quad (5-17)$$

while dimensions W and B of the module in the EP path are the same as those in Equation (5-17), and

$$H=a + 2a \cos \beta + 2b \quad (5-18)$$

where $\alpha = \beta \in [0, \pi/2]$.

For the module in the EP path, the folding angle α in rotation PLGs is a function of β in translation PLGs, and the mathematical expression is

$$\sin \beta = (\sin \alpha + \cos \alpha + \sqrt{2 \sin \alpha \cos \alpha} - 1) / 2 \quad (5-19)$$

The variation of geometric dimensions of the module in the LT path is mainly divided into two stages with $a/b > 1$. When $\beta = \gamma \leq \arcsin(b/a)$, the projection of four PLGs on the side faces in the xoy plane is always within the projection of the rotation PLG ($\alpha = 0$ or $\pi/2$) on top and bottom faces, resulting in W and B remaining constant $a + 2b$. When the folding angle $\beta = \gamma > \arcsin(b/a)$, W and B become elongated simultaneously. Therefore, the dimensions of the module in the LT_z path are

$$W=B = \begin{cases} a+2b, & \text{if } \sin \beta \leq b/a \text{ or } a \leq b \\ a+2a \sin \beta, & \text{if } \sin \beta > b/a \text{ and } a > b \end{cases} \quad (5-20)$$

and

$$H = a + 2b + 2a \cos \beta \quad (5-21)$$

where $\gamma = \beta \in [0, \pi/2]$.

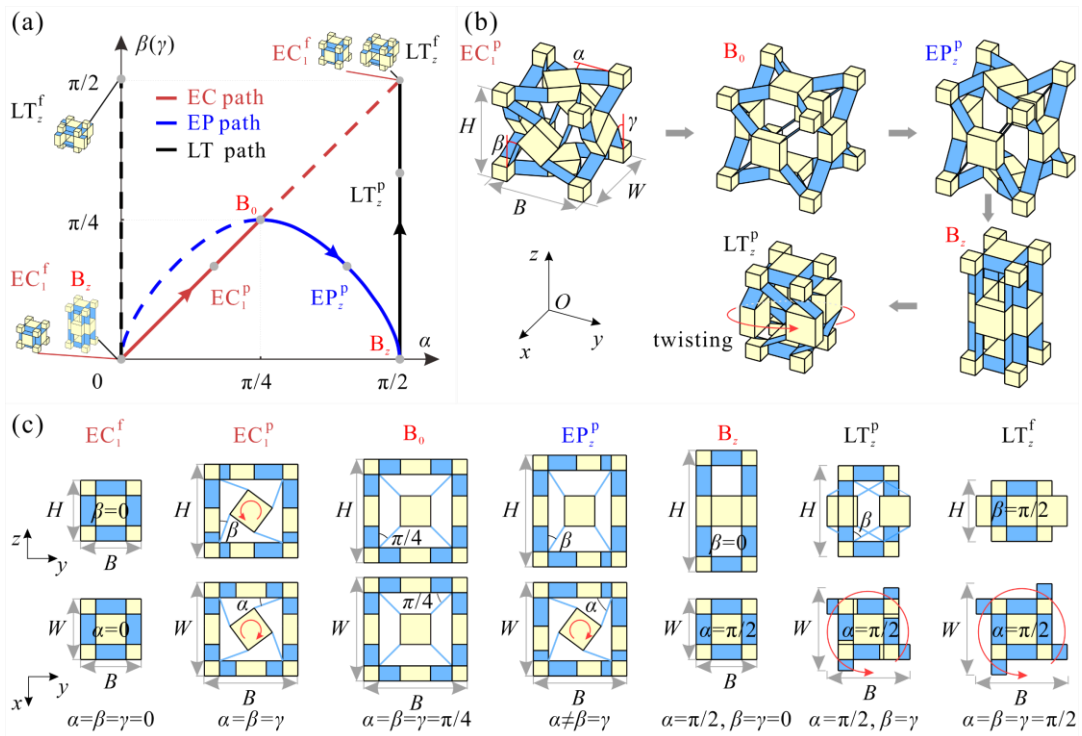


Fig. 5-6 The variations of geometric dimensions of the module in the x , y , and z directions following the EC path, EP path or LT path (a) The kinematic paths; (b) overall view of typical configurations; (c) front and top views of typical configurations.

5.3.2 Mechanical Properties for a Single Module

5.3.2.1 Poisson's Ratio for a Single Module

The Poisson's ratios ν_{HB} in the yoz plane and ν_{BW} in the xoy plane are defined as

$$\nu_{HB} = -\frac{dB}{B} \times \frac{H}{dH}, \quad \nu_{BW} = -\frac{dW}{W} \times \frac{B}{dB} \quad (5-22)$$

Therefore, Poisson's ratios of the module in the EC path are given by

$$\nu_{HB} = \nu_{BW} = -1 \quad (5-23)$$

and Poisson's ratios of the module in the EP path are then derived as

$$\nu_{HB} = \frac{a + 2a \cos \beta + 2b}{\tan \beta (a + 2a \sin \beta + 2b)} \quad (5-24)$$

and

$$\nu_{BW} = -1 \quad (5-25)$$

In addition, Poisson's ratios of the module in the LT path are

$$\nu_{HB} = \begin{cases} 0, & \text{if } \sin \beta \leq b/a \text{ or } a \leq b \\ \frac{a + 2a \cos \beta + 2b}{\tan \beta (a + 2a \sin \beta)}, & \text{if } \sin \beta > b/a \text{ and } a > b \end{cases} \quad (5-26)$$

and

$$\nu_{BW} = \begin{cases} 0, & \text{if } \sin \beta \leq b/a \text{ or } a \leq b \\ -1, & \text{if } \sin \beta > b/a \text{ and } a > b \end{cases} \quad (5-27)$$

Theoretical Poisson's ratios of the module as functions of folding angles and geometric parameters in EC, EP, and LT paths are shown in Fig. 5-7(a-c), respectively. It is evidently observed that Poisson's ratios ν_{HB} and ν_{BW} of the module in the EC path are always -1 independent of geometric parameters (see Fig. 5-7(a)), when the structure is elongated simultaneously in three orthogonal directions. On the contrary, the module in the EP path is anisotropic. Specifically, Poisson's ratios ν_{HB} of the module in the EP path varies continuously in positive values (see Fig. 5-7(b)). Theoretical results also suggest that the Poisson's ratios in the EP path are insensitive to variations in geometrical parameters a/b , as shown in Fig. 5-7(b). Poisson's ratio ν_{HB} decreases sharply from infinity to 1 as the structure expands from a compact prism to a fully unfolded cube. Meanwhile, regardless of the geometric parameter a/b , the Poisson's ratios ν_{BW} of the module in the EP path remain -1. As for the module in the LT path,

Poisson's ratios ν_{HB} and ν_{BW} maintain 0 for $b \geq a$, because the projection of four PLGs on the side faces in the xoy plane is always within the projection of the rotation PLG ($\alpha = 0$ or $\pi/2$) and the length and width remain constant $a+2b$ (see Fig. 5-7(c)). If $b < a$, ν_{HB} and ν_{BW} of the module in the LT path remain 0 until $\beta = \gamma \leq \arcsin(b/a)$, then ν_{HB} suddenly drops to and remains at -1 while ν_{BW} suddenly increases to a positive value and then gradually decreases to 0. One can further program this step point of Poisson's ratios by changing the geometrical parameters a/b . The interval of the ZPR mode lengthens as the value of a/b decreases, eventually reaching a full ZPR mode throughout the deformation process once $a/b \leq 1$.

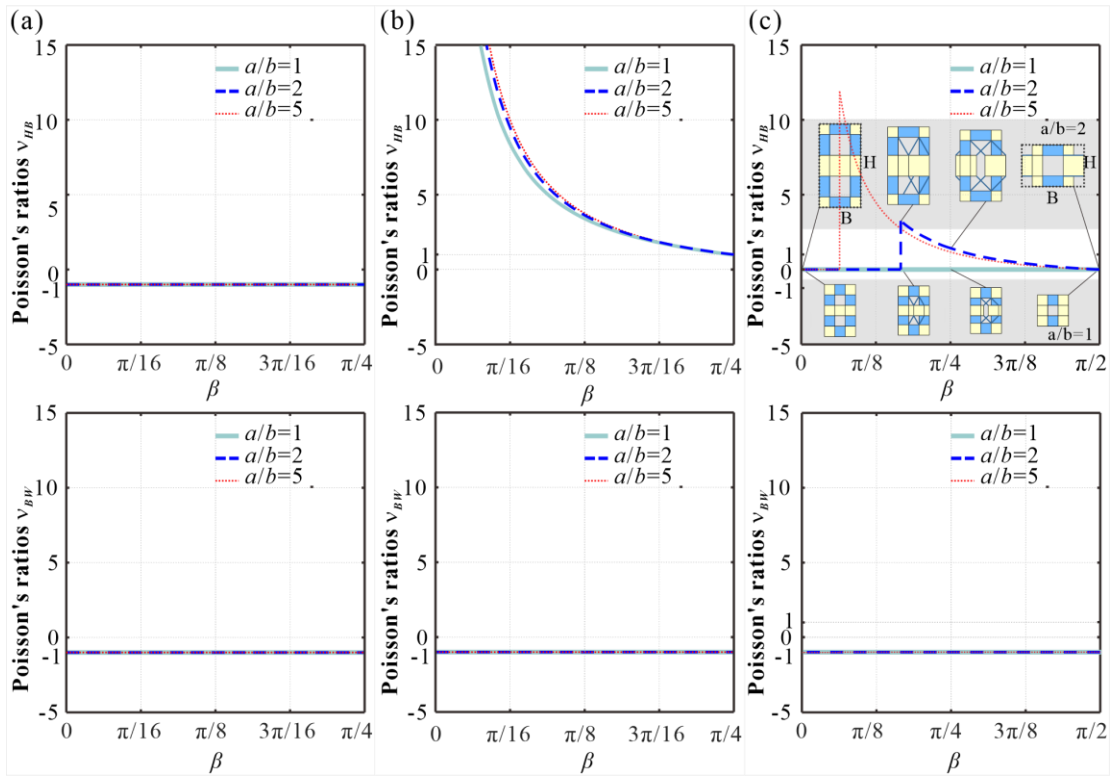


Fig. 5-7 Theoretical Poisson's ratios of the module as functions of folding angles and geometric parameters. (a) EC, (b) EP, and (c) LT paths.

A tension and compression experiment for a single module was then conducted. The experimental setup is depicted in Fig. 5-8(a). To reduce the gravitational effect, the experiment was carried out on a vertical testing machine (Instron 5982). The specimen was sandwiched between two fixtures, allowing rotational displacement at both ends. The specimen was then tensioned (compressed) with 160mm displacement and a 0.5 mm s^{-1} loading rate. The deformation process was captured by a CSI Vic-3D9M digital

image correlation (DIC) system with a camera resolution of 2704×3384 pixels and a frame period of 500ms. For DIC capture, the square faces of the cube connection were painted with black speckles. Based on the coordinate information of the black speckles in the measurement areas, the width W and breadth B under different heights H can be measured. As measuring the angle directly is difficult, the normalized displacement is defined as folding ratios in the loading direction. The recorded deformation process shows that W , B , and H of the module in the EC path increase simultaneously during tension (i-ii-iii-iv-v in Fig. 5-8(b)). Then the specimen goes through another stage (vi-vii-viii-ix-x in Fig. 5-8(b)) after passing through the bifurcation configuration B_0 , where W and B decrease while H increases continuously. After bifurcation point B_z , both W and B of the specimen in the LT path are equal to $a + 2b$ (xi-xii-xii in Fig. 5-8(b)) during compression, until the projection of rotation PLGs ($\alpha = 0$ or $\pi/2$) on the xoy plane cannot cover that of four PLGs on the side faces (xiii-xiv-xv in Fig. 5-8(b)). The quantitative values of the experimental results are in good agreement with theoretical ν_{HB} and ν_{BW} , although results differ slightly at the 75-100 % stage due to gravity.

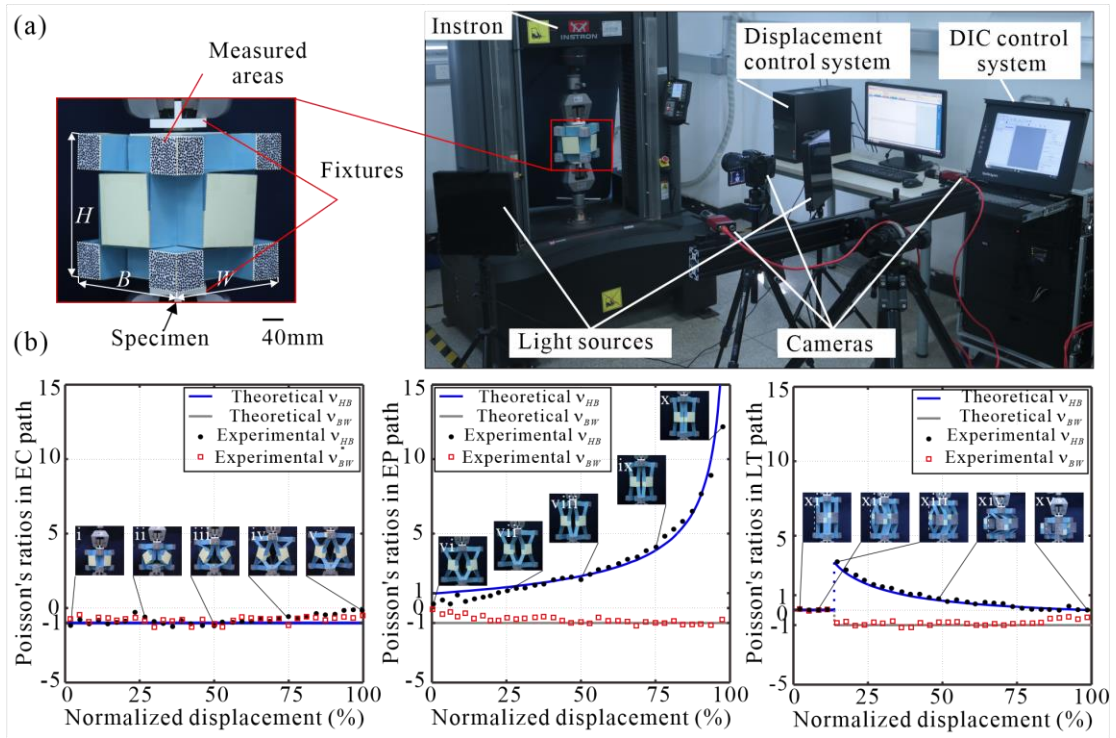


Fig. 5-8 Experiments and results of Poisson's ratio test of a single module. (a) The uniaxial tension and compression experimental setup for a single module; (b) comparison of theoretical and experimental Poisson's ratios of a module in EC, EP, and LT paths with $a/b = 2$.

5.3.2.2 Tuneable Chirality of the Module

From the red arrow-arcs marked in Fig. 5-6 and the experiments in Fig. 5-8, it can be inferred that this module also exhibits distinct chirality properties when moving along different kinematic paths. First, in the EC path, all six rotation PLGs on six faces twist clockwise or counter-clockwise independently to generate enhanced local chirality. Second, in the EP path, only two rotation PLGs on two opposite faces normal to the elongated direction have the local chirality, while the other four do the translation with no chirality. Third, in the LT path, two rotation PLGs on the top and bottom faces are locked at $\alpha = 0$ or $\pi/2$, and four PLGs on the side faces twist clockwise or anti-clockwise about z axis when $\beta = \gamma$ to produce a global chirality.

5.3.2.3 Tuneable Stiffness of the Module

Additionally, the stiffness will also change significantly when the module is switched between different paths. Assuming that the energy of the modules is composed of deformation from linear elastic rotational joints, and k_f as the rotational spring modulus of unit length, the stored energy U of the system is given by

$$U = \frac{1}{2} k_f b [n_1 (\varphi_1 - \varphi_{1,0})^2 + n_2 (\varphi_2 - \varphi_{2,0})^2 + \dots + n_i (\varphi_i - \varphi_{i,0})^2] \quad (5-28)$$

where $\varphi_{i,0}$ is the natural dihedral angles (in the undeformed state) of i -th type of joint, n_i is the number of i -th type of joint, and b is defined as the length of cube connectors. The force F along z direction is

$$F = \frac{dU}{dL} = \frac{dU}{d\varphi} / \frac{dL}{d\varphi} \quad (5-29)$$

where L is the displacement in the z direction.

The stiffness along z direction is thus given by

$$K = \frac{d^2U}{dL^2} = \frac{d}{d\varphi} \left(\frac{dU}{dL} \right) / \frac{dL}{d\varphi} \quad (5-30)$$

Let's first consider configuration EC_1^f as the natural state. As shown in Fig. 5-9, dots of the same color represent the same working mode of the spring under the current path, and φ_i is the angle of i -th type of joints. The rotation angles of the spring of the module in EC_1^p path are

$$\Delta\varphi_1 = \varphi_1 - \varphi_{1,0} = \varphi, \quad \Delta\varphi_2 = \varphi_2 - \varphi_{2,0} = \varphi_1 + \arccos(\cos\varphi_1 - \sin\varphi_1) \quad (5-31)$$

where φ changes from 0 to $\pi/4$.

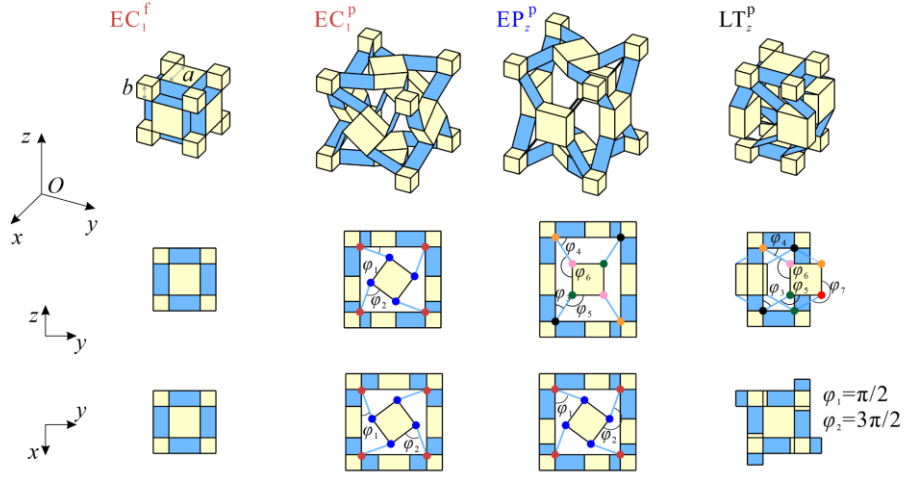


Fig. 5-9 Types of joints and their rotation angles under different paths when configuration EC_1^f is taken as the natural state. Dots of the same color represent the same working mode of the spring under the current path. n_i and φ_i are the number and angle of i -th type of joints respectively.

For the module in EP_z path, rotation angles are

$$\begin{aligned} \Delta\varphi_1 &= \varphi_1 - \varphi_{1,0} = \pi/2 - \varphi, \quad \Delta\varphi_2 = \varphi_2 - \varphi_{2,0} = 3\pi/2 - \varphi - \arccos(\cos\varphi - \sin\varphi) \\ \Delta\varphi_3 &= \varphi_3 - \varphi_{3,0} = \arcsin((\sin\varphi + \cos\varphi + \sin(\arccos(\cos\varphi - \sin\varphi)) - 1)/2) \\ \Delta\varphi_4 &= \varphi_4 - \varphi_{4,0} = \pi/2 - \varphi_3, \quad \Delta\varphi_5 = \varphi_5 - \varphi_{5,0} = \pi/2 + \varphi_3, \quad \Delta\varphi_6 = \varphi_6 - \varphi_{6,0} = \pi - \varphi_3 \end{aligned} \quad (5-32)$$

where φ changes from $\pi/4$ to 0.

For the module in LT_z path, rotation angles are

$$\begin{aligned} \Delta\varphi_1 &= \varphi_1 - \varphi_{1,0} = \pi/2, \quad \Delta\varphi_2 = \varphi_2 - \varphi_{2,0} = 3\pi/2, \quad \Delta\varphi_3 = \varphi_3 - \varphi_{3,0} = \varphi \\ \Delta\varphi_4 &= \varphi_4 - \varphi_{4,0} = \pi/2 - \varphi_3, \quad \Delta\varphi_5 = \varphi_5 - \varphi_{5,0} = \pi/2 + \varphi_3 \\ \Delta\varphi_6 &= \varphi_6 - \varphi_{6,0} = \pi - \varphi_3, \quad \Delta\varphi_7 = \varphi_7 - \varphi_{7,0} = \pi + \varphi_3 \end{aligned} \quad (5-33)$$

where φ changes from 0 to $\pi/2$.

The displacement in the z direction of three paths are

$$\begin{aligned} L_{EC} &= (a \cos\varphi + a \sin\varphi + a \sin(\arccos(\cos\varphi - \sin\varphi))) - a \\ L_{EP} &= 2a \cos(\arcsin((\sin\varphi + \cos\varphi + \sin(\arccos(\cos\varphi - \sin\varphi)) - 1)/2) - \sqrt{2}a \\ L_{LT} &= 2a \cos\varphi - 2a \end{aligned} \quad (5-34)$$

The kinematic paths and corresponding normalized energy, force and stiffness of the module are shown in Fig. 5-10(a). We define normalized energy, force stiffness, and height as $U/(k_f b)$, F/k_f , Kb/k_f and H/H_{\max} , respectively. Normalized energy

U_{EC} , force F_{EC} , and stiffness K_{EC} increase sharply as PLGs on six faces move from $\alpha = \beta = \gamma = 0$ toward $\alpha = \beta = \gamma = \pi/4$, as shown in Fig. 5-10(b-d). At the bifurcation point B_0 , the module deformation energy is unsmooth increasing state (non-differentiable point) as spring joints of PLG on four lateral faces are further rotated as the others on two end faces return toward the natural state (Stored elastic potential energy is released), resulting the force is discontinuous and the stiffness switches from $+\infty$ to $-\infty$. Subsequently, the stiffness K_{EP} in the EP path will undergo a change from negative to positive with the increase of deformation. Meanwhile, the bifurcation point B_z is also a non-differentiable point of system energy, and the stiffness K_{LT} of the module in the LT path increases at a lower level under compression as the joints on the top and bottom faces are locked. It can be concluded that the stiffness is tuneable when the module switches between different paths.

Generally, the stiffness is independent of natural configuration ($\varphi_{i,0}$) due to

$$K = k_f b (n_1 \varphi_1 + n_2 \varphi_2 + \dots + n_i \varphi_i) / \frac{dL}{d\varphi} \quad (5-35)$$

The exception is that the dihedral angle φ_i is the transcendental function of φ , donated as $\varphi_i = f_i(\varphi)$. Then the stiffness can be expressed as

$$K = \frac{k_f b [n_1 ((f_1(\varphi) - \varphi_{1,0}) f_1''(\varphi) + f_1'(\varphi) f_1'(\varphi)) + \dots + n_i ((f_i(\varphi) - \varphi_{i,0}) f_i''(\varphi) + f_i'(\varphi) f_i'(\varphi))]}{\frac{dL}{d\varphi}} \quad (5-36)$$

Next, the effect of natural configuration on stiffness are investigated. The stiffness of the module in the natural state of configurations B_0 and B_z are plotted in Fig. 5-11(a) and (b). In general, the module shows different energy and force with different natural configurations, although the kinematic path is the same. It can be observed that the stiffness of K_{EC} and K_{EP} are completely different in three cases. The reason is that the stiffness is related to the initial configuration because the dihedral angle φ_i is the transcendental function of φ . On the contrary, the stiffness K_{LT} in the three cases are identical because the dihedral angle φ_i is the linear function of φ . In summary, the stiffness is tuneable when the module is in different paths. Furthermore, designing the natural state of the module before fabrication is also a potential way to regulate the stiffness of K_{EC} and K_{EP} .

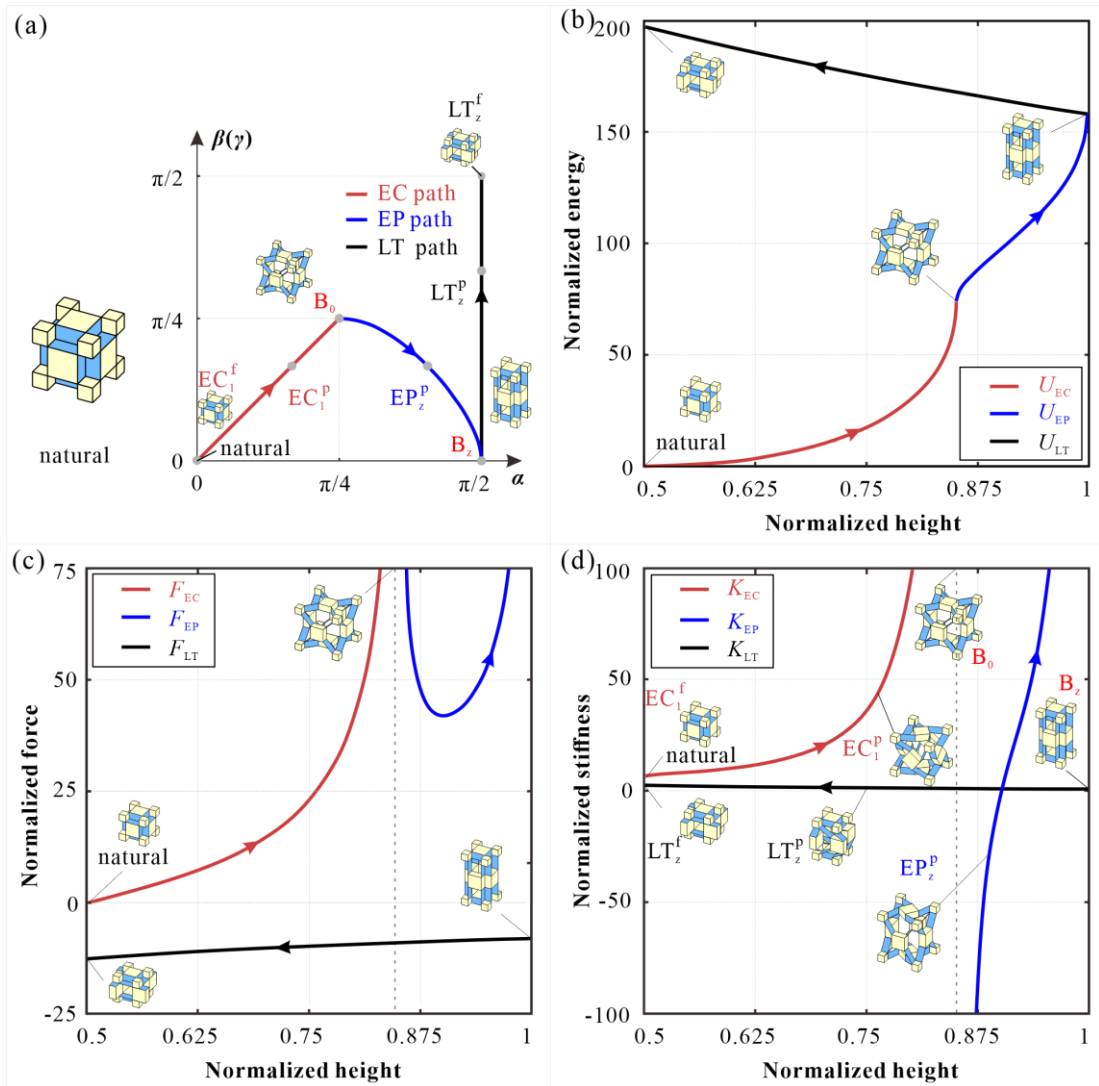


Fig. 5-10 Tuneable stiffness of the module. (a) The kinematic paths and corresponding normalized energy in (b), force in (c), and stiffness in (d) of the module when configuration EC_1^f is taken as the natural state.

5.3.2.4 The Controllable Reconfiguration Methods

Based on the properties on the Poisson's ratios and chirality and stiffness, it is also found that the reconfiguration of one module among three kinematic paths can be controlled through the relative displacements of the cube connectors or the combination of force or torque applied to the square central bodies at the bifurcated points, as shown in Fig. 5-12 and Fig. 5-13.

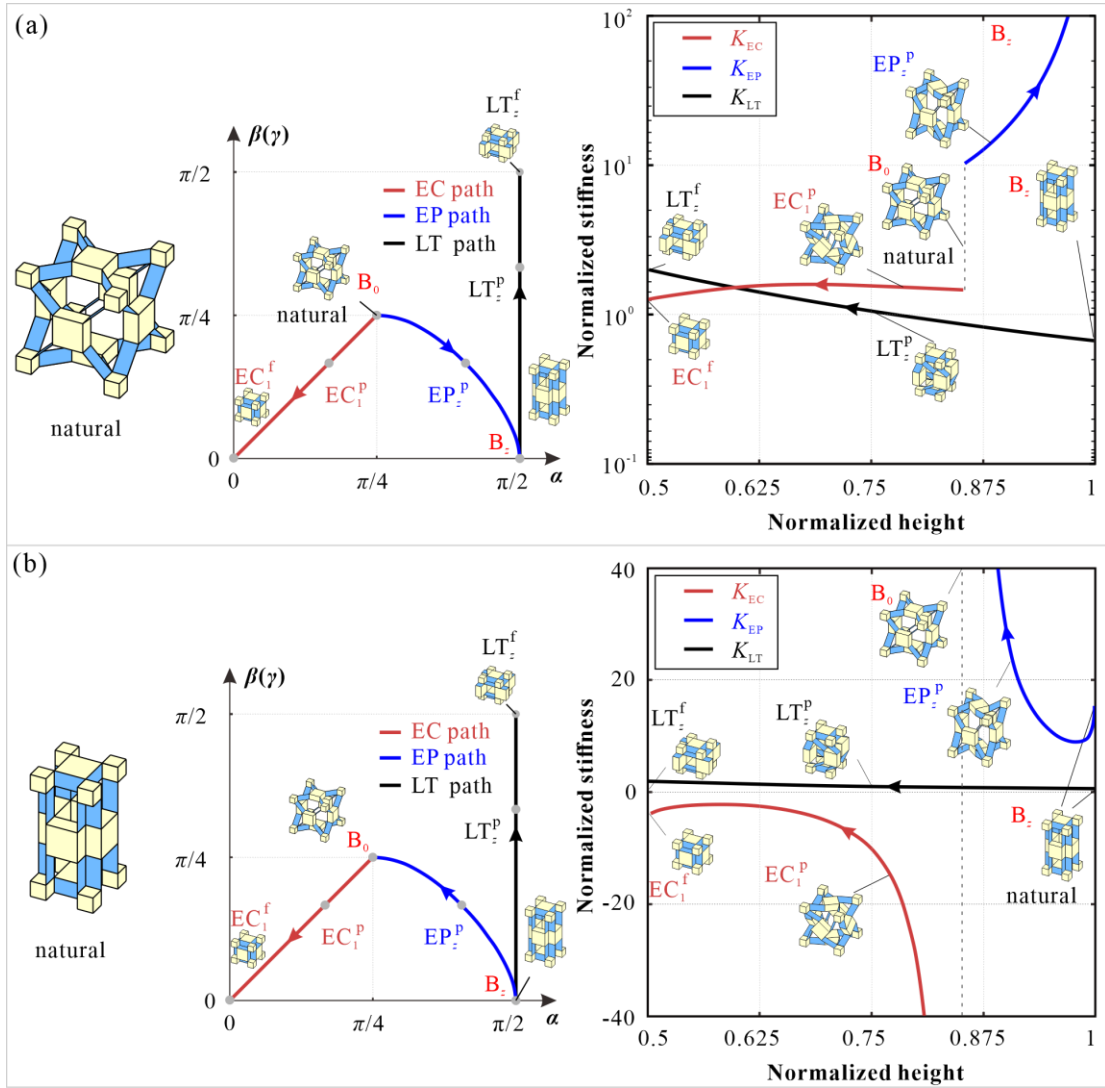


Fig. 5-11 Stiffness of the module in the natural state of configurations B_0 in (a) and B_z in (b).

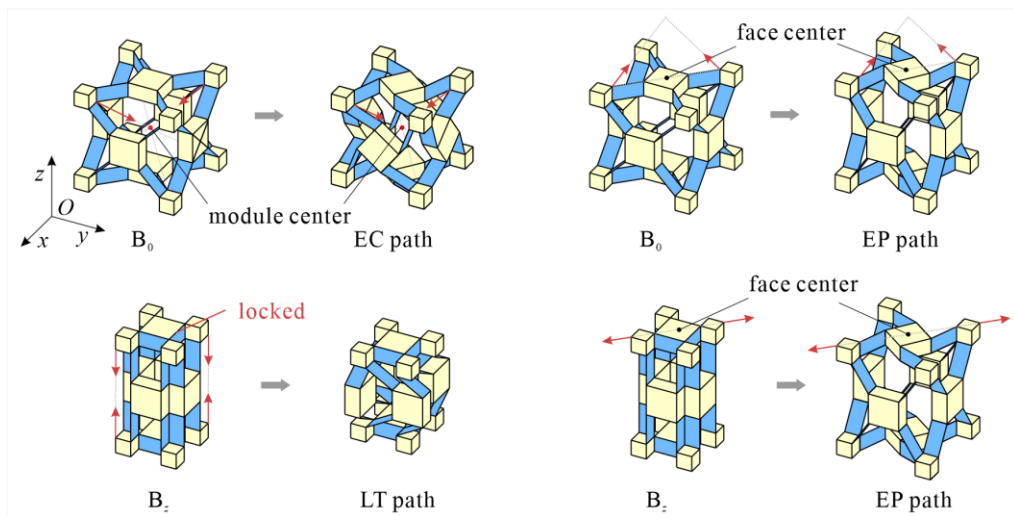


Fig. 5-12 Control the bifurcated paths by the relative displacements of the cube connectors.

As shown in Fig. 5-12, for the single module, the bifurcated path can be controlled by the relative motion of the corner cubes. At bifurcation configuration B_0 , when some of the cube connectors move toward the module centre, the module moves in the EC path, and when the two opposite cube connectors on the top face move towards the face centre and along the positive z direction at the same time, it follows the EP path. At the bifurcation configuration B_i ($i=x, y, z$), when the one set of cube connectors on the top or bottom of the elongated prism are locked at the same distance, the module moves in the LT path, and when they are expanded away from the face centre, it follows the EP path.

Alternatively, the direction of the force F or torque T applied to the square central bodies at the bifurcated points can be controlled so as to choose the desired path. As shown in Fig. 5-13, when the module is at bifurcation configuration B_0 , the tension force on two opposite square central bodies makes the module move along the EP path, or the torque on the adjacent square central bodies leads the module to the EC path. When the module is at bifurcation configuration B_i ($i=x, y, z$), the compression force on two square central bodies of locked PLGs in the i -direction makes the module move in the LT path whilst the module tends to the EP path under torque if the PLGs is unlocked.

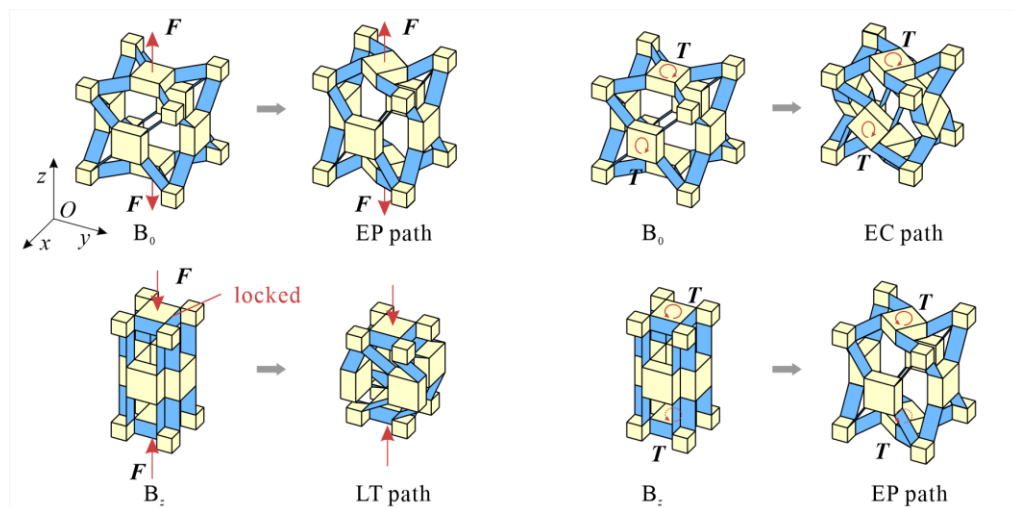


Fig. 5-13 Control the bifurcated paths by the combination of force or torque applied to the square central bodies at the bifurcated points.

5.4 3D Metamaterials with Programmable Poisson's Ratio

If tessellating the module through translation and array in 3D space, periodic metamaterials in Fig. 5-14(a) can be created, whose properties are determined by the single module. In Fig. 5-14(b), this idea is demonstrated by a 2×2 tessellation of modules. The connection between modules is represented by orange solid lines, which is realized by quick-drying glue in the physical model. This 2×2 tessellation has the capability to continuously reconstruct between NPR (I-II-III), PPR (III-IV-V), and ZPR(V-VI) modes, relying on the modules switching between EC path, EP path, and LT path, as shown in Fig. 5-14(c). It is worth noting that the stage of the PPR behaviour of modules in LT path does not occur, due to physical interference between the square centre bodies of PLGs. The current tuneable range of Poisson's ratios for periodic metamaterials, using bifurcations of the module, is $[-1, +\infty)$. However, its programmability is still very limited as theoretical results in Fig. 5-14 suggest that Poisson's ratios in EC and EP paths are insensitive to variations in geometrical parameters a/b .

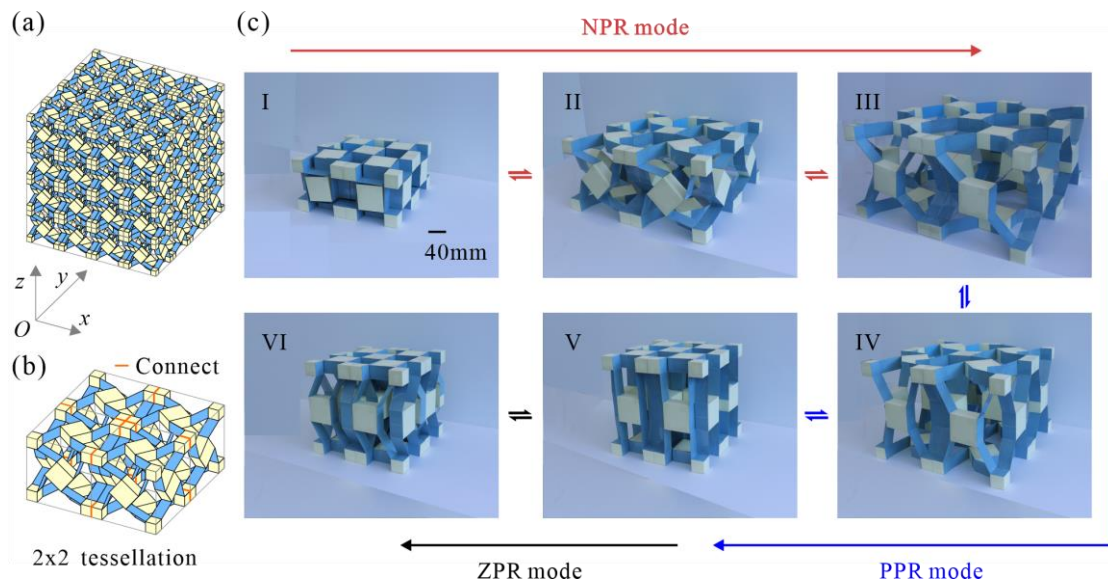


Fig. 5-14 Periodic metamaterials with reconfigurability. (a) 3D metamaterial by tessellating multiple modules; (b) 2×2 tessellation, whose connection between modules is represented by orange solid lines; (c) the motion sequences of the physical model of a 2×2 tessellation, where I-II-III is NPR mode, III-IV-V is PPR mode, V-VI is ZPR mode.

5.4.1 The Series Assembly with (m_z+n_z) Modules

To enhance the programmability of metamaterials, a combinatorial design strategy is proposed, as shown in Fig. 5-15. Generally, under uniaxial tension F , PPR material tends to contract in the direction perpendicular to the applied load (Fig. 5-15(a)). In contrast, the NPR material elongates simultaneously along and perpendicular to the load directions when stretched. If the deformation of two neighbouring units in the loading direction is consistent all the time, the two units can be stacked together in the direction perpendicular to the applied load. This combinational rule can also be extended to 3D PPR material and NPR materials. Take two modules, one in the PPR state on the EP path, and one in the NPR state on the EC path (Fig. 5-15(b)). The dimensions of rotation PLGs are equal as long as their folding angle α is the same, which provides the possibility to connect two modules in EP and EC paths through the shared faces of four cube connectors (see orange lines in Fig. 5-15(b)). For ease of visualization, a green right square prism and a blue regular hexahedron with bumps and dents texture are used for connection to schematically represent the modules in PPR (state “1”) and NPR (state “0”) modes, respectively.

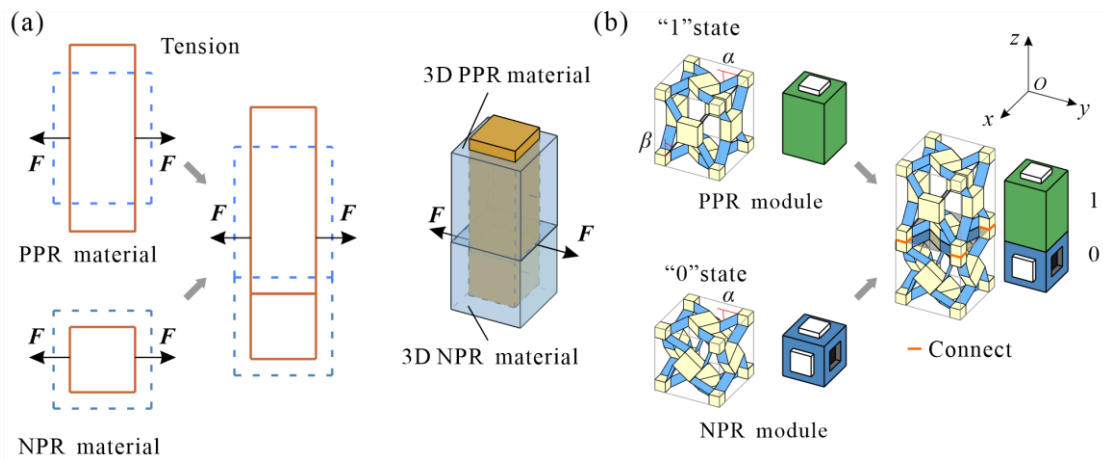


Fig. 5-15 Schematic diagram of a two-module assembly with one in PPR state and one in NPR state. (a) Connection rules for two modules and their (b) visualizations.

The series assembly with $(m_z + n_z)$ modules in Fig. 5-16(a) is then constructed, of which m_z modules in the PPR state and n_z modules in the NPR state. Each module is equipped with the ability to switch between the state “1” and “0” through their inherent kinematic bifurcations. Thus, this unique series assembly after fabrication, is expected

to be reconstructed into ones with arbitrary proportions and arrangement order of PPR and NPR modules. For example, if partial modules switch from the “1” state to the “0” state or vice versa without changing the total number of units, the proportion of NPR and PPR modules n_z / m_z changes. As m_z and n_z are any non-negative whole number, n_z / m_z could be any rational number within $[0, +\infty)$.

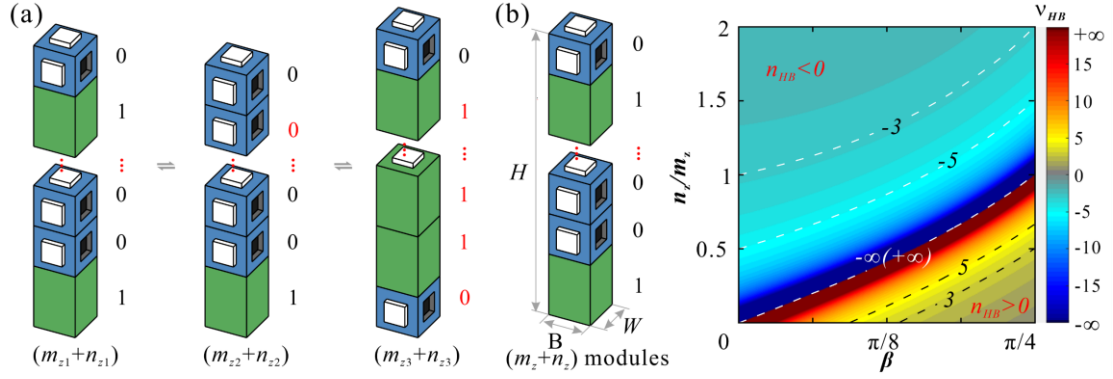


Fig. 5-16 The series assembly with $(m_z + n_z)$ modules. (a) Reconfiguration of module states to regulate n_z / m_z ($m_{z1} + n_{z1} = m_{z2} + n_{z2} = m_{z3} + n_{z3}$); (b) a series assembly of m_z PPR and n_z NPR modules with $a/b=2$ and its contour plot of Poisson's ratio ν_{HB} .

The geometrical dimensions of the series assembly with $(m_z + n_z)$ modules are

$$W=B=a+2a\sin\beta+2b \quad (5-37)$$

and

$$H=m_z(a+2a\cos\beta+2b)+n_z(a+2a\sin\beta+2b) \quad (5-38)$$

where m_z and n_z are the numbers of modules in PPR and NPR states, respectively, and β is the folding angle of the module in the EP path that varied in $[0, \pi/4]$. Therefore, Poisson's ratios of the series assembly with $(m_z + n_z)$ modules are

$$\nu_{HB} = -\frac{dB}{dH} \times \frac{H}{B} = -\frac{am_z(1+2\cos\beta) + an_z(1+2\sin\beta) + 2b(m_z + n_z)}{(n_z - m_z \tan\beta)(a(1+2\sin\beta) + 2b)} \quad (5-39)$$

and

$$\nu_{BW} = -1 \quad (5-40)$$

Notice that the combined design strategy introduces a new design parameter for the Poisson's ratio, i.e., the proportion of NPR and PPR modules n_z / m_z . Then, its analytical contour plot indicates Poisson's ratio ν_{HB} of the series assembly with $a/b=2$ covering the entire design space $(-\infty, +\infty)$ in Fig. 5-16(b) as reconfiguration of module states is a rapid and effective way to regulate n_z / m_z . Specifically, ν_{HB} keeps

negative during the whole folding motion if $n_z / m_z \geq 1$. Otherwise, ν_{HB} changes from a negative value to $-\infty$ with β increasing, then switches to $+\infty$ at $\beta = \arctan(n_z / m_z)$, and finally reaches a positive value. The series assembly with different values of n_z / m_z exhibits distinct but predictable mechanical properties, which provides a new paradigm for the programmability of Poisson's ratio.

Further, uniaxial tension experiments with series assemblies ($n_z / m_z = 2$, $n_z / m_z = 1$, $n_z / m_z = 1/2$) was conducted. Theoretical analysis suggests that there may be a switchable Poisson's ratio effect, which means that the height of the specimen may increase first and then decrease. Therefore, the vertical loading is changed to horizontal loading, and the new experimental setup is shown in Fig. 5-17(a). The specimen is suspended in the diagonal direction on a fixed frame. One end of the specimen is directly glued (solid orange lines) on the frame, and the other end is fixed on the slider located on the frame. The slider is connected with the fixture of the displacement control system by Kevlar ROPE tows (diameter = 0.3mm). The specimen was then tensioned with 160mm displacement and a loading rate of 0.5 mm s^{-1} . The deformation process is captured by the same DIC system with Fig. 5-8.

The comparative plot of theoretical and experimental results for two-module assembly with $a/b = 2$ and $n_z / m_z = 1$ are shown in Fig. 5-17(b). Similar to $n_z / m_z = 1$, the results for three-module assembly with $n_z / m_z = 2$ in Fig. 5-17(c) show that Poisson's ratio ν_{HB} remains negative and decreases with the deformation degree, while ν_{BW} fluctuates around -1. Then one of the PPR modules is reconstructed to NPR state to set $n_z / m_z = 1/2$ (Fig. 5-17(d)). The transition of ν_{HB} from -852.89 to 375.47 is observed, while ν_{BW} remains close to -1. The natures and trends of mechanical response between theoretical and experimental results remain similar, as shown in Fig. 5-17(b-d). However, the difference of values ν_{HB} grows prominent since the effect of gravity on deformation is more significant with the increase in the number of modules.

5.4.2 Metamaterials with the 3D Tessellation of Modules

The metamaterials can be further built in 3D space by tessellating multiple series assemblies. Two design schemes for 3D metamaterials are proposed as follows.

Scheme I: identical series assemblies composed of m_z modules in the PPR state and n_z modules in the NPR state are parallelly and periodically tessellated (Fig. 5-18(a)). There are i and j such columns in the x and y directions, respectively. Each

column's Poisson's ratios are identical. Therefore, the Poisson's ratios of the whole metamaterial are the same as a single column, i.e., ν_{HB} can also be encoded by regulating the proportion of modules in PPR or NPR states according to Fig. 5-16, while ν_{BW} remains -1.

Scheme II: series assemblies with $(m_x + n_x)$, $(m_y + n_y)$, and $(m_z + n_z)$ modules in x , y , z directions respectively are implanted to form the frame of a cuboid tessellation (Fig. 5-18(b)). Note that the corners are always NPR modules because their three common-point faces are used to connect the other three modules simultaneously, i.e., $n_i \geq 2$ ($i=x, y, z$). Therefore, n_i/m_i could be any rational number within $[2/(2+m_i), +\infty)$. The total number and proportion of modules in PPR or NPR states of series assemblies on parallel edges are identical, but the arrangement order of modules is not strictly limited.

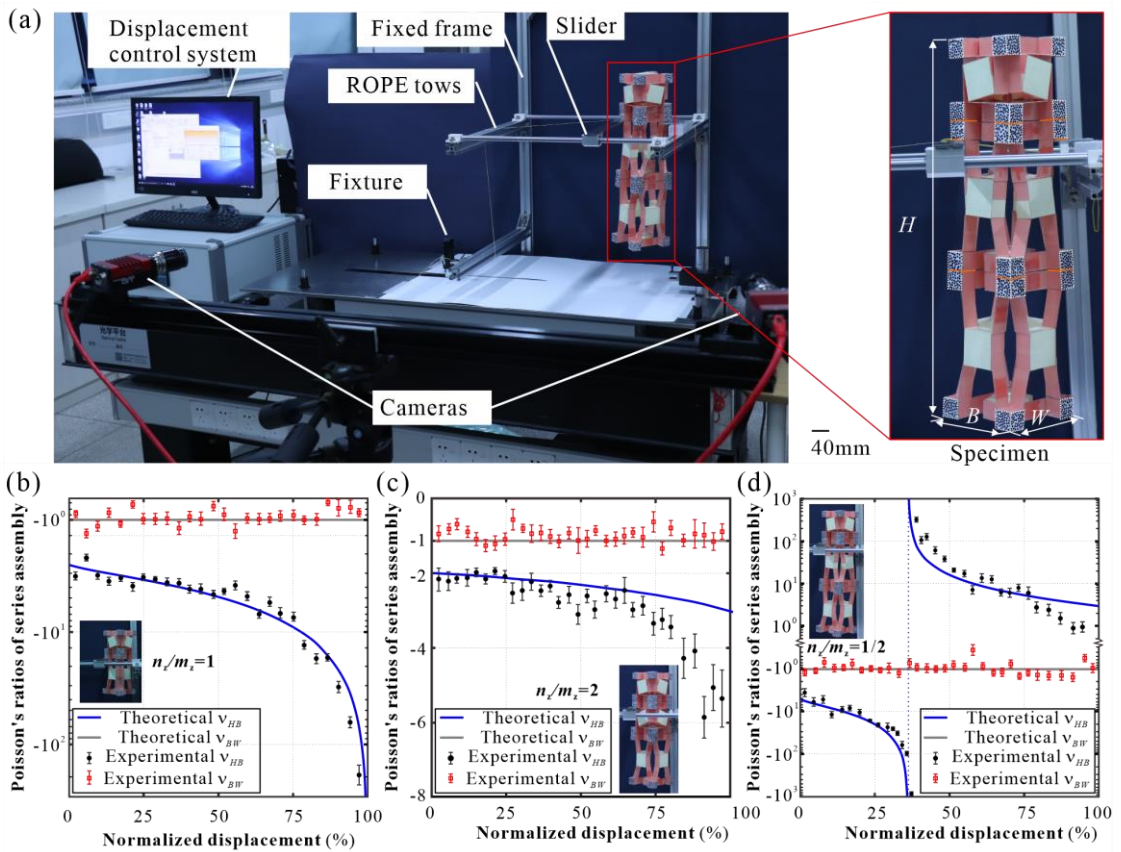


Fig. 5-17 Experiments and results of Poisson's ratio test of series assemblies ($n_z/m_z = 1$, $n_z/m_z = 2$, $n_z/m_z = 1/2$). (a) The uniaxial tension experimental setup for series assembly; (b-d) comparative plots of theoretical and experimental Poisson's ratios of modules stacked in series with $n_z/m_z = 1$, $n_z/m_z = 2$ and $n_z/m_z = 1/2$.

For scheme II, its analytical expressions for W , B , and H are

$$W = m_x(a + 2a \cos \beta) + n_x(a + 2a \sin \beta) + 2b(m_x + n_x) \quad (5-41)$$

$$B = m_y(a + 2a \cos \beta) + n_y(a + 2a \sin \beta) + 2b(m_y + n_y) \quad (5-42)$$

$$H = m_z(a + 2a \cos \beta) + n_z(a + 2a \sin \beta) + 2b(m_z + n_z) \quad (5-43)$$

where m_x, n_x are numbers of PPR and NPR modules in the x direction, and m_y, n_y are numbers of PPR and NPR modules in the y direction, and m_z, n_z are numbers of PPR and NPR modules in the z direction.

In this case, Poisson's ratios ν_{HB} in the yoz plane and ν_{BW} in the xoy plane are

$$\nu_{HB} = -\frac{(n_y - m_y \tan \beta)(am_z(1 + 2 \cos \beta) + an_z(1 + 2 \sin \beta) + 2b(m_z + n_z))}{(n_z - m_z \tan \beta)(am_y(1 + 2 \cos \beta) + an_y(1 + 2 \sin \beta) + 2b(m_y + n_y))} \quad (5-44)$$

and

$$\nu_{BW} = -\frac{(n_x - m_x \tan \beta)(am_y(1 + 2 \cos \beta) + an_y(1 + 2 \sin \beta) + 2b(m_y + n_y))}{(n_y - m_y \tan \beta)(am_x(1 + 2 \cos \beta) + an_x(1 + 2 \sin \beta) + 2b(m_x + n_x))} \quad (5-45)$$

where $\beta \in [0, \pi/4]$ is the folding angle of the module in the EP path.

Since Eq. (5-44) and Eq. (5-45) have similar forms, the focus here is mainly on Poisson's ratios ν_{HB} in the yoz plane. For any negative Poisson's ratio ν_{HB} , it requires

$$\frac{n_y / m_y - \tan \beta}{n_z / m_z - \tan \beta} > 0 \quad (5-46)$$

because H/B are always positive for all values of β .

This requirement is reduced to two derivatives dB and dH have the same sign, i.e.,

$$n_y / m_y - \tan \beta > 0, n_z / m_z - \tan \beta > 0 \quad (5-47)$$

or

$$n_y / m_y - \tan \beta < 0, n_z / m_z - \tan \beta < 0 \quad (5-48)$$

We can get two sets of solutions from the above equations, i.e.,

$$0 < \beta < \arctan(\min(n_y / m_y, n_z / m_z)) \quad (5-49)$$

or

$$\arctan(\max(n_y / m_y, n_z / m_z)) < \beta < \pi/4 \quad (5-50)$$

Then, Poisson's ratios ν_{HB} are positive for the other values of $\beta \in [0, \pi/4]$, i.e.,

$$\arctan(\min(n_y / m_y, n_z / m_z)) \leq \beta \leq \arctan(\max(n_y / m_y, n_z / m_z)) \quad (5-51)$$

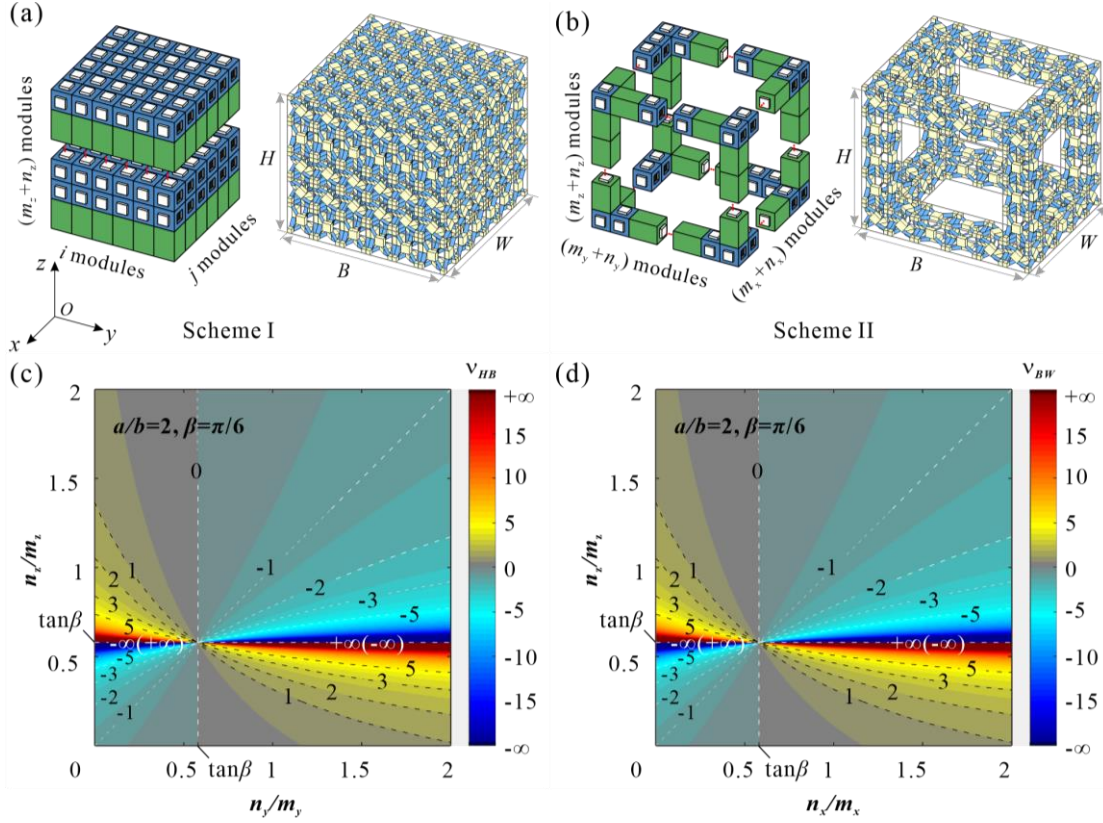


Fig. 5-18 Metamaterials with 3D tessellation of mechanism modules. (a) Design scheme I, where each column consists of $(m_z + n_z)$ modules. (b) design scheme II of 3D metamaterials with $(m_x + n_x)$, $(m_y + n_y)$, $(m_z + n_z)$ modules in x , y , z direction (c-d) The contour plots of ν_{HB} and ν_{BW} for 3D metamaterials in scheme II as a function of n_i / m_i ($i=x, y, z$) when $a/b = 2$ and $\beta = \pi/6$.

Based on the above analysis, it can be inferred that the Poisson's ratios of the 3D metamaterial in Fig. 5-18(b) can be programmed by regulating the combination ratios of PPR and NPR states on EP and EC paths in three directions, n_i / m_i ($i=x, y, z$), independent as well as the folding angle β related to the configuration. First of all, let us fix $a/b = 2$ and $\beta = \pi/6$ to see the effect of n_i / m_i on the Poisson's ratios. For ν_{HB} , there are two boundaries (Fig. 5-18(c)), i.e., $n_y / m_y = \tan\beta$ and $n_z / m_z = \tan\beta$, which are the transitions of ν_{BW} between negative and positive, and divide the design space $(-\infty, +\infty)$ into four regions. Poisson's ratio ν_{HB} can be encoded as any negative values once n_y / m_y and $n_z / m_z \in (0, \tan\beta)$, or n_z / m_z and $n_z / m_z \in (\tan\beta, +\infty)$. Otherwise, ν_{HB} is positive. Apparently, n_x / m_x and n_y / m_y play the same role in the programming of ν_{BW} , see Fig. 5-18(d). Moreover, n_z / m_z and n_x / m_x are independent variables of ν_{HB} and ν_{BW} as characterized in Eq. (5-44) and Eq. (5-45), implying that Poisson's ratios ν_{HB} and ν_{BW} can be programmed independently. Meanwhile, similar

to the single module and series assemblies, the Poisson's ratios of the whole metamaterial can be tuned by configurations described by folding angle β , and they are not insensitive to variations in geometrical parameters a/b .

To demonstrate the programming on the characteristics of metamaterials' Poisson's ratios, let us take an example with $(m_x + n_x = 6)$, $(m_y + n_y = 5)$, $(m_z + n_z = 8)$ modules and $a/b = 2$ (Fig. 5-19). Every module except those eight on the cuboid corners can switch between the PPR and NPR states on EP and EC paths. Hence, there are a total 140 modes with distinct characteristics of Poisson's ratios. In the extremal mode that all the modules in the tessellation are in NPR state, and the metamaterial will be of 3D negative Poisson's ratios with $\nu_{HB} = \nu_{BW} = -1$.

Let us take a random mode with $n_x/m_x = 2$, $n_y/m_y = 3/2$, $n_z/m_z = 1$ (Fig. 5-19, mode I), the metamaterial is with 3D negative Poisson's ratios as both ν_{HB} and ν_{BW} decrease monotonically in negative values due to $n_i/m_i \geq 1$ (blue solid lines in Fig. 5-19(b) and (c)). Then, two NPR modules in each x -direction series assembly are reconfigured to PPR state to set $n_x/m_x = 1/2$ while keeping $n_y/m_y = 3/2$, $n_z/m_z = 1$ (mode II). It is observed that ν_{HB} is the same as that of mode I (the grey dash line coincides with the blue solid line in Fig. 5-19(b)), while ν_{BW} changes from negative to positive passing zero with the increasing folding angle β (grey dash line in Fig. 5-19(c)). Next, one NPR module in each y -direction series assembly is reconfigured to PPR state to set $n_y/m_y = 2/3$ while keeping $n_x/m_x = 1/2$, $n_z/m_z = 1$ (mode III), both ν_{HB} and ν_{BW} have experienced significant changes due to the change of n_y/m_y . It is noted that ν_{HB} increases from -0.71 to $+\infty$ with β , while ν_{BW} first increases from -0.78 to $+\infty$, then switches to $-\infty$ at $\beta = 33.69^\circ$, and finally reaches -1.63 (black solid lines in Fig. 5-19(b) and (c)). Furthermore, if one set $n_z/m_z = 1/3$ by reconfiguring two NPR modules to PPR state and keep $n_x/m_x = 1/2$, $n_y/m_y = 2/3$, ν_{HB} will decrease from -1.86 to $-\infty$, then switches to $+\infty$ at $\beta = 18.42^\circ$, and finally reaches -0.41 (red dash line in Fig. 5-19(b)) due to the change of n_z/m_z compared to mode III, while the value of ν_{BW} is the same with that in mode III as Poisson's ratio ν_{BW} is independent of n_z/m_z (the red dash line coincides with the black solid line in Fig. 5-19(c)). These four modes present the typical characteristics of 3D Poisson's ratios, i.e., both in-plane and out-plane negative ratios, one negative and one positive, or switching between the negative and positive several times during the deformation of metamaterials.

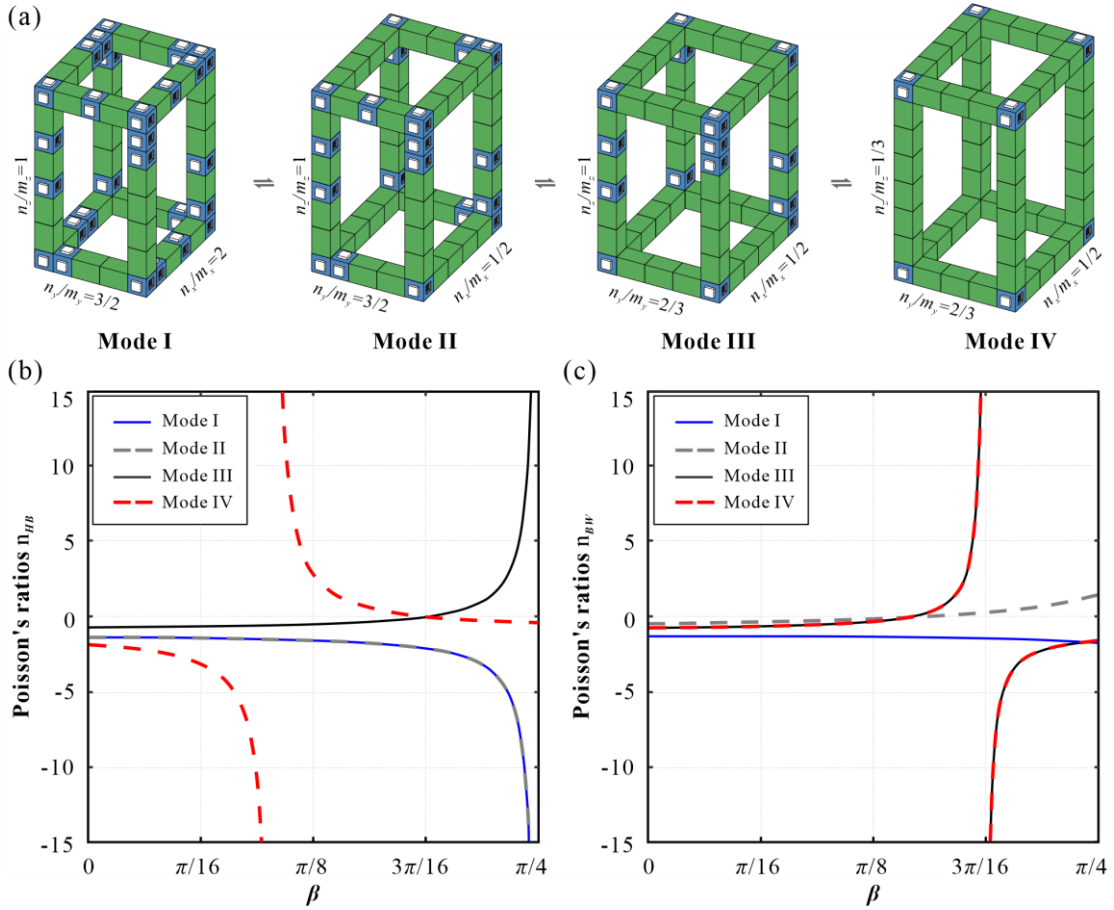


Fig. 5-19 The reconstruction of the metamaterial with $(m_x + n_x = 6)$, $(m_y + n_y = 5)$, $(m_z + n_z = 8)$ modules. (a) Bifurcation configurations in four typical modes and their Poisson's ratios ν_{HB} in (b) and ν_{BW} in (c), where $n_x/m_x = 2$, $n_y/m_y = 3/2$, $n_z/m_z = 1$ in mode I, $n_x/m_x = 1/2$, $n_y/m_y = 3/2$, $n_z/m_z = 1$ in mode II, $n_x/m_x = 1/2$, $n_y/m_y = 2/3$, $n_z/m_z = 1$ in mode III, and $n_x/m_x = 1/2$, $n_y/m_y = 2/3$, $n_z/m_z = 1/3$ in mode IV.

5.5 A Family of Single DOF Reconfigurable Polygon Prisms

Up to this point, the exposition has underscored the strides made in the advancement of single DOF reconfigurable modules formed by embedding multi-DOFs PLGs into a cube for use in metamaterials with tuneable programmable mechanical properties. Directing the focus back to the intricate process of constructing a Wohlhart cube, considerations are extended beyond the confines of a cube. Specifically, if ambition extends to the construction of not just a cube but also encompasses triangular prisms ($N=3$), rectangular prisms ($N=4$), pentagonal prisms ($N=5$), and hexagonal prisms ($N=6$), as delineated in section 4.4.2 of chapter 4, a distinct class of single DOF reconfigurable polygonal prisms can be derived, as visually depicted in Fig. 5-20.

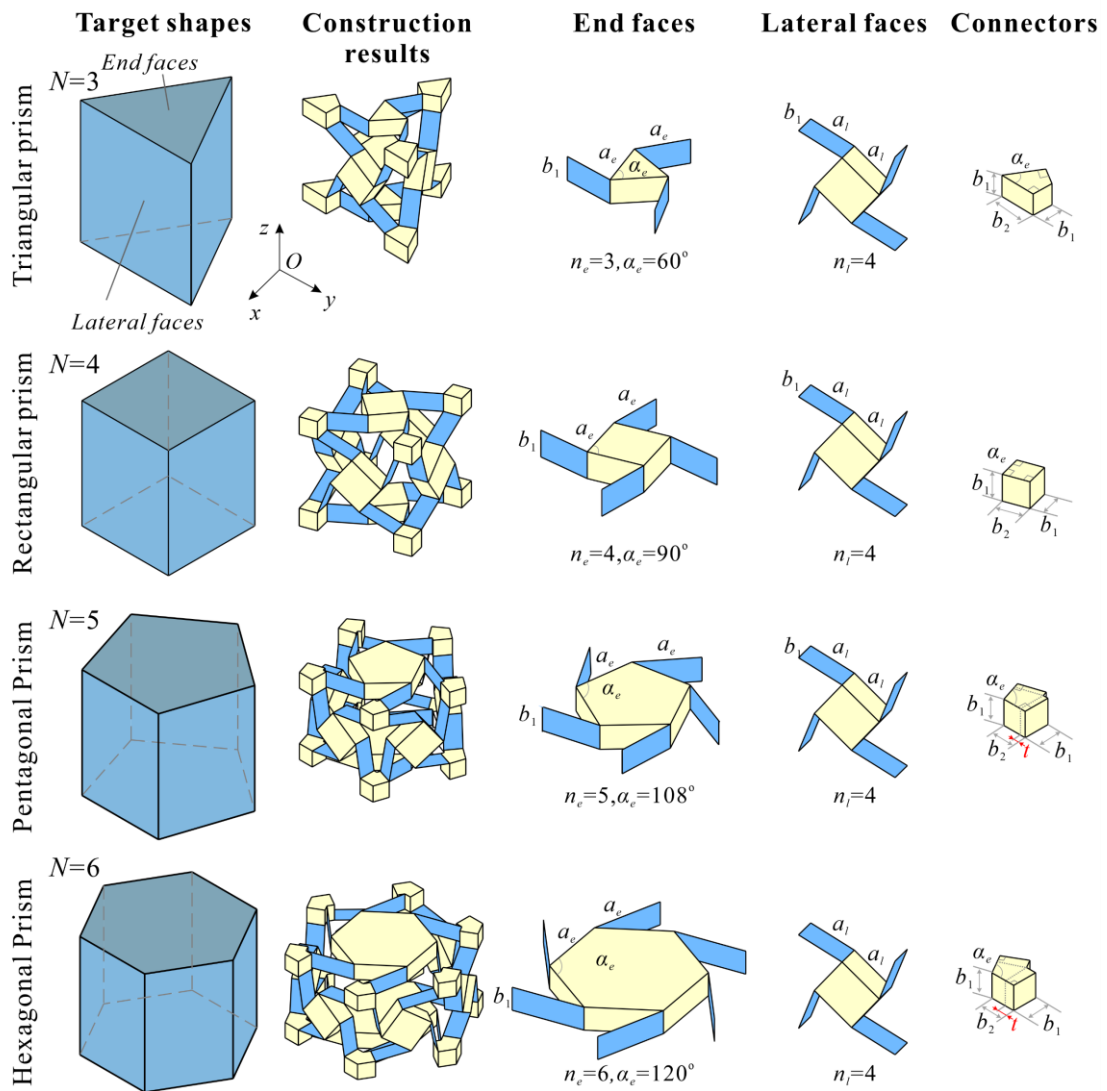


Fig. 5-20 Construction of single DOF reconfigurable polygon prisms.

Within these novel configurations, the PLGs embedded on the end faces consist of $n_e(N)$ rigid links of side length $a_e \times b_1$ and n_e -sided regular polygon characterized by the angle $\alpha_e = (N-2)\pi/N$ and side length a_e , where the subscript e indicates that the parameter pertains to a PLG on the end face. In contrast, the components attached to the lateral faces are always $n_l = 4$ PLGs constructed with four identical rigid links of sides a_l and b_l attached to the square centre body where the subscript l indicates that the parameter pertains to a PLG on the lateral face. Simultaneously, the connector undergoes a transformation, assuming the form of a panel resembling a kite. This distinctive panel is delineated by an angle α_e , two equal opposite angles measuring

90° each, and possesses a thickness b_1 , along with side lengths b_1 and b_2 ($b_2 = b_1 \times \tan(\pi/2 - \alpha_e/2)$).

To achieve the reconfiguration between expandable prism paths and elongated prism paths, as illustrated in Fig. 5-21, it is imperative that the maximum external circle size of the PLGs on end faces surpass or at least equal the diameter of the internal tangent circle formed by the PLGs on the lateral faces when fully unfolded in perfect symmetry. Conversely, for the reconfiguration between elongated prism paths and twist prism paths, a crucial stipulation is that the connection distance between two adjacent connectors in the fully folded configuration must align with both the length of the link and the side length of the polygon on the end faces, denoted as α_e .

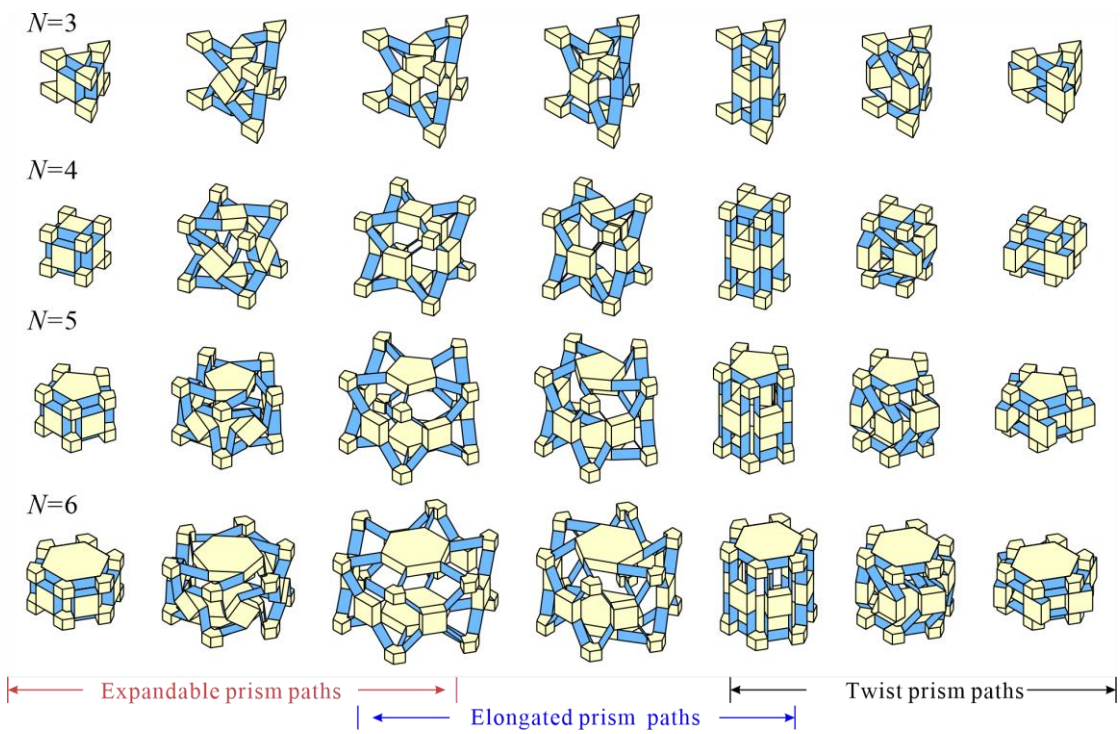


Fig. 5-21 The motion process of single DOF reconfigurable polygon prisms in expandable prism paths, elongated prism paths and twist prism paths.

In cases where $N=3$ and 4, ensuring $a_l = a_e$ satisfies the reconfiguration conditions. However, for cases where $N=5$ and 6, additional panels, characterized by a thickness denoted as t , must be introduced to the kite shape with an angle α_e along both sides to satisfy the first condition, following relationship:

$$\sin(\pi/N)(a_e + a_e / \sin(\pi/N)) = a_l / 2 + \sqrt{2}a_l / 2 + t \quad (5-52)$$

At the same time, the second condition is necessary:

$$a_e = a_l + 2t \quad (5-53)$$

As a result, the culmination of these design considerations ensures that all polygonal prisms undergo continuous bifurcation between expandable prism paths, elongated prism paths, and twist prism paths seamlessly. This intrinsic kinematic bifurcation is accompanied by distinctive mechanical behaviours, namely NPR, PPR, and ZPR, as visually depicted in Fig. 5-21.

5.6 Conclusions

In this chapter, the kinematics of the Wohlhart cube were analysed, revealing three kinematic paths, EC, EP, and LT paths that intersect at bifurcation points, B_0 and $B_x/B_y/B_z$. Taking a single mechanism as the module, it can switch among distinct Poisson's ratios, NPR, PPR, and ZPR under the EC, EP, and LT paths through the bifurcation. Hence, Poisson's ratios can be tuned with the motion of the module but are not sensitive to the geometric parameters. Such module also exhibits tuneable chirality and stiffness along the different kinematic paths. Further studies found that modules in EC path with NPR state and that in EP path with PPR state can deform cooperatively due to compatible topological features, which provides a new paradigm to form a series assembly of the module, whose Poisson's ratios can be programmed by regulating the proportion of modules in PPR or NPR states through the reconfiguration of each module between NPR and PPR states. Next taking this series assembly as a column, 3D metamaterials can be constructed by implanting the columns as the frame of a cuboid tessellation. Owing to the reconfigurability of the module, one can independently program the Poisson's ratios in orthogonal planes within a wide range from $-\infty$ to $+\infty$ by adjusting the ratio of the number of modules in PPR and NPR states, which greatly enhances the flexibility in the design of 3D metamaterials with programmable Poisson's ratios. Finally, the chapter is concluded with the development of a family of single DOF reconfigurable polygon prisms based on the Wohlhart cube, thereby establishing a comprehensive foundation for the subsequent exploration and application of these intriguing mechanisms.

Chapter 6 Final Remarks

At the crossover of kinematics, structural engineering, mechanics, and materials, the design of single DOF reconfigurable zero-thickness origami, thick-panel origami, and modular origami with multi-shape reconfigurations is systematically investigated in this dissertation. The investigation is based on the theory of kinematic bifurcation from the perspectives of MV crease reconfiguration, transferable hinges, reconfigurable closed-loop spatial linkage and open-chain planar linkage, which serves as theoretical foundations and technical support for the development of large-deformation mechanical metamaterials with tunability and programmability. The main achievements of this dissertation are summarized in this chapter, and opportunities for future work are highlighted.

6.1 Main Achievements

First, the challenge of searching for MV assignments that satisfy rigid foldability in large 2D origami tessellations or 3D cellular structures has been addressed by transforming the problem into a chessboard colouring problem and using programming language to solve it. The origami tessellation is initially divided into combinations of modular units, and the motion compatibility conditions for assemblies of spherical linkages are used to establish basic rules for the graphic representation of these modules. The DFS algorithm is then employed to systematically traverse the chessboard, seeking graphical solutions that adhere to the established rules, and translating them back into origami patterns with specific MV assignments. This method provides analytical value and precise assignments of MV creases while eliminating duplicate geometric configurations. The method has been demonstrated through a series of well-known 2D origami tessellations, including double corrugated tessellation, square twist pattern, generalised Mars pattern and so on. It has also been extended to 3D cellular origami structures. In this process, three types of oligo-modal origami tessellations that exhibit a constant number (≥ 2) of rigid MV assignments independent of tessellation size have identified. These types are the dual square twist, generalised Huffman pattern, and Helical pattern. Additionally, pluri-modal cellular origami is proposed, whose number of rigid MV assignments exponentially increases with tessellation size. The analysis of the theoretical and experimental results of mechanical properties shows that

NPR/ZPR/PPR can be achieved under large deformation by manipulating the MV assignments within a single origami structure. This research provides a strong theoretical foundation and technical support for the design of multifunctional structures based on mountain-valley crease reconfiguration.

- **Reconfigurable thick-panel ori-kirigami based on VTJs**

Inspired by the Jacob's Ladder Toy, a design featuring VTJs has been proposed, enabling the redirection of the joint's axis from the top or bottom panel surface to the side surface without increasing the DOF through kinematic bifurcation behaviour. An ori-kirigami unit was then constructed by replacing the four R joints in the origami vertices of a diamond thick-panel with VTJs. Kinematic analysis reveals that this single DOF unit with uniform thickness can transition between an origami, a kirigami, and three ori-kirigami motion branches through the manipulation of vertically transferable joints, thereby altering the underlying linkage type. Subsequently, the thick-panel ori-kirigami unit and its horizontal mirrors were interconnected by R joints with axes in the thickness direction, while the basic unit and its vertical mirrors were linked by VTJs to create a 2×2 tessellation. By maintaining the axes of any transferable joints situated on the upper and lower surfaces of the panel, the uniform-thickness panels can be folded into a compact volume with no gaps in the origami branch. Conversely, by ensuring that the axes of all transfer hinges are located in the thickness direction, the uniform-thickness panels can be deformed in-plane in the kirigami branch. If some joints are positioned on the top and bottom surfaces of the panel and others are located in the thickness direction, the uniform-thickness panels can assume multiple configurations in three ori-kirigami I-III branches. As the tessellation transitions between different motion branches, it demonstrates significant tunability in terms of deployable ratio (with a maximum deployable ratio of 24), Poisson's ratio (ranging from anisotropic values varying from $-\infty$ to $+\infty$ to isotropic values of -1), and load-bearing capacity (ranging from 0.4 to 1567 times its own weight). This endeavour not only enhances the diversity of kirigami and ori-kirigami techniques but also paves the way for utilizing transferable joints to realize one DOF reconfigurable thick-panel structure with tunable properties.

- **Tuneable metamaterials based on spatial 7R linkage in modular origami form**

A modular origami unit with a single-loop spatial 7R linkage with one DOF is first proposed. Its kinematic model is established, and the effects of geometrical parameters on the kinematic behaviours are systematically analyzed. The designed units can be intricately assembled back-to-back to create diverse one DOF reconfigurable modules, exhibiting significant symmetry changes. Experimental demonstrations showcase the active tuning and control of the shape and symmetry of these origami modules through the strategic activation of variable stiffness beams or air pockets. The investigation highlights the potential to realize various 2D discrete symmetry groups, encompassing ten point groups, seven line groups, and seventeen space groups (wallpaper groups), all within a unified design framework. Subsequently, a shoulder-to-shoulder assembly scheme for 7R units is proposed to construct another type of single DOF reconfigurable 2D modules. Geometric dimensional variations induced by reconfiguration between different configurations are investigated based on a kinematic model. The effect on the sign of Poisson's ratio is theoretically analyzed. Additionally, a variety of single DOF 3D modules are formed by integrating the 2D modules on the faces of carefully selected polyhedrons. Theoretical analysis indicates that these proposed 3D modules can achieve purely negative, zero, or positive Poisson's ratios due to the orthogonal decoupling behaviour arising from the kinematic bifurcation. Notably, the 3D module with a rectangular prism ($N=4$) contour is tuneable in all signs of in-plane and out-plane Poisson's ratio.

- **3D programmable metamaterials based on reconfigurable polyhedron modules**

A comprehensive analysis of the kinematics of the Wohlhart cube has been conducted based on closure equations for planar linkage groups under symmetry constraints, revealing three distinctive kinematic paths, EC, EP, and LT paths that insert as at bifurcation points, B_0 and $B_x/B_y/B_z$. When considering a single mechanism as the module, it is demonstrated that the module can switch among distinct Poisson's ratios (NPR, PPR, and ZPR) along the EC, EP, and LT paths through the bifurcation. Notably, Poisson's ratios can be actively tuned with the folding ratio, yet is almost independent of the geometrical parameters. Furthermore, the module exhibits tunable chirality and stiffness along different kinematic paths. Subsequent investigations highlight that

modules following the EC path with the NPR state and those in the EP path with the PPR state can deform compatibly due to compatible topological features. This discovery introduces a novel paradigm for forming a series assembly of modules, where the Poisson's ratios can be programmed by regulating the proportion of modules in PPR or NPR states through the reconfiguration of each module between NPR and PPR states. Building upon this concept, a series assembly is considered as a column, and 3D metamaterials are constructed by implanting these columns as the frame of a cuboid tessellation. Leveraging the reconfigurability of the module, it becomes possible to independently program the Poisson's ratios in orthogonal planes over a wide range from $-\infty$ to $+\infty$. At last, reconfigurable polyhedron modules with NPR, ZPR, and PPR are extended from the Wohlhart cube to a series of single DOF reconfigurable polygon prisms. The metamaterials with switchable Poisson's ratio, local and global chirality and tuneable stiffness in a wider tuneable range are of great application potentials in shape-morphing systems for various fields, such as flexible metamaterials, morphing architectures, bioengineering tissue and robotics.

6.2 Future Work

This dissertation is dedicated to explore the application of kinematic bifurcation to design single DOF origami structures with multiple shape reconfigurations, and to develop them into mechanical metamaterials with tuneable properties. To enhance the practical use of this type of metamaterial, several potential topics can be further explored.

First, due to the rich reconfigurability, proposed method that combines graphic representation and motion compatibility conditions can discover unique homogeneous configurations in many zero-thickness origami structures, especially heterogeneous configurations that are hard to find by human heuristics, providing potential applications for reconfigurable metamaterials and deployable structures with multifunctional requirements. Thanks to the explicit solutions of the closure equation of spherical 4R linkage, proposed method can be highly useful when dealing with the reconfigurability of four-crease origami pattern. With the more profound analysis of the kinematics of spherical 5R and 6R linkages, it is believed that this method can be extended to origami structures with four-, five-, and six-crease mixed vertices, which is next target.

Second, in this work, a series of novel designs with thick-panel origami, kirigami and ori-kirigami motion branches are obtained by embedding transferable joints into a flat-foldable six-crease pattern. The design method is expected to be extended to flat-foldable four-crease and even non-flat-foldable crease patterns and hybrid origami vertex patterns to construct novel origami structures. Among these deformation modes, the thick-panel ori-kirigami modes couple a global out-of-plane deformation with a local in-plane deformation, which is expected to induce fantastic mechanical properties. Hence, the hybrid network of planar-spherical-spatial linkages needs to be investigated in depth to explore the innovative design of such novel thick-panel ori-kirigami mode.

In addition, non-periodic mechanical metamaterials exhibit excellent tunability and programmability for hybrid networks formed by different bifurcation configurations. A major challenge is how to accurately identify all possible configurations of reconfigurable networks of modular origami, and then establish the parametric analytical relationship between the unit cell's configurations, network topologies and metamaterials' properties, so as to lay the foundation for reverse designing the unit cell's configurations and network topologies with the required properties. In addition, this dissertation presented a series of mechanical metamaterials with rich geometrical and shape variations, focusing on physical properties such as Poisson's ratio, symmetry, stiffness, etc., caused by deformation mechanisms. In the future, a multidisciplinary cross-disciplinary approach can be carried out to study the essential correlation between these underlying geometry and shape changes, especially symmetry changes, and acoustics, electromagnetism, and topology^[183–186].

Further, mechanical metamaterials based on kinematic bifurcation significantly reduce the complexity of control compared to multi-DOFs systems, but there are still challenges in cooperative control as well as bifurcation control in the face of mechanical metamaterials with small cell sizes and large numbers of unit cells. Employing smart materials to actuate hundreds or even thousands of hinges in metamaterials is clearly a potential but inefficient approach. The current exploratory study shows that the controllability of this type of metamaterials can be improved from the perspective of linkage and structure coupling design by adopting physical interference, instability, and other “mechanically intelligent” ways of designing the unit cells. At the same time, the “interference” property of smart materials in bifurcation control is enhanced while the actuation property is weakened, and the actuation position and actuation mode of

metamaterials are optimized, which is expected to realize efficient bifurcation control under simple mechanical load by combining mechanical intelligence and material intelligence.

Finally, after solving the design and actuation of metamaterials based on kinematic bifurcation, a major problem is the processing and fabrication of such metamaterials. At present, 3D or 4D printing technology can effectively process three-dimensional complex structures, but its accuracy is limited and it cannot accurately process the cell at the micron and nanometre level. Most of the existing results belong to laboratory technology, and it is impossible to carry out large-scale and mass production and promotion in industrial manufacturing. Therefore, it is urgent to investigate the processing and manufacturing methods that can produce fine cellular metamaterials in large quantities for engineering applications.

References

- [1] Kadic M, Milton G W, Van Hecke M, et al. 3D metamaterials[J]. *Nature Reviews Physics*, 2019, 1(3): 198-210.
- [2] Service R F, Cho A. Strange new tricks with light[J]. *Science*, 2010, 330(6011): 1622.
- [3] Zadpoor A A. Mechanical meta-materials[J]. *Materials Horizons*, 2016, 3(5): 371-381.
- [4] Bertoldi K, Vitelli V, Christensen J, et al. Flexible mechanical metamaterials[J]. *Nature Reviews Materials*, 2017, 2(11): 17066.
- [5] Ren X, Das R, Tran P, et al. Auxetic metamaterials and structures: A review[J]. *Smart Materials and Structures*, 2018, 27(2): 023001.
- [6] Yang H, Ma L. 1D to 3D multi-stable architected materials with zero Poisson's ratio and controllable thermal expansion[J]. *Materials & Design*, 2020, 188: 108430.
- [7] Schenk M, Guest S D. On zero stiffness[J]. *Proceedings of the Institution of Mechanical Engineers, Part C: Journal of Mechanical Engineering Science*, 2014, 228(10): 1701-1714.
- [8] Hewage T A M, Alderson K L, Alderson A, et al. Double-negative mechanical metamaterials displaying simultaneous negative stiffness and negative Poisson's ratio properties[J]. *Advanced Materials*, 2016, 28(46): 10323-10332.
- [9] Ai L, Gao X L. Three-dimensional metamaterials with a negative poisson's ratio and a non-positive coefficient of thermal expansion[J]. *International Journal of Mechanical Sciences*, 2018, 135: 101-113.
- [10] Lim T C. An anisotropic negative thermal expansion metamaterial with sign-toggling and sign-programmable poisson's ratio[J]. *Oxford Open Materials Science*, 2022, 2(1): itac007.
- [11] Zheng X, Lee H, Weisgraber T H, et al. Ultralight, ultrastiff mechanical metamaterials[J]. *Science*, 2014, 344(6190): 1373-1377.
- [12] Zhang H, Paik J. Kirigami design and modeling for strong, lightweight metamaterials[J]. *Advanced Functional Materials*, 2022, 32(21): 2107401.
- [13] Hu Z, Wei Z, Wang K, et al. Engineering zero modes in transformable mechanical metamaterials[J]. *Nature Communications*, 2023, 14(1): 1266.
- [14] Lee R H, Mulder E A B, Hopkins J B. Mechanical neural networks: Architected materials that learn behaviors[J]. *Science Robotics*, 2022, 7(71): eabq7278.

- [15] El Helou C, Buskohl P R, Tabor C E, et al. Digital logic gates in soft, conductive mechanical metamaterials[J]. *Nature Communications*, 2021, 12(1): 1633.
- [16] Hyatt L P, Harne R L. Programming metastable transition sequences in digital mechanical materials[J]. *Extreme Mechanics Letters*, 2023, 59: 101975.
- [17] Mei T, Meng Z, Zhao K, et al. A mechanical metamaterial with reprogrammable logical functions[J]. *Nature Communications*, 2021, 12(1): 7234.
- [18] Meng Z, Chen W, Mei T, et al. Bistability-based foldable origami mechanical logic gates[J]. *Extreme Mechanics Letters*, 2021, 43: 101180.
- [19] Xin X, Liu L, Liu Y, et al. 4D printing auxetic metamaterials with tunable, programmable, and reconfigurable mechanical properties[J]. *Advanced Functional Materials*, 2020, 30(43): 2004226.
- [20] Yan C. Review on kinematic metamaterials[J]. *Journal of Mechanical Engineering*, 2020, 56(19): 2.
- [21] Lang R J. Twists, tilings, and tessellations: Mathematical methods for geometric origami[M]. CRC Press, 2017.
- [22] Zirbel S A, Lang R J, Thomson M W, et al. Accommodating thickness in origami-based deployable arrays[J]. *Journal of Mechanical Design*, 2013, 135(11): 111005.
- [23] Melancon D, Gorissen B, García-Mora C J, et al. Multistable inflatable origami structures at the metre scale[J]. *Nature*, 2021, 592(7855): 545-550.
- [24] Lee D Y, Kim J K, Sohn C Y, et al. High-load capacity origami transformable wheel[J]. *Science Robotics*, 2021, 6(53): eabe0201.
- [25] Deng Y, Liu W, Cheung Y K, et al. Curved display based on programming origami tessellations[J]. *Microsystems & Nanoengineering*, 2021, 7(1): 101.
- [26] Ma J, Dai H, Chai S, et al. Energy absorption of sandwich structures with a kirigami-inspired pyramid foldcore under quasi-static compression and shear[J]. *Materials & Design*, 2021, 206: 109808.
- [27] Li S, Stampfli J J, Xu H J, et al. A vacuum-driven origami “magic-ball” soft gripper[C]. 2019 International Conference on Robotics and Automation (ICRA). Montreal, QC, Canada: IEEE, 2019: 7401-7408.
- [28] Suzuki H, Wood R J. Origami-inspired miniature manipulator for teleoperated microsurgery[J]. *Nature Machine Intelligence*, 2020, 2(8): 437-446.
- [29] Zhang Z, Xu Z, Emu L, et al. Active mechanical haptics with high-fidelity perceptions for immersive virtual reality[J]. *Nature Machine Intelligence*, 2023, 5(6): 643-655.
- [30] Li D, Dong L, Lakes R S. A unit cell structure with tunable Poisson’s ratio from positive to negative[J]. *Materials Letters*, 2016, 164: 456-459.

-
- [31] Florijn B, Coulais C, Van Hecke M. Programmable mechanical metamaterials[J]. *Physical Review Letters*, 2014, 113(17): 175503.
- [32] Sinha P, Mukhopadhyay T. Programmable multi-physical mechanics of mechanical metamaterials[J]. *Materials Science and Engineering: R: Reports*, 2023, 155: 100745.
- [33] Origami-Kunst A B. Origami crane folded from one uncut square of paper[EB/OL]. <https://www.flickr.com/photos/origami-kunst/478379801/>.
- [34] Miyamoto Y. RES Octagon Star[EB/OL]. https://www.flickr.com/photos/yoshinobu_miyamoto/14299237028/.
- [35] Mancini F. Snap Icosahedron[EB/OL]. <https://www.flickr.com/photos/mancinerie/3617018985/>.
- [36] Coulais C, Sounas D, Alù A. Static non-reciprocity in mechanical metamaterials[J]. *Nature*, 2017, 542(7642): 461-464.
- [37] Tsai L W. The mechanics of serial and parallel manipulators[M]. John Wiley & Sons, Inc, 1999.
- [38] Dai J S, Rees Jones J. Mobility in metamorphic mechanisms of foldable/erectable kinds[J]. *Journal of Mechanical Design*, 1999, 121(3): 375-382.
- [39] Hull T. Project origami: Activities for exploring mathematics, second edition[M]. 0 ed. A K Peters/CRC Press, 2012.
- [40] Yang F, Chen Y, Kang R, et al. Truss transformation method to obtain the non-overconstrained forms of 3D overconstrained linkages[J]. *Mechanism and Machine Theory*, 2016, 102: 149-166.
- [41] Tachi T. Generalization of rigid foldable quadrilateral mesh origami[C]. *Proceedings of the International Association for Shell and Spatial Structures (IASS) Symposium*. Valencia, 2009: 2287-2294.
- [42] Chen Y, Lv W, Peng R, et al. Mobile assemblies of four-spherical-4R-integrated linkages and the associated four-crease-integrated rigid origami patterns[J]. *Mechanism and Machine Theory*, 2019, 142: 103613.
- [43] Zimmermann L, Stanković T. Rigid and flat foldability of a degree-four vertex in origami[J]. *Journal of Mechanisms and Robotics*, 2020, 12(1): 011004.
- [44] Zhang X, Chen Y. Vertex-splitting on a diamond origami pattern[J]. *Journal of Mechanisms and Robotics*, 2019, 11(3): 031014.
- [45] Feng H, Peng R, Zang S, et al. Rigid foldability and mountain-valley crease assignments of square-twist origami pattern[J]. *Mechanism and Machine Theory*, 2020, 152: 103947.

- [46] Denavit J, Hartenberg R S. A kinematic notation for lower-pair mechanisms based on matrices[J]. *Journal of Applied Mechanics*, 1955, 22(2): 215-221.
- [47] Chen Y, Peng R, You Z. Origami of thick panels[J]. *Science*, 2015, 349(6246): 396-400.
- [48] Zhang X, Chen Y. The diamond thick-panel origami and the corresponding mobile assemblies of plane-symmetric Bricard linkages[J]. *Mechanism and Machine Theory*, 2018, 130: 585-604.
- [49] Zhang X, Chen Y. Mobile assemblies of Bennett linkages from four-crease origami patterns[J]. *Proceedings of the Royal Society A: Mathematical, Physical and Engineering Sciences*, 2018, 474(2210): 20170621.
- [50] Yang J, Zhang X, Chen Y, et al. Folding arrays of uniform-thickness panels to compact bundles with a single degree of freedom[J]. *Proceedings of the Royal Society A: Mathematical, Physical and Engineering Sciences*, 2022, 478(2261): 20220043.
- [51] Yang Y, You Z. Geometry of transformable metamaterials inspired by modular origami[J]. *Journal of Mechanisms and Robotics*, 2018, 10(2): 021001.
- [52] Beggs J S. *Advanced mechanism*[M]. Macmillan.
- [53] Chen Y, Feng H, Ma J, et al. Symmetric waterbomb origami[J]. *Proceedings of the Royal Society A: Mathematical, Physical and Engineering Sciences*, 2016, 472(2190): 20150846.
- [54] Tachi T. Designing freeform origami tessellations by generalizing Resch's patterns[J]. *Journal of Mechanical Design*, 2013, 135(11): 111006.
- [55] Wohlhart K. Kinematotropic linkages[M]. Lenarčič J, Parenti-Castelli V. *Recent Advances in Robot Kinematics*. Dordrecht: Springer Netherlands, 1996: 359-368.
- [56] Galletti C, Fanghella P. Single-loop kinematotropic mechanisms[J]. *Mechanism and Machine Theory*, 2001, 36(6): 743-761.
- [57] Zhang L, Wang D, Dai J S. Biological modeling and evolution based synthesis of metamorphic mechanisms[J]. *Journal of Mechanical Design*, 2008, 130(7): 072303.
- [58] Kong X, Pfurner M. Type synthesis and reconfiguration analysis of a class of variable-DOF single-loop mechanisms[J]. *Mechanism and Machine Theory*, 2015, 85: 116-128.
- [59] Yan H S, Kuo C H. Topological representations and characteristics of variable kinematic joints[J]. *Journal of Mechanical Design*, 2006, 128(2): 384-391.
- [60] Yan H S, Liu N T. Finite-State-Machine Representations for Mechanisms and Chains With Variable Topologies[C]. Volume 7A: 26th Biennial Mechanisms and

- Robotics Conference. American Society of Mechanical Engineers Digital Collection, 2000: 57-63.
- [61] Zhang K, Fang Y, Wei G, et al. Structural representation of reconfigurable linkages[M]. Dai J S, Zoppi M, Kong X. *Advances in Reconfigurable Mechanisms and Robots I*. London: Springer London, 2012: 127-137.
- [62] Aimedee F, Gogu G, Dai J S, et al. Systematization of morphing in reconfigurable mechanisms[J]. *Mechanism and Machine Theory*, 2016, 96: 215-224.
- [63] Kuo C H, Dai J S, Yan H S. Reconfiguration principles and strategies for reconfigurable mechanisms[C]. 2009 ASME/IFTToMM International Conference on Reconfigurable Mechanisms and Robots. London, UK: 1-7.
- [64] Carroll D W, Magleby S P, Howell L L, et al. Simplified manufacturing through a metamorphic process for compliant ortho-planar mechanisms[C]. ASME International Mechanical Engineering Congress and Exposition: Vol. 42150. 2005: 389-399.
- [65] Zhang L, Dai J S. An overview of the development on reconfiguration of metamorphic mechanisms[C]. 2009 ASME/IFTToMM International Conference on Reconfigurable Mechanisms and Robots. London, UK, 2009: 8-12.
- [66] Chen Y, You Z. An extended Myard linkage and its derived 6R linkage[J]. *Journal of Mechanical Design*, 2008, 130(5): 052301.
- [67] Chen Y, You Z. Two-fold symmetrical 6R foldable frame and its bifurcations[J]. *International Journal of Solids and Structures*, 2009, 46(25-26): 4504-4514.
- [68] Song C Y, Chen Y. Multiple linkage forms and bifurcation behaviours of the double-subtractive-Goldberg 6R linkage[J]. *Mechanism and Machine Theory*, 2012, 57: 95-110.
- [69] Song C Y, Chen Y, Chen I M. A 6R linkage reconfigurable between the line-symmetric Bricard linkage and the Bennett linkage[J]. *Mechanism and Machine Theory*, 2013, 70: 278-292.
- [70] Song C Y, Feng H, Chen Y, et al. Reconfigurable mechanism generated from the network of Bennett linkages[J]. *Mechanism and Machine Theory*, 2015, 88: 49-62.
- [71] Chai X, Kang X, Gan D, et al. Six novel 6R metamorphic mechanisms induced from three-series-connected Bennett linkages that vary among classical linkages[J]. *Mechanism and Machine Theory*, 2021, 156: 104133.
- [72] Chen Y, Chai W H. Bifurcation of a special line and plane symmetric Bricard linkage[J]. *Mechanism and Machine Theory*, 2011, 46(4): 515-533.

- [73] Feng H, Chen Y, Dai J S, et al. Kinematic study of the general plane-symmetric Bricard linkage and its bifurcation variations[J]. *Mechanism and Machine Theory*, 2017, 116: 89-104.
- [74] Zhang K, Dai J S. Screw-system-variation enabled reconfiguration of the Bennett plano-spherical hybrid linkage and its evolved parallel mechanism[J]. *Journal of Mechanical Design*, 2015, 137(6): 062303.
- [75] Li L, Li T fei, Dai J sheng, et al. A novel line-symmetric Goldberg 6R linkage with bifurcation property[J]. *Journal of Central South University*, 2020, 27(12): 3754-3767.
- [76] Tang Z, Dai J S. Multi-furcation variations of two novel double-centered mechanisms based on higher order kinematic analyses and singular value decomposition[J]. *Journal of Mechanisms and Robotics*, 2024, 16(5): 051011.
- [77] Lu S, Zlatanov D, Ding X, et al. Reconfigurable chains of bifurcating type III Bricard linkages[M]. Ding X, Kong X, Dai J S. *Advances in Reconfigurable Mechanisms and Robots II: Vol. 36*. Cham: Springer International Publishing, 2016: 3-14.
- [78] Kong X, Huang C. Type synthesis of single-DOF single-loop mechanisms with two operation modes[C]. *2009 ASME/IFTOMM International Conference on Reconfigurable Mechanisms and Robots*. London, UK, 2009: 136-141.
- [79] Zhang K, Müller A, Dai J S. A novel reconfigurable 7R linkage with multifurcation[M]. Ding X, Kong X, Dai J S. *Advances in Reconfigurable Mechanisms and Robots II: Vol. 36*. Cham: Springer International Publishing, 2016: 15-25.
- [80] Cao W ao, Zhang D, Ding H. A novel two-layer and two-loop deployable linkage with accurate vertical straight-line motion[J]. *Journal of Mechanical Design*, 2020, 142(10): 103301.
- [81] Kong X. A variable-DOF single-loop 7R spatial mechanism with five motion modes[J]. *Mechanism and Machine Theory*, 2018, 120: 239-249.
- [82] Zhou C, Chen H, Guo W, et al. Novel bundle folding deployable mechanisms to realize polygons and polyhedrons[J]. *Mechanism and Machine Theory*, 2023, 181: 105210.
- [83] Chai X, Zhang C, Dai J S. A single-loop 8R linkage with plane-symmetry and bifurcation property[C]. *2018 International Conference on Reconfigurable Mechanisms and Robots (ReMAR)*. 2018: 1-8.
- [84] Peng R, Ma J, Chen Y. The effect of mountain-valley folds on the rigid foldability of double corrugated pattern[J]. *Mechanism and Machine Theory*, 2018, 128: 461-474.

-
- [85] Zhang K, Dai J S. Reconfiguration of the plane-symmetric double-spherical 6R linkage with bifurcation and trifurcation[J]. Proceedings of the Institution of Mechanical Engineers, Part C: Journal of Mechanical Engineering Science, 2016, 230(3): 473-482.
- [86] Zhang K, Dai J S. Trifurcation of the evolved Sarrus-motion linkage based on parametric constraints[M]. Advances in Robot Kinematics. Cham: Springer International Publishing, 2014: 345-353.
- [87] Zhang K, Dai J S. A kirigami-inspired 8R linkage and its evolved overconstrained 6R linkages with the rotational symmetry of order two[J]. Journal of Mechanisms and Robotics, 2014, 6(2): 021007.
- [88] Ma X, Zhang K, Dai J S. Novel spherical-planar and Bennett-spherical 6R metamorphic linkages with reconfigurable motion branches[J]. Mechanism and Machine Theory, 2018, 128: 628-647.
- [89] Feng H, Peng R, Ma J, et al. Rigid foldability of generalized triangle twist origami pattern and its derived 6R linkages[J]. Journal of Mechanisms and Robotics, 2018, 10(5): 051003.
- [90] Liu W, Chen Y. A double spherical 6R linkage with spatial crank-rocker characteristics inspired by kirigami[J]. Mechanism and Machine Theory, 2020, 153: 103995.
- [91] Liu W, Chen Y. Origami/kirigami-inspired reconfigurable 6R linkages and tessellations[C]. International Conference on Mechanism and Machine Science. Springer, 2022: 1333-1357.
- [92] Tang Z, Dai J S. Bifurcated configurations and their variations of an 8-bar linkage derived from an 8-kaleidocycle[J]. Mechanism and Machine Theory, 2018, 121: 745-754.
- [93] Wang R, Song Y, Dai J S. Reconfigurability of the origami-inspired integrated 8R kinematotropic metamorphic mechanism and its evolved 6R and 4R mechanisms[J]. Mechanism and Machine Theory, 2021, 161: 104245.
- [94] Kang X, Zhang X, Dai J S. First- and second-order kinematics-based constraint system analysis and reconfiguration identification for the queer-square mechanism[J]. Journal of Mechanisms and Robotics, 2019, 11(1): 011004.
- [95] Roschel O. A fulleroid - like mechanism based on the cube[J]. Journal for geometry and graphics, 2012, 16(1): 19-27.
- [96] Li R, Sun X, Chen Y, et al. Design and analysis of reconfigurable deployable polyhedral mechanisms with straight elements[J]. Journal of Mechanisms and Robotics, 2019, 11(4): 044502.

- [97] Li R, Yao Y an, Kong X. A class of reconfigurable deployable platonic mechanisms[J]. *Mechanism and Machine Theory*, 2016, 105: 409-427.
- [98] Li R, Yao Y an, Kong X. Reconfigurable deployable polyhedral mechanism based on extended parallelogram mechanism[J]. *Mechanism and Machine Theory*, 2017, 116: 467-480.
- [99] Hao Y, Li R, Sun X, et al. Design and motion pattern analysis of reconfigurable cube mechanism[J]. *Journal of Mechanical Engineering*, 2020, 56(13): 120-127.
- [100] Liu J, Zhao X, Ding H. A class of N-sided antiprism deployable polyhedral mechanisms based on an asymmetric eight-bar linkage[J]. *Mechanism and Machine Theory*, 2020, 150: 103882.
- [101] Zhang X, Zhou X, Li M, et al. Three-dimensional mobile assemblies based on threefold-symmetric Bricard linkages[J]. *Journal of Mechanisms and Robotics*, 2023, 16(044501).
- [102] Wei G. Geometric analysis and theoretical development of deployable polyhedral mechanisms[D]. King's College London, 2012.
- [103] Kiper G. A historical review of polyhedral linkages[M]. Ceccarelli M, Aslan Seyhan I. *Explorations in the History and Heritage of Machines and Mechanisms: Vol. 47*. Cham: Springer Nature Switzerland, 2024: 227-242.
- [104] Tarnai T. Kinematic bifurcation[M]. *Deployable Structures*. Springer, 2001: 143-169.
- [105] Kumar P, Pellegrino S. Computation of kinematic paths and bifurcation points[J]. *International Journal of Solids and Structures*, 2000, 37(46-47): 7003-7027.
- [106] Pellegrino S. Structural computations with the singular value decomposition of the equilibrium matrix[J]. *International Journal of Solids and Structures*, 1993, 30(21): 3025-3035.
- [107] Gan W W, Pellegrino S. Numerical approach to the kinematic analysis of deployable structures forming a closed loop[J]. *Proceedings of the Institution of Mechanical Engineers, Part C: Journal of Mechanical Engineering Science*, 2006, 220(7): 1045-1056.
- [108] Gan D, Dai J S, Liao Q. Constraint analysis on mobility change of a novel metamorphic parallel mechanism[J]. *Mechanism and Machine Theory*, 2010, 45(12): 1864-1876.
- [109] Koryo M. Method of packaging and deployment of large membranes in space[J]. *The Institute of Space and Astronautical Science report*, 1985, 618: 1-9.
- [110] Ma J, Feng H, Chen Y, et al. Folding of tubular waterbomb[J]. *Research*, 2020, 2020: 2020/1735081.

-
- [111] Lang R J, Magleby S, Howell L. Single degree-of-freedom rigidly foldable cut origami flashers[J]. *Journal of Mechanisms and Robotics*, 2016, 8(3): 031005.
- [112] Schenk M, Guest S D. Geometry of miura-folded metamaterials[J]. *Proceedings of the National Academy of Sciences*, 2013, 110(9): 3276-3281.
- [113] Wei Z Y, Guo Z V, Dudte L, et al. Geometric mechanics of periodic pleated origami[J]. *Physical Review Letters*, 2013, 110(21): 215501.
- [114] Liu Z, Fang H, Xu J, et al. A novel origami mechanical metamaterial based on miura-variant designs: Exceptional multistability and shape reconfigurability[J]. *Smart Materials and Structures*, 2021, 30(8): 085029.
- [115] Nauroze S A, Novelino L S, Tentzeris M M, et al. Continuous-range tunable multilayer frequency-selective surfaces using origami and inkjet printing[J]. *Proceedings of the National Academy of Sciences*, 2018, 115(52): 13210-13215.
- [116] Ma J, Song J, Chen Y. An origami-inspired structure with graded stiffness[J]. *International Journal of Mechanical Sciences*, 2018, 136: 134-142.
- [117] Yuan L, Dai H, Song J, et al. The behavior of a functionally graded origami structure subjected to quasi-static compression[J]. *Materials & Design*, 2020, 189: 108494.
- [118] Wang H, Zhao D, Jin Y, et al. Modulation of multi-directional auxeticity in hybrid origami metamaterials[J]. *Applied Materials Today*, 2020, 20: 100715.
- [119] Filipov E T, Tachi T, Paulino G H. Origami tubes assembled into stiff, yet reconfigurable structures and metamaterials[J]. *Proceedings of the National Academy of Sciences*, 2015, 112(40): 12321-12326.
- [120] Mousanezhad D, Kamrava S, Vaziri A. Origami-based building blocks for modular construction of foldable structures[J]. *Scientific Reports*, 2017, 7(1): 14792.
- [121] Tachi T, Miura K. Rigid-foldable cylinders and cells[J]. *Journal of The International Association for Shell and Spatial Structures*, 2012, 53(4).
- [122] Yasuda H, Yang J. Reentrant origami-based metamaterials with negative Poisson's ratio and bistability[J]. *Physical Review Letters*, 2015, 114(18): 185502.
- [123] Yasuda H, Gopalarethinam B, Kunimine T, et al. Origami-based cellular structures with in situ transition between collapsible and load-bearing configurations[J]. *Advanced Engineering Materials*, 2019, 21(12): 1900562.
- [124] Yu Y, Chen Y, Paulino G. Programming curvatures by unfolding of the triangular Resch pattern[J]. *International Journal of Mechanical Sciences*, 2023, 238: 107861.

- [125] Zhao Y, Endo Y, Kanamori Y, et al. Approximating 3D surfaces using generalized waterbomb tessellations[J]. *Journal of Computational Design and Engineering*, 2018, 5(4): 442-448.
- [126] Feng H, Ma J, Chen Y, et al. Twist of tubular mechanical metamaterials based on waterbomb origami[J]. *Scientific Reports*, 2018, 8(1): 9522.
- [127] Mukhopadhyay T, Ma J, Feng H, et al. Programmable stiffness and shape modulation in origami materials: Emergence of a distant actuation feature[J]. *Applied Materials Today*, 2020, 19: 100537.
- [128] Lv C, Krishnaraju D, Konjevod G, et al. Origami based mechanical metamaterials[J]. *Scientific Reports*, 2014, 4(1): 5979.
- [129] Hull T C, Urbanski M T. Rigid foldability of the augmented square twist[A]. *arXiv*, 2018.
- [130] Wang L C, Song W L, Fang H, et al. Reconfigurable force–displacement profiles of the square-twist origami[J]. *International Journal of Solids and Structures*, 2022, 241: 111471.
- [131] Lu L, Leanza S, Zhao R R. Origami with rotational symmetry: A review on their mechanics and design[J]. *Applied Mechanics Reviews*, 2023, 75(5): 050801.
- [132] Liu B, Liao Y, Yang Y, et al. Design and analysis of reconfigurable and deployable thin-walled architectural equipment inspired by mirror-miura origami patterns[J]. *Engineering Structures*, 2023, 286: 116059.
- [133] Pratapa P P, Liu K, Paulino G H. Geometric mechanics of origami patterns exhibiting Poisson’s ratio switch by breaking mountain and valley assignment[J]. *Physical Review Letters*, 2019, 122(15): 155501.
- [134] Yamaguchi K, Yasuda H, Tsujikawa K, et al. Graph-theoretic estimation of reconfigurability in origami-based metamaterials[J]. *Materials & Design*, 2022, 213: 110343.
- [135] Liu Z, Fang H, Xu J, et al. Discriminative transition sequences of origami metamaterials for mechanologic[J]. *Advanced Intelligent Systems*, 2023, 5(1): 2200146.
- [136] Kolken H M A, Zadpoor A A. Auxetic mechanical metamaterials[J]. *RSC Advances*, 2017, 7(9): 5111-5129.
- [137] Cho H, Seo D, Kim D N. Mechanics of auxetic materials[M]. Schmauder S, Chen C S, Chawla K K, et al. *Handbook of Mechanics of Materials*. Singapore: Springer, 2019: 733-757.
- [138] Wu G, Cho Y, Choi I, et al. Directing the deformation paths of soft metamaterials with prescribed asymmetric units[J]. *Advanced Materials*, 2015, 27(17): 2747-2752.

- [139] Tang Y, Yin J. Design of cut unit geometry in hierarchical kirigami-based auxetic metamaterials for high stretchability and compressibility[J]. *Extreme Mechanics Letters*, 2017, 12: 77-85.
- [140] Cho Y, Shin J H, Costa A, et al. Engineering the shape and structure of materials by fractal cut[J]. *Proceedings of the National Academy of Sciences*, 2014, 111(49): 17390-17395.
- [141] Dudte L H, Choi G P T, Becker K P, et al. An additive framework for kirigami design[J]. *Nature Computational Science*, 2023, 3(5): 443-454.
- [142] Choi G P T, Dudte L H, Mahadevan L. Compact reconfigurable kirigami[J]. *Physical Review Research*, 2021, 3(4): 043030.
- [143] Choi G P T, Dudte L H, Mahadevan L. Programming shape using kirigami tessellations[J]. *Nature Materials*, 2019, 18(9): 999-1004.
- [144] Jiang C, Rist F, Wang H, et al. Shape-morphing mechanical metamaterials[J]. *Computer-Aided Design*, 2022, 143: 103146.
- [145] Jin L, Forte A E, Deng B, et al. Kirigami-inspired inflatables with programmable shapes[J]. *Advanced Materials*, 2020, 32(33): 2001863.
- [146] Konaković M, Crane K, Deng B, et al. Beyond developable: Computational design and fabrication with auxetic materials[J]. *ACM Transactions on Graphics*, 2016, 35(4): 1-11.
- [147] Castle T, Cho Y, Gong X, et al. Making the cut: Lattice *kirigami* rules[J]. *Physical Review Letters*, 2014, 113(24): 245502.
- [148] Castle T, Sussman D M, Tanis M, et al. Additive lattice kirigami[J]. *Science Advances*, 2016, 2(9): e1601258.
- [149] Sussman D M, Cho Y, Castle T, et al. Algorithmic lattice kirigami: A route to pluripotent materials[J]. *Proceedings of the National Academy of Sciences*, 2015, 112(24): 7449-7453.
- [150] Xie R, Chen Y, Gattas J M. Parametrisation and application of cube and eggbox-type folded geometries[J]. *International Journal of Space Structures*, 2015, 30(2): 99-110.
- [151] Eidini M, Paulino G H. Unraveling metamaterial properties in zigzag-base folded sheets[J]. *Science Advances*, 2015, 1(8): e1500224.
- [152] Eidini M. Zigzag-base folded sheet cellular mechanical metamaterials[J]. *Extreme Mechanics Letters*, 2016, 6: 96-102.
- [153] Jamalimehr A, Mirzajanzadeh M, Akbarzadeh A, et al. Rigidly flat-foldable class of lockable origami-inspired metamaterials with topological stiff states[J]. *Nature Communications*, 2022, 13(1): 1816.

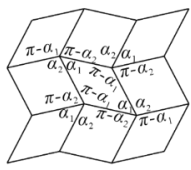
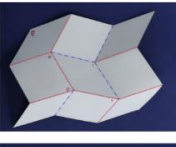

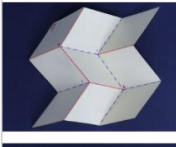
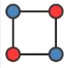
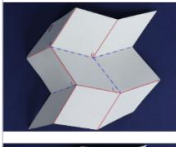
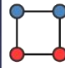
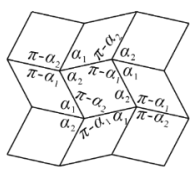
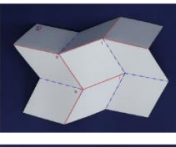

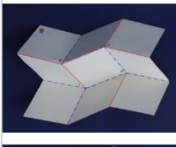
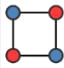
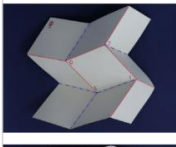
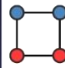
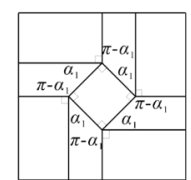
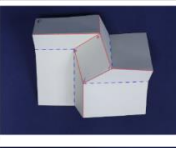
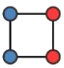
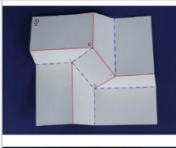
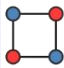

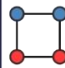
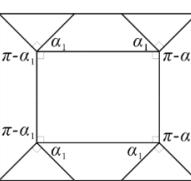

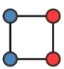
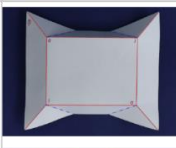
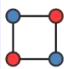
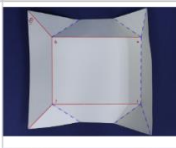
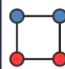
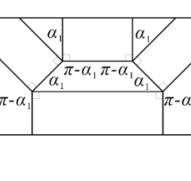
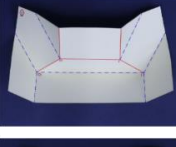
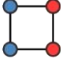
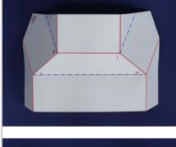
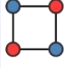
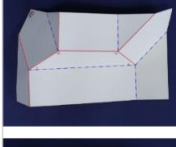

- [154] Tang Y, Li Y, Hong Y, et al. Programmable active kirigami metasheets with more freedom of actuation[J]. *Proceedings of the National Academy of Sciences*, 2019, 116(52): 26407-26413.
- [155] Zhang X, Ma J, Li M, et al. Kirigami-based metastructures with programmable multistability[J]. *Proceedings of the National Academy of Sciences*, 2022, 119(11): e2117649119.
- [156] Gu Y, Chen Y. Origami cubes with one-DOF rigid and flat foldability[J]. *International Journal of Solids and Structures*, 2020, 207: 250-261.
- [157] Zhang Y, Gu Y, Chen Y, et al. One-DOF rigid and flat-foldable origami polyhedrons with slits[J]. *Acta Mechanica Solida Sinica*, 2023, 36(4): 479-490.
- [158] Callens S J P, Zadpoor A A. From flat sheets to curved geometries: Origami and kirigami approaches[J]. *Materials Today*, 2018, 21(3): 241-264.
- [159] Sun Y, Ye W, Chen Y, et al. Geometric design classification of kirigami-inspired metastructures and metamaterials[J]. *Structures*, 2021, 33: 3633-3643.
- [160] Tarnai T, Kovács F, Fowler P W, et al. Wrapping the cube and other polyhedra[J]. *Proceedings of the Royal Society A: Mathematical, Physical and Engineering Sciences*, 2012, 468(2145): 2652-2666.
- [161] Simon L, Arnstein B, Gurkewitz R. *Modular origami polyhedra: Revised and enlarged edition*[M]. Courier Corporation, 2012.
- [162] Sarrus P. Note sur la transformation des mouvements rectilignes alternatifs, en mouvements circulaires, et reciproquement[J]. *Comptes. Rendus, Acad. Sci., Paris*, 1853, 36: 1036-1038.
- [163] Yang Y, You Z. A modular origami-inspired mechanical metamaterial[J].
- [164] Yang Y, Zhang X, Maiolino P, et al. Linkage-based three-dimensional kinematic metamaterials with programmable constant Poisson's ratio[J]. *Materials & Design*, 2023, 233: 112249.
- [165] Ma J, Jiang X, Chen Y. A 3D modular meta-structure with continuous mechanism motion and bistability[J]. *Extreme Mechanics Letters*, 2022, 51: 101584.
- [166] Yang N, Silverberg J L. Decoupling local mechanics from large-scale structure in modular metamaterials[J]. *Proceedings of the National Academy of Sciences*, 2017, 114(14): 3590-3595.
- [167] Overvelde J T B, De Jong T A, Shevchenko Y, et al. A three-dimensional actuated origami-inspired transformable metamaterial with multiple degrees of freedom[J]. *Nature Communications*, 2016, 7(1): 10929.
- [168] Overvelde J T B, Weaver J C, Hoberman C, et al. Rational design of reconfigurable prismatic architected materials[J]. *Nature*, 2017, 541(7637): 347-352.

- [169] Xiao K, Liang Z, Zou B, et al. Inverse design of 3D reconfigurable curvilinear modular origami structures using geometric and topological reconstructions[J]. *Nature Communications*, 2022, 13(1): 7474.
- [170] Li Y, Yin J. Metamorphosis of three-dimensional kirigami-inspired reconfigurable and reprogrammable architected matter[J]. *Materials Today Physics*, 2021, 21: 100511.
- [171] Li Y, Zhang Q, Hong Y, et al. 3D transformable modular kirigami based programmable metamaterials[J]. *Advanced Functional Materials*, 2021, 31(43): 2105641.
- [172] Tarjan R. Depth-first search and linear graph algorithms[J]. *SIAM Journal on Computing*, 1972, 1(2): 146-160.
- [173] Barreto R L P, Morlin F V, De Souza M B, et al. Multiloop origami inspired spherical mechanisms[J]. *Mechanism and Machine Theory*, 2021, 155: 104063.
- [174] Liu S, Lv W, Chen Y, et al. Deployable prismatic structures with rigid origami patterns[J]. *Journal of Mechanisms and Robotics*, 2016, 8(3): 031002.
- [175] Zhai J, Zhang D, Li M, et al. An approximately isotropic origami honeycomb structure and its energy absorption behaviors[J]. *Materials*, 2023, 16(4): 1571.
- [176] Liu W, Jiang H, Chen Y. 3D programmable metamaterials based on reconfigurable mechanism modules[J]. *Advanced Functional Materials*, 2022, 32(9): 2109865.
- [177] Nelson T G, Lang R J, Magleby S P, et al. Curved-folding-inspired deployable compliant rolling-contact element (D-CORE)[J]. *Mechanism and Machine Theory*, 2016, 96: 225-238.
- [178] Grima J N, Evans K E. Auxetic behavior from rotating squares[J]. *Journal of Materials Science*, 2000, 19: 1563-1565.
- [179] Hunt K H. *Kinematic geometry of mechanisms*[M]. Oxford: New York: Clarendon Press; Oxford University Press, 1978.
- [180] Home C E, Hann M A. The geometrical basis of patterns and tilings: A review of conceptual developments[J]. *Journal of the Textile Institute*, 1998, 89(1): 27-46.
- [181] Liu L, Choi G P T, Mahadevan L. Wallpaper group kirigami[J]. *Proceedings of the Royal Society A: Mathematical, Physical and Engineering Sciences*, 2021, 477(2252): 20210161.
- [182] Wohlhart K. Regular polyhedral linkages[C]. *Proceedings of the 2nd Workshop on Computational Kinematics*. Seoul, 2001.
- [183] Bingham C M, Tao H, Liu X, et al. Planar wallpaper group metamaterials for novel terahertz applications[J]. *Optics Express*, 2008, 16(23): 18565.

- [184] Padilla W J. Group theoretical description of artificial electromagnetic metamaterials[J]. *Optics Express*, 2007, 15(4): 1639.
- [185] Yu P, Kupriianov A S, Dmitriev V, et al. All-dielectric metasurfaces with trapped modes: Group-theoretical description[J]. *Journal of Applied Physics*, 2019, 125(14): 143101.
- [186] Mao Y, He Q, Zhao X. Designing complex architected materials with generative adversarial networks[J]. *Science Advances*, 2020, 6(17): eaaz4169.
- [187] Gogu G. Mobility of mechanisms: A critical review[J]. *Mechanism and Machine Theory*, 2005, 40(9): 1068-1097.

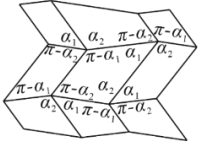
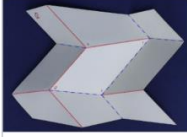
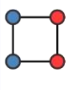
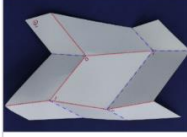
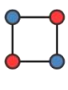
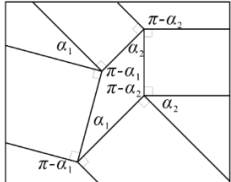
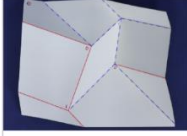
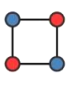
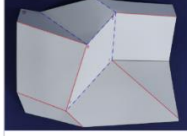
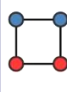
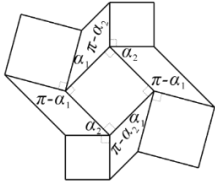
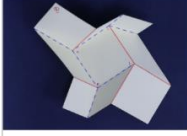
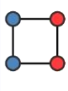
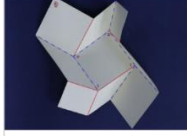
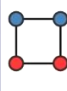
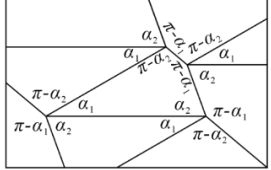
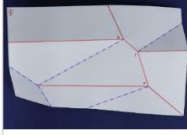
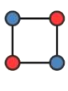
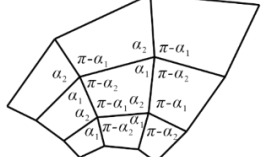
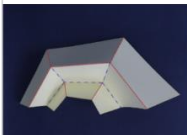
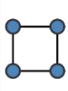
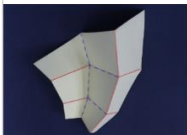
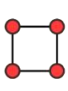
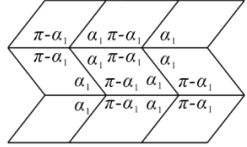
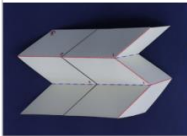

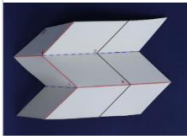

Appendix

A. The Prototypes Made up of Cardboard of 18 Typical Modules

	Modules	Prototypes and their graphic representations					
1	$\alpha_1=30^\circ, \alpha_2=70^\circ$ 						
2	$\alpha_1=30^\circ, \alpha_2=70^\circ$ 						
3	$\alpha_1=45^\circ$ 						
4	$\alpha_1=45^\circ$ 						
5	$\alpha_1=45^\circ$ 						

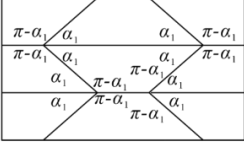
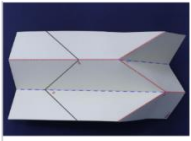
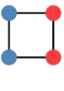
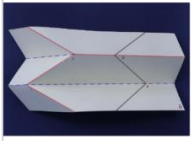
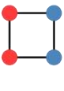
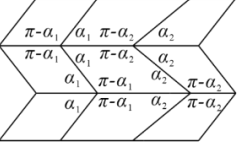
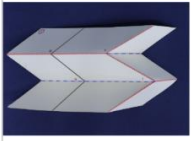
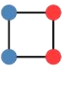
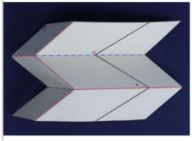
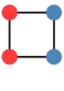
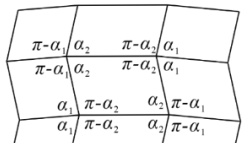
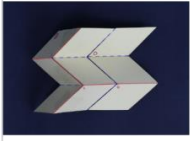

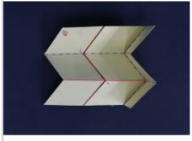

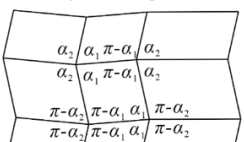
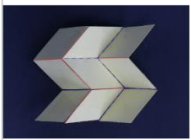
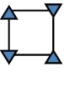
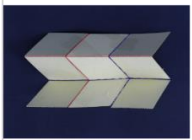
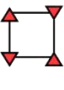
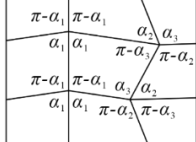
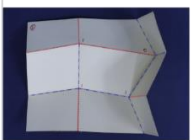

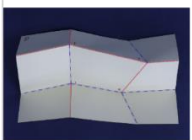

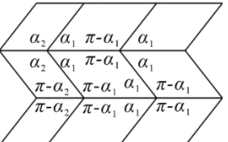


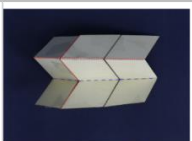

continued on next page

continued

	Modules	Prototypes and their graphic representations			
6	$\alpha_1=30^\circ, \alpha_2=60^\circ$ 	 	 		
7	$\alpha_1=30^\circ, \alpha_2=45^\circ$ 		 	 	
8	$\alpha_1=30^\circ, \alpha_2=45^\circ$ 	 		 	
9	$\alpha_1=30^\circ, \alpha_2=70^\circ$ 		 		
10	$\alpha_1=70^\circ, \alpha_2=100^\circ$ 	 	 		
11	$\alpha_1=60^\circ$ 	 	 		

(continued on next page)

continued

	Modules	Prototypes and their graphic representations			
12	$\alpha_1 = 45^\circ$ 				
13	$\alpha_1 = 60^\circ, \alpha_2 = 45^\circ$ 				
14	$\alpha_1 = 45^\circ, \alpha_2 = 70^\circ$ 				
15	$\alpha_1 = 45^\circ, \alpha_2 = 70^\circ$ 				
16	$\alpha_1 = 70^\circ, \alpha_2 = 45^\circ, \alpha_3 = 105^\circ$ 				
17	$\alpha_1 = 45^\circ, \alpha_2 = 70^\circ$ 				

(continued on next page)

continued

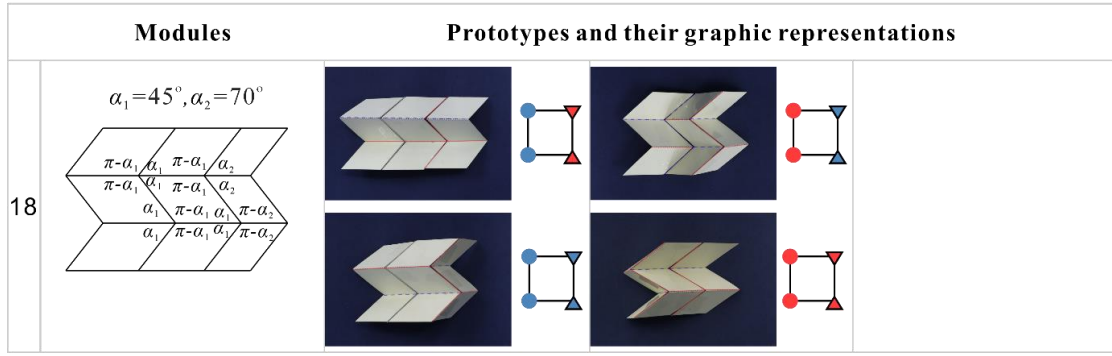
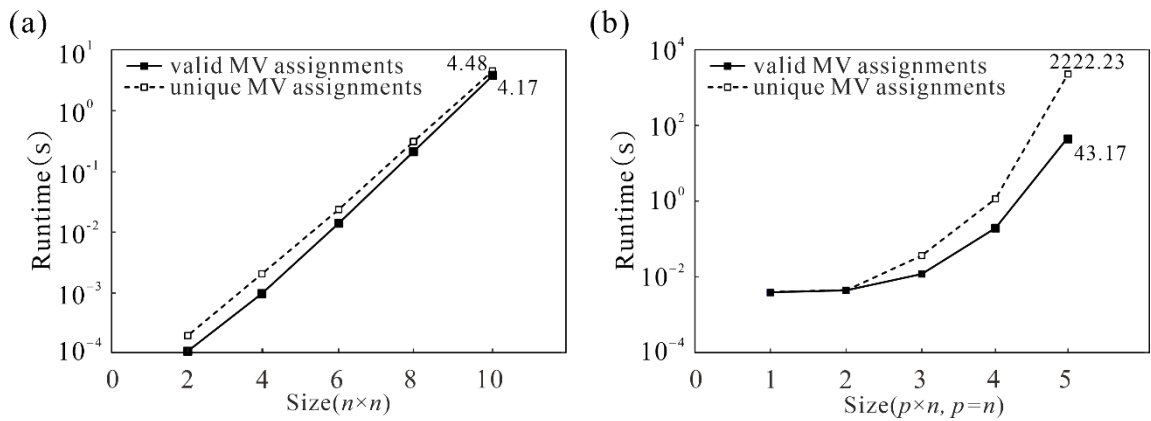


Fig. A1 Prototypes and graphic representations of eighteen typical modules.

B. Runtime of the Algorithm

The runtime of the algorithm is provided in Fig. B1, performed on a Linux Ubuntu 20.04 server with two Intel Xeon Silver 4310 2.10 GHz CPUs, 128GB memory. For the 2D tessellation, the runtime of the algorithm for obtaining valid MV assignments increases from about 1×10^{-4} s to 4.17s when the tessellation size is increased from 2×2 to 10×10 , and even with the removal of duplicate configurations, it takes only 4.48s. For a large 3D tessellation, e.g., $5 \times 5 \times 5$ tessellations (contains 2×10^8 valid MV assignments), it takes about 43.17s to compute all MV assignments that satisfy rigid foldability and 2222.23s to remove duplicate configurations. These results fully demonstrate the efficiency of the proposed algorithm.


 Fig. B1 Runtime of the algorithm for (a) the $n \times n$ double corrugated pattern and (b) the $m \times n \times p$ cellular origami structure.

C. All Unlocking Possibilities of VTJs in a Single Reconfigurable Ori-Kirigami Unit

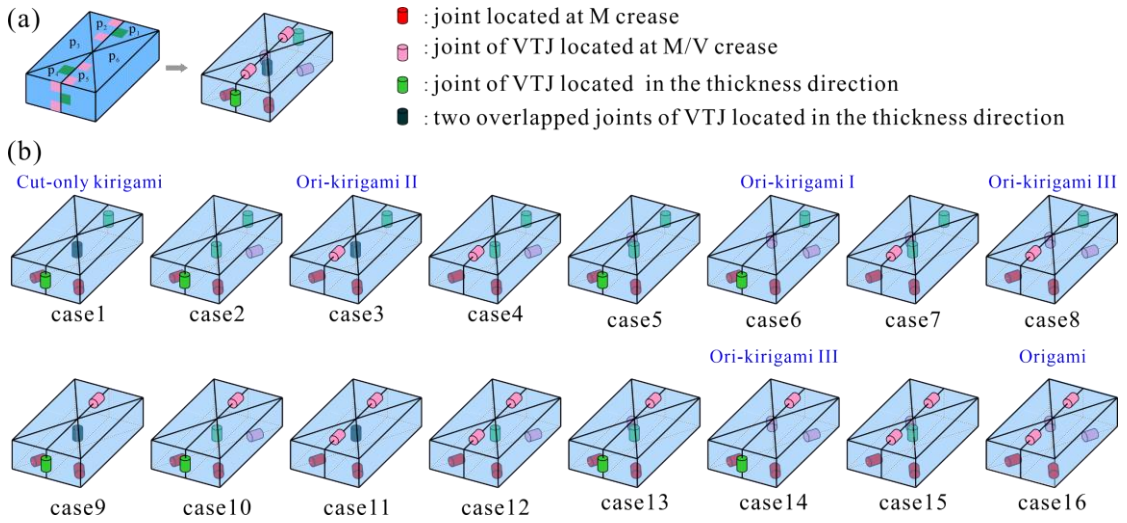


Fig. C1 All unlocking possibilities of VTJs in a single reconfigurable ori-kirigami unit. (a) Linkage form of the thick-panel unit after the crease has been replaced by VTJs; (b) sixteen unlocking options, where case 1, case 3, case 6, case 8, case 14, and case 16 have global mobility.

D. All 25 Configurations of the Origami Module with $n=4$.

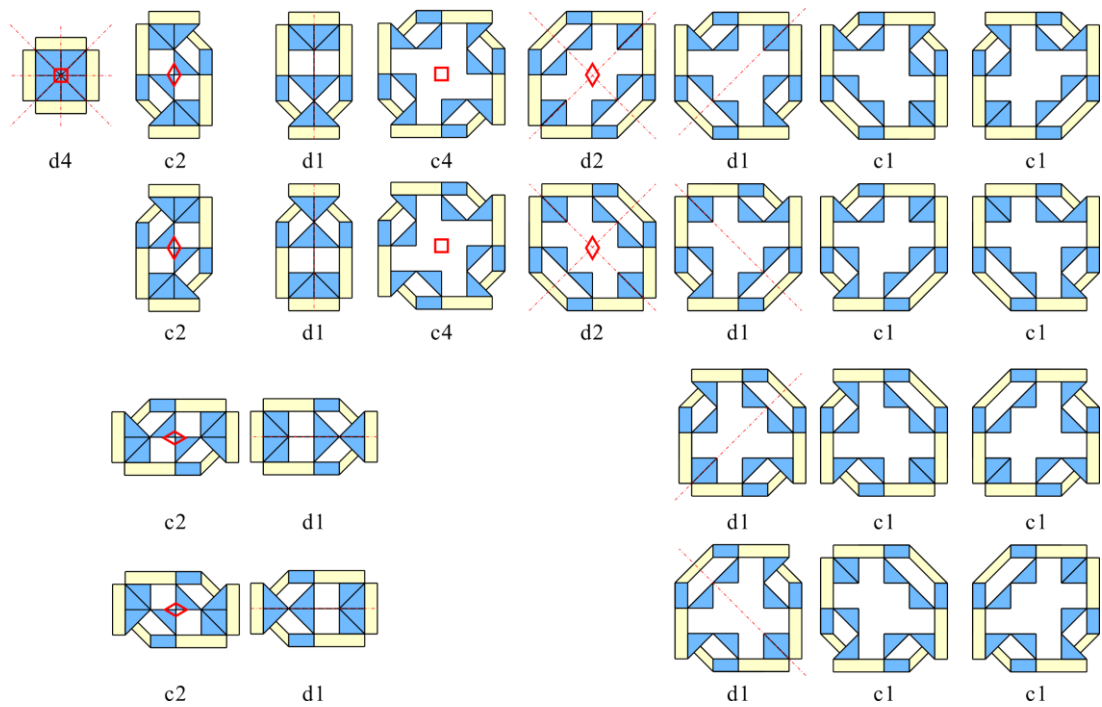


Fig. D1 All 25 Configurations of the origami module with $n=4$.

E. Analysis of the Degrees of Freedom of the Tessellations

The results of the kinematic analysis in sections 4.2 and 4.3 show that the module is single DOF. The upper platform of the module is always located in the plane. Two rectangular panels in the same 7R unit make a relative translational motion along the V shape of angle α . Hence, each 7R unit can be regarded as a prismatic joint, then the 2×2 tessellation of the modules with $n=4$ obtained in Fig. E1(a) left can be simplified as an equivalent mechanism with four prismatic joints donated by P_1 to P_4 as indicated in Fig. E1(a) right. Therefore, referring to the Grübler-Kutzbach criterion^[187], DOF of the equivalent mechanism can be determined by $\text{DOF} = d(n - g - 1) + \sum_i^g f_i$, where d is given by the dimension of the displacement subgroup associated with the kinematic chain ($d=2$ for the mechanism with only prismatic joints), n is the number of rigid links, g is the number of kinematic pairs, and f_i is the number of DOFs for the i th kinematic pair. Hence, DOF of planar 4P mechanism is $\text{DOF} = 2(4 - 4 - 1) + 4 = 2$.

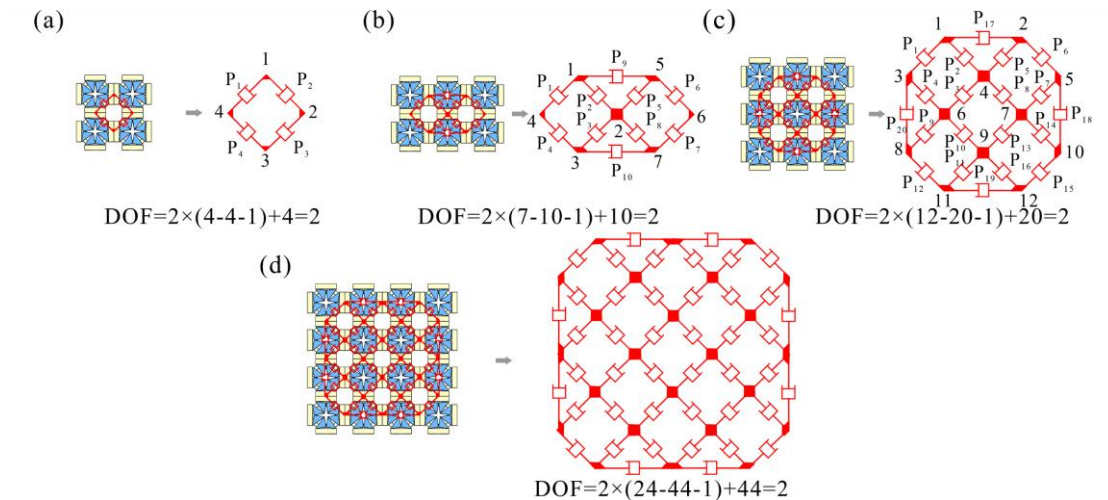


Fig. E1 The schematic diagram of equivalent mechanism with prismatic joints for the tessellation of the modules with $n=4$.

As the number of modules in the horizontal direction increases, another loop is formed, again creating a 4P (P_5 to P_8) mechanism. The middle modules connecting the two planar 4P mechanisms is single degree of freedom. Therefore, prismatic joints (P_9 to P_{10}) can be added to form planar 3P mechanisms (P_2, P_5, P_9 , or P_3, P_8, P_{10}) with one DOF to represent this constraint, as shown in Fig. E1(b). Consequently, DOF of 2×3 tessellation of the modules with $n=4$ is 2. Similarly, as the number of modules in

the vertical direction increases, the DOFs are maintained at 2, because two adjacent planar 4P mechanisms on the outer loop share a single DOF planar 3P mechanism. Overall, the DOFs of the tessellation of the modules with $n=4$ are constant 2.

Using a similar approach, the DOF of the tessellation of the modules with $n=6$ is constant 1, since its equivalent mechanism with prismatic joints is an assembly of planar 3P mechanisms with one DOF, as indicated in Fig. E2.

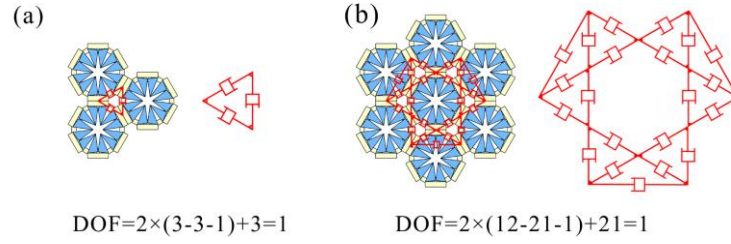


Fig. E2 The schematic diagram of equivalent mechanism with prismatic joints for the tessellation of the modules with $n=6$.

F. Kinematic Paths When the Basic Unit Switches Between M1 and M3

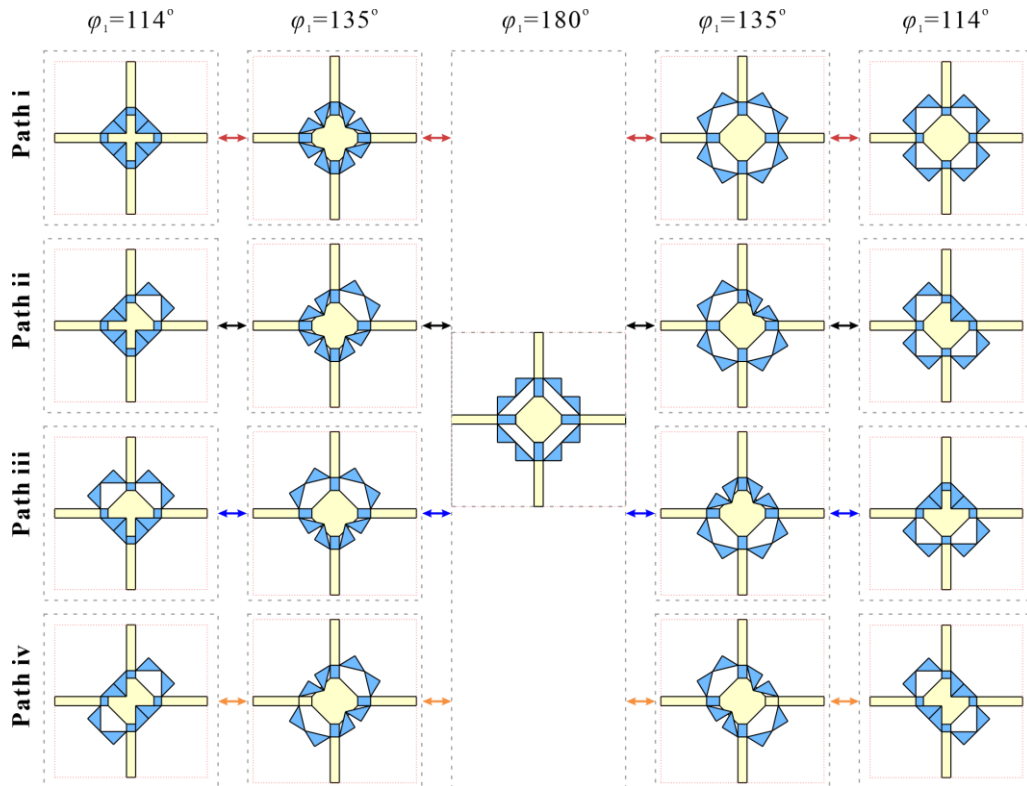
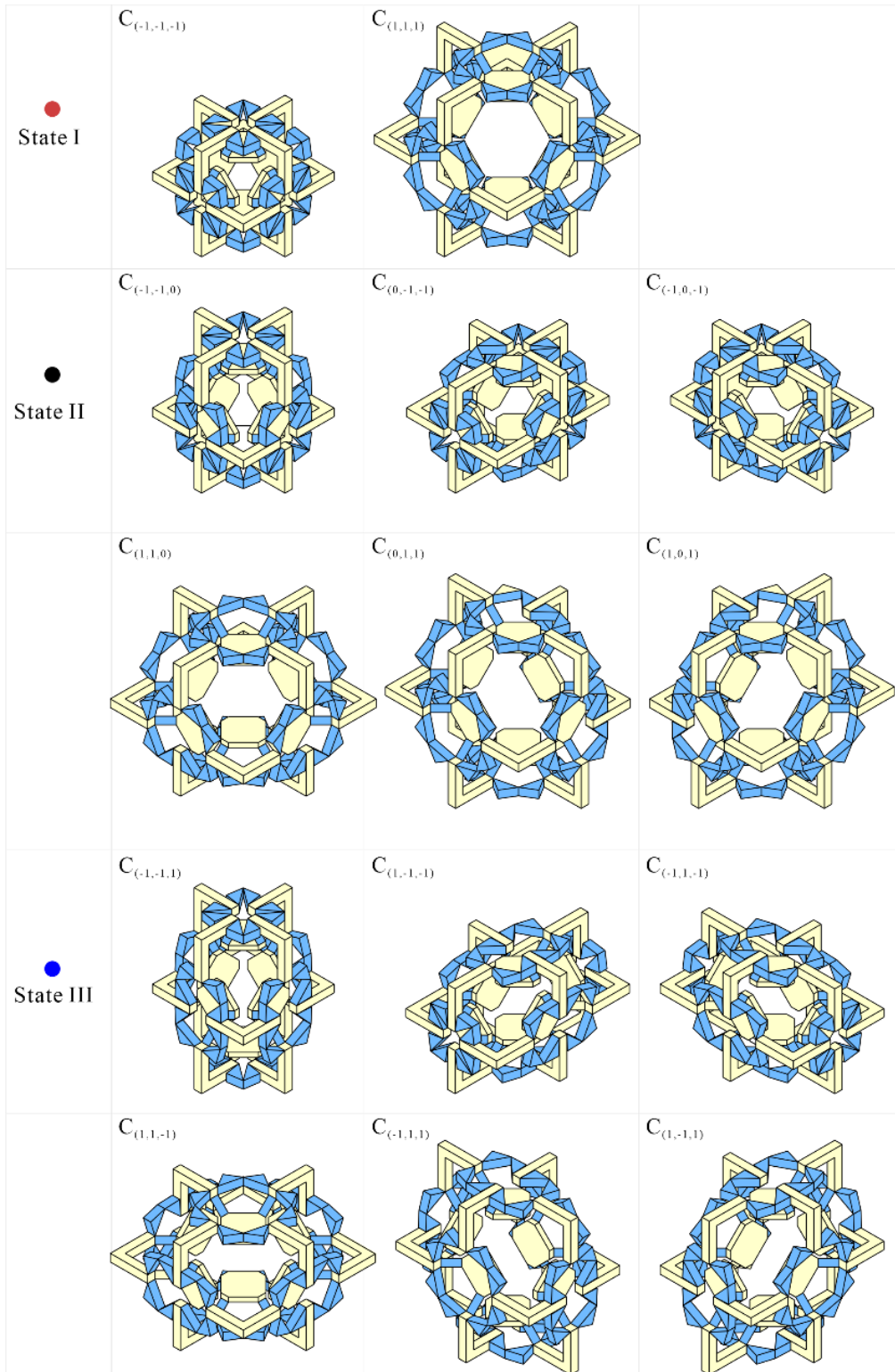


Fig. F1 Top view of kinematic paths of the 2D module with $b/a = \sqrt{2}$, $\alpha = 90^\circ$ when the basic unit switches between M1 and M3.

G. 27 Cases of 3D Modules with a Rectangular Prism ($N=4$) Contour



(continued on next page)

(continued)

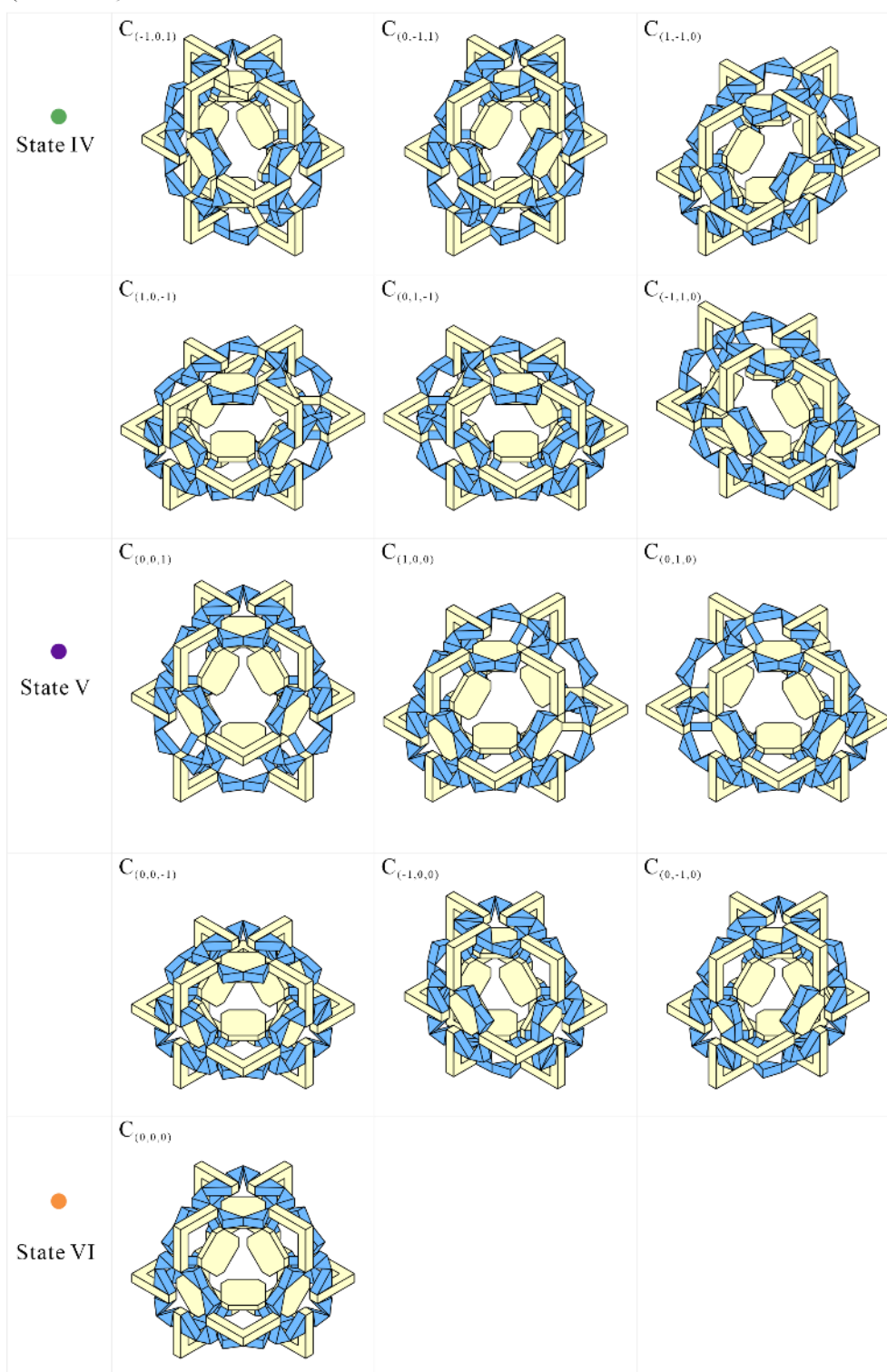


Fig. G1 $3^3 = 27$ cases of 3D modules with a rectangular prism ($N=4$) contour. The marker at the top left of configurations, $C_{(x,y,z)}$, $x, y, z = -1, 0,$ and 1 , indicates that rectangular prisms in the x, y, z direction are positioned in “-1”, “0”, and “1” states and that the sign of the infinitesimal strains $\varepsilon_B, \varepsilon_W,$ and ε_H strain is either negative, zero or positive.

H. Utilising Flexible Beam for Achieving Bistability

The introduction of a flexible beam offers the potential for achieving bistability. As shown in Fig. H1(a), a 2D module with $b/a = \sqrt{2}$, $\alpha = 90^\circ$, $t_3 = t_2 = t_1 = a/2$ and $\beta = \gamma = 45^\circ$ in a back-to-back assembly is employed to exemplify this concept. In this case, the fully folded module exhibits bi-directional expansion along path I, even past the bifurcation point $\varphi_1 = \pi/2$, ultimately reaching the end configuration where $\pi/2 < \varphi_1 < \pi$. In this fully unfolded configuration, the rectangular panels form multiple trapezoids with rigid sheets, granting the module load-bearing capacity (Fig. H1(b)).

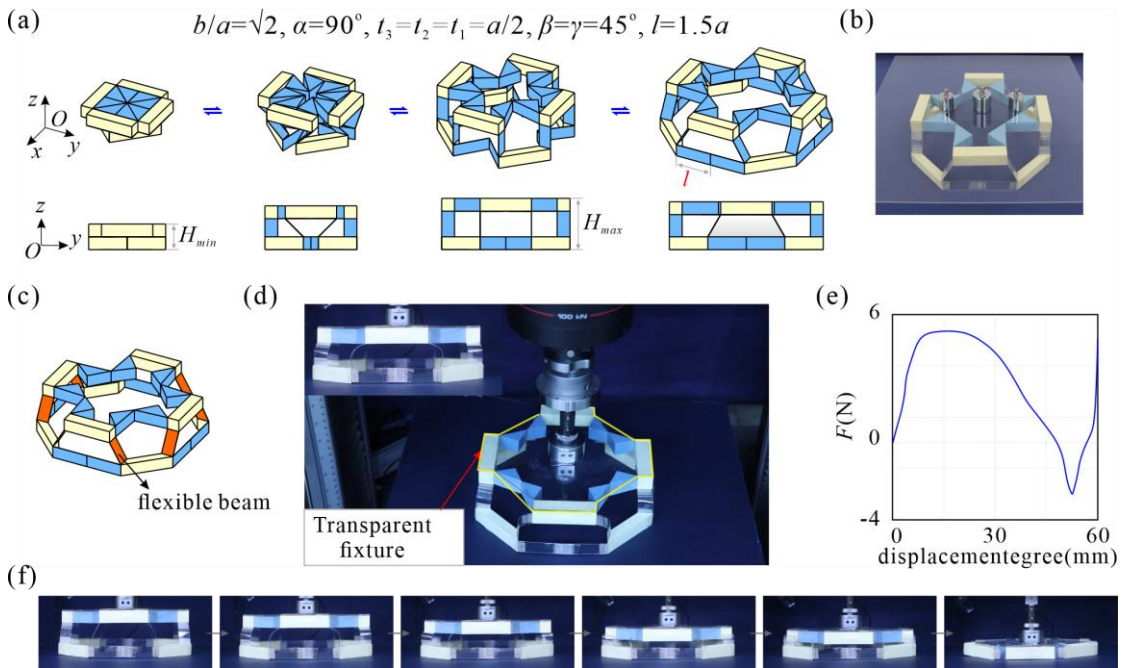


Fig. H1 Bi-stable module using flexible beam. a) Rigid unfolding process of the module; b) load-bearing state; (c) origami module containing flexible beams; (d) experimental setup; (e) experimental results of force-displacement curve; (f) recorded deformation processes.

To implement bistability, the rigid sheets connecting the two platforms in the origami module are replaced with eight flexible beams (made of PET, $t=0.2\text{mm}$). A quasi-static test was conducted using a vertical testing machine (Instron 5982) with a transparent fixture (60mm displacement and a 0.5 mm s⁻¹ loading rate), as depicted in

(c). The deformation process was recorded by cameras positioned above and in front of the setup. The recorded force-displacement response during folding and unfolding is displayed in Fig. H1(e), while corresponding recorded deformed

configurations presented in Fig. H1(f). In the initial phase, as the displacement increased, the beam started to bend, leading to a nearly linear increase in the recorded force from 0 N. As the displacement continued to increase, the beam began to rotate around the connecting edge with the panel, and the force started to decrease. When the two connecting edges of the beam approached a horizontal position, a snap-through was observed, resulting in a negative force (-2.4 N) and reaching the second stable state of the structure. Finally, the entire module was compacted, and the force began to increase dramatically as the distance decreased, with the load reverting its sign to positive.

中文大摘要

机械超材料是一种人工设计的新型复合材料或结构，由于特殊的胞元几何和空间排布，表现出自然材料所不具备的非常规机械特性。随着对超材料的深入研究，机械超材料的发展经历了从基于固定拓扑几何结构的定性设计，逐渐演变为在使用过程中通过拓扑的主动或被动变化对其性能进行调控和编程的阶段。因此，涌现出一大批利用结构的形状变形来实现大变形机械超材料的可控性和可编程性的方法。在这些方法中，基于机构运动的机械超材料的变形模式类似于底层机构的零能量运动，使得胞元间形变传递衰减较小，变形路径可靠且易于建模，这对于实现可控性和可编程性至关重要。

刚性折纸是一类基于机构运动的折纸结构，通过沿预定折痕将二维材料折叠成复杂的三维结构。在其成型过程中，变形仅发生在折痕区域，而主体板面则不发生扭曲或拉伸等变形。刚性折纸为基于机构运动的大变形机械超材料设计提供了一种新思路。刚性折纸的运动学模型主要是球面机构及其网格，虽然具有明确的几何参数与机械性能的理论模型关系，但其变形模式相对单一。包括纯剪纸与折剪一体的剪纸技术通过引入剪痕突破了机构胞元球面几何的束缚，使得其设计更加灵活。模块化折纸结构作为折纸领域的生力军，与折纸与剪纸不同，它允许粘接并具有无穷的设计空间和丰富的变形模式。然而，针对单一结构的多变形模式机械超材料，现有的折纸设计缺乏底层机构理论指导，导致超材料的胞元要么形状变化不显著，要么是需要相对复杂控制的多自由度系统。

除了多自由度，实现多构型重构的另一种机构学方法是运动分岔，它指的是多条运动路径的交点。运动学分岔与多自由度系统的不同之处在于，前者只能在分岔点的运动路径之间切换。一旦通过该点，后续运动就由选定的路径决定。因此，具有运动学分岔能力的单自由度折纸结构使其成为设计具有可调性能的大变形超材料的理想选择。除了特殊拓扑的胞元结构，胞元间的连接方式对超材料的大变形行为也有着决定性的作用。因此，可以借鉴机构组网的研究成果，根据胞元的变形特征，利用平面、球面、与空间机构的混合机构网格研究不同分叉构型之间的几何与运动协调性，以保持和协调胞元的运动变形与重构特征，从而利用超材料可靠的、可重构的大变形来实现性能的可调控性可编程性。

综上所述，机械超材料在构建过程中面临的一大难题是可控性和可编程性。尽管基于机构运动的折纸结构在设计空间、变形能力、性能调控范围等方

面的优势明显，但在具有多变形模式的单自由度结构设计、以及性能调控和编程策略方面，仍然缺少系统的研究方法。

本文基于可重构机构的设计方法与组网原理，旨在利用机构的运动分岔来实现多形状重构的单自由度折纸结构的创新设计，以期发展为具有可调和可编程性能的机械超材料。本文首先以零厚度四折折痕纸图案为研究对象，提出了一种结合机构运动协调条件和图形表示的通用算法，在大型 2D 和 3D 折纸镶嵌中精准辨识所有满足刚性可折叠性的山谷线分布方案并去除重复构型。其次，基于可垂直转移铰链技术，设计了具有折纸、纯剪纸、折-剪纸变形模式的单自由度可重构厚板结构。接着，设计了基于单环路空间 7R 机构的模块化折纸单元，提出两种单元装配方案，形成了两套单自由度折纸模块，并分别发展为可实现所有晶体学平面对称群和可定制泊松比符号的可重构 2D 和 3D 超材料。最后，研究了开环平面连杆组的运动学为行为，揭示了单自由度立方体模块在运动分叉过程中伴随着的可调的泊松比、手性以及刚度等特性。还提出了组合设计策略，以增强 3D 超材料的泊松比的可编程性。本文的工作主要包括如下四个部分：

• 四折痕折纸及其镶嵌的山谷线重构

在本文第二章中，将在大型二维折纸镶嵌或三维蜂窝结构中寻找所有满足刚性可折叠性的山谷线分布方案转化为棋盘着色问题，并使用编程语言进行求解，解决了这一难题。首先，采用模块化思想，将折纸镶嵌划分为由基本模块和连接模块组成的棋盘格。随后，利用球面 4R 机构网格的运动协调条件，建立这些模块图形与矩阵的表达形式。最后，利用深度优先算法系统地遍历棋盘，寻找符合既定规则的图形方案，并最终将其转换为具有特定折痕图的折纸图案。这种方法不仅精确提供了的所有满足刚性可折叠性的山谷线分布方案，还利用图案的对称性消除了大量重复的几何构型。所提出的方法通过一系列著名的二维折纸镶嵌（包括 double corrugated 图案，square twist 图案，generalised Mars 图案等）得到验证，并进一步扩展到三维蜂窝折纸结构。在研究过程中，发现了三种类型的寡模态折纸图案，即 dual square twist 图案，generalised Huffman 图和 Helical 图案，其特点是山谷线分布数量 (≥ 2) 与镶嵌大小无关，设计了山谷线分布数量随镶嵌大小呈指数增长的多模式蜂窝折纸结构。其理论分析和实验结果表明，可以通过操纵单个零厚度折纸结构中的山谷线分布，实现在大变形下的负、零和正的面内泊松比可调。

第二章工作为基于山谷线重构原理的多功能结构设计提供了理论基础与技术支撑。

• 基于可转移铰链的可重构厚板剪纸

针对工程折展结构的厚度不能忽略、多模式折叠过程中存在严重的物理干涉等问题，第三章从可重构铰链的视角，提出了具有厚板折纸、剪纸、折-剪纸模式的单自由度可重构厚板剪纸结构。

首先，受 Jacob's Ladder Toy 的启发，提出了垂直转移铰链。该可重构铰链通过运动分叉行为，能够改变铰链的轴线方向而不增加系统的自由度。然后，将 diamond 厚板折纸顶点中的四个普通旋转铰链替换为垂直转移铰链，构造了一个可重构剪纸单元。该可重构单元具有厚板折纸、剪纸、折-剪纸等五条运动分支。接着，通过求解可重构单元在不同运动分支下对应的机构的闭环方程，分析了设计参数对折叠行为的影响。通过轴线位于厚度方向的旋转铰链连接基本单元及其水平镜像，同时用垂直转移铰链连接基本单元及其垂直镜像，构造了具有单自由度特性的 2×2 镶嵌。当可重构单元中垂直转移铰链在展平构型下的全部解锁为位于面板的上下表面时，表现为厚板折纸模式，其镶嵌从具有均匀厚度的方形面板折叠为紧密无缝隙的一摞。当可重构单元中垂直转移铰链在展平构型下的全部解锁为位于面板的厚度方向时，表现为剪纸模式，方形面板其镶嵌可在面内打开。当可重构单元中垂直转移铰链在展平构型下部分解锁为位于面板的厚度方向，部分解锁为位于面板的上下表面时，表现为三种厚板折-剪纸模式镶嵌，同时产生面内和面外变形。折纸镶嵌在不同运动分支重构时，均存在面内负泊松比。最有趣的是剪纸分支，该镶嵌存在两级变形。在第一级变形过程中的泊松比是各向异性的，而当其进入第二级变形时，泊松比是各向同性的-1。此外，还考虑了当折纸镶嵌进入不同的运动分支时，折展比的变化。以平板构型为参考，折纸模式折叠后的截面投影为原来的 $1/8$ ，剪纸模式模式可以展开到原来的 3 倍投影面积，整个结构的整体折展比可以达到 $1/24$ 。还研究了五个运动分支完全折叠或完全展开构型下的承载能力，实验结果表明折纸运动分支下的紧密折叠行为使得三个方向均能承载，45 克的卡纸模型能够承受 705N 的载荷，实现了 1567 倍自重的高承载能力，剪纸运动分支在展开构型下两个方向均表现为易折叠的状态。同时折-剪纸分支 I 在展开构型下的自锁行为使三个方向的承载能力分别达到 86, 74, 274 倍自重的承载，并且这种承载能力还被折-剪纸分支 III 的面接触自锁构型得到显著增强。

第三章所提出的设计方法不仅适用于构造多变形模式厚板结构，而且为从机构学的角度深入理解折纸、剪纸、折-剪纸结构的折叠变形奠定了基础。

● 基于单环路空间 7R 机构的性能可调超材料

第三章的可重构厚板剪纸研究表明机构的运动分叉是实现折纸多构型变化、超材料性能大范围可调的关键。因此，第四章将具有运动分叉的能力的连杆机

构设计成构型更规则、参数更丰富，功能更强大模块化折纸，并发展为超材料。

首先，提出了一种单环路的空间单自由度 $7R$ 机构的模块化折纸单元。建立了其运动学模型，系统分析了几何参数对该基本单元的运动分支的数量、区间，构型演变规律，和物理干涉等运动学行为的影响。运动学分析结果表明，该 $7R$ 单元可能存在 $M1-M4$ 共 4 种典型的运动模式，且在 $M1$ 和 $M2$ 运动模式之间分叉时，形状和对称性会发生明显变化。其次，以折叠后形成紧密的 n 多边形为目标，将 n 个 $7R$ 单元按照背靠背的方式装配在一起，并通过额外的连杆形成的单环路约束，确保整个模块仍然具有一个自由度。通过合理设计几何参数，使得每个单元在模块中仍然具有在 $M1$ 和 $M2$ 运动模式之间分叉的能力。系统地分析了 2D 模块重构过程引起的面内对称性变化，其中 $n=4$ 的模块和 $n=6$ 的模块的对称性变化涵盖了全部 10 个晶体学平面点群。接着，构造了模块的线性镶嵌和平面镶嵌，其中 $n=4$ 的模块的线性镶嵌可以实现全部 7 个晶体学平面线群，而 $n=4$ 和 $n=6$ 的模块的平面镶嵌涵盖了全部 17 个晶体学平面空间群（壁纸组）。根据模块的变形特点，提出了一种基于变刚度智能材料的对称性主动控制方法。将模块中连接上下平台的八根梁用变刚度材料替代，然后通过电流独立地编码控制变刚度梁处于“软”或“硬”状态，从而使整个模块在单轴压缩载荷下自动的变形到所需的对称性构型。还提出了响应速度更快的气动控制方案。在单个模块的四个关节处安装 8 个气囊，利用气囊通气变直效应，选择性的激活不同的气囊，可以在 2 秒内将模块及其镶嵌调控到所需的对称性构型。此外，将 n 个 $7R$ 单元按照肩并肩的方式装配在一起，形成了一套新的单自由度 2D 模块。基于运动学模型的变形分析结果表明，所有的模块都存在解耦的运动分叉行为，其中 $n=4$ 的 2D 模块表现出面内的负、零和正泊松比。将 $n=3, 4, 5, 6$ 的 2D 模块分别嵌入到正三、四、五、六棱柱的上下面，并用 $n=4$ 的模块嵌入侧面，从而构造出了一类能在负、零、正泊松比模式之间重构 3D 多面体模块。其中立方体模块存在 27 种分叉构型，涵盖了正交平面上所有的泊松比符号组合的可能性。

第四章基于单环路空间 $7R$ 机构设计的两套单自由度机构模块及其构造的 2D 和 3D 可调超材料实现了晶体学平面对称群和泊松比符号的全覆盖，充分展示了从机构运动分叉角度设计性能可调的模块化折纸超材料的先进性。

• 基于可重构多面体机构模块的三维可编程超材料

与第四章的单环路机构相比，采用多面体布局的多环路过约束多面体机构具有更规则的形状和更简单的组网方式，有望直接用作 3D 模块化折纸超材料的构建模块。第五章研究了嵌入多自由度平面连杆组而构建的单自由度 Wohlhart 立方体的运动学行为，并发展为具有性能可大范围调控和编程的机械超材料。

首先，建立了开环平面连杆组在对称性约束下的运动学模型，推导了其闭环方程以揭示了运动过程中存在的分叉现象。以不同分叉构型下的平面连杆组为组件，协调地嵌入多面体的表面以重新构造 Wohlhart 立方体。发现单自由度的 Wohlhart 立方体可以通过固有的运动学分岔在可膨胀立方体、拉长棱柱和锁定的扭转路径之间连续重构。通过理论分析和实验结果共同证明了在分叉过程中伴随着的负泊松比、正泊松比和零泊松比行为。还研究了在分叉过程中伴随着的局部和整体手性，可调控的刚度，以及介绍了位移控制和力（扭矩）控制两种潜在的模块分叉控制方案。接着，将多面体模块在三维空间内通过平移、镜像、阵列等方式装配，构建了周期性的 3D 超材料，能够通过运动分叉在负泊松比、正泊松比和零泊松比模式之间连续切换。然而，它的可编程性仍然非常有限，因为理论分析的结果表明泊松比对几何参数的变化不敏感。为增强超材料的泊松比可编程性，基于几何与运动协调性提出了一种组合设计策略：取两个模块，一个在拉长棱柱路径上处于正泊松比状态，一个在可膨胀立方体路径上处于负泊松比状态，通过共用相邻面的方式连接在一起形成柱状装配体。利用模块固有的运动学分岔能力，主动地调控柱状装配体中正泊松比和负泊松比状态下的模块的比例。理论分析和实验结果表明，具有不同正泊松比和负泊松比状态下的模块比值的柱状装配体表现出可编程的机械性能，为泊松比的可调性提供了新的范式。混有正泊松比和负泊松比状态下模块的柱状装配体既可以以周期性的方式继续组装，又可以在正交方向上组装成非周期超材料。这种基于机构胞元协调运动的非周期性的 3D 超材料将原来的周期性结构的泊松比的设计空间从 $(-1, +\infty)$ 拓宽到了 $(-\infty, +\infty)$ 。且正交方向上的泊松比 ν_{HB} 和 ν_{BW} 具有和正泊松比和负泊松比状态下的模块比值相关的独立设计变量。因此通过重新配置各个方向上模块在正泊松比或负泊松比状态下的比例，首次实现了超材料在正交平面上的泊松比独立编程。最后，将伴随负、正、零泊松比模式的可重构模块从 Wohlhart 立方体推广到了一类单自由度的可重构棱柱结构。

第五章的工作为从基于运动分叉的可重构机构的角度探寻可编程超材料的胞元创新设计和空间排布，以及通过重构的手段实现性能的编程开辟了新道路。

• 总结与展望

本文在机构学、结构工程、力学和材料等学科的交叉领域，系统研究了机构分岔理论指导设计具有多形状变化能力的单自由度可重构模块化折纸的方法，为发展具有可编程性和可调控性的大变形机械超材料及其工程应用提供理论基础与技术支撑。

由于时间与精力有限，未来本文的工作还可以在如下几方面进行深入研究：

(1) 结合运动协条件和图形表示的通用算法, 可以进一步在具有丰富构型的可重构折纸结构中发现独特的均质构型, 并通过编程语言发现人力难以企及的异质构型, 这为设计和分析具有复杂机械特性的异质超材料提供了一种新思路。

(2) 将转移铰链嵌入可平折四折痕甚至是不可平折的厚板单元以及混合四、六折痕顶点的折纸图案中, 有望构造新颖的可重构剪纸结构。深入研究混合平面-球面-空间机构的网络, 有助于折剪一体折纸和模块化折纸模式的创新设计。

(3) 研究表明多自由度机构形成的单自由度机构网格表现出丰富的构型变化, 解决如何系统地用多自由度的机构单元构造单自由度的机构网格这一机构学难题不仅可以实现多模式变形结构的创新设计, 还有望带来物理性能的突破。

(4) 基于不同分叉构型形成的混合机构网格的超材料表现出优异的可调性与可编程性。当前的一大挑战是如何精准识别模块化折纸所有运动分支, 然后建立胞元构型、网格拓扑与超材料性能之间的参数化解析关系, 为所需性能逆向设计胞元几何构型与网格拓扑奠定基础, 实现超材料性能调控的飞跃性突破。

(5) 本文提出的一系列具有丰富的几何、形状变化的机械超材料, 重点关注变形引起的泊松比、对称性、刚度等物理性能的变化。这些机械超材料所具备的复杂空间几何关系、多样的变形模式以及折叠诱发的全局强非线性本构关系, 为动力学研究带来了诸多新挑战和机遇。未来将加强对机械超材料折叠诱发的动力学行为、包括双稳态和多稳态动力学行为的深入分析。同时, 开展多学科交叉的方式研究这些底层几何和形状变化尤其是对称性变化与电磁学、声学、拓扑学的本质关联。

(6) 最后, 基于机构运动分叉的机械超材料同多自由度系统相比, 虽然显著降低了控制的复杂性, 但面对胞元尺寸小、数量多的机械超材料, 仍然存在协同控制以及分叉控制方面的挑战。目前的探索性研究表明, 可以从机构-结构耦合设计的角度, 采用物理干涉、稳态跳转等“机械智能”的方式设计机构胞元, 提高该类超材料的可控性; 同时增强智能材料在分叉控制中的“干扰”属性而弱化驱动属性, 优化超材料的驱动位置和与驱动方式, 结合“机械智能+材料智能”的方式有望实现在简单机械载荷下的高效分叉控制。解决了大变形超材料的设计与驱动之后, 迎面而来的一大难题是大批量生产这类超材料的制造方法与加工工艺。

关键词: 分叉可重构机构, 折纸超材料, 零厚度折纸, 厚板折-剪纸, 模块化折纸

Publications and Research Projects during PhD's Study

Journal Papers:

- [1] Liu W, Cao S, Chen Y*. Mountain-valley crease reconfiguration of 4-crease origami vertices and tessellations[J]. International Journal of Mechanical Sciences, 2024, 273, 109224.
- [2] Liu W, Jiang H, Chen Y*. 3D programmable metamaterials based on reconfigurable mechanism modules[J]. Advanced Functional Materials, 2022, 32(9): 2109865.
- [3] Liu W, Chen Y*. A double spherical 6R linkage with spatial crank-rocker characteristics inspired by kirigami[J]. Mechanism and Machine Theory, 2020, 153: 103995.
- [4] Liu W, Song Y, Chen Y*, Zhang X*. Reconfigurable thick-panel structures based on a stacked origami tube[J]. Journal of Mechanisms and Robotics, 2024, 16(12): 121005.

Conference Papers:

- [1] Liu W, Chen Y*. Origami/kirigami-inspired reconfigurable 6R linkages and tessellations[C]. International Conference on Mechanism and Machine Science. Singapore: Springer Nature Singapore, 2022: 1333-1357.

Patents:

- [1] 陈焱、刘伟奇、杜玥宁、张霄，一种具有紧密折叠且平整展开表面的单自由度厚板结构，申请号：2023113422814，发明专利，申请日：2023.10.17.

Research Projects Participated in:

- [1] 国家自然科学基金重点项目：可编程超材料的构建理论与性能调控策略研究，项目编号 52035008.

- [2] 国家自然科学基金杰出青年项目：机构运动学与折展结构，项目编号 51825503.
- [3] 国家自然科学基金重大项目：机构-结构刚柔复合系统协同设计与连续光滑变形机理，项目编号 52192631.
- [4] 国家自然科学基金青年科学基金项目：基于运动等价的空间可展结构过约束数减少策略研究，项目编号 52105032.

Acknowledgements

Completing this PhD thesis has been a journey filled with challenges, growth, and invaluable support from numerous individuals and institutions who have played pivotal roles in my academic pursuit. First and foremost, I would like to extend my deepest gratitude to my supervisor, Prof. Yan Chen, whose guidance and mentorship have been the cornerstone of this research endeavour. Her unwavering support, insightful feedback, and dedication to my intellectual development have been instrumental in shaping both the content and quality of this thesis. Her dedication to fostering a spirit of inquiry and excellence has left an indelible mark on my intellectual pursuits.

I am also grateful to Prof. Jiayao Ma and Dr. Xiao Zhang for their advice and assistance with my research. Beyond the academic realm, their mentorship has extended to the broader aspects of life during my PhD journey. I would also like to thank my collaborators, Prof. Hanqing Jiang and Dr. Zhuang Zhang from Westlake University, whose meaningful discussions and unique perspectives enriched the scope and depth of my research. I would also like to thank the discussions with Prof. Zhong You from University of Oxford, Prof. Zijia Li from Academy of Mathematics and Systems Science of Chinese Academy of Sciences, and Prof. Jinkyu Yang from Seoul National University.

I would also like to thank Dr. Yuanqing Gu, Mr. Sibao Chai, Mr. Zhenhao Jia, Mr. Mengyue Li, Mr. Zhibo Wei, Mr. Yuehao Zhang, Miss Kaili Xi, Miss Chenjie Zhao, Mr. Weilin Lv, Mr. Jinrui Yu, Mr. Xinfeng Sun, Mr. Peng Liu, Mr. Xuesong Chen, Mr. Yuxing Song, Miss Can Lu, Miss Yuening Du. To each member, thank you for your camaraderie, support, and shared passion for research. I am grateful for the collaborative and enriching atmosphere that has defined my time in the MSL lab.

A special note of appreciation goes to my love and family, their unwavering love, encouragement, and sacrifices have been the bedrock of my academic journey.

Finally, I would like to express my gratitude for the financial backing provided by the National Natural Science Foundation of China (Projects 52035008 and 51825503). The University PhD Scholarship from Tianjin University and the National Scholarship for Doctoral Students is also gratefully appreciated.

